Fractures and faults in tight gas sandstones: a study using laboratory and field data

From the Faculty of Georesources and Materials Engineering of the
RWTH Aachen University

Submitted by

Zoltán Komoróczi, MSc

from Budapest

in respect of the academic degree of

Doctor of Natural Sciences

approved thesis

Advisors: **Univ.-Prof. Dr. Janos Urai**
apl. Prof. Dr. rer. nat. Christoph Hilgers

Date of the oral examination: 15. October 2014

Table of Contents

Acknowledgements 5
Abstract 7
Zusammenfassung 9
1 Introduction 11
1.1 Project rationale 11
1.2 Theoretical background of strength, fracturing and brittleness 12
1.3 Classification of fractures 19
1.4 Fluid flow in granular materials 27
1.5 Aim of the thesis 31
1.6 Thesis outline 32
2 Large scale analyses of fractures in sandstone – natural field analogue 33
2.1 Introduction to field study in Moab, Utah 33
2.2 Study area 38
2.3 Geology setting of the Moab area 41
2.3.1 Structural history 41
2.3.2 Stratigraphy 44
2.4 Method 46
2.5 Results 47
2.5.1 Courthouse Junction 47
2.5.2 Klondike Bluffs 57
2.6 Discussion 68
2.7 Conclusion and outlook 80
3 Microstructure analysis of sandstone fractures 83
3.1 Introduction 83
3.2 Geology setting of North Sea 88
3.2.1 Stratigraphy 88
3.2.2 Structural history of the North Sea area 89
3.3 Method 91
3.4 Results of Moab samples 92
3.4.1 Courthouse Junction samples 92
3.4.2 Klondike Bluffs samples 111
3.5 Natural fractures in North Sea sandstone samples 124
3.5.1 Sample: L5-9-1 124
3.5.2 Sample: L5-9-3 128
3.5.3 Sample: L5-9-4 134
3.6 Discussion 136
3.7 Conclusion and outlook 138
4 Correlation analysis between mechanical properties and borehole log properties in North Sea sandstones 141
4.1 Introduction of correlation analysis of mechanical properties 141
4.1.1 General introduction 141
4.1.2 Data 145
4.2 Method 147
4.2.1 Sampling method – quality control 147
4.2.2 Sample preparation 150

4.2.3 Rock physical measurements 151
4.2.4 Rock mechanical measurements 151
4.2.5 Regression analysis 154
4.3 Results 156
4.3.1 Quality control of the log data 156
4.3.2 Rock physical and mechanical measurement results 162
4.3.3 Results of regression analysis of UCS versus well logs 166
4.3.4 Results of regression analysis of elastic moduli versus well logs 180
4.3.5 Analyses of relation between laboratory-measured rock properties 187
4.4 Discussion 190
4.4.1 Mechanical characterisation of Rotliegend and Lower German Triassic Sandstone Groups 190
4.4.2 Discussion of regression analysis of UCS data 193
4.4.3 DISCUSSION OF REGRESSION ANALYSIS OF ELASTIC MODULI DATA 196
4.4.4 INTERPRETATION OF THE PREDICTED LOGS 203
4.4.5 COMPARISON OF OUR RESULTS WITH OTHER CORRELATION MODELS 203
4.5 Conclusion 208
5 Brittleness Index for North Sea sandstones 211
5.1 Introduction and background 211
5.2 Proposed new brittleness index equation (BRI_3): 218
5.3 Results: Brittleness Index logs 223
5.4 Discussion 229
5.5 Conclusion 239
6 References 241

Acknowledgements

Firstly I'd like to say a big thank to Janos Urai for the opportunity to be part of this comprehensive and very exciting PhD project that involved a wonderful filed work, microscopy study and rock mechanical tests with state of the art devices. Thank you for your guidance and support. It was a pleasure to work with you. I really enjoyed being part of your great team.

This PhD project was part of Wintershall Tight Gas Initiative. I would also like to say many thanks to Wintershall Holding GmbH and Wintershall Noordzee B.V. for this great project and for the excellent and unique data that was provided to my work. And special thanks go to Wintershall Noordzee B.V., Energie Beheer Nederland B.V. (EBN) and Dana Petroleum Netherlands B.V. for facilitating the early release of data from their L06-08 well data. Many thanks to Bert de Wijn and Andreas Frischbutter for their support and help with this project.

I would like to thank my other supervisor, Heijn van Gent for your help especially with the field work in Utah that was one of my greatest adventures of my live. I learned a lot from you. Thank you Heijn. Many thanks go to Werner for the thin sections, the sample preparation and many help with technical questions. I would like to thank to GED team: Steffen, Guillaume, Joyce, Ben, Jop, Maartje, Max, Michael, Simon, Shiyuan, Sohrab, Susan and the Hiwis for every help. I would also like to thank Dr. Norbert Klitzsch and Lothar Ahrensmeier for helping me with geophysical measurements and all helps.

Furthermore, I would like to thank to all my best friends for the lot of help, especially to Ákos and special thanks go to Zsuzsi.

I would like to thank to my parents. Köszönöm Apu és Anyu a rengeteg segítséget, amit kaptam tőletek az életem során és a támogatást, ami nélkülözhetetlen volt ahhoz, hogy elérjem mindezt.

And last, I would like to thank to Andi my wife for motivating me to start this PhD study and supporting me all the time in both our private life and at work too and thank you Andi and to my son, Ádam for being my solid background.

I would like to dedicate this thesis to my family.

Abstract

In low permeability, tight gas sandstone reservoirs, an understanding of fracture systems is important in hydrocarbon exploration and production, because fracture networks affect the fluid flow properties in such reservoirs. Rocks can deform either in a ductile or brittle way depending on the rock mechanical properties and the stress condition. To better understand the fluid flow characteristics of a fault system within a reservoir, the knowledge of the mechanical properties and the stress condition of the reservoir and the geometry of the fracture networks, both in seismic-scale and micro-scale, is important. This thesis presents a multidisciplinary and multi-scale analysis of the rock mechanical properties in sandstones relevant to tight reservoirs.

Fractures and the geometry of fault damage zones were studied in two normal faults in Moab, Utah. The Courthouse Junction fault, which is a branch of the Moab Fault (with a throw of about 80 m) is characterised by cataclastic deformation bands and slip planes and minor fluid-flow alteration. In the cataclastic bands, grain and pore sizes range from about 1 to 0.1 μm in diameter, about two orders of magnitude smaller than those of the host rock; so significantly reducing the permeability of this fault zone. The other fault is located at the Klondike Bluffs area (the maximum throw of about 10 m) which is characterised by minor cataclasis, strong diagenesis and dislocation or disaggregation deformation bands. In the deformation bands, the grains are not crushed and the average pore size is nearly double, which increases the permeability within the fractures. As a result of past fluid flow, calcite now fully fills the fractures, so rendering them as impermeable barriers. In general, the fracture density decreases logarithmically outwards from the fault core; however, irregularities tend to often disrupt this tendency. Peaks, i.e. increases in deformation band density, are not always related to faults. The orientations of the deformation bands are sub-parallel and their dip varies between 70° and 90°. The width of the damage zone in the footwall at Klondike Bluffs is about 150 m and at the Courthouse Junction this varies from 200 to >300 m. In the hanging wall at Klondike Bluffs, the damage zone ranges from 180 to 300 m. Along the faults, the width and the deformation band distribution change significantly; the range of dip and dip-direction varies moderately, while the fracture characteristics remain constant.

The microstructure of fractures in North Sea Rotliegend Sandstone core samples and in the Moab field samples was analysed. The results show that the characteristics of the fractures and the host rocks of both the field study samples and the North Sea core samples are similar. In conclusion, the Moab sandstones may provide a good analogue to that of these North Sea sandstones.

The second aim of the study was to analyse the relationship between the rock mechanical properties, log properties and the brittleness of rocks. The relationship between unconfined compressive strength (UCS), Young's modulus and wireline well logs (i.e. acoustic velocity, density, resistivity, natural gamma-ray, spectral gamma-ray and neutron-porosity) was studied in North Sea Lower Germanic Triassic Sandstone (depths range 2700 to 4050 m) and Rotliegend Sandstone (depths range 3900 to 4900 m). A multivariate regression method was used to calculate the empirical correlation equations. In the Triassic sandstone, acoustic velocity has a much weaker dependence on velocity than it has in the Rotliegend sandstone. Multivariate regressions using more prediction variables provided better-fit correlation equations. A significant increase was observed in the goodness of regression using spectral gamma logs. The highest squared regression coefficient was attained as a result of a UCS-log

multivariate regression for Rotliegend samples: $R^2 = 0.84$ using spectral gamma logs, and for Triassic samples $R^2 = 0.55$ when using a cumulative gamma log (due to the unavailability of spectral gamma logs). This same tendency was found in the results of regressions made for Young's moduli and log properties. Strong dependency was exhibited between UCS and Young's moduli ($R^2 = 0.9$) in the Rotliegend samples; however, dependency was much lower in the Triassic samples ($R^2 = 0.46$).

Based on the brittleness index approach of Ingram and Urai (1999) and Hoogerduijn-Strating and Urai (2003), a new brittleness index equation has been developed in which stress conditions and UCS are considered. The derived UCS-log correlation equations were used to calculate brittleness logs in the wells from where the rock samples originate. By applying the calculated BRI logs to characterise the brittle, less brittle and ductile formations or intervals of North Sea sandstones were identified and provided good examples for the application of this BRI concept.

The results of my work can provide a better understanding of the properties of faults and fractures, together with hydrocarbon migration through tight sandstone reservoirs, and may be applied to improve the seismic interpretation of faults.

Zusammenfassung

Risse und Störungen in „tight gas“ Sandsteinen: Eine Studie über Labor- und Geländedaten

In Exploration und Produktion von Kohlenwasserstoffen ist in gering permeablen, gasdichten Sandsteinreservoiren (engl.: “tight gas reservoirs”) ein umfassendes Verständnis über Risssysteme wichtig, da diese die Fluidflusseigenschaften von Reservoiren beeinflussen. Gesteine können entweder duktil oder spröde deformieren, je nach mechanischen Gesteinseigenschaften und Spannungszustand. Um die Fluidflusseigenschaften in Risssystemen beschreiben zu können, ist es notwendig die in-situ gesteinsmechanischen Eigenschaften sowie die Geometrie des Rissnetzwerkes vom Seismik- bis hin zum Mikrometermaßstab zu verstehen. Diese Arbeit zeigt eine maßstabsübergreifende, interdisziplinäre Analyse von Rissen und mechanischen Eigenschaften von Reservoir-Sandsteinen, welche in der Betrachtung gasdichter Reservoirs von Bedeutung sind.

An zwei Abschiebungen in Moab (Utah, U.S.A.) wurden Risse und Störungszonengeometire untersucht. Die Courthouse-Junction-Störung, eine Seitenstörung der Moab Hauptstörung mit einem Versatz von 80 m, weist kataklastische Deformationsbänder, Harnischflächen und geringe Fluidfluss Alterationen auf. In den kataklastischen Bändern reichen Poren- und Korngrößen von 1 µm bis zu 0,1 µm, in etwa zwei Größenordnungen kleiner als Poren und Körner im Umgebungsgestein. Dies führt zu einer Permeabilitätsverringerung innerhalb der Störungszone. Die zweite Abschiebung (maximaler Versatz um 10 m) liegt im Klondike-Bluff Gebiet. Die Störung ist durch geringe Kataklase, starke Diagenese und Dislokation oder Auflockerung innerhalb von Deformationsbändern gekennzeichnet. Die Körner der Deformationsbänder sind nicht zerbrochen, die durchschnittliche Porengröße ist fast verdoppelt gegenüber dem Umgebungsgestein. Dies hat eine Permeabilitätserhöhung zur Folge. Durch Paleo-Fluidfluss konnte Kalzit in den Rissen ausfällen, was diese zu undurchlässigen Fluidsperren macht. Im Allgemeinen verringert sich die Rissdichte logarithmisch mit zunehmender Entfernung zum Störungskern, Ausnahmen unterbrechen jedoch diesen Trend. Eine Dichte von Deformationsbändern ist nicht immer Störungsgebunden. Die Orientierung der Deformationsbänder ist sub-parallel und ihr Fallen liegt zwischen 70° bis 90°. Die Breite der äußeren Störungszone (engl.: “damage zone”) variiert von 200 m bis > 300 m. Im Hangenden der Klondike-Bluff-Störung ist die äußere Störungszone 180 m bis 300 m breit. Breite und Häufigkeit der Deformationsbänder entlang der Störungen ist sehr variable. Das Fallen und Streichen der Bänder variiert ebenfalls leicht, während die Rissart gleichbleibend ist.

Die Mikrostruktur der Risse in Bohrkernen des Rotliegend Sandsteins der Nordsee sowie die Moab Geländeproben wurden untersucht. Die Ergebnisse zeigen, dass Risse und Umgebungsgesteine der Moab Geländestudie mit den der Nordseebohrkernproben vergleichbar sind. Die Moab Sandsteine können ein gutes Analogon zu den Rotliegend Sandsteinen der Nordsee sein.

Das zweite Ziel dieser Studie war es, Korrelationen von gesteinsmechanischen Eigenschaften, Borchlochloggindaten und der Brüchigkeit der Gesteine zu analysieren. Es wurde eine Korrelation zwischen der einaxialen Druckfestigkeit, dem E-Modul und Bohrloggingdaten (Schallwellengeschwindigkeit, Dichte, Wiederstand, natürliche Gamma-Strahlung, spektrale Gamma- und Neutronporosität) für Nordsee Sandsteine der unteren Trias (Tiefe: 2700 m bis 4050 m) und für Rotliegend Sandsteine (Tiefe: 3900 m bis 4900 m) untersucht. Die empirischen Beziehungen wurden durch multivariate Regression errechnet. Triassischer Sandstein zeigt einen viel kleineren Regressionskoeffizienten der Schallwellengeschwindigkeit, also eine geringere Geschwindigkeitsabhängigkeit, als Rotliegend Proben bei univariabler Regression. Multivariate Regression mit weiteren Einflussvariablen zeigt ein Ergebnis mit größeren Korrelationskoeffizienten. Ein bemerkenswerter Anteil der Regressionsqualität ist auf Daten des spektralen Gamma Logs zurückzuführen. Der größte Korrelationskoeffizient der einaxialen Druckfestigkeit lag bei Rotliegend Proben bei $R^2 = 0.84$ (mit spektralen Gamma-Log Daten) und für triassische Proben bei $R^2 = 0.55$ (mit kumulativem Gamma-Log). Die gleiche Tendenz zeigt sich in den Regressionsergebnissen zu E-Modul und Log-Daten. Eine deutliche Abhängigkeit liegt zwischen einaxialer Druckfestigkeit und E-Modul der Rotliegend Proben vor ($R^2 = 0.9$). Allerdings war die Abhängigkeit für triassische Proben viel geringer ($R^2 = 0.46$).

Die errechneten Logs der einaxialen Druckfestigkeit wurden zur Vorhersage der Brüchigkeit genutzt. Basierend auf Studien von Ingram und Urai (1999) sowie von Hoogerduijn-Strating und Urai (2003) wurde eine neue Gleichung zu Brüchigkeitsbestimmung (engl.: „brittleness index“) entwickelt. Mithilfe dieser Gleichung wurden Brüchigkeits-Logs für die untersuchten Schichten berechnet und brüchige und weniger brüchige Sandsteingruppen erkannt.

Die Ergebnisse meiner Arbeit geben ein besseres Verständnis von Störungs- und Risseigenschaften im Zusammenhang mit Kohlenwasserstoffmigration durch gasdichte Sandsteinreservoire. Diese Ergebnisse können genutzt werden um seismische Störungsinterpretationen zu verbessern.

1 Introduction

1.1 Project rationale

Sandstones are common reservoir rocks. The porosity and the permeability of sandstones are usually relatively high hence they are able to store large volumes of fluid or gas that can be produced relatively easily. These properties make sandstones a potential reservoir rock and a main target of conventional hydrocarbon explorations. However, there are sandstones, which have significant storage capacity but have low permeability. These low-permeability sandstones are commonly called tight sandstone reservoirs or tight gas reservoirs. The definition of the tight gas reservoirs by Holditch is based on the economical flow rate of the production (Holditch 2006). Law and Curtis (Naik 2003) defined the tight gas reservoirs of the United States where permeability is lower than 0.1 mD. On the contrary, reservoirs with permeability lower than 0.6 mD are considered as tight gas reservoirs by the German Society for Petroleum, Coal Science and Technology (DGMK) (Naik 2003). With increasing energy prices and available technology, production of tight gas reservoirs became profitable, playing an increasing role in hydrocarbon research all over the world (e.g. North America, Northern Africa) these decades. Moreover, tight reservoirs might provide large potential for energy resources for the following decades according to estimations of GTI E&P Services (Holditch 2006). In Europe, the Middle Permian Rotliegend aeolian sandstones are considered potential tight reservoir. According to the estimation of BGR (Cramer et al. 2009) more than 100 billion m^3 is stored in the Southern Permian Basin.

Thorough understanding of characteristics of the tight sandstone reservoirs is essential for successful hydrocarbon production. Many factors control the hydrocarbon systems in sandstones; for instance, depositional environment, palaeo-topography, syn-depositional tectonics, diagenetic processes, which involve quartz cementation (Walderhaug 2000, Taylor et al. 2010, Tobin et al. 2010), plagioclase albitization (Perez and Boles 2005), fibrous illite formation (Franks and Zwingmann 2010) etc. Tectonic events are one of the most important factors that have significant effects on fluid flow and hydrocarbon migration of a reservoir (Aydin 2000). As a result of tectonic processes, different types of fractures can occur in brittle regime, for instance: faults, joints, veins, cracks or deformation bands. Reflection seismic provides an opportunity to map the underground structures; however, even the highest resolution seismic data provide only about 2-3 m vertical resolution. Hence, only the larger structures (e.g. faults) are visible in the seismic images. Well bore measurements and core samples can provide information on investigated rocks in more details; however, might not be representative in an inhomogeneous reservoir environment. Therefore, prediction of reservoir quality is a great challenge (Ajdukiewicz and Lander 2010). Natural field analogues can provide invaluable opportunity to obtain information to better understand the properties of reservoirs which are similar to those in the depth. Outcrops allow studying the 3D architectures of the reservoirs in large scale and also in small scale i.e. microstructures of fractures.

1.2 Theoretical background of strength, fracturing and brittleness

The stress theory was introduced by Cauchy using the concept of traction (Jaeger et al. 2007). Traction ($\underline{p}$) is a vector which is defined at a point ($\underline{x}$) on a plane whose outward normal unit vector is $\underline{n}$ as the ratio of the resultant force ($\underline{F}$) and the area *A* across which the force acts:

$$\underline{p} = \frac{\underline{F}}{A} \qquad \textbf{Eq. 1-1}$$

To specify the traction at a given point, the differential resultant force (*dF*) acting on the infinitesimal area (*dA*) is calculated:

$$\underline{p}\left(\underline{x},\underline{n}\right) = \lim_{dA\to 0}\frac{1}{dA}\underline{dF} \qquad \textbf{Eq. 1-2}$$

According to Cauchy stress theory, the traction acting on a plane can be given by the stress tensor $\underline{\underline{\sigma}}$.

$$\underline{p} = \underline{n}\underline{\underline{\sigma}} \qquad \textbf{Eq. 1-3}$$

In 3D, the stress tensor has 9 components. The diagonal terms describe the normal stresses, and the off-diagonal terms describe the shear stresses acting on each plane of the coordinate system. If the forces are balanced, the stress tensor is symmetric ($\sigma_{xy} = \sigma_{yx}$, a $\sigma_{xz} = \sigma_{yz}$ and $\sigma_{yz} = \sigma_{zy}$); therefore, it can be transformed into a diagonal matrix by calculating its eigenvectors, which are the principal stresses. In this way, the stress-state of a point can be described by three orthogonal normal stress vectors: σ_1 being the maximum, σ_2 being the intermediate and σ_3 being the least principle stress.

$$\underline{\underline{\sigma}} = \begin{vmatrix} \sigma_{xx} & \sigma_{xy} & \sigma_{xz} \\ \sigma_{yx} & \sigma_{yy} & \sigma_{yz} \\ \sigma_{zx} & \sigma_{zy} & \sigma_{zz} \end{vmatrix} = \begin{vmatrix} \sigma_1 & 0 & 0 \\ 0 & \sigma_2 & 0 \\ 0 & 0 & \sigma_3 \end{vmatrix} \qquad \textbf{Eq. 1-4}$$

The stress tensor can be visualised as a stress ellipsoid, with its axes, the principal stresses, oriented normal to the principal planes of stresses.

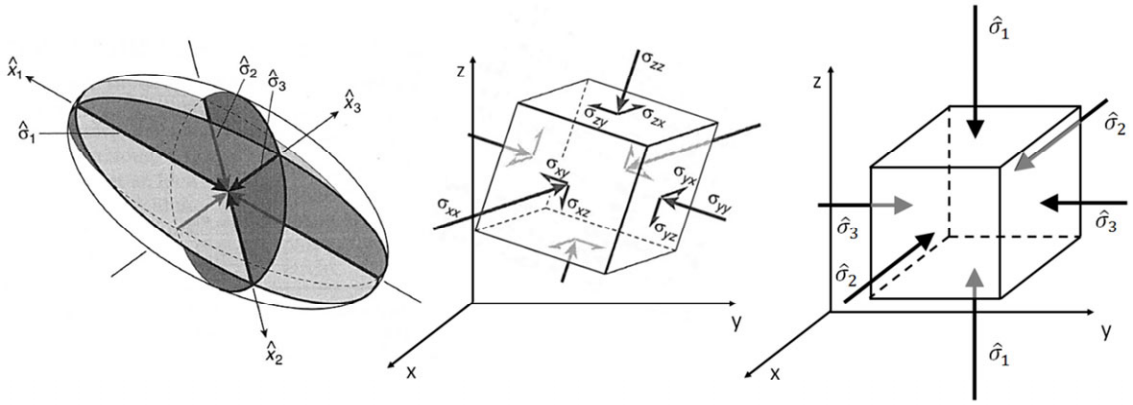

Figure 1-1 A) The stress ellipsoid is a three-dimensional visualisation of the stress state of all possible plane in an infinitesimal cube ($\hat{\sigma}_1$, $\hat{\sigma}_2$, $\hat{\sigma}_3$ are the principle stresses and $\hat{x}_1$, $\hat{x}_2$, $\hat{x}_3$ are the principle coordinates). B) The general stress components on the panes normal to the coordinate axes of the general coordinate system in an infinitesimal cube. C) The principal stress components are shown in a principal coordinate system in an infinitesimal cube. (modified after Twiss and Moores 2007)

The two dimensional graphical representation of the state of the stress of a given point is the Mohr's diagram (Figure 1-3). In the Mohr diagram, the horizontal axis represents the normal stress and the vertical axis represents the shear stress acting on a particular plane at a given point. The Mohr's circle represents all normal-shear stress relations acting on planes of all possible orientation at a given point, where the angle of the given plane (θ) is half of the angle between the radius to the given point and the radius to the point of maximum stress.

$$\sigma_N = \left(\frac{\sigma_1+\sigma_3}{2}\right)+\left(\frac{\sigma_1-\sigma_3}{2}\right)\cos 2\theta \qquad \textbf{Eq. 1-5}$$

$$\tau = -\left(\frac{\sigma_1-\sigma_3}{2}\right)\sin 2\theta \qquad \textbf{Eq. 1-6}$$

Equations 1-5 and 1-6 describe the equation of the Mohr circle in the (σ_N-τ) space, with its centre being at the point $\{\sigma_N = (\sigma_1+\sigma_3)/2; \tau = 0\}$ and with its radius being $r = \sigma_1 - \sigma_3$.

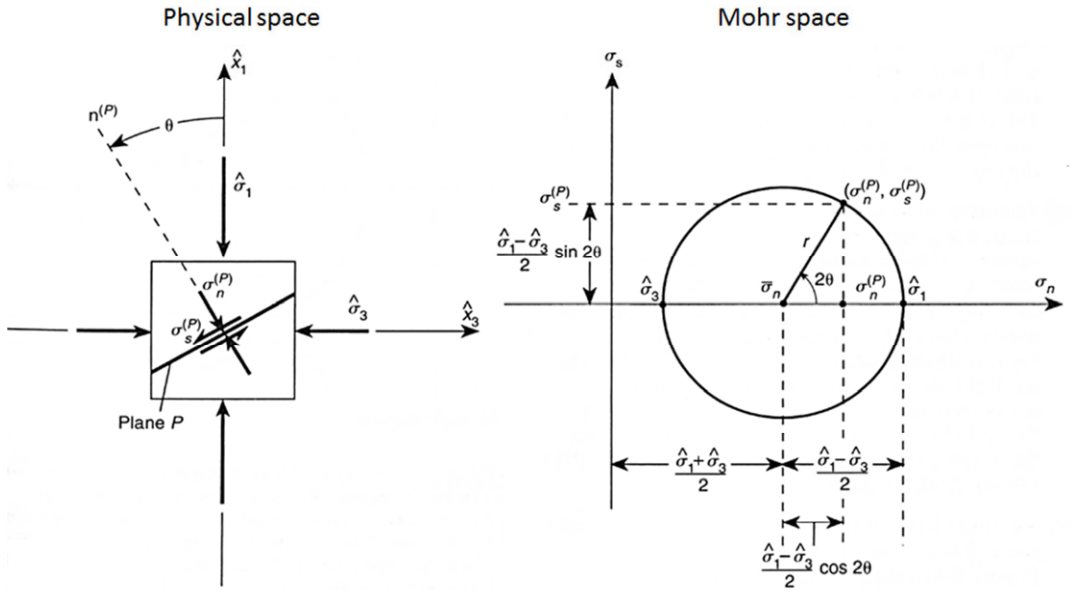

Figure 1-2 A) The stress diagram in physical space in the principal coordinate system shows the relationships between the stress components and the plane P where n(P) is the normal of the plane P stresses with superscripts (P) indicate stress components acting on plane P. B) The stress on the plain in figure "A" showed in a Mohr diagram in 2D. (modified after Twiss and Moores 2007)

The Mohr's diagram is often used to determine the failure of rocks. The Mohr-failure-envelope (Figure 1-3) is the curve, which describes the critical states of stresses where a given rock fails. Parameter of the failure envelope (internal friction angle, cohesion) is different for every rock.

Strength is an important parameter of the rocks; therefore, it has been extensively studied. In the field of rock mechanics, several strength theories have been developed since the beginning of last century. These theories use different approaches; Asszonyi and Richter and then later Ván and Vásárhelyi analysed the rock strength as a thermo dynamical system (Asszonyi and Richter 1974, Asszonyi and Richter 1979, Ván 2001, Ván and Vásárhelyi 2001); other theories use mechanical, physical and/or statistical approaches and many empirical failure criterion were created that are based on well-known theories (Andreev 1995).

The Coulomb-Navier theory describes the shear failure, a rock or soil fails along a plane due to shear stress acting on that plane. It also states that the fractures only form if the internal strength (cohesion) of the rock is exceeded (Griffith 1921, Panich and Yong 2005, Jaeger et al. 2009). The Coulomb-fracture-criteria describe the state of the stress at which a given rock under compression fails. In the Mohr diagram the Coulomb fracture criteria are shown as a straight line with the internal fiction of the rock (μ) representing the slope of the line, and the cohesion (C) of the rock is the intercept of the line.

$$\sigma_S = C + \sigma_N \cdot \tan\phi = C + \sigma_N \cdot \mu \qquad \textbf{Eq. 1-7}$$

Based on the Griffith theory, the tensile strength of the rock is defined. He assumed that both tensile and shear fractures develop from planar microdefects or microfractures. Griffith

proposed non-linear relationship between the principal stresses for a critically stressed rock. In the Mohr-space the representation of the Griffith failure criterion (Eq. 1 8) is a parabola, where the tensile strength of the rock is the intersection with the horizontal axis. (Griffith 1921, Fossen 2010)

$$\sigma_S{}^2 + 4T\sigma_N - 4T^2 = 0 \qquad \textbf{Eq. 1-8}$$

When the rock deforms in ductile way, the failure of the rock can be estimated by a constant shear stress criterion, referred to as the von Mises criterion; its representation in the Mohr space is a horizontal line *(σ_s=constant)* (Mises 1913).

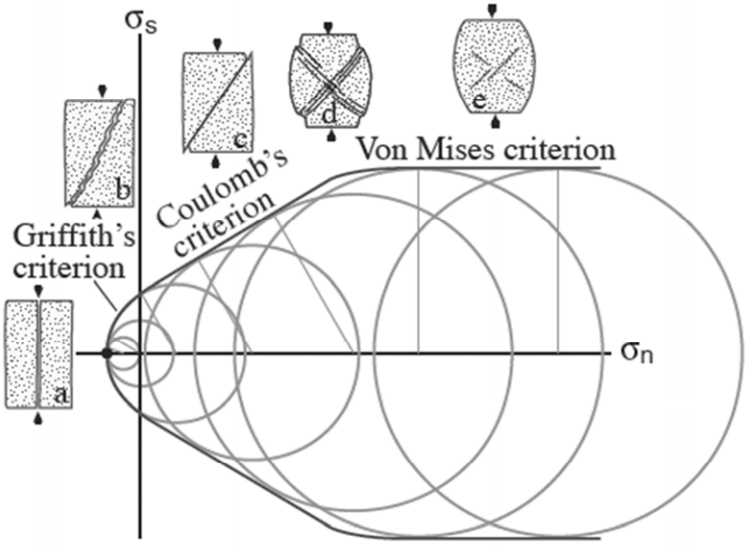

Figure 1-3: The fracture criterions (Griffith, Coulomb and Von Mises) in 2D Mohr space with related fracture types brittle to ductile (modified after Fossen, 2010).

In porous rock, the stress due to the weight of the overlying rock layers (lithostatic or overburden stress) is distributed over the grain contact area. The pressure of the pore fluid reduces the effective stress. Terzaghi (1923) defined the effective stress σ'_{ij} as the difference between externally applied stresses σ_{ij} and internal pore pressure P_p:

$$\sigma'_{ij} = \sigma_{ij} - \delta_{ij}P_p \qquad \textbf{Eq. 1-9}$$

This means that pore pressure influences the diagonal elements of the stress tensor (normal stresses, σ_{11}, σ_{22}, σ_{33}) and not the off-diagonal elements (shear components σ12, σ23, σ13) (Zoback 2007).

In a porous elastic solid saturated with a fluid, the theory of poroelasticity describes the constitutive behaviour of rock. Empirical data showed that the effective stress concept of Terzaghi is a good approximation for intact rock strength and the frictional strength of faults, but for other rock properties it is needs to be modified. Nur and Byerlee (1971) proposed a formula which works well for volumetric strain:

$$\sigma'_{ij} = \sigma_{ij} - \delta_{ij}\alpha P_p \qquad \textbf{Eq. 1-10}$$

where α is the Biot parameter ($\alpha = 1 - K_b/K_g$) and K_b is drained bulk modulus of the rock or aggregate and K_g is the bulk modulus of the rock's individual solid grains.

There have been several studies, which examined the different parameters, that affect the strength of a given rock, such as porosity (Brace and Riley 1972, Dunn et al. 1973, Scott 1989, Palchik 1999), mineralogical properties (Fahy and Guccione 1979, Winkler 1985, Singh 1988, Shakoor and Bonelli 1991, Haney and Shakoor 1994, Ulusay et al. 1994, Schön 1996, Bell and Culshaw 1998, Tuğrul and Zarif 1999, Hale and Shakoor 2003, Jeng et al. 2004, Meng and Pan 2007, Pomonis et al. 2007, Hsieh et al. 2008), clay content (Jizba 1991, Samsuri et al. 1999, Swanson et al. 2002, Takahashi et al. 2007, Li and Zhang 2011), moisture content (Colback and Wiid 1900, Simpson and Fergus 1968, Broch 1974, Ballivy et al. 1976, Michalopoulos 1976, Priest and Selvakumar 1982, Venkatappa Rao et al. 1985, Dyke and Dobereiner 1991, Hawkins and McConnell 1992, Hale and Shakoor 2003, Shakoor and Barefield 2009), fabric (Paterson and Wong 2005, Li and Zhang 2011). In addition to rock properties, there are also external factors which can determine the strength of a given rock, such as effective confining pressure (Jaeger, et al. 2009), principal stresses (Paterson and Wong 2005), strain rate (Sangha and Dhir 1972, Fischer and Paterson 1989), pore pressure and temperature (Fischer and Paterson 1989).

Failure of the rock can occur in a ductile or brittle way. The ductile deformation is a continuous deformation at the scale of observation; without macroscopic fracturing; it can be the result of plastic or brittle micromechanisms as it can be seen on Figure 1-4. Ductile deformation usually occurs in metamorphic rocks in the middle and lower crust; however, soils and poorly consolidated sediments can also deform in a ductile way. The ductile deformations in the middle and lower crust are usually due to plastic mechanism; such as, dislocation creep, twinning or diffusion. In contrast, the ductile deformation of poorly consolidated sediments is usually the result of brittle mechanisms; such as, microfracturing, rolling or frictional sliding of the grains. The brittle deformation is discontinuous deformation by fracturing. The complex fracture process is basically a combination of microscopic cracks and frictional movement (Brace et al. 1966). As the stress closes to critical point, the number of micro-cracks increases and reaches critical condition, at which the rock fails along through-going shear plane (Lockner et al. 1991). Griggs and Handin (1960) distinguished two styles of fractures; such as, shear fracture and extension fracture. Later, Ramsey and Chester (2004) inferred that also hybrid fractures can formed as a combination of compression and tensile states. Wong and Baud (2012) showed that there is an intermediate regime between the brittle and the ductile field, which is associated with the localized strain. However, style of fracturing depends on several different properties of the rock and also external physical parameters. Experimental studies show, that the mode of the fracturing depends on deformation style, which is affected by the confining pressure (Figure 1-5). During brittle deformation, without confining pressure, extensional fractures develop, and as the confinement increases, the fractures turn into shear fractures and shear bands and during ductile deformation plastic flow occurs. The temperature also has an effect on the brittle ductile transition of rocks; however, in the upper crust, this effect is not dominant. In the continental upper crust to approximately ten kilometres depth, rocks have in general brittle behaviour (Figure 1-6).

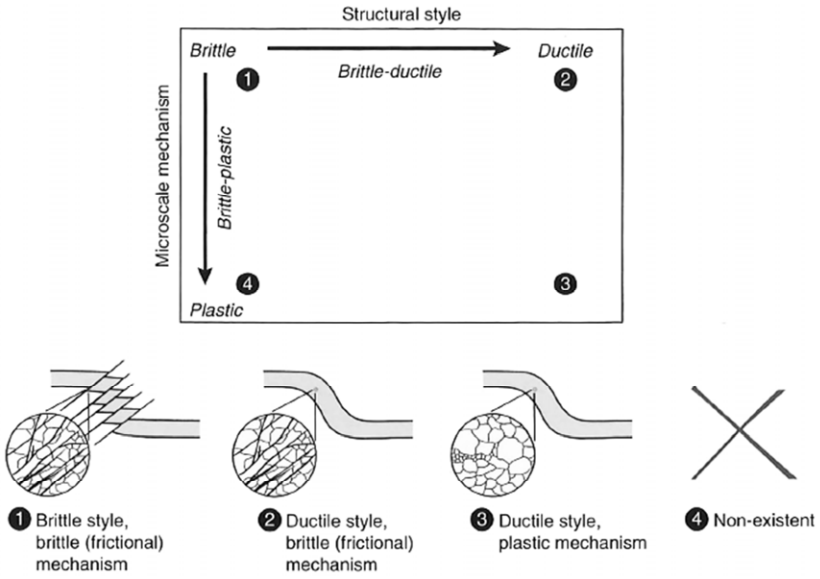

Figure 1-4 – Illustration of brittle, ductile and plastic deformation styles. (modified after Fossen 2010)

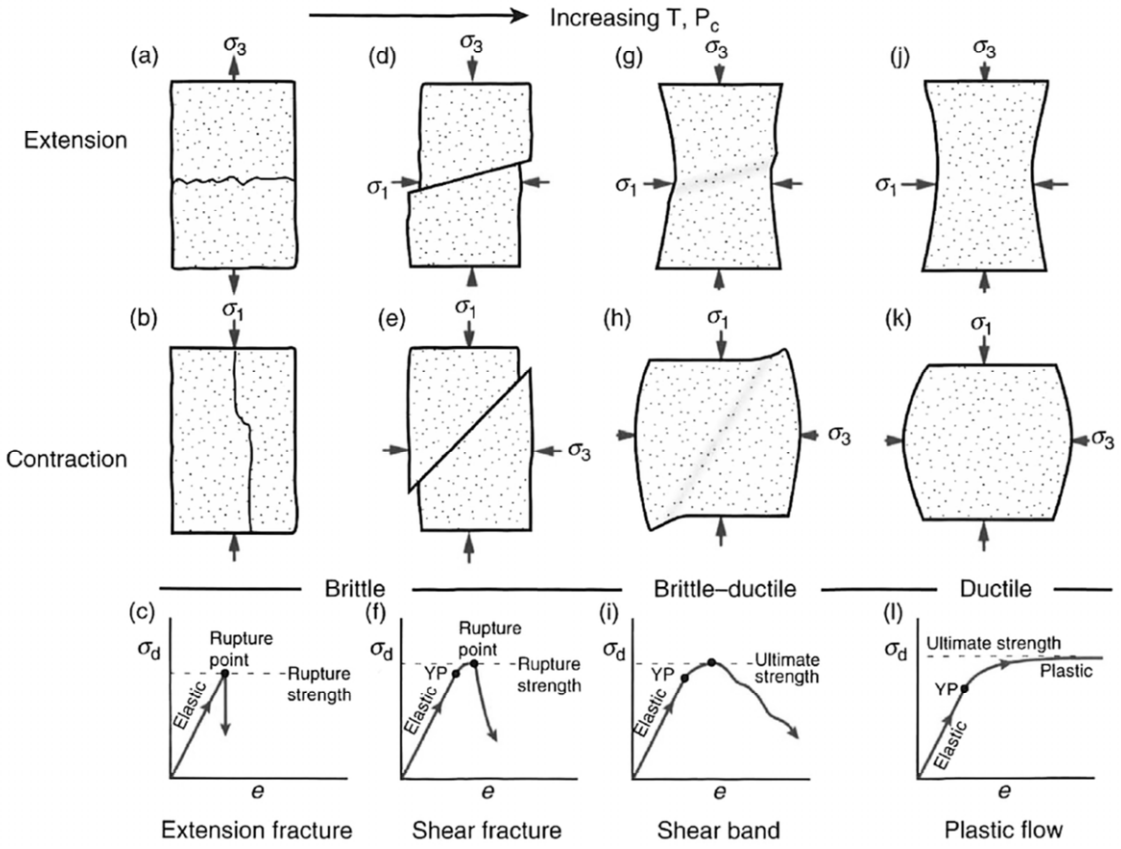

Figure 1-5 – Experimental deformation structures (P, T). (modified after Fossen 2010)

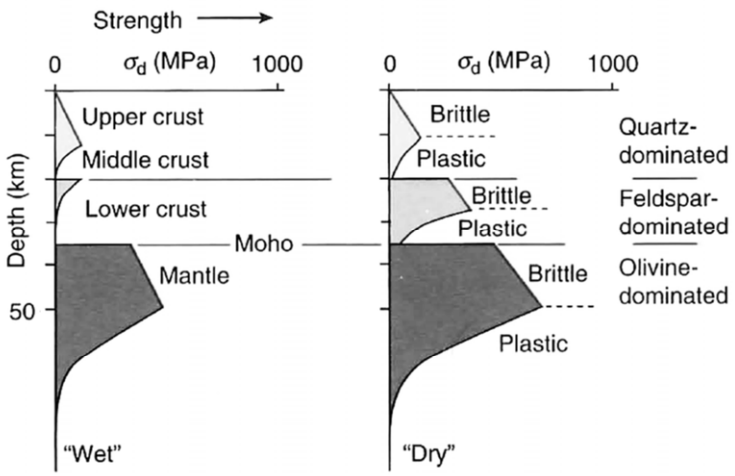

Figure 1-6 – Rheological stratigraphy of continental lithosphere. (Fossen 2010)

There have been several studies on the brittle and the ductile characteristic of rocks, which tried to define the parameters that distinguish the brittle and the ductile deformation. In some cases, the brittle-ductile transition was characterized by the permanent strain before failure; for the brittle rock, the strain was 3% according to Paterson and Wong (2005) and Heard (1960); and for the ductile rock, strain was more than 5% (Paterson and Wong, 2005 and Heard, 1960). Other studies focused on the brittleness of the rock, which was estimated based on the Mohr diagram (Hucka and Das 1974), or the ratio of the reversible strain or total strain or energy (Hucka and Das, 1974); or the ratio of Brazilian tensile strength and uniaxial compressive strength of the given rock (Table 5.2); or the results of punch penetration or impact tests (Protodyakonov 1962, Blindheim and Bruland 1998, Copur et al. 2003, Yagiz 2009, Yagiz and Gokceoglu 2010). However, in some cases, the terms brittle and ductile are used in an unconventional way. The ductile deformation of mudrocks was defined with the lack of dilatancy and the associated creation of fracture permeability. In contrast, the brittle deformation of mudrocks was defined with the presence of dilatancy and consequently the increase of fracture permeability (Urai and Wong 1994, Urai 1995, Ingram and Urai 1999). Furthermore, Wong and Baud (2012) reviewed several studies of brittle-ductile transitions including constitutive models for plasticity and micromechanical models for the brittle and ductile failure, however, complete model of the brittle-ductile transition is still lacking.

1.3 Classification of fractures

Fractures can be classified by the relative displacement that has occurred across the fracture surface during formation. For extensional fractures, i.e. mode I fractures, the displacement is normal to the fracture walls (Figure 1-7 A). For shear fractures, the relative motion is parallel to the surface. There are two modes of shear fractures: in case of mode II shear fractures, there is a sliding motion normal to the edge of the fracture (Figure 1-7 B); whereas, in case of mode III shear fractures, there is a sliding motion parallel to the fracture edge (Figure 1-7 C). There are also oblique extensional, or fracture mixed mode fractures, when the displacement along the fracture has both parallel and perpendicular components. (Twiss and Moores 2007)

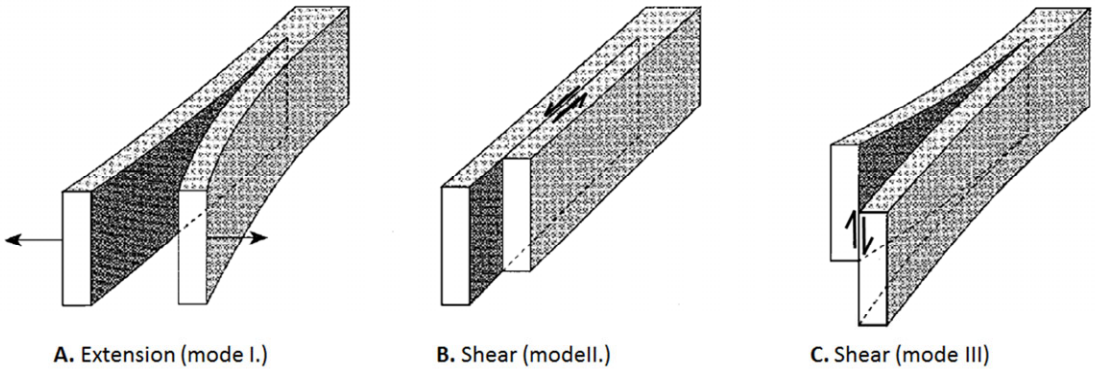

Figure 1-7– The three most characteristic fracture types classified based on the relative displacement are: A. extensional fracture or mode I. - the displacement is perpendicular to the fracture (opening); B. Shear fracture or mode II. - The displacement is parallel to fracture and perpendicular to the fracture edge; C. fracture or mode III. - The displacement is parallel to fracture and to the fracture edge. (modified after Twiss and Moores 2007)

Based on its mode of formation, fractures can be classified as the following (Aydin 2000):

- Dilatant-mode fractures/joints, veins, dikes, sills
- Contraction/compaction-mode fractures/pressure solution seams and compaction bands
- Shear-mode fractures/faults

Dilatant fractures exhibit displacement normal to their surface. There are more types of dilatant fractures; such as, joints, veins or dykes. Joint are dilatant fractures with no or very small displacement (Twiss and Moores 2007). Veins are filled with mineral deposits (Twiss and Moores 2007). Hydrofractures are generated by high fluid pressure (Hubbert and Willis 1957) and may be vertical (dikes) or horizontal (sills) or a combination of the two depending on the interplay between the state of stress and the abnormal fluid pressure leading to fracturing (Mandl and Harkness 1987).

In contraction/compaction-mode fractures, the fracture walls move towards each other, which may be characterized as anti-crack (Fletcher and Pollard 1981). This class of structures includes pressure solution surfaces and compaction bands (Aydin 2000).

Faults are defined as structures across which appreciable (minimum a metre or more) shear displacement discontinuities occur. Fractures with shear displacement of a centimetres or less are called shear fractures, and shear fractures at the scale of a millimetre or less are microfaults that may be visible only under microscope. (Twiss and Moores 2007)

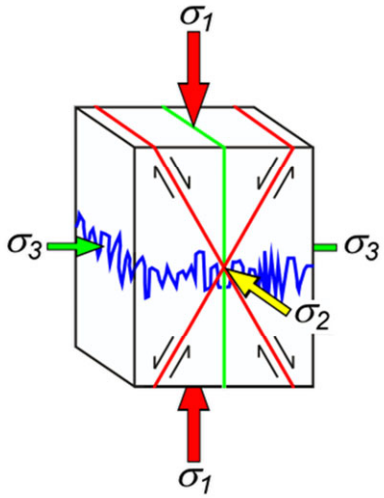

Figure 1-8, The orientation of different types of fractures formed in intact rock relative to the principal stress orientations: Stylolites are perpendicular to the maximum principal stress direction (σ1); faults, shear fractures are parallel to the intermediate principal stress direction (σ2); joints are perpendicular to minimum principal stress direction (σ3). (modified after Lacazette, 2009)

The orientation of the different mode of fractures is determined by the orientation of the principal stresses. Joints grow normal to least principal stress (σ3). Faults usually form with an approximately constant acute angle to the maximum principal stress (σ1) and the orientations of the faults and their conjugates ranges from 25° to 40° but in general about 30°. Compaction bands form normal to σ1 (Lacazette 2009). Faults are often accompanied by conjugate fractures which are two sets of small-scale shear fractures at approximately 60° angle to each other with opposite senses of shear (Twiss and Moores 2007). In many cases, there are smaller-scale faults which are parallel to major fault and have the same sense of shear and are called as synthetic faults; or they are in the conjugate orientation and referred as antithetic faults (Twiss and Moores 2007).

The fault separates the rock into two blocks. The one above the fault is the hanging wall and the one below the fault is the footwall. The zone connecting the footwall and the hanging wall of the fault is referred as the relay zone (Peacock and Sanderson 1991). One major parameter of the fault is the displacement blocks. The lateral component of the displacement along the fault is the horizontal separation. The vertical component of the displacement is the throw and the horizontal component of the displacement normal to the fault is the throw (Figure 1-9). (Twiss and Moores 2007)

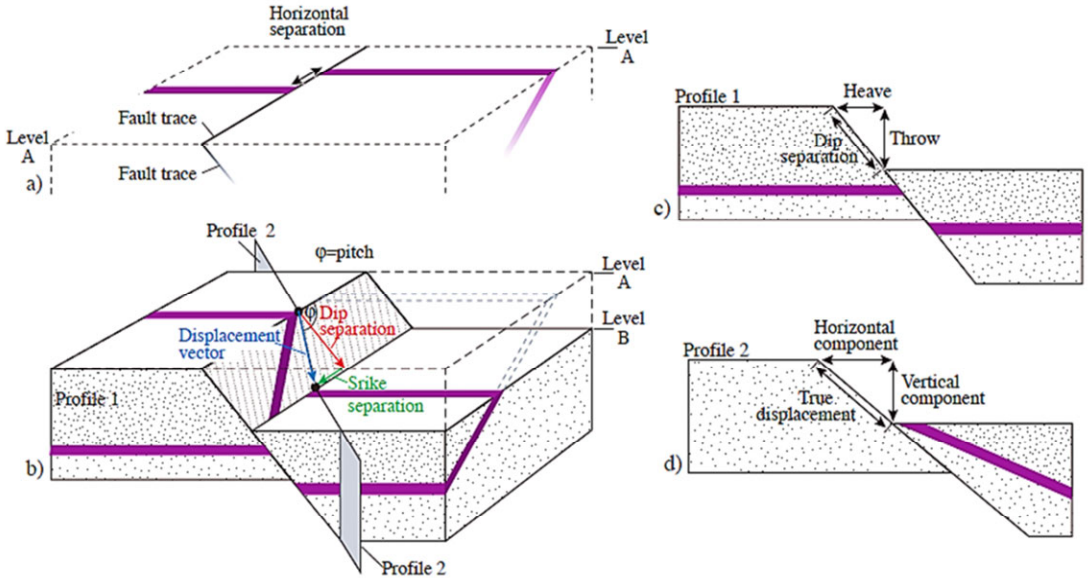

Figure 1-9 – The general geometrical properties of fault are illustrated by a normal with a dextral (right-handed) component. (modified after Fossen, 2012)

The surface of the fault planes are often smooth as a result of shearing on the fault planes or in the fault gouge, this features is referred as slickensides. Furthermore, fault surfaces can contain strongly oriented linear features, known as slickenlines, slickenside lineations, or striations, that are parallel to the direction of slip. (Twiss and Moores 2007)

Fault can be categorised based on the dynamics of faulting as it was described by Anderson (1905). According to this Andersonian classification scheme, there are three classes: reverse faults, normal faults and strike slip faults with respect to the relative orientation of the principal stresses acting on the fault planes. If the maximum principal stress is vertical, it is a normal fault; if the minimum principal stress is vertical, it is reverse fault and if the intermediate stress is vertical, it is a strike-slip fault.

The 3D architecture of fault arrays was analysed by Walsh et al. (1999). Seismic mapping of normal fault arrays allows 3D geometries, slip variations and branch-lines to be determined objectively by mapping of numerous branch-points. Branch lines are defined as lines of intersection between a master fault and a synthetic splay, or between two segments of a multi-strand fault. The shape of branch lines varies between straight lines and closed loops representing different stages in the failure of relay zones and in the progressive replacement of fault tip-lines with fault branch-lines.

Faults can be classified into displacement-normal offsets, displacement-parallel offsets and displacement-oblique offsets. Displacement-normal offsets faults are associated with neutral relays. Displacement- parallel offsets and displacement-oblique offsets can be further subdivided into those which are constrictional and extensional and are associated with restraining relays and releasing relays respectively. (Peacock and Sanderson 1991)

Neutral, restraining and releasing relays can develop in normal, reverse and strike-slip faults. As a combination of these, 9 different branch line structures can develop. An important factor to control the structure of the branch lines is the orientation of the axis of a

relay and its associated bends relative to a fault slip direction. This relative orientation determines how the relay strain is accommodated and hence it also determines the degree of hard-linkage and development of branch-lines. (Walsh, et al. 1999)

Field observations showed that seismic size faults (throw is larger than seismic resolution) and also faults below the seismic resolution have complex 3D architecture (Chester et al. 1993, Sibson 1977, Wallace and Morris 1986), they usually consist of two structural elements: the fault core and the damage zone. The core of the fault, which is often referred as fault slip zone, shows the largest displacement of the fault (Gudmundsson et al. 2010). Most of the displacements occur in the central part of the zone, the fault core (Caine et al. 1996), where slip planes and fine- to ultra-fine grained rocks e.g. cataclasites, gouges can be found. It contains many small fractures and also breccias and cataclastic rocks. The fault core often shows ductile or semi brittle behaviour as the core rock is crushed into a fine grain material. The thickness of the core usually varies from several metres to a few tens of metres (Berg and Skar 2005, Agosta and Aydin 2006, Tanaka et al. 2007, Li and Malin 2008, Gudmundsson, et al. 2010); however, very large faults zones, such as transform faults, may develop several fault cores and damage zones (Faulkner et al. 2006, Gudmundsson 2007).

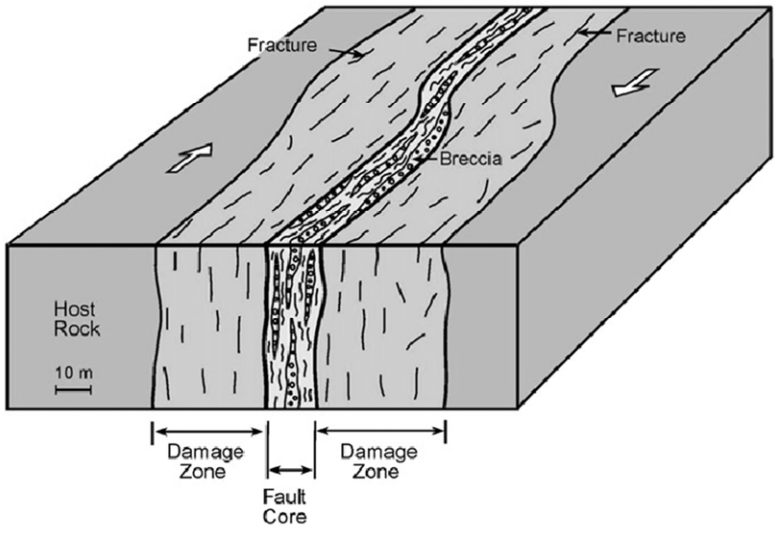

Figure 1-10 A schematic illustration of the structure of a (strike-slip) fault zone is showed. The fault core consists of breccia and/or cataclastic rock and the damage zone is characterized by fractures (modified after Gudmundsson et al. 2010).

The damage zone of a fault, which is also referred to as the transition zone, is fractured host rock, where the fracture density decreases with distance from the fault core (Bruhn et al. 1994). The damage zone deforms in a brittle way, therefore it consists of mainly lenses of breccias and other heterogeneities, less extension fractures, and also some shear fractures present (Gudmundsson et al. 2002). According to Aydin (2000), the width of the damage zone and the density of joints therein are related to the magnitude of slip across the fault. Furthermore, in some studies, a third element of the fault zone is described, which is

the protolith zone, where only minor fracturing can be observed in the host rock (Sibson 1977, Chester 1993, Sági 2013)

Usually, there is no sharp boundary between the damage zone and the host rock. In the literature, the host rock is defined as the zone where the number of fractures is significantly less than that of the damage zone. The boundaries between the fault core and the damage zone are sharper than those between the damage zone and the host rock. All these boundaries vary along the length of the fault and change in time and space with the evolution of the fault zone. (Gudmundsson et al. 2010)

Faults have three fundamental elements that impact on hydrocarbon flow: (1) juxtaposition, (2) fault rock, and (3) the surrounding damage zone. Juxtaposition of layers across a fault is an important factor of the fault core and has a large impact on the fluid flow as it allows the hydrocarbon flow from one permeable unit to another even if the reservoir rock has a low permeability. Fault rock forms the core of a fault and is usually composed of fine grain material and has lower porosity and permeability than the host rock. Due to the several extensional fractures, the permeability of the damage zone is usually higher than fault core (Gudmundsson et al. 2010). Also, there are other parameters which are crucial for faults and fractures and fluid flow, such as the magnitude of the slip, the cementation, the present stress state and the time. (Aydin 2000)

In order to better understand the structure of reservoirs, numerous models of fault zones were developed in different approaches e.g. based on mechanical process (Wilson et al. 2003, Blenkinsop 2008, Mitchell and Faulkner 2009), Andersonian model of fault formation (Anderson 1942), fault tip propagation (Scholz et al. 1993, Vermilye and Scholz 1998), interaction of multiple fault tips, wavy frictional fault surfaces (Scholz 1987, Chester and Chester 1998) or the model of off-fault deformation (Rudnicki 1980, Wilson et al. 2003). The properties of fractures (geometry, width, intensity etc.) can differ significantly within each different fault zone domain (fault core, damage zone and protolith) (Chester 1993) that is influenced by the lithology of the host and the associated fault rocks (Antonellini and Aydin 1994, Faulkner et al. 2003, De Paola et al. 2008).

Fault zones can contain different deformation structures, such as slip planes, veins, joints or deformation bands. In general, fracture development within fault zones depends on the velocity of faulting, pressure and also temperature conditions (Sibson 1977). In the uppermost kilometres of the Earth's crust, stiff rocks deform primarily by fracturing. These fractures form by the linking of micro-fractures or the linking of mesoscopic joints (Pollard and Fletcher 2005). In porous rock, like many types of sandstone, strain is accommodated, on the one hand, by sheared joint-based faulting, which involves shearing along pre-existing joints forming of secondary and higher order joints, fragmented rock (Flodin 2003 and its references). On the other hand, strain commonly forms deformation bands in sandstones (Aydin 1978, Aydin and Johnson 1978, Aydin and Johnson 1983, Antonellini et al. 1994). Deformation bands are low-displacement deformation zones, where thickness ranges from millimetres to centimetres. These structures can be observed on many excellent outcrops all over the world; for instance, in cretaceous sandstone (Provence, France) (Saillet and Wibberley 2013), in Eocene eolian sandstone (Vértes and Buda Hills, Hungary) (Fodor 2010),

in Palaeozoic sandstones (Western Sinai, Egypt) (Rotevatn et al. 2008) and in many places in Entrada and Navaho Sandstones (Utah and Nevada, USA) (e.g. Antonellini, et al. 1994, Fossen 2010). From hydrogeological and petroleum geological point of view, fluid flow systems are one of the most important factors. And in general, fractures have significant effect on fluid flow; they can behave differently. Role of deformation bands in fluid flow was studied whether they are seal or conduit for fluid flow (Antonellini and Aydin 1994, Antonellini and Aydin 1995, Antonellini et al. 1999).

The terms used for description of deformation band varies widely; such as, microfault, cataclastic fault, fault, (micro)fracture, shear band, cataclastic slip band, Lüder's band, deformation band shear zone, granulation seams. One reason for the wide variety of names of this structure might be that there are several different types of deformation bands. It is important to know the characteristics of deformation bands to distinguish them from ordinary fractures. Deformation bands occur in porous granular media (e.g. sand or sandstones). Certain amount of pore space is required for grain rotation and translation, whether grain-crushing or friction sliding along grain boundaries happens during fracturing. Grain rotation and translation are essential elements of deformation band formation. Deformation bands form as either individual bands or zone (bundle) of bands, which does not have a slip surface. In general, the offset of individual deformation bands is less than few centimetres even if lengths of the bands are 100 m. In sandstone, larger displacements are accommodated in slip surfaces. The deformation bands commonly develop related to vertical uplift and monoclinal folds in rifts (Fisher and Knipe 2001), around salt structures (Antonellini, et al. 1994), around thrusts and reverse faults, above shale diapirs (Cashman and Cashman 2000) or gravity driven collapse (Hesthammer and Fossen 1999). (Fossen et al. 2007)

Deformation bands were classified by Fossen et al. (2007). The deformation bands can be classified kinematically: there are compactional-, shear-, dilatational bands; and the combinations of these: compactional shear bands and dilatational shear bands (Figure 1-11). And the deformation bands can be classified according to the mechanisms of the deformation (Figure 1-12).

We can distinguish *cataclastic bands* where the main deformation mechanism is grain fracturing as described e.g. by Aydin (1978), Aydin and Johnson (1983) and Davis (1999). In the core of the structure, high grain size and pore space reduction and angular grains can be observed, while compaction and slightly fractured grains are typical in the surrounding area. As a result of grain crushing, the grain interlocking increases which promotes strain hardening (Aydin 1978). Cataclastic bands form mostly at burial depth of 1.5-2.5 km. However, evidence for cataclastic band was found at depth of less than 50 m (Cashman and Cashman 2000). Grain crushing may generate approximately up to one order of magnitude drop in porosity, that reduces the permeability by around two, three (locally even six) orders of magnitude within the bands (Antonellini and Aydin 1994, Gibson 1998, Antonellini et al. 1999, Jourde et al. 2002, Shipton et al. 2002). Permeability can decrease to 0.001 mD in the cores of deformation bands where porosity is very low (porosity < 1%).

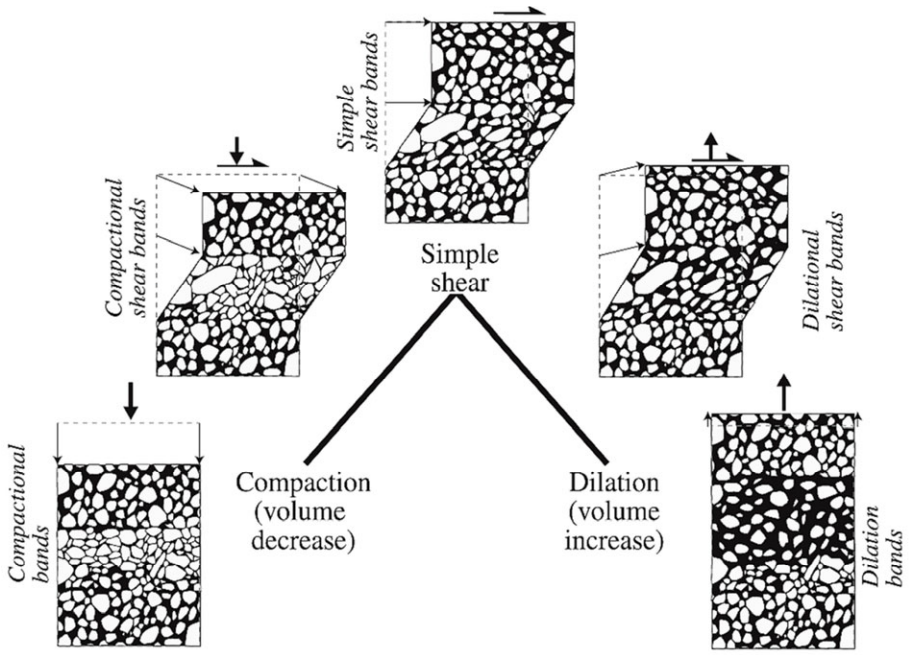

Figure 1-11: Kinematic classification of deformation bands (modified after Fossen 2007)

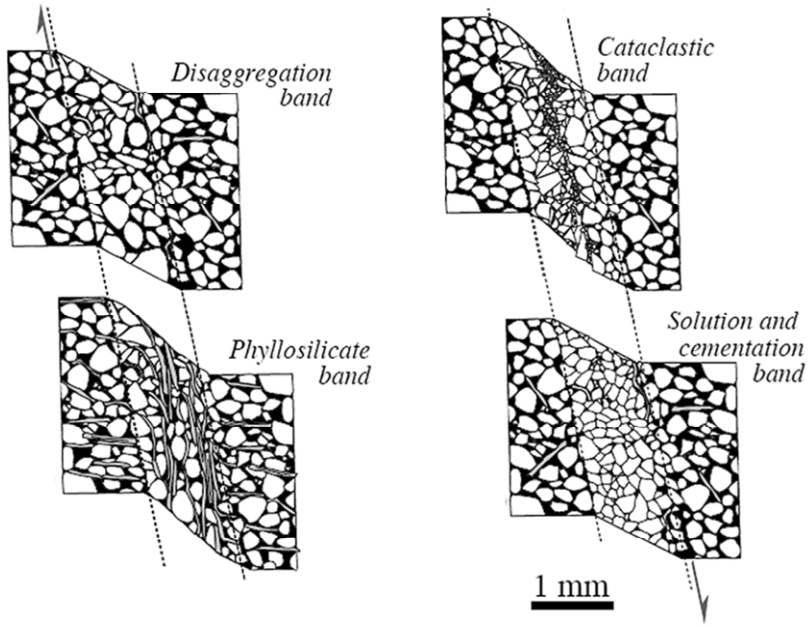

Figure 1-12: Classification of deformation bands by deformation mechanism (modified after Fossen 2010)

Other deformation band types are *solution, cementation and diagenesis bands* which are characterised by little grain size reduction in comparison to the host rock matrix without significant cataclasis but commonly with dissolution, in particular quartz dissolution. Dissolution bands occur frequently at shallower depth. Dissolution is promoted by clay minerals on grain boundaries. Cementation can occur preferably on uncoated quartz surface as a result of grain crushing, localised tensile fractures or grain boundary sliding. The coating prevents cementation within the deformation band. Partial cementation occurs if grains are coated with diagenetic minerals for instance illite (Storvoll et al. 2002) or chlorite (Ehrenberg 1993). These fractures can increase and also reduce porosity and permeability. Initial dilation opens a path way for fluids (Bernabe and Brace 1990) into these structures which can be the explanation of the bleaching of deformation bands (Parry et al. 2004). Within cataclastic deformation bands, the same mechanism can promote the cementation.

Furthermore, *disaggregation (dislocation) bands* form by disaggregation of the grains as granular flow (Twiss and Moores 1992) or particular flow which involves grain boundary sliding, grain rolling, breaking of cementation. Disaggregation bands mainly occur in sand or poorly consolidated sandstones. Shearing and compaction can be observed along the structure. In compacted sandstones, shearing related dilation can be observed initially, which later might be reduced due to grain reorganization. Displacement within the bands is a few centimetres in general; the lengths of the bands are not longer than a couple of meters. The thickness of the band, in general, is up to approximately 5 mm which depends on the grain size; in fine-grain sandstone thickness is less than 1 mm. Porosity increases by up to 8 % in disaggregation bands characterised by dilatational component (Antonellini et al. 1994, Du Bernard et al. 2002). Due to porosity increase, permeability also increases according of fluid flow observation of Bense et al. (2003). Where cataclasis is dominant within a disaggregation band, porosity decreases. Nevertheless, the porosity and also permeability contrasts are not significant in these structures therefore their effect on fluid flow is also not significant.

Finally, *phyllosilicate bands* develop in sand or sandstones which have platy mineral content of higher than 10-15%. These bands show similarities in fracturing mechanism to disaggregation bands where the main process is frictional grain boundary sliding promoted by platy minerals while cataclasis is not significant. In sandstones, platy minerals are commonly clay minerals that mix with other mineral during the deformation procedure called deformation-induced mixing (Gibson 1998). If the clay content higher than approximately 40 %, clay smear forms (Fisher and Knipe 2001). Permeability is often reduced in phyllosilicate bands. The degree of the reduction depends on for instance: type, abundance and distribution of the phyllosilicates and, offset of the band (Knipe 1992). The permeability reduction is around two orders of magnitude on average. Fisher and Knipe (2001) found that this value can increase up to five orders of magnitude if the grain size is less than 5 μm for North Sea reservoirs. Phyllosilicate bands can occur at various depths (Fossen et al. 2007).

There have been studies to analyse the effect of deformation bands on fluid flow. In most cases, the deformation bands reduce the permeability of the rocks, although their role is not completely understood yet (Fossen, et al. 2007). In case of single phase flow, the thickness and the permeability of the deformation band zone are the most important parameters. It has been shown by numerical simulations, that the increased number of deformation bands in a deformation band zone decreases the permeability of the rock (Matthäi et al. 1998, Walsh et al. 1998). Moreover, as a consequence also reduces the productivity in oil wells (Harper and Moftah 1985). In the case of two phase flow, the capillary entry pressure is the most important factor. Deformation bands can hold up to 20 m (Harper and Lundin 1997) or even up to 75 m (Gibson 1998) high column of hydrocarbons. Irrespectively of the case of one or two phase flow, the continuity or variation in thickness and 3D permeability are important parameters. The pattern of the fluid flow can change, if the deformation bands have a preferred orientation. For example, because of the clay content of the low permeability deformation bands, it can behave as a channel for groundwater flow through the vadose zone (Sigda et al. 1999). Similar effect can be observed in oil reservoirs, when water is pumped into the well to increase the productivity of oil; residual oil can be trapped in shadow zone because of the capillary entry pressure (Manzocchi et al. 2002).

1.4 Fluid flow in granular materials

In sedimentary rocks, fluid can flow within the interconnected pore system or along fractures or faults. The pressure gradient is the most effective transport driving mechanism. The fluid flows from a place where the pressure is higher toward the low pressure place. The velocity and quantity of the fluid depend on many factors, such as texture and properties of grain and pore system of the rock (including for instance: grain and pore size, grain and pore shape, grain and pore size distribution or mineral composition). Most important parameters are porosity, permeability and tortuosity regarding the fluid flow.

Porosity (sign: Φ) measures the void space within a porous medium as a ratio of the volume of the total pore space to the bulk volume of the studied material. Porosity is a dimensionless number; it is often given in per cent. See (Eq. 1-11) and (Eq. 1-12)

$$\Phi = \frac{V_{pore}}{V_{bulk}} \qquad \textbf{(Eq. 1-11)}$$

$$\Phi = \frac{V_{bulk} - V_{grain}}{V_{grain}} \qquad \textbf{(Eq. 1-12)}$$

Primary porosity is the remaining void space after physical compaction for example burial process of a rock body. *Secondary porosity* occurs as a result of additional processes such as fracturing or dissolution. The entire pore space within a material is called total or absolute porosity. However, certain part of the entire pore space can be isolated from other pores that are not interconnected and are available for fluid or gas. The ratio of the interconnected pore volume to the bulk volume of a measured material is called *effective*

porosity. Furthermore, a part of the interconnected pore space does not take part of the fluid flow system because of dead-end pores. The porosity where dead-end pores are not included in the pore space is called transport porosity. (Urai et al. 2008)

The permeability is another important physical property regarding the fluid flow which quantifies the fluid transport capability of a porous material. One type of fluid transport is separate phase flow. Volume flux (Darcy velocity) (sign: *v*, SI unit: m/s) is derived from the rate of the volumetric fluid flow (sign: *q*, SI unit: m^3/s) and the area of the cross section of the material. Furthermore, volume flux depends on the permeability (sign: k, SI unit: m^2), pressure gradient (SI unit: Pa/m) and the viscosity of the fluid (sign: μ; SI unit: Pa.s) (Eq. 1-13). This permeability definition (absolute permeability) assumes that the pore system is fully saturated with one single type of fluid (single phase flow).

$$v = \frac{q}{\mathrm{A}} = -\frac{k}{\mu}\left(\frac{dp}{dx}\right) \qquad \textbf{(Eq. 1-13)}$$

In case of multi-phase flow, pore space contains more than one phase (e.g. gas, water, oil) and the permeability of this system, called *relative permeability*, depends on the relative volume fraction of the phases. The effective permeability is the sum of all the phases in a given system, which is always lower than the absolute permeability. The Kozeny-Carman equation is a fundamental correlation equation between porosity and permeability (Eq. 1-14); where K_T is effective zoning factor (depending on for instance: pore size, pore shape, grain size, grain shape, their distribution or tortuosity) and S_{pore}^2 is specific surface area of pores. Several different type of permeability models have been developed earlier; such as, sand pack, grain-based, surface area or pore size mode (Table 1-1). (Urai et al., 2008)

$$k = \frac{\Phi^3}{\mathrm{K}_T S_{pore}^2 (1-\Phi)^2} \qquad \textbf{(Eq. 1-14)}$$

Model	Author	Equation
Sand pack	Krumbein and Monk (1943)	$k = 0.76\ D_g^2\ e^{-1.31\sigma}$
Grain-based	Berg (1970)	$k = 80.8 D^2 \Phi^{5.1}\ e^{-1.385p}$
Grain-based	Van Baaren (1970)	$k = 10 D_d^2\ \Phi^{3.64+m}\ C^{-3.64}$
Surface area	Timur (1968)	$k = 0.136\ S_{wi}^{-2}\ \Phi^{4.4}$
Surface area	Sen et al. (1990)	$k = 0.794\ T^{l2.15}\ \Phi^{m+2.15}$
Pore size model	Kozeny-Carman in Carman (1956)	$k = 400\ R_h^2\ \Phi^m$
Pore size model	Winland in Pittman (1992)	$k = 49.4\ R_{35}^2\ \Phi^{1.47}$
Pore size model	Katz and Thompson (1986)	$k = 17.9\ R_c^2\ \Phi^m$

Table 1-1 – List of different permeability models and correlation equations (Urai et al. 2008). Where k: permeability coefficient, D: grain diameter, σ: standard deviation of the grain diameter, Φ: fractional porosity, m: formation factor (consolidation for sand and sandstones), C: sorting index for grain diameters, Swi: sorting index, Rc: characteristic radius and Rh: hydraulic radius.

In addition to separate phase flow, the other type of fluid transport of hydrocarbon is the diffusional transport. Methane and light hydrocarbons dissolve in water and this gas can flow through the seals of reservoirs by diffusion. This can be an important mechanism in the leakage of seals in geologic time scale. In water-saturated system, diffusional flux is controlled by gradient of equilibrium concentration in hydrostatic column. (Urai et al. 2008)

A certain amount of pressure difference is required for oil or gas to move through pore throats in a water-wet rock (Berg 1975, Schowalter 1979). This pressure difference is called capillary pressure and it is given by the following equation where r is pore throat radius, θ is the wetting angle and γ is surface tension.

$$p_c = \frac{2\gamma \cos\theta}{\mathrm{r}} \qquad \textbf{(Eq. 1-15)}$$

Based on the equation above, height (*h*) of hydrocarbon column held by capillary pressure can be calculated by the equation below (Eq. 1-16) assuming stationary fluid. Where g is the gravitational acceleration and $\Delta\rho$ is the density difference between the two media.

$$h = \frac{2\gamma \cos\theta}{\mathrm{rg}\Delta\rho} \qquad \textbf{(Eq. 1-16)}$$

In sedimentary reservoirs, top seal and fault seals play a significant role in distribution of fluid pressure hence also in accumulation of hydrocarbon. Evaporites, organic rich rock and shales are found to be the most effective seals. Lateral continuous, ductile rocks with high capillary pressure are potential seals; ranked by lithology (from better seal to less effective seal): salt, anhydrite, organic-rich shales, clay shales, silty shales, carbonate mudstones and cherts (Downey 1984). A given layer can be a seal for fluid flow as long as capillary entry pressure is higher than the pressure of the hydrocarbon in the reservoir. Hydrocarbon can start leaking if capillary entry pressure of top seal is lower than the fluid pressure or the top seal in not water-wet. Furthermore, leaking of a top seal can occur by fractures or diffusion. Figure 1-13 shows the illustration of microstructures and pressure regime of the above mentioned top seal leakage situations.

In multi-phase fluid system, a single pore throat diameter is sufficient for calculation of capillary entry pressure or capillary displacement pressure. Capillary displacement pressure is defined as the pressure which can result in significant saturation (approximately 10 %) related to the second phase permeability. Analogue approach to the above mentioned, is to calculate the maximum hydrocarbon pressure based on the relevant properties of the fluid and the rock (Berg 1975, Schowalter 1979, Watts 1987, Ingram et al. 1997).

$$h_{max} = \frac{2p_{dHC}}{\mathrm{g}\Delta\rho} \qquad \textbf{(Eq. 1-17)}$$

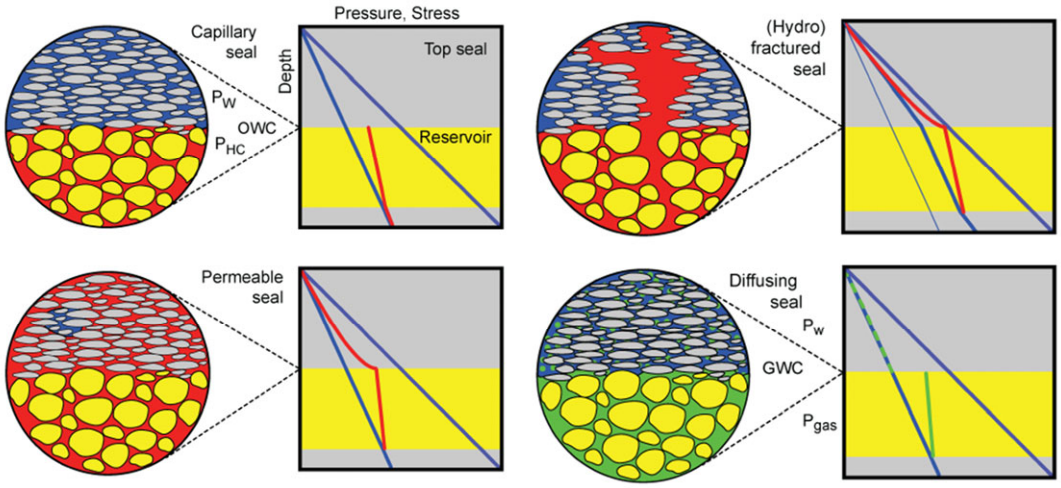

Figure 1-13 – Sealing mechanism (a) and leakage (b, c and d) at micro scale and pressure regimes in reservoir (Urai et al. 2008)

In order to describe the behaviour of the fluid in porous rock, a complete pore map is required, in which all the pores from the smallest to the largest pore size are quantitatively represented. In sedimentary rocks, the size of the pores covers a wide range from nanometres to hundreds of micrometres; therefore it presents a challenge to analyse them quantitatively (Radlinski et al. 2004). However, not only the pore size, but also the pore-throat size is an important parameter to characterize the flow particularly in tight sandstones (Nelson 2009). The pore throat radius was investigated by several studies (Dullien and Dhawan 1974, Wardlaw and Cassan 1978, Swanson 1981, Katz and Thompson 1986, Thompson and Raschke 1987, Ioannidis et al. 1996). It was shown, that there is a relationship between the pore throat, permeability and porosity (Heid et al. 1950, Kolodzie 1980, Aguilera 2002). Furthermore, it was also found, that permeability is influenced by the size distribution of pore throats, the connectivity properties of the pore network and the spatial correlation of pore sizes (Constantinides and Payatakes 1989, Bryant et al. 1993, Ioannidis and Chatzis 1993). Based on these relationships, Ziarani and Aguilera (2012) built a model to estimate the pore throat using the permeability and the formation factor (resistivity factor).

1.5 Aim of the thesis

The main aim of this thesis is to better understand the fracture and fracture networks which affect the fluid flow system in sandstone reservoirs especially in low permeability tight gas sandstone reservoirs. This study has basically two targets. Firstly, to analyse natural faults and fractures on large scale (Chapter 2) and on small scale (Chapter 3). Secondly, the intact host rock was analysed in order to estimate the mechanical parameters of deep located reservoirs and consequently estimate the tendency for open fracturing (Chapter 4 and 5).

In reflection seismic sections, only the larger faults with several meters offset can be seen; however, smaller faults which are invisible in seismic sections have also large impact on the hydrocarbon migration. The full structure of the faults systems can be studied by natural field analogues. In this study the spatial distribution and orientation of subseismic scale fractures were analysed relative to the seismic scale faults. One aim of this study is to analyse the spatial distribution, orientation and other physical parameters of fractures and fracture networks of fault zones.

Further aim is to better understand the microstructure of the fault related fractures and accordingly determine the types of fractures. The key question is whether a fracture is dilatant or compacting and accordingly the permeability of the rock and the fluid flow rate increase or decrease by the fracture. And, also the type of the fracture allows us to estimate the brittleness of the rock at the moment of fracturing.

The other main objective of this work is to study the mechanical properties (e.g. unconfined compressive strength and Young's modulus) of the intact rock body in borehole core samples, in order to be created correlation equation between rock mechanical properties and wireline log data. Wireline log data are available almost always from boreholes but core samples are rarely. Therefore log based correlation equations may provide a useful tool to predict rock mechanical properties of reservoirs. Numerous correlation equations have already been developed for many different types of sandstones. However, the available equations show relatively high uncertainty. Therefore, in this work multivariate regression method is applied in order to analyse the relation between different log data (acoustic velocity, density, resistivity, natural gamma, spectral gamma and neutron porosity) and rock strength and create correlation equation with lower uncertainty.

Brittleness is not a well-defined material property. Having developed brittleness indices, authors have tried to quantify the degree of brittleness of rocks. In most of the studies, the brittleness was determined using the parameters of the rock. However, other parameters, such as stress conditions have large effect on the brittleness of rocks. This study aims to create a new brittleness index based on formula of Urai (1995); furthermore to predict brittleness index logs for the studied sandstones.

1.6 Thesis outline

Chapter 1: gives a general overview of the relevant areas starting with the project rationales in Chapter 1.1. In Chapter 1.2, the theoretical background of strength, fracturing and brittleness is presented followed by an introduction of fault and fractures focusing on the fractures specific in sandstones in Chapter 1.3. In Chapter 1.4, general overview of fluid flow properties of granular material is discussed. Finally, the objectives and aims of all the parts of this study are summarised in Chapter 1.5.

Chapter 2: architecture of fracture network in fault damage zone is analysed at two normal faults: one is a branch fault of Moab Fault at the Courthouse Junction the other one is at the Klondike Bluff in Utah. Properties of the fractures were measured along the scan lines; such as, distance on the line, dip, dip direction, thickness and signs of fluid flow in order to analyse the effect of the fracture network of the fault damage zone on the fluid flow.

Chapter 3: microstructures of different type of fractures of sandstones were analysed. Samples studied from both analogue field area (Courthouse Junction and Klondike Bluffs) and additionally five samples were analysed from the Rotliegend Sandstone of North Sea. Fractures were studied by transmitted light microscope in thin sections and also in BIB polished samples by scanning electron microscope. Microstructures of fractures and host rock were compared to show how pore space, pore throats and grain sizes changed inside the structure and estimate the effect of the fractures on fluid flow.

Chapter 4: the relation between mechanical properties and wired line well log properties were studied in order to be able to predict rock mechanical properties from well logs. Therefore, unconfined compressive strength and Young's moduli of Rotliegend and Lower German Triassic samples from the North Sea were measured in this work. The relations were analysed by multivariate regression technique.

Chapter 5: the final chapter is focusing on prediction of brittleness of rock. Brittleness is related to the developing fracture types. In this work a new brittleness index equation was proposed in order to quantify the rock brittleness. In the brittleness index equation rock strength and stress is considered. Furthermore, brittleness index log were calculated for the North Sea wells which were involved in the Chapter 4. And based on these logs brittleness characteristic of Rotliegend and Lower German Triassic sandstone layer were predicted.

2 Large scale analyses of fractures in sandstone – natural field analogue

2.1 Introduction to field study in Moab, Utah

Faults, including the damage zone around them, are very often large size structures which play an important role in the subsurface fluid flow systems. The permeability of faults varies widely. Faults can act either as baffle to fluid flow reducing or stopping the fluid migration or can be conduit for fluid flow creating fluid pathways. Therefore, the knowledge of the permeability of the faults is essential to better understand the fluid flow system in faulted reservoirs. Several factors can control the permeability of the fault zones. Some properties of faults can be studied in reflexion seismic data and also in borehole data. These data sources have limitations, such as seismic data have limited resolution, or borehole can provide information from a very small volume which might not be representative. Field analogues can provide good opportunity to gain information on the properties of the structures of the fault zones in detail from km to micrometre scale. In the fault damage zone, fracture network can be found, formed by relatively thick fractures, with thickness up to few centimetres (e.g. Fossen et al. 2007, Rotevatn et al. 2008, Solum et al. 2010). These fracture networks can influence the fluid flow significantly. For example, disaggregation bands, which are related to gravitational or fluid expulsion-controlled processes or non-cataclastic granular flow have little or no influence on fluid flow; in contrast, phyllosilicate deformation bands can reduce the permeability by 0–6 orders of magnitude (Fisher and Knipe 2001) and tectonic related disaggregation and cataclastic deformation bands reduce the permeability of the rock by up to 3-4 orders of magnitude (Fossen 2010).

This study aimed to analyse the fractures networks (fracture type, geometry of the fracture, spatial distribution of the fracture) related to major faults in sandstones to better understand the architectures of the fault damage zone and the effect of the fault damage zones on the permeability and the fluid flow system. These data can help to improve the seismic interpretations and to improve our understanding of the properties of subsurface structures.

One of the most famous and most visited areas is the vicinity of Moab (Utah, USA) where many excellent sandstone outcrops can be found along the Moab Fault and also around the Arches National Park. The geological setting of the sandstones of Moab region is similar to the sandstones in the North Sea. Both areas are characterized by normal faults, extended salt tectonics, the burial depth at the time of faulting were in the same range approximately 2000 m and also similar type of sandstones (e.g. aeolian dune formation) (e.g. Doelling 1985, Draut 2005, Wong et al. 2007, Doelling 2010).

Many geoscientists (e.g. Aydin 1978, Cruikshank et al. 1991, Cruikshank and Aydin 1994, Cruikshank and Aydin 1995, Fossen and Hesthammer 1997, Fossen 2010) have studied the sandstone outcrops in the Moab area from many aspects. The geometrical and petrophysical properties of the fractures have been the subject of several studies. Fossen

and Hesthammer (1997) studied the displacement, the length and the linkage of the deformation bands in Jurassic Entrada sandstone in south-eastern Utah. According to their observations, deformation bands show various structures, they can be isolated, soft or hard linked; furthermore, they can form dense cluster zones with associated slip surfaces. Shipton and Cowie (2001) analysed the 3D architecture of fault zones along two normal faults in Navajo sandstone, Utah. They found that the damage zone consist of deformation bands and slip surfaces which are sub-parallel to the faults, and outside the damaged zone only few or no deformations were observed. The zone of deformation bands is about 12 m wide around the Blueberry fault, and continues for 45 m beyond the fault tip (Shipton and Cowie 2001).

The scaling relation between the maximum displacement (D) and the length (L) was also investigated by several studies. Basically, the displacement profile of deformation bands is qualitatively similar to the displacement profile of faults; for instance, both develop along strike with a central maximum (Fossen and Hesthammer 1997, Fossen and Hesthammer 1998, Fossen, et al. 2007). However, there are also some differences. The scaling relationship usually can be expressed by a power-law function with an exponent of approximately one to nine orders of magnitude for small faults (approx. 10 cm long). However, for deformation bands, the exponent is about 0.5 (Fossen and Hesthammer 1997). The lower D/L ratio of deformation bands in Orange, France was explained by the lower shear moduli of porous sandstones compared to other coarse grained sedimentary rocks (Wibberley et al. 2000). Also low D/L ratio was observed for Entrada sandstone, due to lithological layering; namely, it was difficult for deformation bands which nucleate in sandstone layers to propagate into the adjacent low porosity silty layers (Schultz and Fossen 2002).

Kolyukhin et al. (2009) showed, that the density of deformation band is the highest close to the fault core (up to 200 bands/m), and decrease moving away from the fault core. However, at certain distances, significantly large deformation band clusters also exist. Similar tendency was found by Gudmundsson et al. (2010) where the number of deformation started to decrease at about 10 m from the core. Roznovsky and Aydin (2001) showed that there is strong correlation between the rapid changes of fold strikes and increases in deformation band density within the Waterpocket monocline of the Colorado Plateau. Berg and Skar (2005) studied the fault zone architecture of the Bartlett fault which is a branch fault of the Moab fault. They found that the fault damage zone can be divided into subzones based on the deformation band distribution (Figure 2-1): The inner zone is a relatively short section adjacent to the fault core where the deformation band distribution is the highest. The outer zone is next to the inner zone where the deformation band distribution is significantly lower than that of the inner zone. The transitional zone is next to the outer zone where the deformation band distribution is approaching zero.

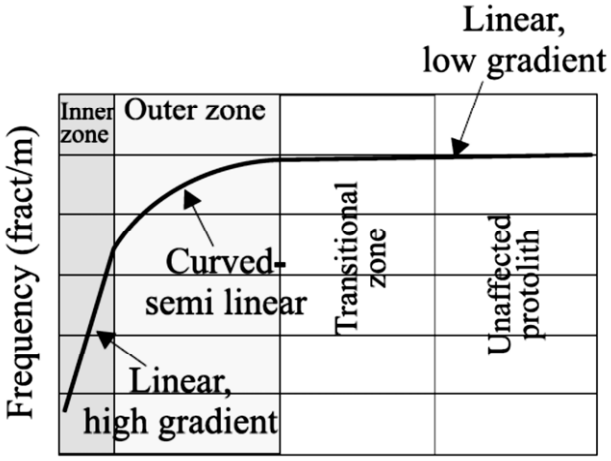

Figure 2-1 – The diagram shows the theoretical sub-zones (inner zone, outer zone and transitional zone) of fault damage zone based on fractures distribution (modified after Berg 2005).

The orientation of the deformation bands was also analysed by several studies. In the fault damage zone, the deformation bands are generally sub-parallel to the major faults (e.g. Kolyukhin et al. 2009); however, the range of the orientation of the deformation bands varies. For example, Shipton and Cowie (2001) studied the deformation bands around normal faults in Utah: In the case of Big Hole Fault, the orientation of the deformation bands varied by about 25°, and in the case of Blueberry fault the variation of the orientation was about 30°. In both cases, the scatter of deformation bands was approximately symmetrical around the main fault. In contrast, the deformation bands around the Moab fault (Utah) show very wide scatter of orientation, although the majority of the deformation bands are sub-parallel to the fault (Fossen 2010). Similarly, wide scatter of the orientation with fault parallel tendency were reported in Muley Tanks region (Utah), and in Oak Creek area (Utah) (Roznovsky and Aydin 2001). Furthermore, in some cases, the orientation of the deformation bands trend are oblique to the main fault (Flodin et al. 2001, Jourde, et al. 2002). However, the change of orientation of the deformation bands along a line normal to the fault has not been extensively analysed yet.

The deformation bands usually have synthetic or antithetic dip (Antonellini and Aydin 1994, Shipton and Cowie 2001, Johansen and Fossen 2008, Kolyukhin et al. 2009). It was shown that in the case of large faults (displacement > 30 m), the synthetic and antithetic structures are coeval and in equal proposition; whereas, in the case of smaller faults (displacement < 30 m), the synthetic structures are dominant (Antonellini and Aydin, 1994). It was also observed, that the deformation bands within a cluster (max. 10 cm to each other) usually have the same dip direction (Hesthammer et al. 2000, Shipton and Cowie 2001, Odling et al. 2004, Kolyukhin et al. 2009).

Kolyukhin et al. (2009) studied the effect of the different properties of the deformation band networks in comparison to a reference model where the fracture network is simple and has only minor influence on the fluid flow (Figure 2-2). Several properties were

taken into consideration, such as relative facture permeability i.e. contrast between the host rock and the fracture permeability (KDB/KHR), deformation band density, dip and dip direction of the deformation band, clustering of the deformation band (Dc) (fracture distribution around faults which is 1 if the distribution is uniform and about 0.1 if most of the fractures are very close the fault core and about 0.8 if the distribution is decreasing logarithmically going away from the fault core), fragmentation of the fault (i.e. discontinuities, "holes" in the fault planes) and the distribution of the fragmentation. The model of Kolyukhin et al. (2009) showed that in addition to the most characteristic parameters relevant to fault zone permeability, the relative permeability and the fracture density, fracture orientation relative to fluid flow direction, fracture clustering, fracture fragmentation and its distribution may have considerable impact on the bulk permeability of fault zones.

To gain a better understanding of natural fracture networks of fault damage zones in sandstones, two normal faults with different characteristics were analysed in sandstone outcrops: one at the Moab fault and the other at the Klondike Bluffs (Utah, USA), where excellent quality outcrops are available in eolian sandstones (Slick Rock Member of Entrada Sandstone and Moab Member of Curtis Formation). These sandstone structures can provide good analogue to the subsurface sandstone reservoirs and can provide information for better understanding of seismic interpretation. This study focuses on the type of fractures, dip and dip direction of the fractures, thickness, distribution and density of fractures in the damage zones of faults. The two studied fault segments are close to fault junctions. Two scan-lines were measured along each fault in order to be able to study the change of the fracture network along the fault relative to fault junctions.

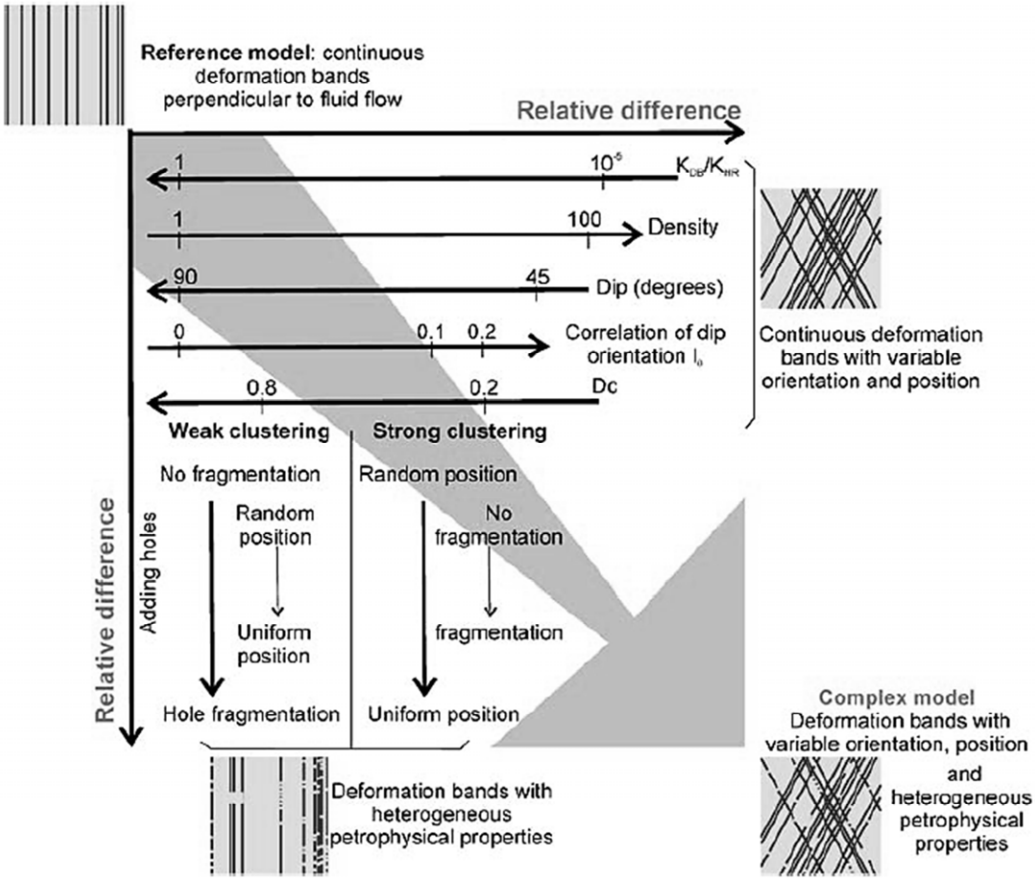

Figure 2-2 – The figure shows the summary of the parameters of the deformation band network model of Kolyukhin (2009). By this model, the effect of the different properties of the deformation band network on the bulk permeability. Parameters of the model are: relative facture permeability i.e. contras between the host rock and the fracture permeability (K_{DB}/K_{HR}), deformation band density, dip and dip direction of the deformation band, clustering of the deformation band (Dc), fragmentation of the fault (i.e. discontinuities, "holes") and the distribution of the fragmentation. (modified after Kolyukhin et al. 2009)

2.2 Study area

Faults were studied in two sandstone outcrops. One of the outcrops is located at Courthouse Junction and the other is at Klondike Bluffs about 7 km from each other near Moab city in Utah, USA (Figure 2-3, Figure 2-4) to the west from the Arches National park between the Green- and Colorado River.

Courthouse Junction Area

The Courthouse Junction area is located to the north-west from Moab city and to the west from the Arches National Park (Figure 2-6). The area is close to one of the major junction points of the Moab Fault where the main fault splits into more, smaller faults branches. This fault system is normal faulted. Close to the junction point, the offset of the main fault branch segment is about 70-80 metres. Only the footwall of the fault is uncovered. Cretaceous and Quaternary formations cover the hanging wall of the fault. The total length of the outcrop of this fault branch is around 10 km long, which is divided by canyons where the studied sandstone layers are completely eroded. Along this fault branch, about 7-8 tower-like outcrops can be found. In the centre of the junction point a triangular shape, intensively fractured outcrop can be found that was studied by many authors (see Chapter 2.1). The first segment of these outcrops is the Courthouse Rock that is an about 110 m wide and about 1000 m long rock block is about 100 m from the centre of the Moab Fault. On the top of the Courthouse Rock, the upper most Moab Member of the Curtis Formation is heavily eroded especially close to the junction point. The second segment is between the Courthouse Canyon and Mill Canyon, about 300 m from the Moab Fault, and it is about 650 m wide and about 1000 m long. This relatively large outcrop was in the focus of this study which is only locally covered by vegetation. The upper most rock is Moab Member of the Curtis Formation which covers most of the surface of the outcrop. Underneath, the Slick Rock Member of Entrada Sandstone can be found on the surface where the top layer is missing.

Klondike Bluffs area

The Klondike Bluffs area is located to northwest from the Arches National Park (Figure 2-4) and 1.5 km from the Salt Valley anticline which is part of the Pennsylvanian Paradox Basin area of SE Utah and SW Colorado. Klondike Bluffs area is about 7 km to NNE from the Courthouse Junction area. The surface rock is the Moab member of Entrada Sandstone at this outcrop. The fault is approximately 1000 m long and striking in NE-WS orientation. The main fault splits up into three fault branches. The fault tips can be found approximately 600 m from the branch point to the SW. The main fault has a maximum offset of around 10 m at the south part of the fault. The fault at this branch point was strongly eroded and covered by vegetation so these values are only rough estimates.

Figure 2-3 - Topographical map of area of Moab and Arches National Park (Doelling 2010).

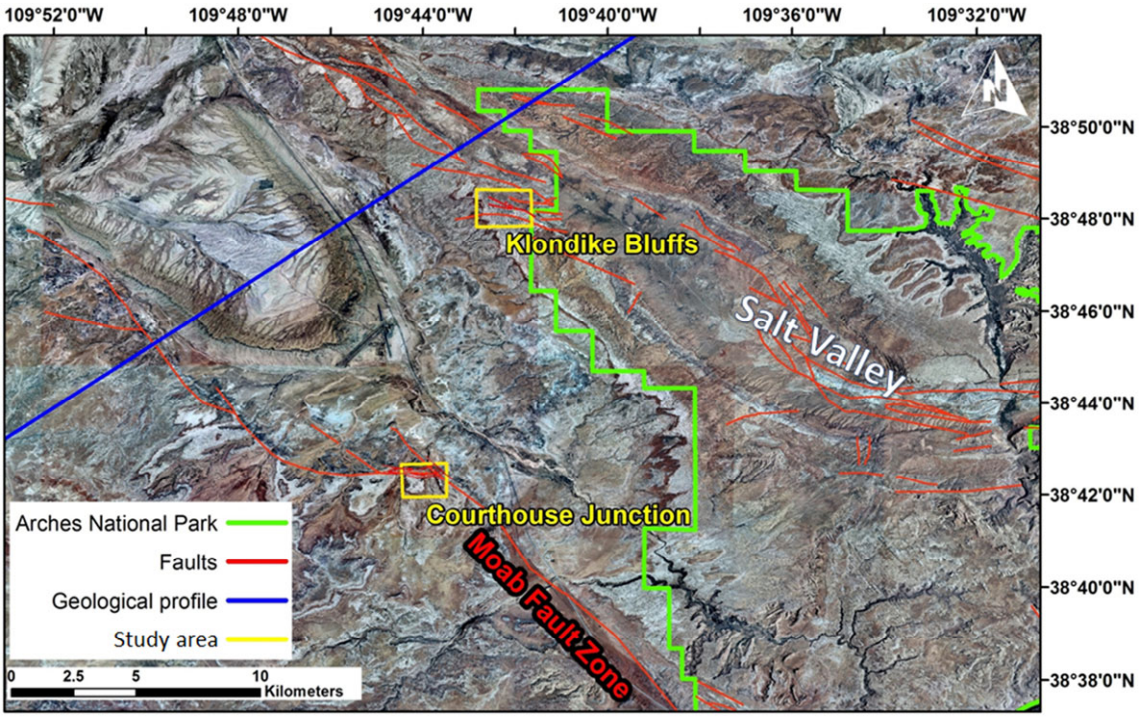

Figure 2-4 - Overview map of the Moab Fault Zone and its vicinity, yellow boxes indicate the two study areas. The geological profile can be seen in Figure 2-5. (satelite image source: NAIP, 2009; fault structure after Doelling, 2010)

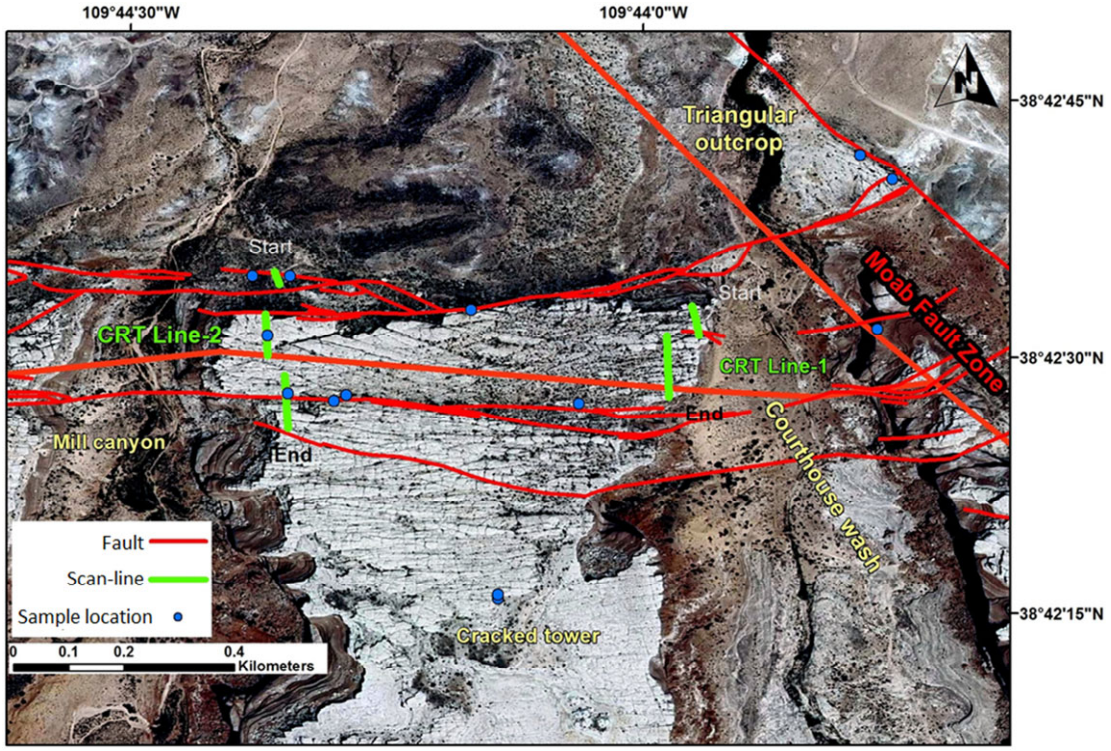

Figure 2-6 - Satellite image map of the Courthouse Junction area. (satelite image: NAIP, 2009; faults structure: Davatzes et al., 2005)

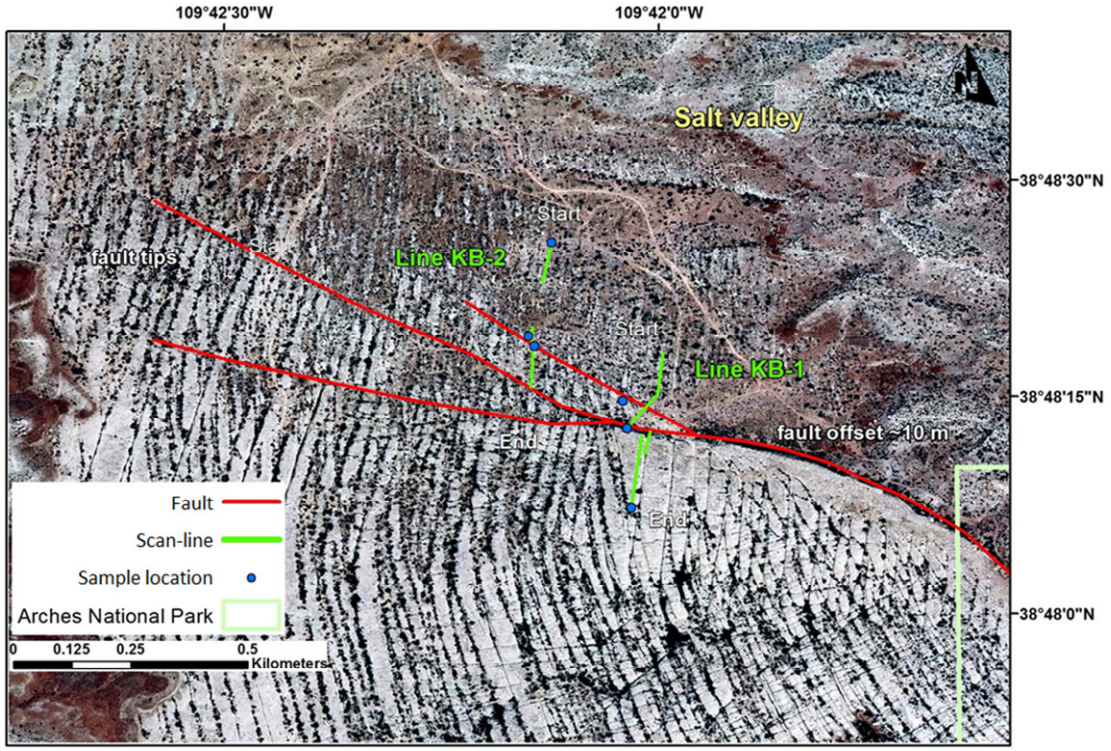

Figure 2-7 - Satellite image map of the Klondike Bluffs area. (satelite image: NAIP, 2009)

2.3 Geology setting of the Moab area

The two studied normal faults, the Courthouse Junction which is a branch fault of the Moab fault and the Klondike Bluffs in the Salt Valley fault zone, are part of the fault and fold belt of the Paradox basin. The area is affected by Triassic salt tectonics started at Middle Pennsylvanian. As a result of the tectonic activities, several fault systems developed in this area. The Moab Member of Curtis Formation, the Slick Rock Member of Entrada Sandstone, the Salt Wash and the Tidwell Member of Morrison Formation are present at the surface now (Doelling 2010).

2.3.1 Structural history

About 300 million years ago, SE-Utah and SW-Colorado subsided to form a basin called Paradox basin. This basin was formed as mostly northwest trending and normal faults were intermittently activated. In the basin, evaporitic sediments were deposited. After being covered and confined by heavier sediments, the salt moved upward toward the surface as enormous salt walls (salt cored anticlines) parallel to the faults. This process continued for 75 million years. Several boreholes indicate that the sides of the salt walls are mostly very steep and about 3.2 km high. (Doelling 2010)

During the Jurassic and Cretaceous periods, the area stayed near sea level, receiving continental deposition during Early Cretaceous time and marine deposition during Late Cretaceous time. During the Late Cretaceous and the early Tertiary, the rocks in the Arches area were faulted and folded. Relatively large-sized uplifts and basins developed in the Colorado Plateau region after the withdrawal of the Late Cretaceous Western Interior Seaway (Mancos Sea). The Arches area lies between the Uinta Basin to the north and the Monument Unwrap to the south and the regional dip of the area is 2° to 4° northwards. (Foxford 1993, Doelling 2010)

The major tertiary normal faults are associated with each of the salt walls. The Moab fault is located in the north of Moab Valley and cuts through the middle of the 3.2 km wide Moab salt wall parallel to its strike. The downthrown block is on the northeast side. The Honaker Trail Formation is abutted against the Entrada Sandstone, indicating a displacement of 730 m across the Moab fault. The Moab fault has two branches. A thin slice of Moenkopi Formation separates the Honaker Trail Formation from Entrada Sandstone. A similar, but less obvious fault cuts the middle of the salt under Salt and Cache Valley. On one side of the fault, cupolas of Paradox Formation caprock are covered by the upper Chinle Formation. Gardner et al (2001) reconstructed the burial history of the Jurassic sandstone units adjacent to the Moab Fault and found that the deformations related to the Moab fault occurred at the maximum depth of burial of about 2 km. (Doelling 2010)

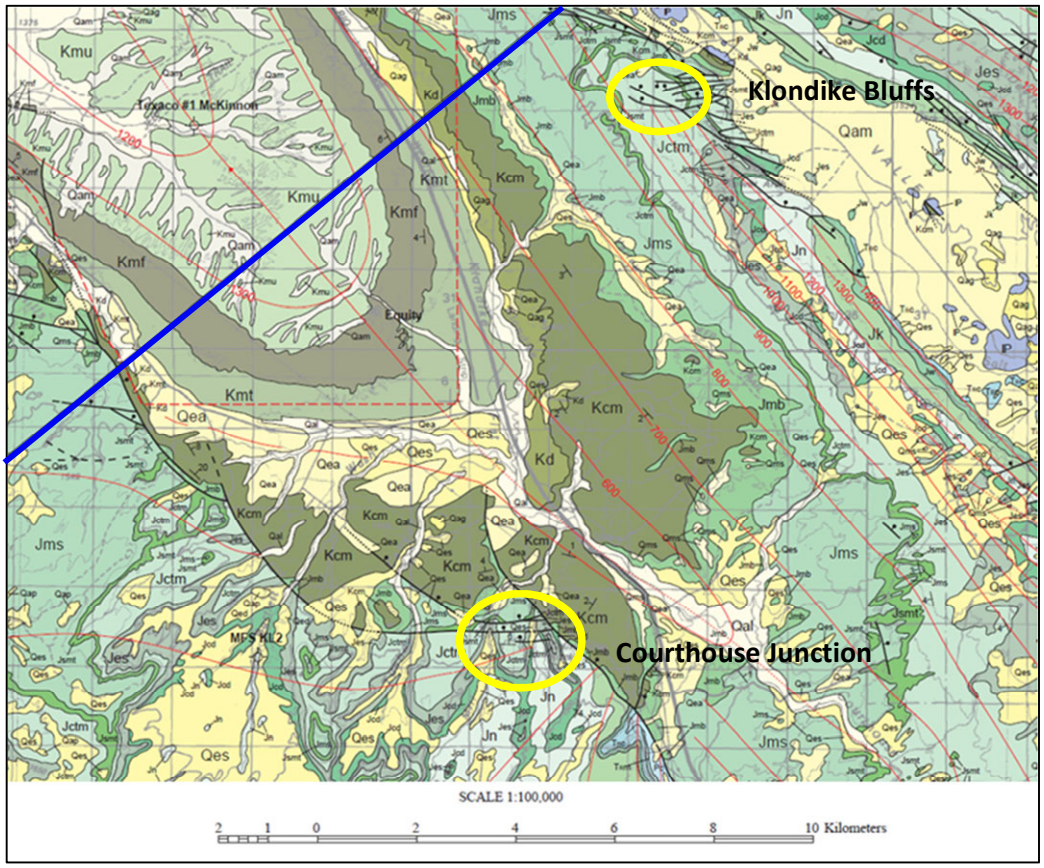

Figure 2-8 – Geologic map of the study areas (yellow circles), where blue line indicates the location of the geologic cross section in Figure 2-9. (modified after Doelling, 2010).

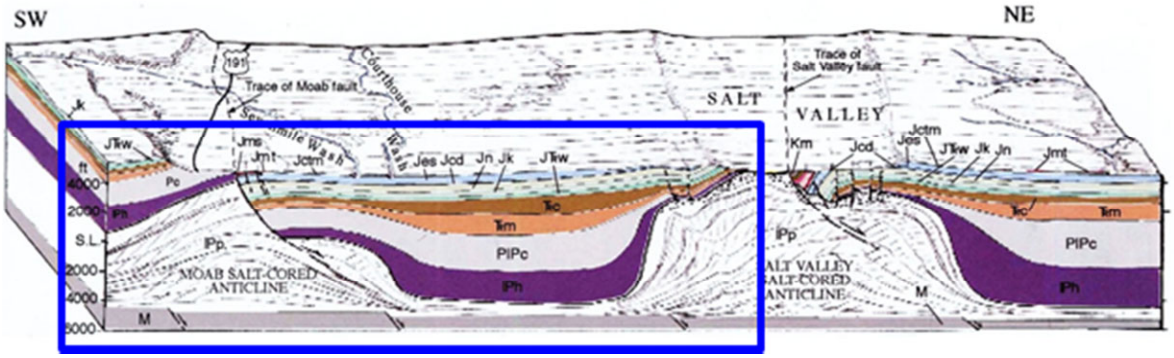

Figure 2-9 - Cross-sectional block diagram of geological layers of area of Arches National Park (Doelling 2010), blue rectangular indicates the part of cross-section that can be seen on the map of the study area above by the blue line.

During the Late Tertiary – Quaternary, about 15 million years ago, the Colorado Plateau area began rising in elevation. Erosion gradually stripped away overlying rock formations; the detritus is being carried to the sea by the Colorado River and its tributaries. Joints and faults provided the plumbing for fresh water to reach and dissolve salt in the upper parts of the salt walls. As dissolution progressed, graben valleys developed over the salt walls and gradually widened. The rocks on the top of the salt wall were undermined and collapsed into the graben valleys along fractures that opened parallel to the valleys. The collapse created graben-valleys that overlie the salt walls today. Brittle hard sandstones rolled over into the salt dissolution valleys or grabens and were eroded into thin fins along their previously formed, now-opened joints. Weathering then attacked weak the horizontal zones such as formational boundaries, bedding planes and soft partings, forming alcoves and arches in and through the fins. (Foxford et al. 1996, Doelling 2010)

The brittle sandstone formations of the Arches area are generally intensely fractured. The most part the fractures are sub-parallel to the northwest trends of the salt anticlines, but locally their trends vary. A swarm of northwest-trending normal faults are sub-parallel to the Moab anticline northwest of Moab Valley. These are essentially joints along which there has been some vertical movement. Gardner et al (2001) reconstructed the burial history of the Jurassic sandstone units adjacent to the Moab Fault and found that the deformations related to the Moab fault occurred at the maximum depth of burial of about 2 km.

In the Cache and Salt Valley, the fracturing occurred in the Tertiary and Quarternary, during and following the Colorado Plateau uplift and the Colorado River incision (Doelling and Kuehne, 2013). The oldest fractures of the Salt Valley area are the deformation band. According to Aydin & Johnson (1978), the Klondike bluffs area is characterized by at least two sets of deformation bands, striking N55°-75°E and dipping to either the south or north. Field observation showed that the presence of the deformation bands has not affected the development of systematic joints except where a slip surface has formed along a zone of deformation bands, which happened for example in the case of Klondike Bluffs fault (Aydin & Johnson 1978, Cruikshank and Aydin 1995). Joints in the Entrada Sandstone appear to be related to the salt-cored Salt- and Cache-Valley structures, and do not reflect a regional pattern (Doelling 1988, Cruikshank and Aydin 1995). In the Salt Valley Anticline, three generations of joint can be distinguished according to their orientation. First, N5°-10°E striking joints formed within the Moab Member. Then, N15°-22°W striking joints generated in the Moab Member. Finally, N20°-28°W striking joints developed in the Slick Rock Member. (Cruikshank and Aydin 1995).

2.3.2 Stratigraphy

In this study, two formations, the Slick Rock Member of Entrada Sandstone and the Moab Member of Curtis Formation, are in the focus. These two types of sandstones form the surface of the studied areas, and also most of the other places where sandstone outcrop can be found.

Slick Rock Member of Entrada Sandstone (JES):

The Slick Rock Member is the only member of the Entrada Sandstone, which overlies the Dewey Bridge Member of Caramel Formation. The thickness of the layer is 20-150 m. The Slick Rock Member is a massive, well-intruded, red-orange or brown, very fine to fine-grained sandstone. It contains spare and scattered medium to coarse grains, which are held together with calcite and iron-oxide cement. It commonly weathers to form smooth cliffs and bare-rock slope. Parts of this member are cross stratified eolian deposition other parts are planned bedded. The member is cut by numerous closely spaced vertical joints and also other fractures can be found here such as deformation bands and veins. (Doelling 2010)

Moab Member of the Curtis Formation (Jctm)

The Moab Member overlies the Slick Rock Member. The unconformable contact between these two members is sharp. This is a conspicuous, resistant sandstone that forms a capping surface on the Entrada sandstone. It is mostly a pale-orange, gray-orange, pale-yellow-brown, or light gray, fine- to medium-grained sandstone that weathers white or light gray. It is typically well intruded, exhibits low angle cross-stratification, and is in general highly jointed in the outcrop. The thickness of this member varies from 20 to 35 m. (Doelling 2010)

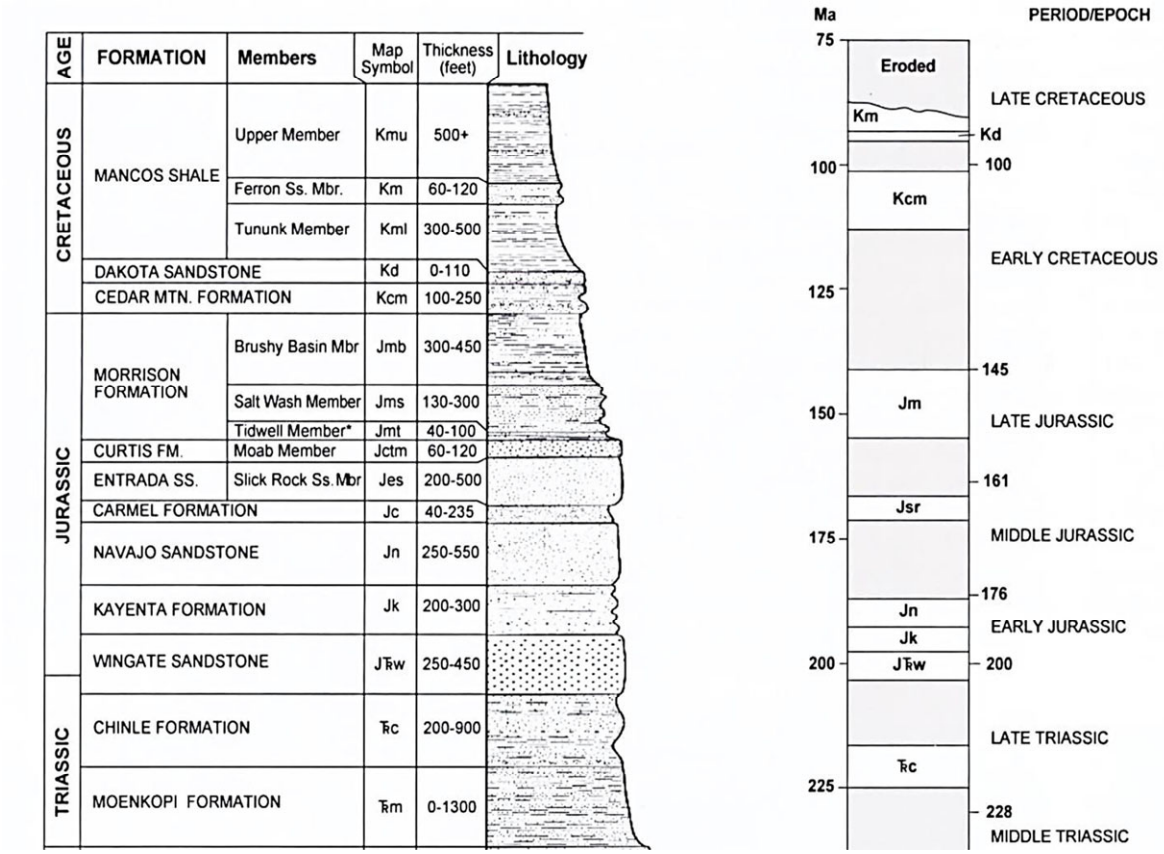

Figure 2-10 – Lithologic column of Moab area (modified after Doelling 2010)

2.4 Method

One of the main purposes of the fieldwork is to measure the spatial location and the orientation of the fractures and the related geological features (e.g. mineral concretion) in order to be able to study the properties of the fracture network in the fault zones. With this purpose, scan-lines were measured perpendicular to the strike of the master faults to gain information on the structures. The measurement was done with measuring tape, which was laid on the surface. The length and dip of every dipping section was measured at every section. The location, position, orientation and dip of every single structure was measured and also other properties of the structures, such as type, thickness, colour and the shape of the fractures relative to the host rock were noted. In this thesis, the shape of the fractures means the shape of the fractures relative to the host rock. Fractures can be in plane with the host rock or if the fracture is eroded it is lower than the host rock i.e. concave or if the fracture is higher, out of the host rock i.e. convex. This can indicate the weakness of the fracture or its resistance against the weathering. The fractures microstructures were studied by loupe to identify the types of the fractures.

The reading uncertainty of the distance measurements by measuring tape is ± 0.5 mm. The uncertainty of the horizontal distance measurement along the lines is higher because of the uncertainty of dip measurement, where the reading uncertainty of dip measurement ± 0.5 degree. And also the measuring tape may have deviation from the straight line which can cause 0.5 - 3 m error in distance at a 100 m long line depending on the variety of surface undulation.

The different types of field data are visualized by diagrams. The fracture frequency is plotted in 1 and 5 m resolution against the horizontal distance along the lines starting from north. In addition, cumulative number of the deformation bands is plotted in the frequency plot. Furthermore, the different other properties of the fractures and the outcrops is plotted along the lines (in the lower part of fracture frequency plots). In the plots, the master faults (vertical solid line) and the smaller faults (vertical dashed line) are plotted too. The dip and dip direction of the fractures are plotted in rose diagrams and stereographic lower-hemisphere projections.

2.5 Results

2.5.1 Courthouse Junction

Two scan-lines were measured approximately perpendicular to the main fault segment on the foot wall (Figure 2-6) at the Courthouse Junction outcrop. Line CRT-1 is closer to the junction point at the east part of the outcrop about 300 metres from the Moab fault; and, Line CRT-2 is about 360 m far from Line CRT-1 to the west. Deformation structures were investigated around the studied faults to gain information on the characteristics of the fractures of the fault zone. This fault zone is characterised by major cataclasis. The majority of the deformation structures were cataclastic deformation bands. In addition, many slip planes were observed along the studied fault segment. Slickenlines can be observed on the surface of the slip plains. Only minor, local fluid flow alterations (small spots - diameter < 1-2 meters), such as mineral concretions (nodules) and mineral precipitations were observed close to the fault core (distance < 25-30 meters).

Line CRT-1

Figure 2-11 shows the deformation band frequency of all the deformation bands including bands in bundles and also the position of the different types of the deformation structures along the scan-line. The line starts from the estimated start of the damage zone of the fault. The first 45 m long section of this 212 m long line was a steeply dipping, strongly eroded and covered section. It was not appropriate for scan-line measurements. However, based on field observations, short not covered areas showed relatively high fracture density close to the fault core, so it is assumed as the inner zone of the damage zone. In the first 10 metres of the measured line, only few joints and one slip plain were observed. In the following 20 metre long section of the line, the deformation band density is significantly higher than the rest of the line. Besides, in the same section, also the density of the deformation band bundles is higher. Only few joints were observed farther from the main fault. Most of the slip plains were located in the section of the line between 60 m and 120 m and only one was found farther. Fault throws were measured at four structures: at about 58 m, the first faulted structure had a throw of about 1.5 m where slip plain was not observed; the other three measurable throw were observed at slip planes. At 102 m, the slip plain had also 1.5 m throw and around this, the deformation density locally increased. The slip plain at 183 m had a throw of only about 25 cm, and there was no fractures observed around it. The last marked structure was out of the line, the surface was covered at this section. It was not possible to measure the structure. It was a relatively large 40-50 wide faulted zone which had a throw of about 2 m and started about 10 metres from the end of this line (at 222 m) marked in the plot. At the end of the measured line, there is no noticeable increase in the fracture density even though this relatively large fault zone is close to the line end.

The deformation band frequency plot (Figure 2-11) shows a decreasing overall tendency. However, the deformation band frequency does not decrease monotonously. There are local

peaks in the deformation band frequency; shorter section at 105, 145, 168 m and slightly longer sections at 116 to 121 m. The deformation band density peaks are not located at faults in general. The number of the deformation bands exceeds 5-7 deformation bands per metre close to the main fault from 65 m to 88 m. The number of the deformation bands exceeds 5-6 bands per metre at only few places. There are several metre long sections without any fractures from 88 m to 167 m. From 88 m, the most common deformation band frequency is 1-2 deformation bands per metre. Farther than 167 m number of the deformation bands is maximum 2 deformation bands per metre.

The cumulative deformation band curve (Figure 2-11) can be divided into two main sections. One is closer to the main fault which is a 23 m long steep sub-linear section from 65 – 88 m where 50 % of the deformation bands are located showing only slightly decreasing tendency in deformation band frequency. The other section is 130 m long from 88 m – 218 m less steep section where the deformation band density is significantly lower (except local peaks) and decreasing more intensively. The plots do no show unambiguous relation between the locations of the faults and the distribution of the deformation bands.

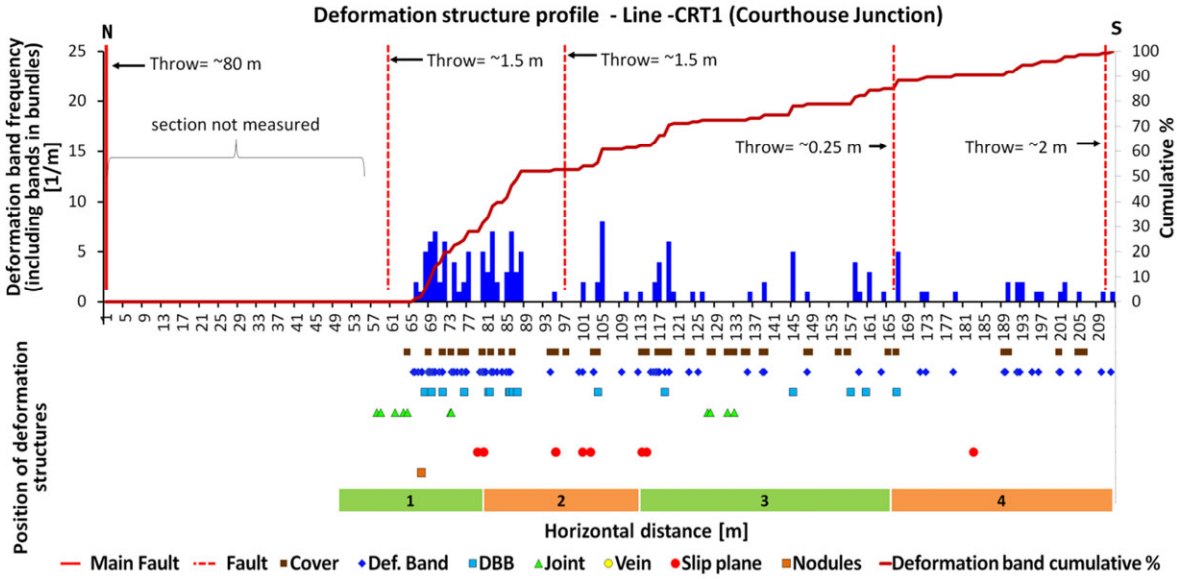

Figure 2-11 – The deformation band frequency (bin size=1 m), the cumulative deformation band frequency in percentage (including deformation bands in bundles) and the location of the fractures are shown along the line CRT-1 in the plot. The numbered sections show the separated sections for stereographic projections on Figure 2-15.

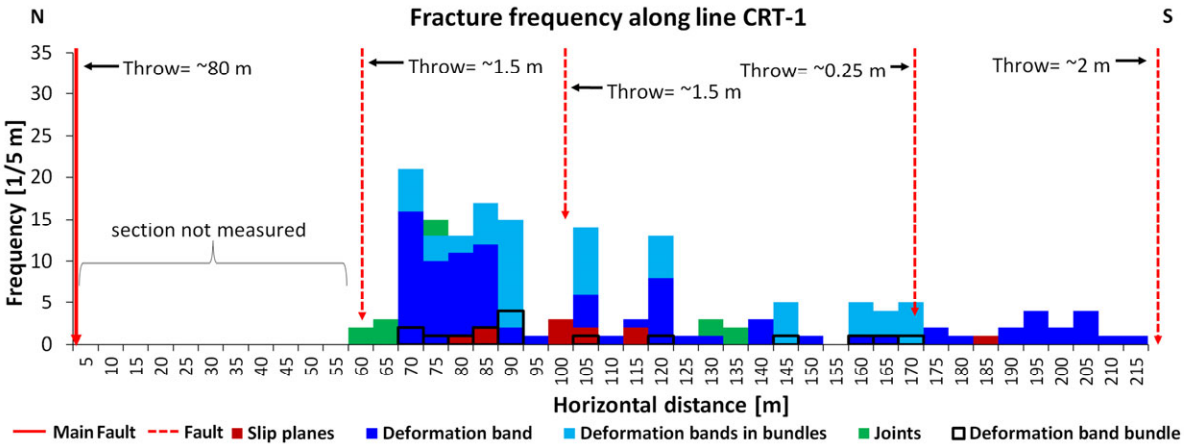

Figure 2-12 – The deformation frequency of the structure along line CRT-1 (bin size=5 m). There are 145 deformation bands (including those are in bundles); 87 single deformation bands; 16 deformation band bundles; 12 slip planes; no veins and 11 joints in this line.

The combined fracture frequency plot (Figure 2-12) shows that majority of the deformation structures are deformation bands along the line CRT-1. The deformation band bundle density has a similar decreasing tendency to the combined deformation band tendency. However, there are more deformation bands which are within bundles in the middle of the line (90 m – 120 m) similarly to the occurrence of the slip plains. There are only few slip planes and joints in the line.

Orientation and thickness of the fractures

Figure 2-13 shows the stereographic projection of all the fractures along the entire CRT-1 scan line. The orientations of the structures are in one group having about east-west (80°-260°) direction and they vary in a range of about 30°. Only very few fractures are out of this range. The dip direction of each type of fractures is plotted separately in rose diagrams (Figure 2-14). The dip direction of the majority of all type of fractures is between 170-180 degrees.

To study the changes in fracture orientation going away from the main fault, the scan-line was cut into four segments. The fracture orientations of each segment were plotted in stereographic projection (Figure 2-15). Stereographic projections show only the fractures of which dip was measured; therefore, dip and dip directions of the fracture planes are also plotted separately along the line (Figure 2-16, Figure 2-17). In the stereographic projections of the segments (Figure 2-15) and also in the dip direction plot (Figure 2-16), it can be seen, that the scatter of dip direction decreases slightly going away from the fault core. There are only very few structures which strike is fairly different from the mean strike. The orientation of the structures in the segments and the mean orientation of the structures are nearly the same. This constant dip direction along the line also can be seen in Figure 2-17. The dip of the structures shows larger difference along the line. The dips of the structures are more scattered close to the main fault and less scattered away from it (Figure 2-17). The majority of the dip of the structures are in the range of 70 -90 degrees.

The thickness of the bands is also nearly constant; it varies between 1 and 2 mm (Figure 2-18). The thickness of deformation band bundles and also the shape of the bands do not show any trend along the line. The number of the deformation bands in bundles is increasing going away from the main fault.

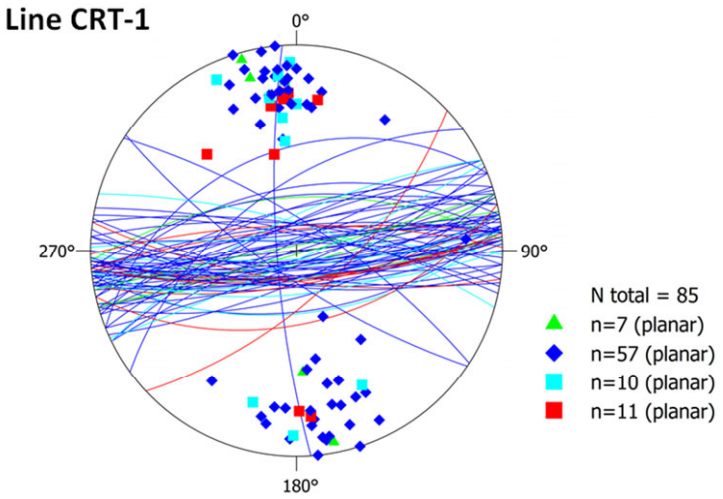

Figure 2-13 – Stereographic lower-hemisphere projection of the planes of all the fractures along line CRT-1 (red: slip plane; blue: deformation band; cyan: deformation band bundle; green: joint).

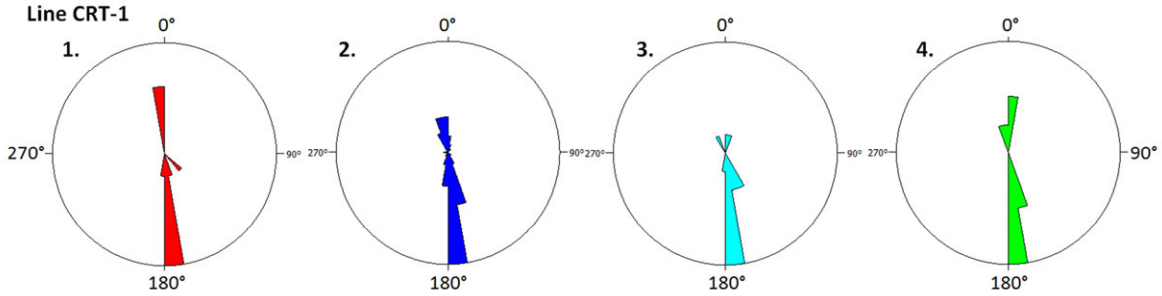

Figure 2-14 – Rose diagram of the dip directions of the fractures along the line CRT-1 per fracture type (red: slip plane; blue: deformation band; cyan: deformation band bundle; green: joint).

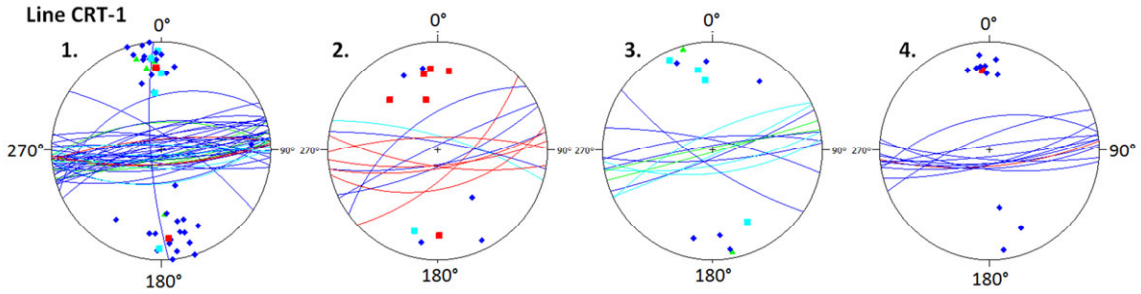

Figure 2-15 – Stereographic lower-hemisphere projection of the four sections of line CRT-1 (red: slip plane; blue: deformation band; cyan: deformation band bundle; green: joint).

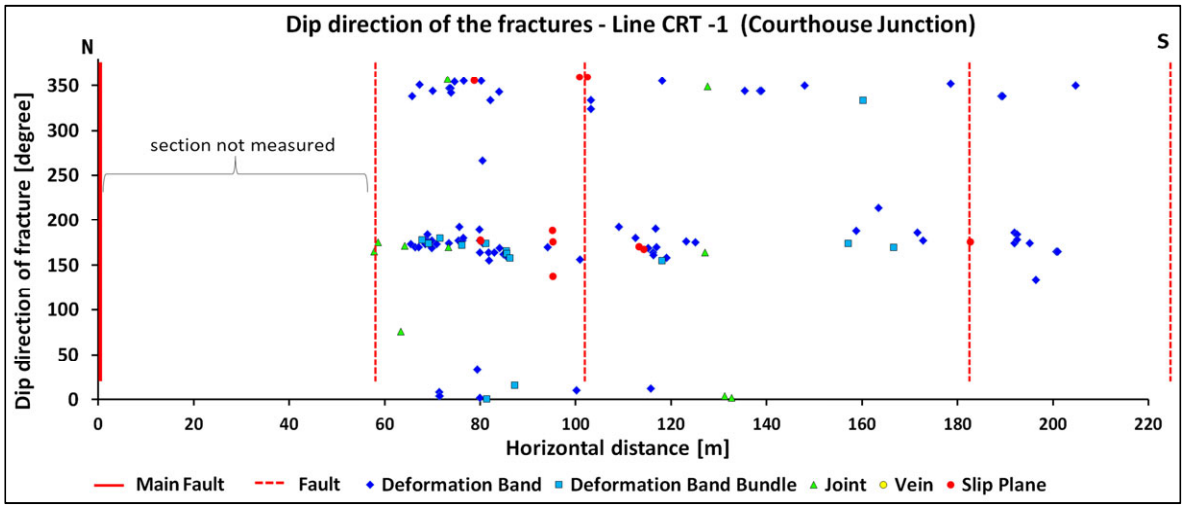

Figure 2-16 – Dip direction of the fractures along the Line CRT-1.

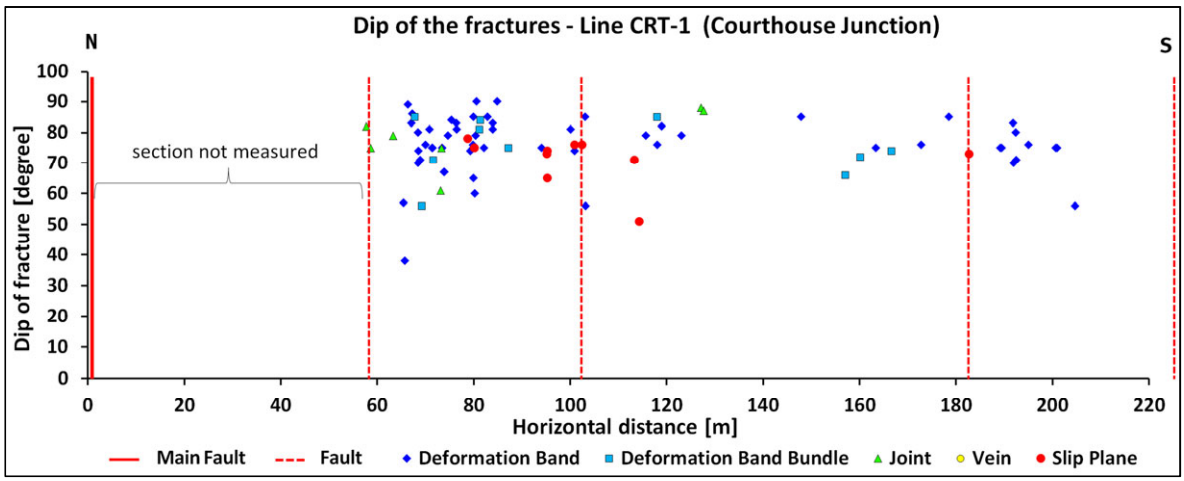

Figure 2-17 – Dip of the fractures along the Line CRT-1.

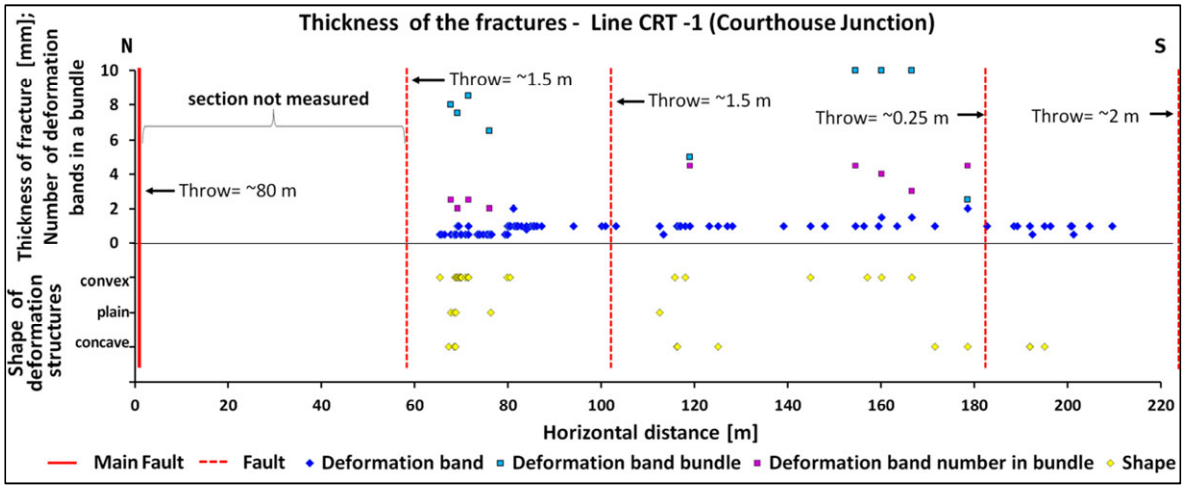

Figure 2-18 - The thickness, the shape (referenced to the host rock) of the deformation bands and the number of the deformation bands in bundles along Line CRT-1.

Line CRT-2

This line starts at a large slip plane, which has fine, polished, white colour slickenlines on the surface and it is presumably very close to the core of the studied fault branch. There is a not measured section in the first part of the line from 14 m to 64 m where the surface was weathered and covered and was not appropriate to measure scan-line. However, the short, not covered areas showed relatively high fracture density in this section. The fault zone shows a more complex structure in comparison with the line CRT-1 and smaller faults were observed in the far third of the line. The fracture frequency plots (Figure 2-19, Figure 2-20) show a moderate decreasing tendency in the deformation band frequency; however, there are several peaks evenly distributed along the line. There is no clear relation between the occurrence of the peaks and occurrence of the faults. The number of the deformation bands exceeds 8-10 deformation bands per metre close to the main fault from 0 m to 14 m. The number of the deformation bands exceeds 20-22 band per metre at peaks only locally (sections <1 m). And at end of the line, deformation band frequency often exceeds 3-4 bands per metre. There are some several metres long gaps without any fractures. The occurrence of the joints shows also a moderately decreasing tendency; however, more slip planes were observed at the end of the line than close to the main fault.

The cumulative deformation band curve (Figure 2-19) contains sequences of steep and less steep sections. The curve can be divided into five sections: The first one is a 23 m long steep section from 0 m – 14 m at the main fault where 20 % of the deformation bands are located with decreasing deformation band frequency from the main fault. The second section is 130 m long from 88 m – 210 m less steep where the deformation band density is significantly lower including a 30 m long gap, the cumulative deformation band reach 50 % by the end of the section. The next section is a short 15 m long steep section which contains 20 % of deformation bands; followed by a 45 m long from plateau from 228 m – 273 m and at end of the line there is again a steep section involving 26 % of the deformation bands. The plots do no show unambiguous relation between the locations of the faults and the distribution of the fractures.

Along this line, the majority of the deformation structures are also deformation bands (Figure 2-20). The deformation band bundles are in the middle (65-115 m) and at the end of the line (>225 m) only, and their numbers range between 1 to 5 bundles per 5 metres. The total number of the single deformation bands is only slightly higher than the total number of deformation bands inside bundles. However, in the same bins where deformation band bundles occur, the number of the deformation bands which are within bundles significantly higher. There are two sections (65-115 m and 225 m to the end) which are characterised by deformation band bundles.

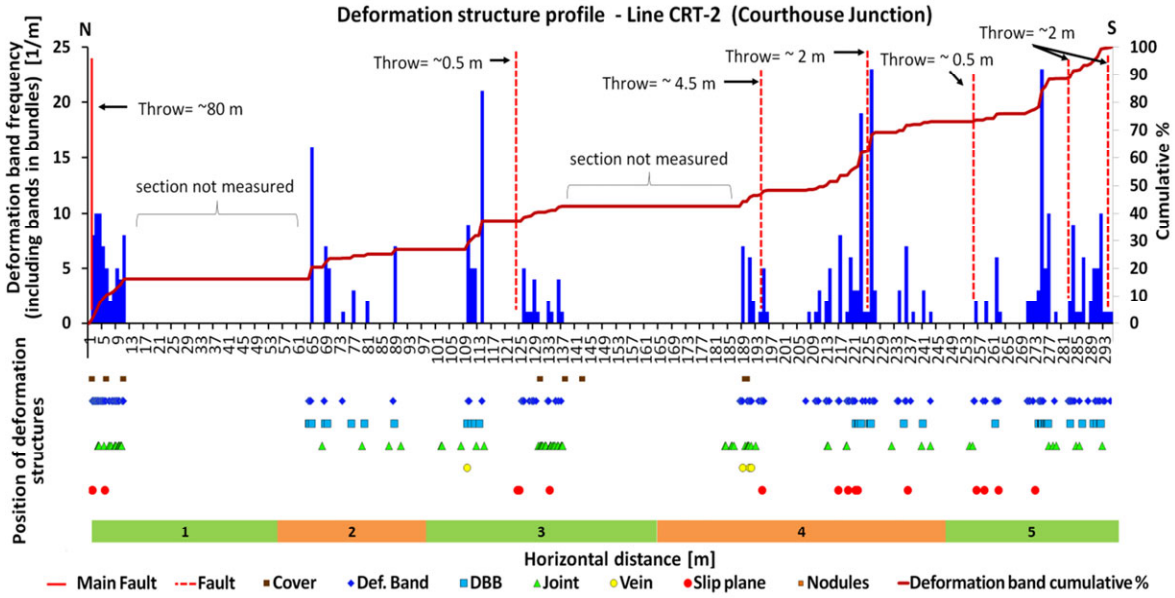

Figure 2-19 – The deformation band frequency, the cumulative deformation band frequency in percentage and the location of the fractures and features are shown along the line CRT-2 in the plot. The numbered sections show the separated section for stereographic projection of Figure 2-22.

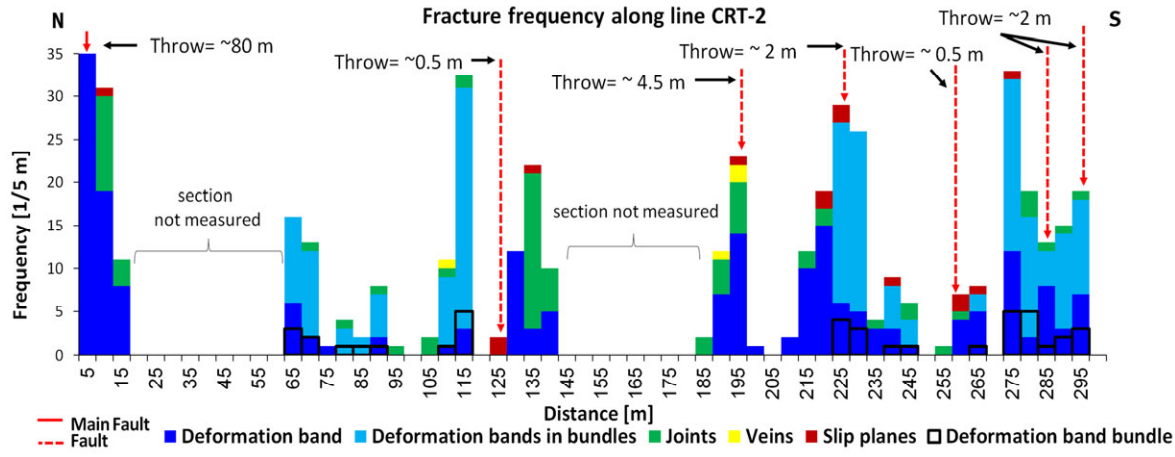

Figure 2-20 - Deformation structure frequency along line CRT-2 (bin size=5 m). There are 383 deformation bands (including those are in bundles); 205 single deformation bands; 40 deformation band bundles; 16 slip planes; 4 veins and 77 joints in this line.

Orientation and thickness of the fractures

The stereographic projection of all the fractures in the entire line CRT-2 scan is shown in Figure 2-21. The orientations of the fracture planes are about 90-270°, east-west bounding having a 40° wide homogeneous scatter. However, the majority of the planes scatter within a range of 20 degrees. The rose diagrams of Figure 2-22 show that the dip directions of the majority of the slip planes, joints and veins are about 200°; the dip directions of the majority of the deformation bands are 180° and 200°; the dip directions of the majority of the deformation band bundles are 175°. The variation of the dip directions of the joints is the largest about 80 degrees, much larger than the others fractures.

This line is cut into five segments and fracture plain orientations plotted in stereographic lower-hemisphere projections (Figure 2-23). Plots show larger angle scatter in the fracture plain orientations (about 80-90°) close to the main fault than farther (where variation is about 40°) showing similar tendency to line CRT-1. In the first segment, two groups of the fractures can be distinguished; in the other segments only one main orientation was dominant. The graph of dip and dip direction of all the fractures (Figure 2-24, Figure 2-25) shows, that in the zones near to the main branch fault, the variations of both dip and dip direction are larger; but farther from the fault, the variations are smaller. The variation of the dip directions is larger locally around at the main fault, the faults at 222 m and 285 m; and the variation of the dip is larger locally around the faults at the main fault, at 125 m, 195 m and 222 m.

The thickness of the deformation bands exceeds 2-3 mm at the main fault and further the thickness is less than 1 mm. Number of deformation bands in bundles ranges between 2 and 5 along the entire line; it increases to 9 around the fault at 222 m. The shape of the bands does not show any trend along the line. More convex deformation band can be found along the line than concave or plain; consequently, the majority of the fractures are stronger than the host rock.

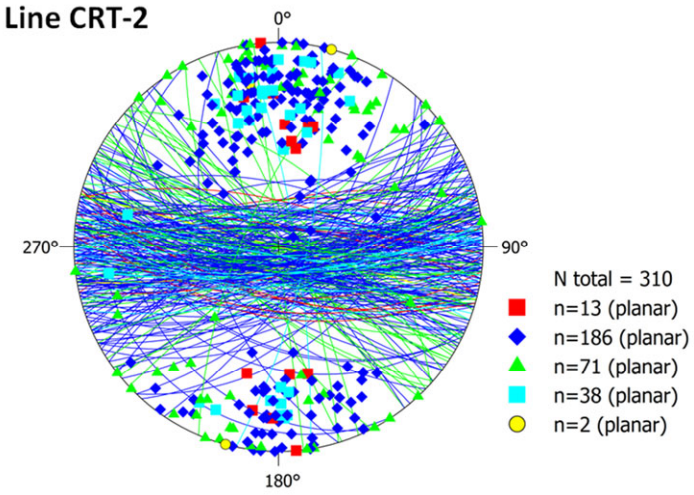

Figure 2-21 - Stereographic lower-hemisphere projection of the planes of all the fractures along line CRT-2 (red: slip plane; blue: deformation band; cyan: deformation band bundle; green: joint; yellow: vein).

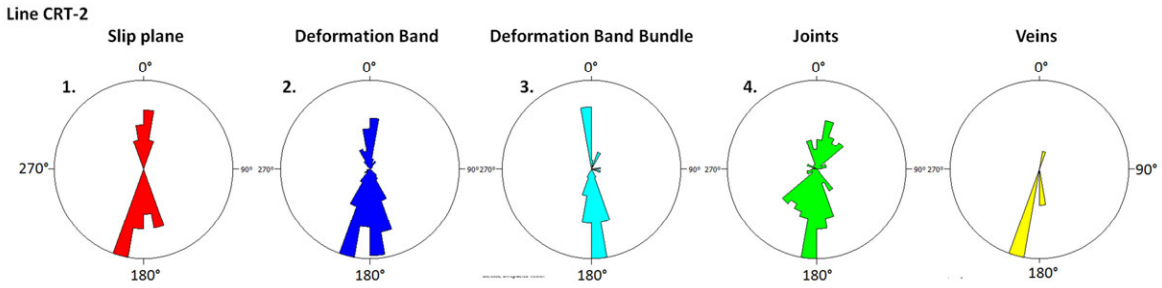

Figure 2-22 - Rose diagrams of the dip directions of the fractures of the Line CRT-2.

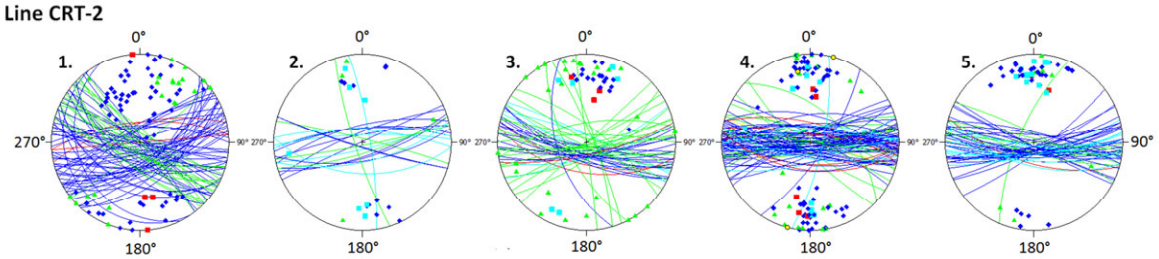

Figure 2-23 - Stereographic lower-hemisphere projection of the sections of Line CRT-2 (red: slip plane; blue: deformation band; cyan: deformation band bundle; green: joint; yellow: vein).

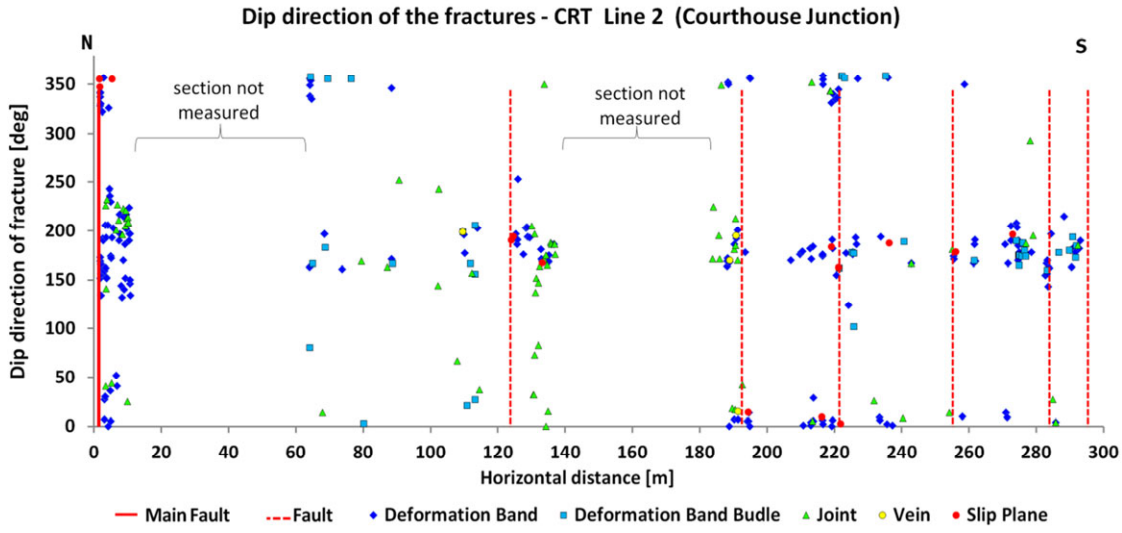

Figure 2-24 - Dip direction of the fractures on line CRT-2.

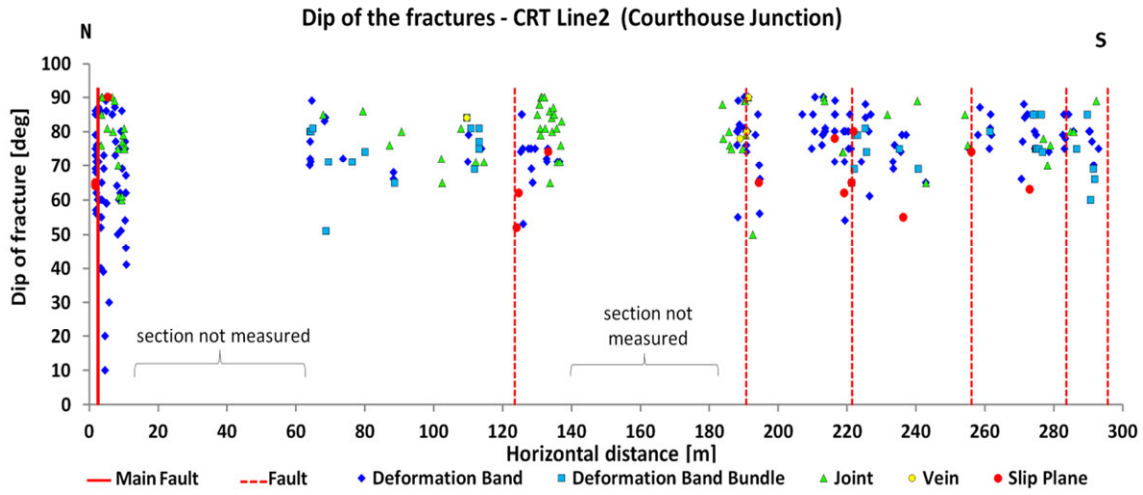

Figure 2-25 - Dip of the fractures along line CRT-2.

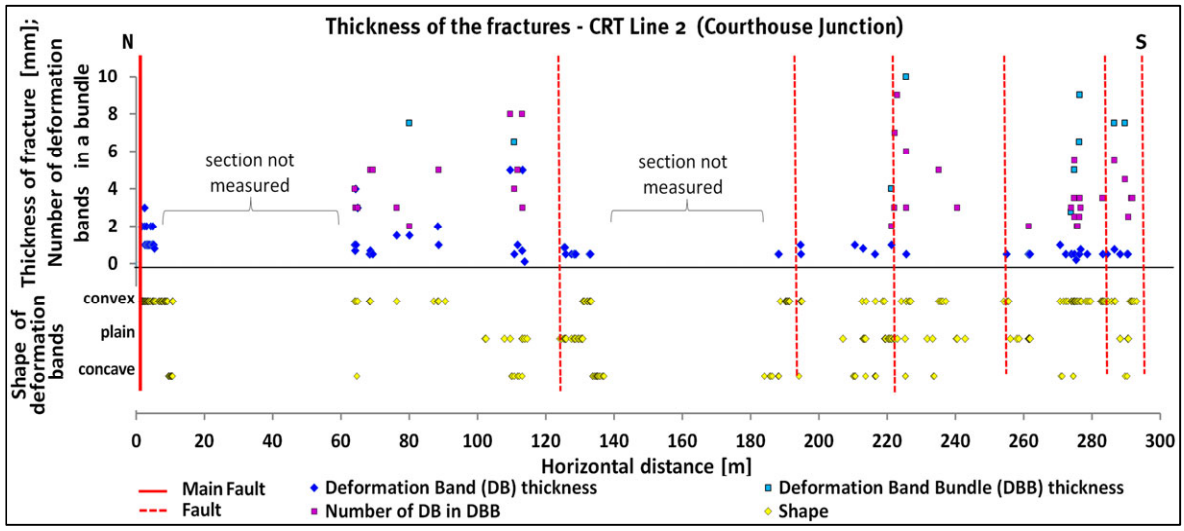

Figure 2-26 - The thickness of the deformation bands, the shape of the deformation bands relative to the host rock surface, and the number of the deformation bands in a deformation band bundle along line CRT-2.

2.5.2 Klondike Bluffs

Two scan-lines were measured approximately perpendicular to the master fault (Figure 2-7). Line KB-1 is located closer to the junction point at the east part of the fault on both the foot wall and on the hanging wall of the fault. The line KB-2 is located about 250 m far to the west from the line KB-1 and about 700 m from the fault tip on the hanging wall of the fault. The main fault has a maximum offset of about 10 m at the south part of the fault. The fault at this branch point was strongly eroded and covered by vegetation so these values are only rough estimations. The offset of the main fault at the first branch point (the eastern one) is approximately 4-5 m and the branch fault in the hanging wall has an offset of approximately 50 cm. At the second branch point on the west, the main fault has a throw of about 2-3 m; and the branch fault is to the south from the main fault has a throw of about 1 m. The fault core was not distinguishable.

This entire outcrop is characterised by minor cataclasis and fluid flow alteration. The majority of the deformation structures are disaggregation or dislocation bands. The pore space of the majority of the fractures is filled by mineral precipitation. Only few slip planes were observed without slickenside and any cataclasis. The other larger fault with larger throw was weathered so the erosion might destroy them. Fluid flow alterations were observed at many relatively large areas on this outcrop. Copper alteration was observed close to the fault core and mineral (calcite and iron) concretions were observed locally at part of the outcrop. The diameter of the concretions ranges from 0.5 mm to 5 mm in general. However, their diameter exceeds 15 cm close to the fault core (diameter of the spot < 3-4 m). In addition, two smaller spots (diameter of the spot < 1-2 metres) of mineral concretions, nodules were observed on this outcrop.

Line KB-1

Line KB-1 is located between two junction points. One of the fault junctions is about 60 m to the east from this line and the other fault junction is about 100 m to the east (Figure 2-7, Figure 2-27). The north part of the line is on the hanging wall, which has a length of about 180 m. The south part of the line is on the footwall of the fault having a length of about 150 m. The main fault is located at 180 m and a smaller fault branch is at about 123 m in the line. On the foot wall section of the line, the direction of the fractures was measured. The line was covered only at several ten centimetres long section on the hanging wall. Mineral concretions are mainly calcite on the hanging wall and mainly iron the foot wall of the fault.

The deformation band frequency plot can be seen on Figure 2-27. On the hanging wall of the fault the deformation band frequency is higher than on the foot wall. Around the main fault close to the fault core, the deformation band frequency exceeds the 25 fractures per metres and frequency remains high in about 10 metres radius around the main fault. Next to the centre of the fault, there are about 10 long gaps with no fractures on either part of the fault. From 215 m to 255 m in the line, the deformation band frequency increases only

locally. The deformation band frequency increases around the smaller fault at 123 m exceeding 10 fractures per metre.

On the hanging, the decreasing tendency of the deformation band frequency is more constant; however, this is not the case along the foot wall. In the foot wall, the typical deformation band frequency is 2-3 per metre; however, there is an increase in the frequency between 270 m and 290 m (5-7 deformation bands per metre). At the hanging wall, the cumulative deformation band frequency curve (Figure 2-27) increases steeply from main fault to 60 m; this section contains 90 % of the fractures of the hanging wall. The cumulative deformation band curve of foot wall increases very steeply close to the fault centre where about 30 % of the fractures are located. From 193 m to 250 m, the curve is flat, and from 250 m to the end of the scan-line, the cumulative frequency curve increases having a similar steepness to curve in the hanging.

Along this line, the majority of the deformation structures are also deformation bands (Figure 2-28). The majority of the deformation bands are in bundles on the foot wall. In the hanging wall, the number of the single deformation bands is higher than the number of the deformation bands in bundles. Far from the faults between 0 m and 35 m, only single deformation bands were observed. The number of the deformation band bundles ranges between 4 and 5 bundles per 5 metres around the main fault (130 m – 195 m). At other part of the line, the deformation band bundle frequency varies between 1 and 3 bundles per 5 metres. Only few joints can be found on the hanging wall slightly closer to the main fault.

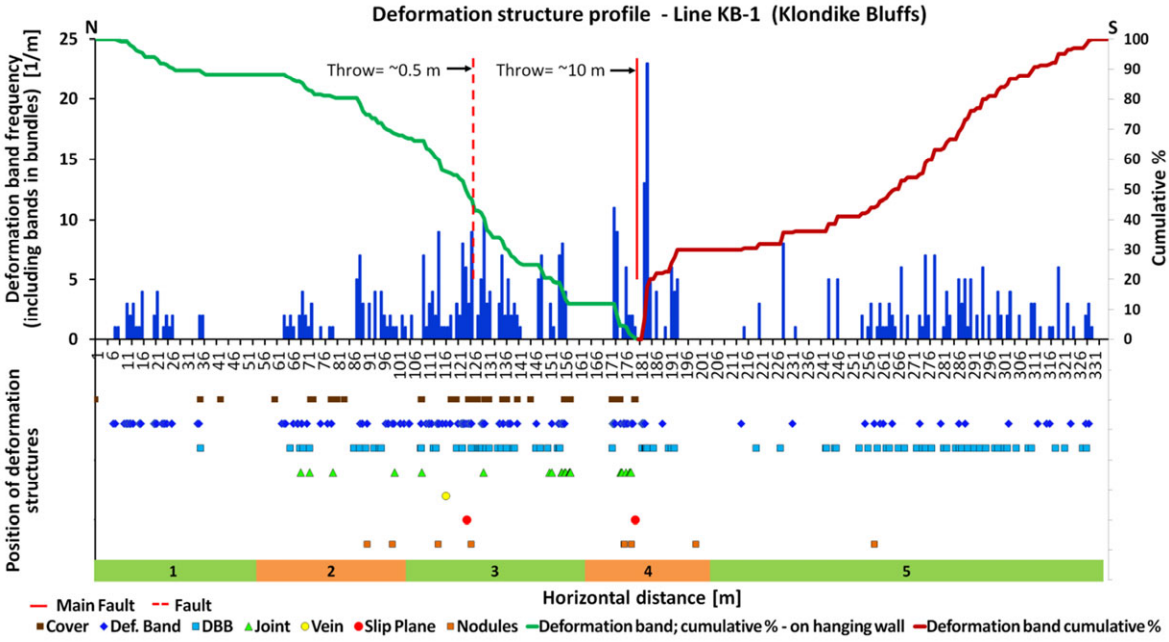

Figure 2-27 - Deformation band frequency and fracture location along line KB-1.

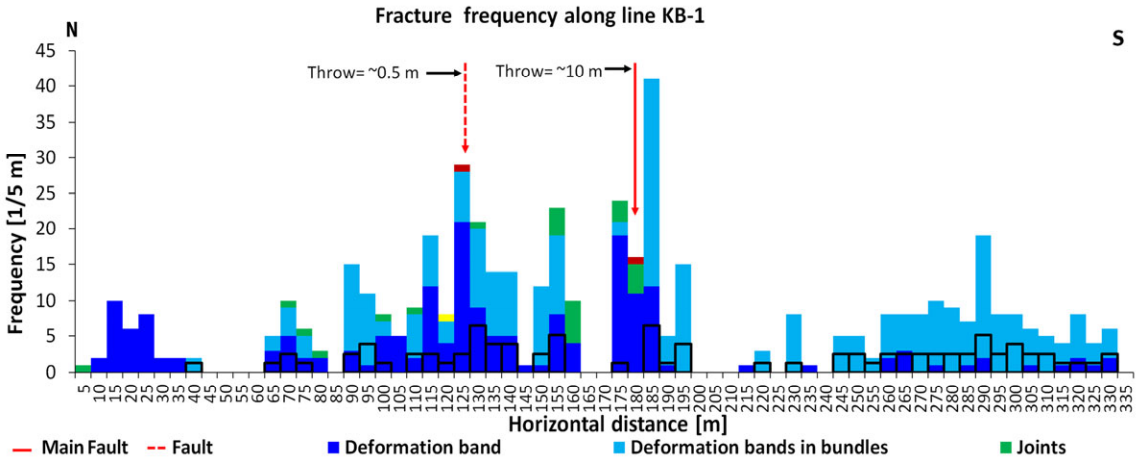

Figure 2-28 - Deformation structure frequency along line KB-1 (bin size=5 m). There are 189 deformation bands (including those are in bundles); 473 single deformation bands; 82 deformation band bundles; 2 slip planes; 1 veins and 25 joints in this line.

Orientation and thickness of the fractures

Figure 2-29 shows the stereographic lower-hemisphere projection of the planes of all the fractures. Two groups can be distinguished based on the dip directions. The group which contains the majority of the fractures is east-west bounding. The other group has an orientation of 120-300°. The angle between the two groups is about 25° which is about the same as the angle between the main fault and the branch fault. Orientation of the planes of each group has about 30 degrees variation. The fault branch is conjugate of the main faults.

The rose diagrams of the dip direction of the fractures (Figure 2-30) shows that single deformation bands are sub-parallel to the branch fault and the majority of the deformation band bundles sub-parallel to the main fault. The orientation of the majority of the joints is similar to the branch fault; however, the orientation of the joints has a wide variation.

To show the variation in dip directions of the fracture plane along the line, the data set is cut into five sections and these sections are plotted in stereographic projection (Figure 2-31). The stereographic projections show only those fractures where dips also were measured; therefore, the dip and the dip directions of the fracture planes are plotted separately along the line (Figure 2-32 and Figure 2-33). These plots show that the variation of the direction of the fractures is large close to the main fault in the first 5 metres of the hanging wall. On the hanging wall from about 60 m to 160 m, the dip direction of the fractures varies between about 160-250° and 50-350°. The average orientation in this section is sub-parallel to the smaller fault branch. The dip direction of the fractures varies between 160° and 210° at the far end of the hanging wall from 0 m to 30 m where the mean strike of the fractures is more similar to the strike of the main fault. The strike directions of the deformation structures are sub-parallel to both the main fault and the branch fault around the main fault from 160 m – 200 m (section 4). Most of the fractures are conjugate to the main fault. The majority of the dip of the fractures range between 60° and 90°; only few fracture have dips below this range. The lowest dip was 42 degrees.

The thickness of the deformation bands is higher (exceeding 10 mm) around the faults. However, the majority of the deformation band thicknesses are about 1 mm (Figure 2-34). The number of deformation bunds in bundles ranges between 2 and 8 along this line. More convex deformation band can be found along the line than concave or plain; consequently, the fractures are assumed to be stronger than the host rock in general.

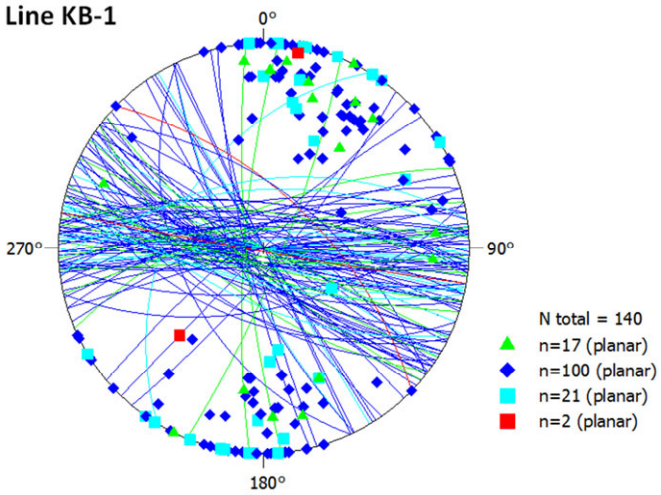

Figure 2-29 - Stereographic lower-hemisphere projection of the planes of all the fractures along line KB-1 (red: slip plane; blue: deformation band; cyan: deformation band bundle; green: joint; yellow: vein).

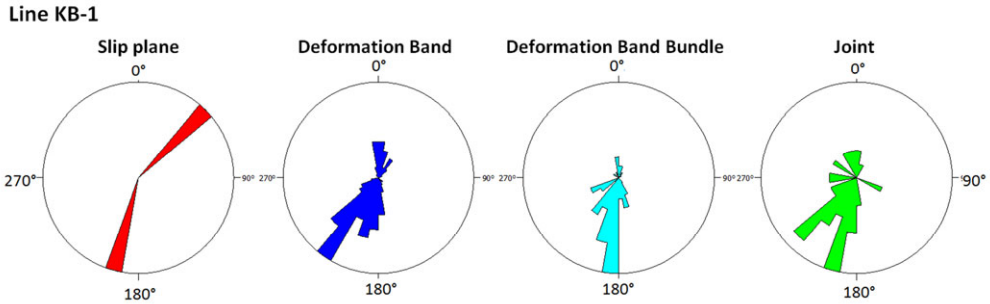

Figure 2-30 - Rose diagram of the fractures of the whole Line KB-1 (red: slip plane; blue: deformation band; cyan: deformation band bundle; green: joint).

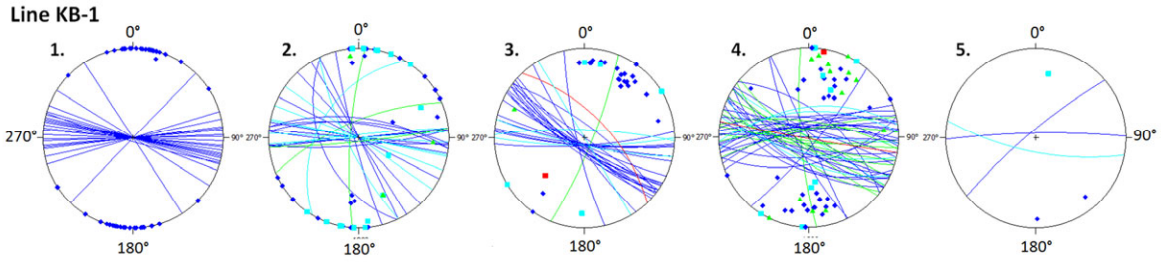

Figure 2-31 - Stereographic lower-hemisphere projection of the sections (see Figure 2-27) of line KB-1 (red: slip plane; blue: deformation band; cyan: deformation band bundle; green: joint).

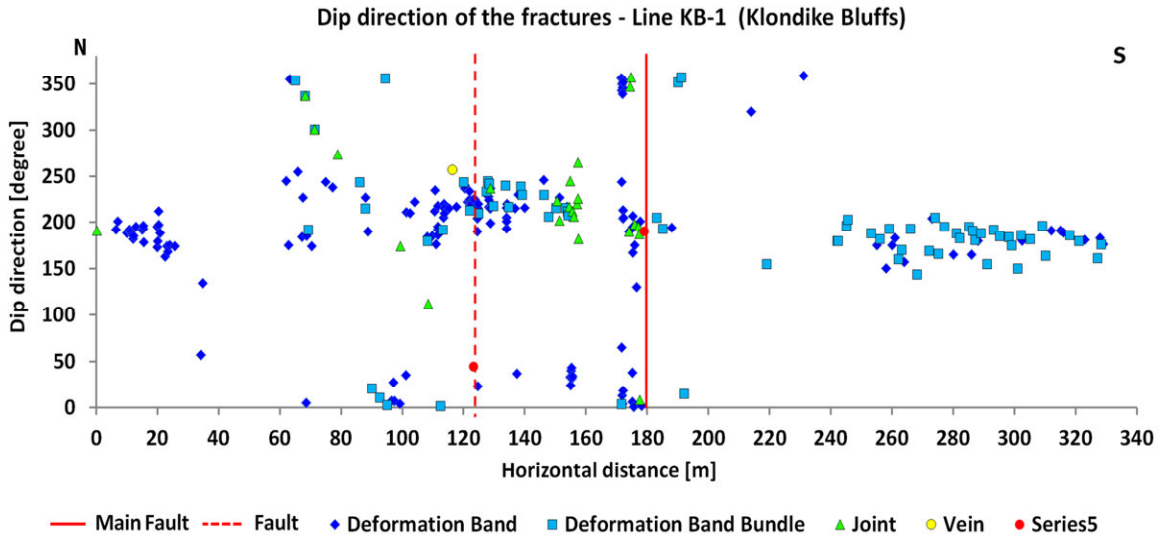

Figure 2-32 - Dip direction of the fractures along line KB-1.

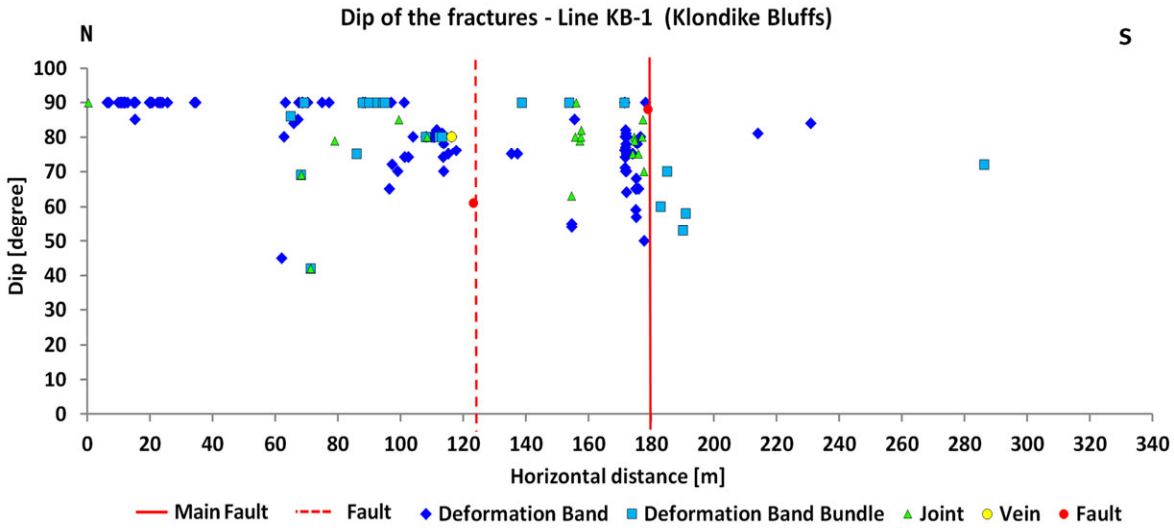

Figure 2-33 - Dip of the fractures along line KB-1

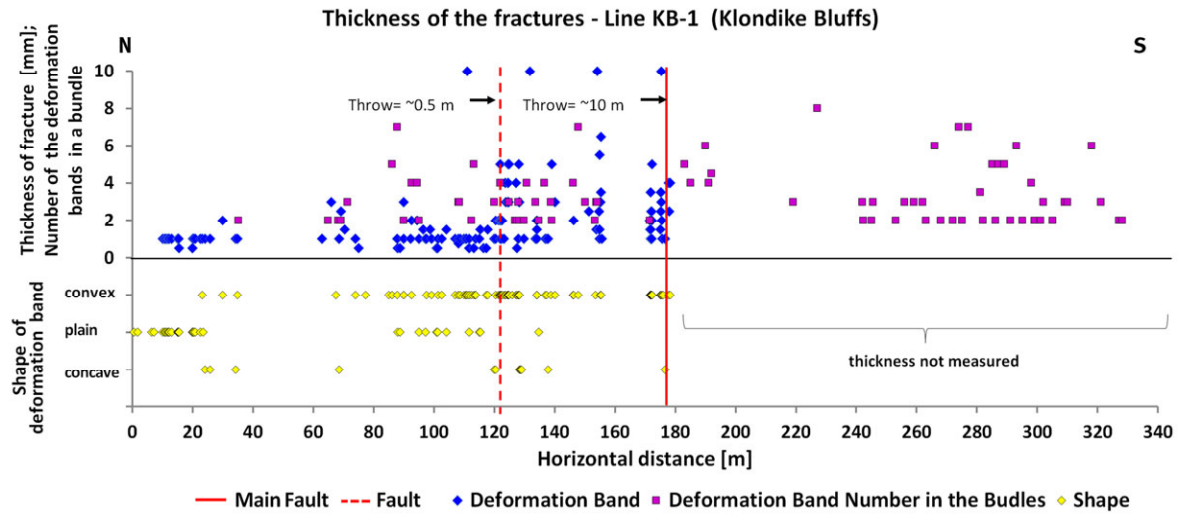

Figure 2-34 - The thickness of the fractures, the shape of the deformation fractures, related to the host rock, and the number of the deformation bands in a deformation band bundle on line KB-1.

Line KB-2

Line KB-2 is located approximately 190 m to the west from the line KB-1 (Figure 2-7), about 130 m to the west from the western fault junction and about 300 m from the east fault junction point. This line is located on the hanging wall of the fault. The south end of the line is at the main fault where the fault throw is about 2 m and the strike of this fault at the line is about 124°. The throw of the branch fault is located at about 194 m in the line and from main fault is about 0.1 m. The strike of this fault branch is about 136°. In the middle of the line, an about 100 m long section was not measured, because it was covered by soil and vegetation.

The deformation band frequency plot (Figure 2-35) shows that the deformation band frequency is the highest next to the main fault. However, only locally, deformation band frequency exceeds the 25 bands per metre at the north branch fault. The deformation band frequency tendency decreases but not monotonously going farther from the faults. Several local peaks can be seen along the line. The magnitude of the peaks of the deformation band frequency decreases gradually going away from the faults at distance of 280 m to 210 m and 90 m to 0 m along the line. At about 240 m horizontal distance in the line, the deformation band frequency has a minimum between the two faults from where the trend increases steeper towards the north fault and a less steep trend towards the main fault.

These tendencies can be seen in the cumulative deformation band curve too (Figure 2-35). The segment of the decreasing trend next to the main fault between 240 m – 305 m contains the 40 % of the deformation bands. The segment with the increasing trend next to the north fault between 240 m – 195 m contains 37 % of the bands, nearly the same number of deformation band as the other larger fault. 10 % of the deformation bands can be found at the first peak of the north section of the line between 90 m - 70 m distance. The other part of this section is 70 m long and the remaining 15 % of the bands are located here. The steps in the cumulative curve show that the deformation band distribution is not uniform but there are local fracture groups. At many paces, mineral concretions were observed between the two faults; majority of these are close to the main fault. At the north part of the line, less mineral concretions were observed and their distribution shows correlation with the deformation band frequency peaks.

Figure 2-36 shows that the majority of the deformation structures are deformation bands and deformation bundles. The distribution of the deformation bund bundles is very similar to the distribution of the deformation band bundle with lower amplitudes. The deformation bundle number exceeds 8 bundles per 5 metres in the south section of the line and 5 bundles per 5 metres farther from the faults in the north section of the line. Along the entire line, the majority of the deformation bands are in bundles.

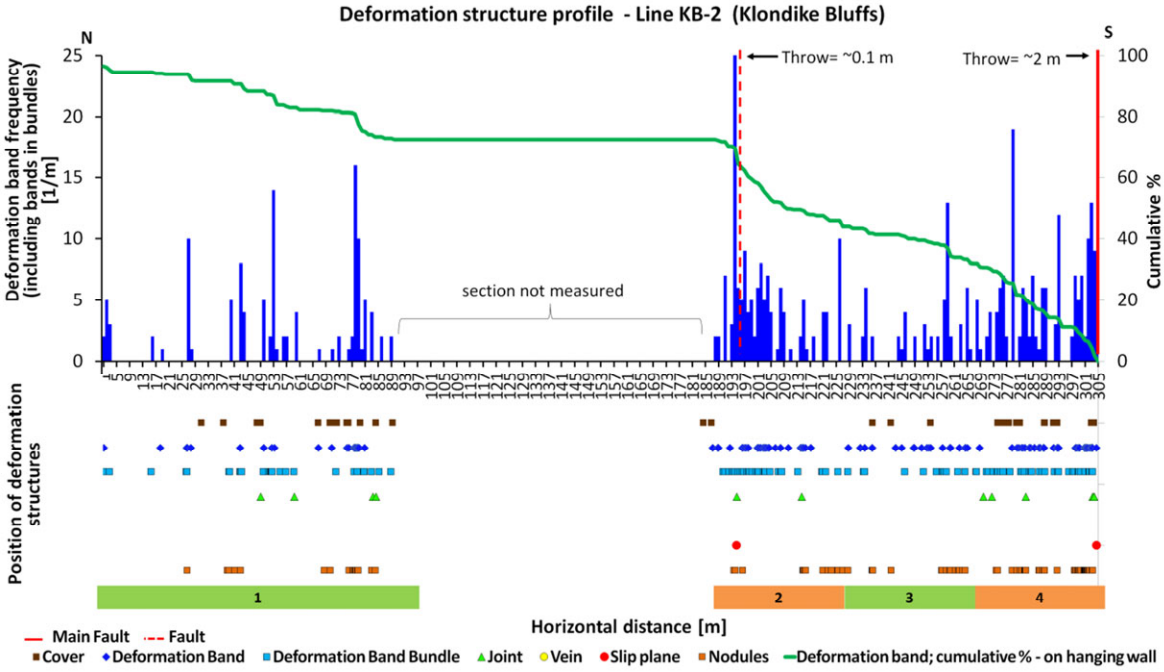

Figure 2-35 – The deformation band frequency, the cumulative deformation band frequency in percentage and the location of the fractures and features are shown along line CRT-2 in the plot. The numbered sections show the separated section for stereographic projection on Figure 2-22.

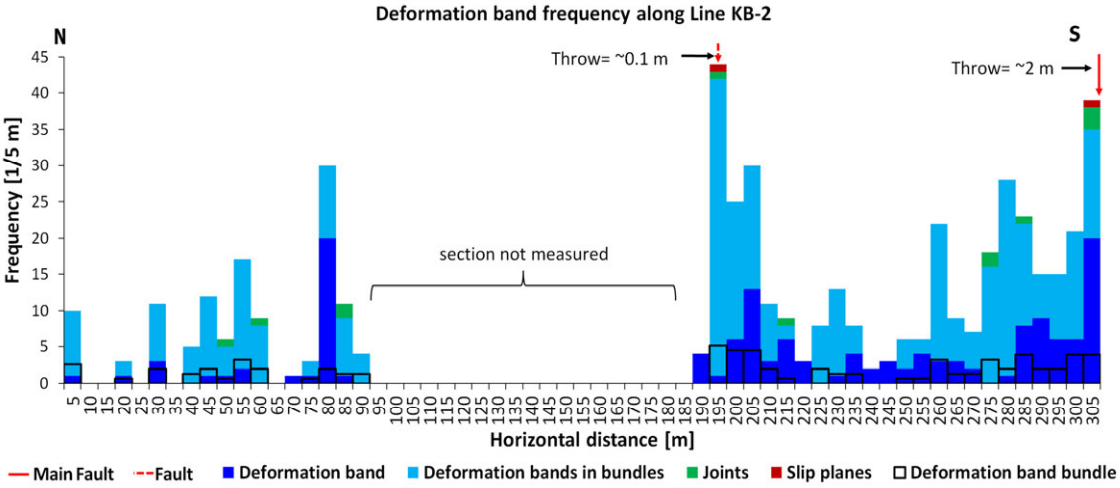

Figure 2-36 - Deformation structure frequency along line KB-2 (bin size=5 m). There are 142 deformation bands (including those are in bundles); 493 single deformation bands; 106 deformation band bundles; 3 slip planes; 0 veins and 12 joints in this line.

Orientation and thickness of the fractures

The stereographic projection of the all the fractures in the entire scan line (Figure 2-37) shows that the mean fracture orientation is about 290° - 110° and scatters in a range of about ± 40°. This range of the fracture orientation covers the direction of the two fault groups of the orientations cannot be distinguished in this plot. The rose diagrams of the dip direction of the fractures (Figure 2-38) show that the majority of the deformation bands and deformation band bundles are sub-parallel to the faults. In the rose diagrams of the deformation bands and deformation band bundles, two sets of deformation bands can be distinguished. The direction of one of the sets is similar to the major fault and the other set is sub-parallel to the branch fault. The few number of joints do not show unambiguous main direction; some of the joints have similar directions to the faults some of them are nearly perpendicular to the directions of faults.

The variations of dip and dip direction of the fracture planes along the line are shown by four stereographic projections (Figure 2-39) and the dip and the dip directions of the fracture planes are plotted separately along the line (Figure 2-40 and Figure 2-41) similarly to the previous lines. The variations of the dips and the dip directions of the fractures show similar trends. Close to the faults, the variation of the orientations of the fractures larger is larger than farther from them. The dip of the fractures ranges between 50 and 90 degrees. The majority of the fractures are conjugates to the faults.

The thickness of the deformation band bundles is extremely high; their thickness exceeds the 40 mm between the faults and farther from the faults the maximum thickness of the bundles is 6 mm (Figure 2-42). The thickness of the deformation bands varies between 0.5- 4 mm along the line. Majority of the deformation bands have a convex shape along the line especially between the two faults indicating that the deformation bands are stronger than the host rock.

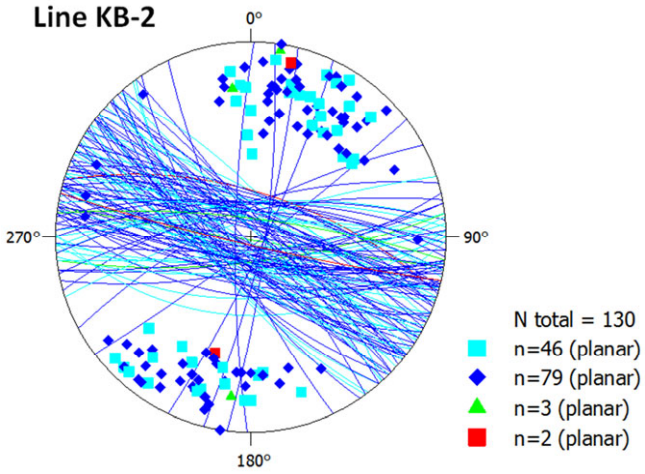

Figure 2-37 - Stereographic lower-hemisphere projection of the planes of all the fractures along line KB-2 (red: slip plane; blue: deformation band; cyan: deformation band bundle; green: joint).

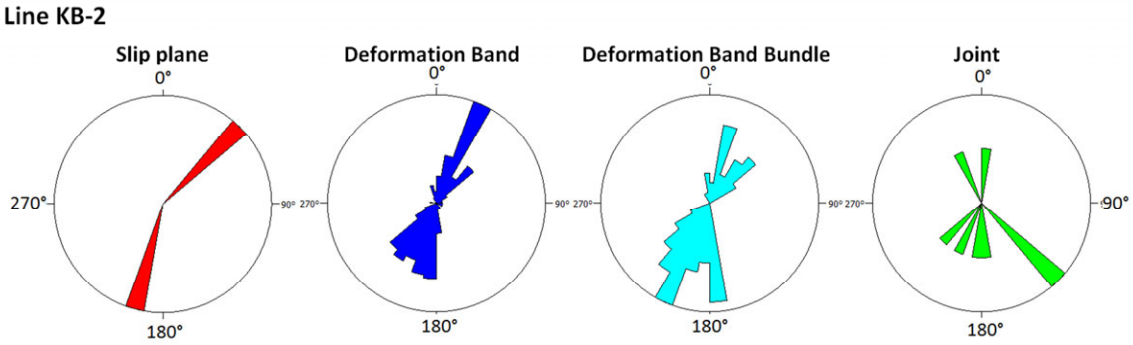

Figure 2-38 - Rose diagram of the fractures of the whole Line KB-2.

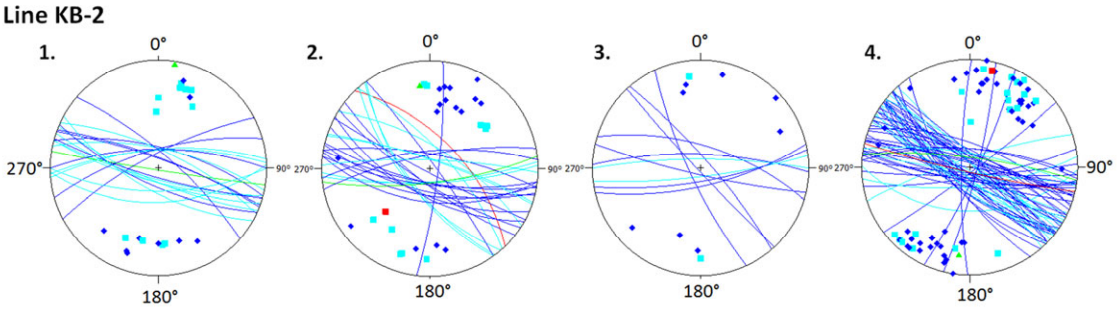

Figure 2-39 - Stereographic lower-hemisphere projection of the sections of line KB-2 (red: slip plane; blue: deformation band; cyan: deformation band bundle; green: joint).

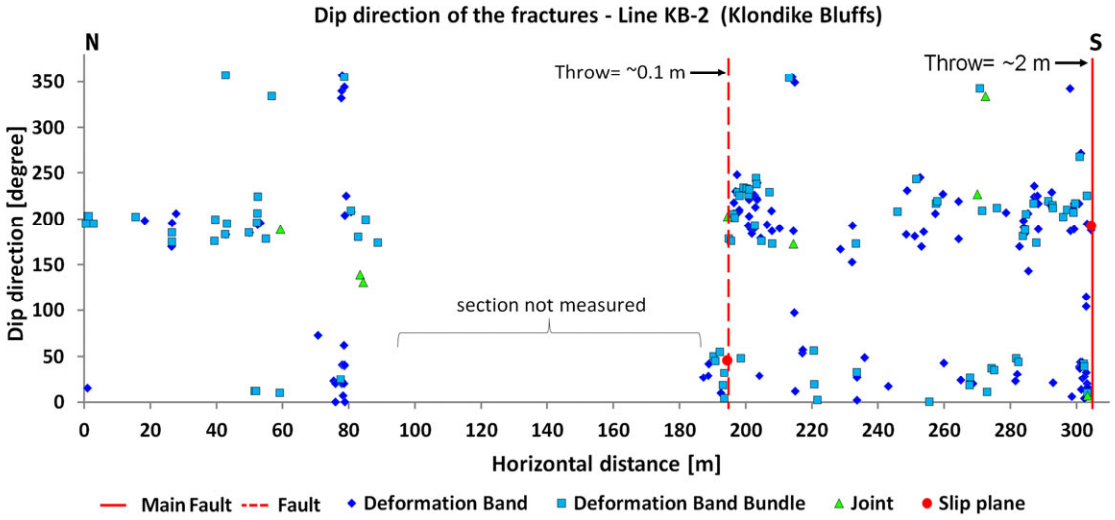

Figure 2-40 - Dip direction of the fractures on line KB-2.

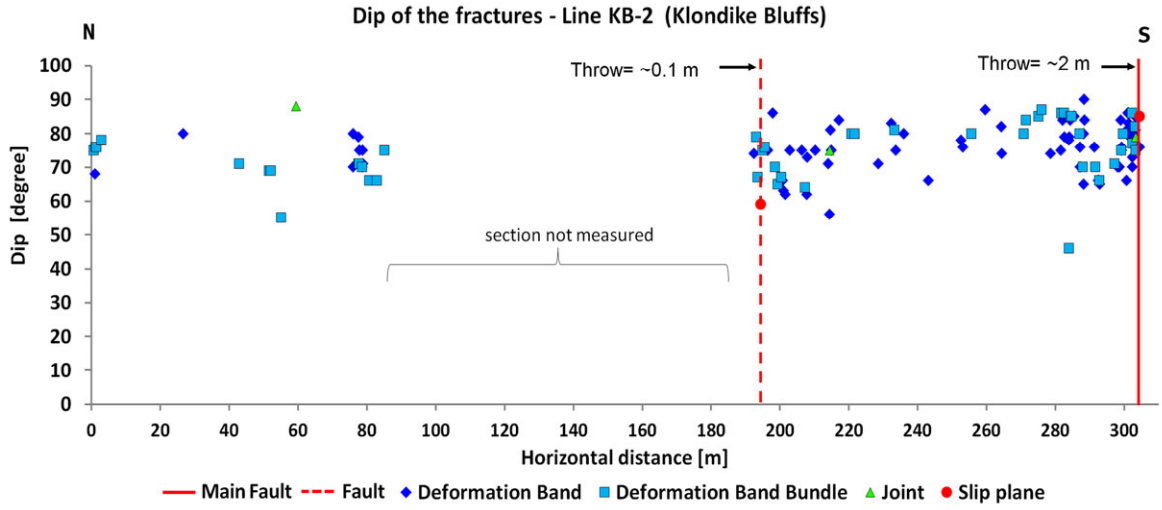

Figure 2-41 - Dip of the fractures on line KB-2.

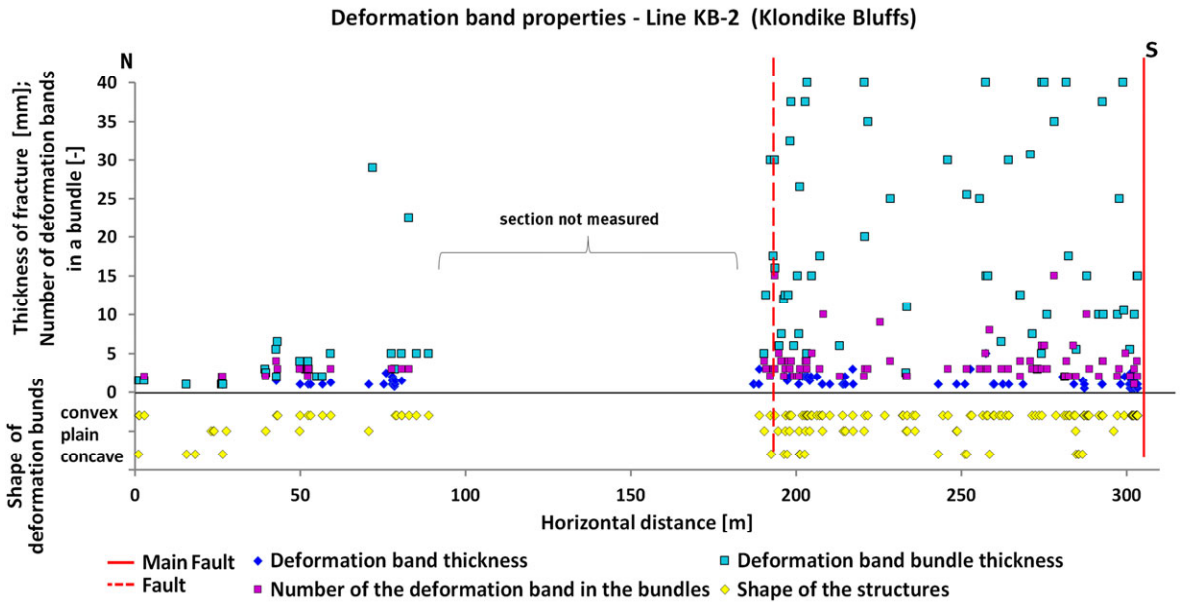

Figure 2-42 - The thickness of the fractures, the shape of the deformation fractures, related to the host rock, and the number of the deformation bands in a deformation band bundle on line KB-2.

2.6 Discussion

In this study, the architectures of two normal faults were analysed in order to better understand the properties of the fracture networks in fault zones. The types of the observed fractures were: deformation band, deformation band bundles, joints, veins slip planes in the studied outcrops along the scan-lines. The upper part of Table 2-1 shows the elementary data of the measured scan lines and the number of the different type of fractures. Only very few veins, 15 at Courthouse Junction and 4 at Klondike Bluffs lines were found. Combined about 130 joints were observed along the lines, majority of them (77) were along line CRT-2 at the Courthouse Junction. No slip planes with slickensides were observed at the Klondike Bluffs faults; however, 26 slip planes with slickensides at Courthouse Junction fault. Majority of the fractures were deformation bands along the scan lines. The normalised deformation band number (number of the fractures divided by the length of the measured section) is significantly lower (less than half) at scan-line CRT-1 which is closer to the fault junction than at scan-line CRT-2 at the Courthouse Junction fault. The normalised deformation band number is higher farther from the junction on the Klondike Bluffs but the difference between the values is not significant. The same relations can be seen at the normalised total deformation band number values. The normalised deformation band bundle numbers show a similar relation to the normalised deformation band at the Courthouse Junction. However, at the Klondike Bluffs, the numbers of bands are significantly higher with the increase in distance from the junction. The typical deformation band number based on the total numbers of the deformation band is on one hand, close to the junction point and on the other, farther from them in both areas.

Table 2-1 – The tables shows the basic statistics of the deformation bands (DB) and deformation band bundles (DBB) along each scan-line.

*** Thickness was calculated for the not measured section using the average thickness of the line KB-2.**

Line ID	Total length [m]	Measured length [m]	Total number of deformation bands (DB)	Number of deformation bands	Number of deformation band bundles (DBB)	Number of slip planes	Number of veins	Number of joints
CRT-1	161	161	145	87	16	11	0	11
CRT-2	295	180	383	205	40	16	4	77
KB-1	334	334	473	189	82	0	1	24
KB-2	305	215	477	142	106	0	2	12

Line ID	Average (median) of the number of DB in the DBB	Normalised DB per meter (DB/ measured length)	Normalised DBB per meter (DBB/ measured length)	Normalised total DB per meter (total DB/ measured length)	Average (median) of the thickness of DB [mm]	Average (median) of the thickness of DBB [mm]	Summ of the deformation band thickness [mm]
CRT-1	3.6 (3)	0.54	0.10	0.90	0.8 (1)	13.2 (10)	266 (0.17 %)
CRT-2	4.5 (4)	1.14	0.22	2.13	1 (0.7)	14.8 (11.4)	442 (0.25 %)
KB-1	3.5 (3)	0.57	0.25	1.42	2.2 (1.5)	not measured	1012 (0.30 %) *
KB-2	3.2 (2)	0.66	0.49	2.22	1.3 (1.0)	18.0 (10.8)	1843 (0.86 %)

Table 2-1 also shows some statistics of the deformation bands and bundles which were the most relevant to the study. In addition to the average, the median of the deformation bands and bundles were calculated too. The median provide a more robust statistics which is not biased by the outlier values in general. The average and median of the number of deformation bands in the bundles do not show significant differences in comparison with of the scan-lines of either areas. At the two outcrops, typically 3-4 deformation bands can be found in the deformation band bundles.

The typical thickness of the deformation bands is 1 mm at the Courthouse Junction and farther from the junction at the Klondike Bluffs. However, closer to the junction at the Klondike Bluffs the average thickness is about 2 mm. The average of the deformation band bundle thickness is 13-15 mm at the Courthouse Junction and 18 mm at the Klondike Bluffs. However, the median of the deformation band bundle thickness is smaller about 10-11 at each line showing that the average is biased by the higher values. Rotevatn et al. (2008) analysed the cataclastic deformation bands in Western Sinai, Suez rift, Egypt and found that the average thickness of the bands is 0.8 mm. Solum et al. (2010) studied the deformation bands around a reverse and a normal fault in Utah. They found that the deformation band thicknesses at Buckskin Gulch (in a reverse-faulting environment) have a skewed normal distribution, with a maximum at 1–2 mm or approximately 3–6 times the mean grain size. Whereas, deformation band thicknesses at the Big Hole fault show an exponential distribution with a maximum at less than 1 mm (smallest bin size) (Solum et al. 2010).

The Courthouse Junction fault is a seismic scale fault branch of the major Moab fault, which is much larger and more complex than the Klondike Bluffs fault system. At both areas, the deformation band distribution has a decreasing tendency from the main faults along the scan-lines (lines CRT-1 and KB-1). At Courthouse Junction, the deformation band frequency at the fault is lower than that of the Klondike Bluffs and the degree of the decrease is slower i.e. the envelope of the fracture frequency curve is less steep. The deformation band frequency decrease is irregular, not monotonous with distance. There are local smaller or larger peaks, irregularities in the deformation band frequency. Similar deformation band distribution style is documented for example: in Wadi el Khaboba (Sinai) in sandstone by Rotevatn et al. (2008), also by Solum et al. (2010) at Buckskin Gulch and the Big Hole faults in Navajo Sandstone, Utah. Similar irregular, decreasing deformation band distribution was reported by Berg and Skar (2005) at the Bartlett fault segment. The Bartlett fault segment is part of the same fault branch of the Moab fault (in the same sandstone formations) as was studied in this work. It is about 3 km from the studied Courthouse Junction outcrop to the west. Furthermore, similar fracture characteristics were observed in damage zones of normal fault in other rock types, such as gneiss (Gudmundsson et al. 2010) or tuff (Riley et al. 2010).

The deformation bands occur in local groups; there are irregularities (i.e. peaks and gaps) in the deformation band frequency which break the deformation band distribution trend. Berg and Skar (2005) found that deformation bands appear either isolated from each other or they occur associated with slip surfaces and joints and deformation band distribution also related to lithology changes. The results of the present study partly support

this statement. Based on visual observation and microstructure analysis of some rock samples, there was not any significant change observed in lithology in either of the studied faults. Furthermore, the results show that irregularities and increase in deformation band frequency, occur just at some of the faults (throw>10 cm). However, the deformation band frequency increases also where there was no fault, joint or slip surface. The degree of the increases of the deformation band frequency in the studied scan-lines does not show a significant relationship with the throw. The deformation band distribution around a fault is not affected by the throw of the fault. This observation is in agreement with the observation of Schueller et al. (2013).

Solum et al. (2010) analysed the deformation band networks in Utah sandstones, and found them to be really extensive and lacking of association with discrete faults at the area of Buckskin Gulch. Whereas, the presence of the deformation band network was limited to the damage zone at Big Hole Fault. Both areas are characterized by similar lithology, porosity, permeability and deformed at similar burial depth (1.5-3 km). However, the Buckskin Gulch formed in a contractional tectonic setting, whereas the Big Hole Fault formed in an extensional tectonic setting. Solum et al. (2010) explained the differences of the deformation bands distribution by the different tectonic regimes. Fossen and Rotevatn (2012) stated that the tectonic regime has some influence on the distribution of deformation bands; however, the lithological and petrophysical parameters, and the tectonic style or boundary conditions can have larger effect, than the tectonic regime. Solum et al. (2010) reported that the average deformation band density is 24.6 deformation bands per metre (DB/m) in contractional environment and significantly lower, 5.1 DB/m in extensional environment. In this study, at Klondike Bluffs the band density is 1.4 DB/m and 2.2 DB/m and at the Courthouse Junction 0.9 DB/m and 2.1 DB/m. In addition, Solum et al. (2010) observed that the average deformation band thickness is 2.2 mm in contractional environment and 1.9 mm in extensional environment. These thicknesses are similar to average deformation band thicknesses (1.3 – 2.2 mm) at Klondike Bluffs. However, the average deformation band thickness at the Courthouse Junction is about half of that about 0.8 – 1.0 mm. It was also shown by several studies (e.g. Aydin 1978, Hesthammer and Fossen 2001, Mair et al. 2002, Fossen et al. 2007), that the number of deformation bands is affected by the vertical stress i.e. burial depth. The average or normalized deformation band number is in the same order of magnitude at the Klondike Bluffs and the Courthouse Junction area. However, the two areas are characterized by different types of deformation bands: cataclastic and dislocation band which indicates that the differences in stress conditions between the two areas.

Several works aimed to define models for fracture distribution in fault zones. Some of the models use analytical, other models use numerical approach. Anders and Wiltschko (1994) analysed the deformation bands and micro-fractures in the Navajo and the Entrada sandstones in Arches National Park. They found that fracture distribution follows an exponential decrease as a function of the distance from the fault core. Similar exponential decrease was reported by Mitchell and Faulkner (2009) who studied fractures in the granodiorite and diorite of the Atacama fault system. Power law function based approach was used by Savage and Brodsky (2011) to model the fracture density decay. Others

observed that there is a logarithmic decrease of fracture density with increasing distance from the fault core (Scholz et al. 1993, Anders and Wiltschko 1994, Vermilye and Scholz 1998, Chester et al. 2004, Schueller et al. 2013). According to Kolyukhin et al. (2009) and Schueller et al. (2013) there is a logarithmic decrease in the frequency of deformation bands away from the fault core which can be defined as: Y =A + Ln(X), where Y is the frequency of deformation bands per metre and X is the distance from the fault core (Figure 2-43). This model can be used to calculate the theoretical width of the damage zone and also the average deformation band density at a certain distance from the fault core.

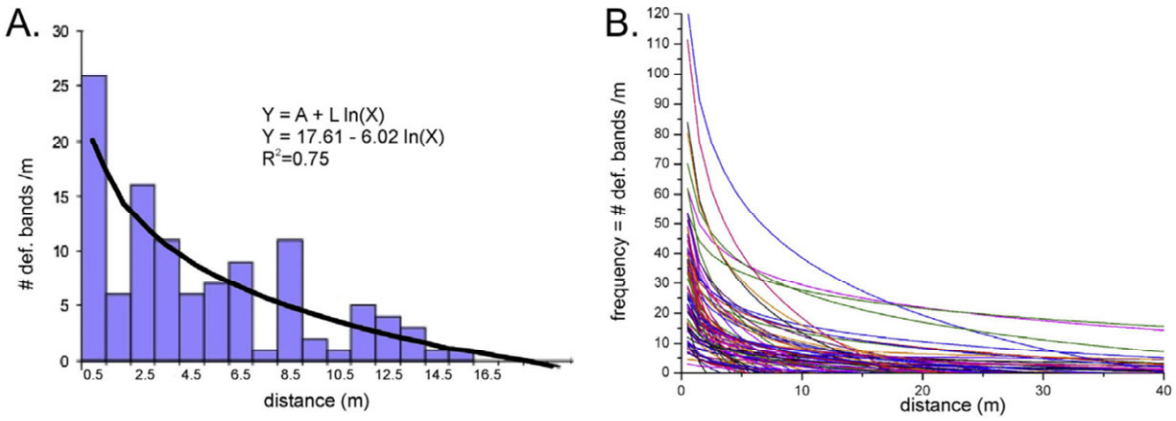

Figure 2-43 – Deformation band frequency plot, on the left, shows logarithmical like decreasing tendency from the fault core (at 0 metre); on the right, a combined logarithmic fit deformation band density plot based on normal fault measurement database of Schueller et al. (2013) is shown. (modified after Schueller et al. 2013)

The fracture distribution analysis along the four studied scan-lines at Klondike Bluffs and Courthouse Junction showed that the best fitting function to the distribution is the logarithmic in general. At analysing the correlation between the logarithmic curve and the deformation band frequency was significantly lower for the entire line than for sections of the lines next to faults. Figure 2-44 shows an example for this. In two segments (length are 50 m and 65 m) of the line KB-2 between the two faults, the correlation is much higher than at the entire line. Along the local irregularities has significant effect on the deformation band trend. In a smaller vicinity of fault the logarithmic trend is more valid. The lengths of the sections vary widely from 15 m up to 75 m; however, the logarithmic trend has a relatively good approximation along the entire line for example where no significant frequency irregularity (Figure 2-45) exist.

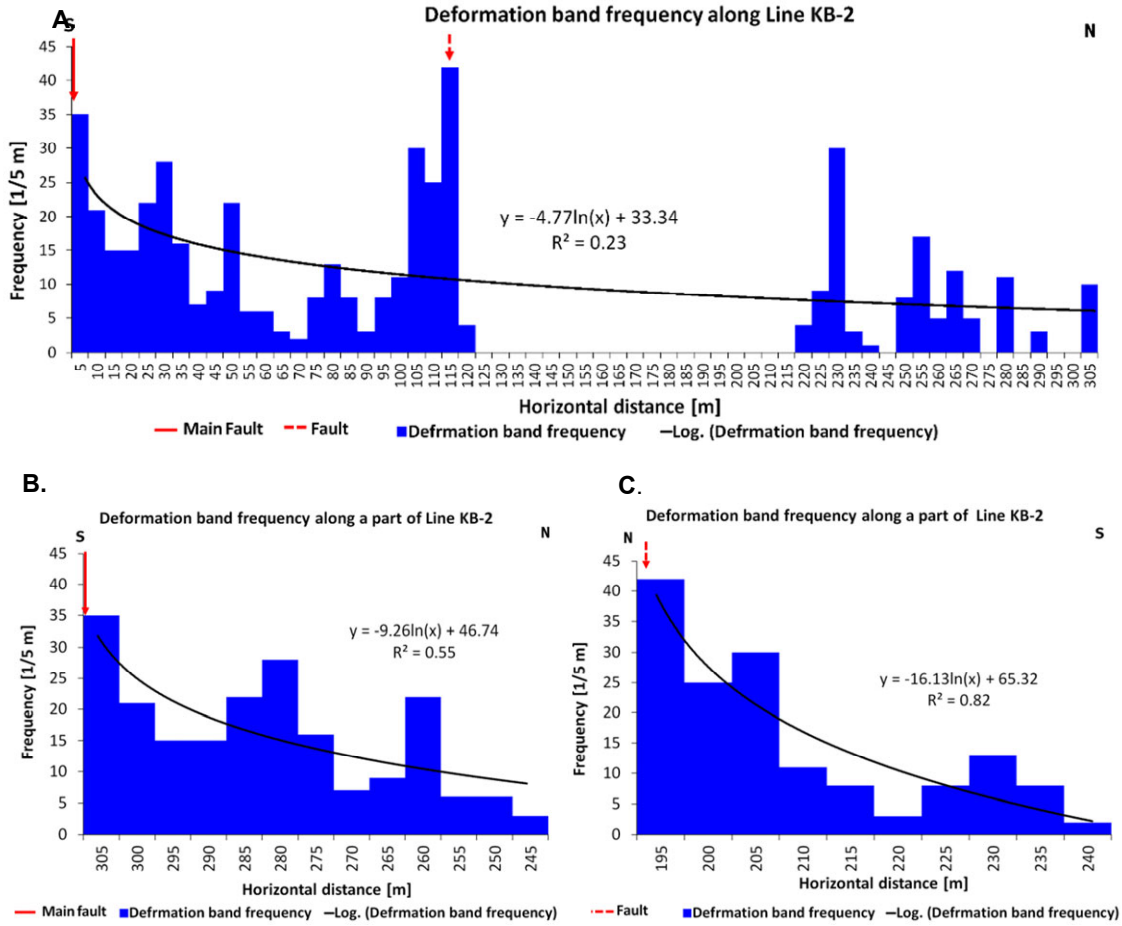

Figure 2-44 – Logarithmic deformation band frequency trends of the entire KB-2 line (plot A.) and sections of this line (plot B. and C.) are shown. To the calculation of the logarithmic curve, the distance scale started at the faults at zero in all the cases.

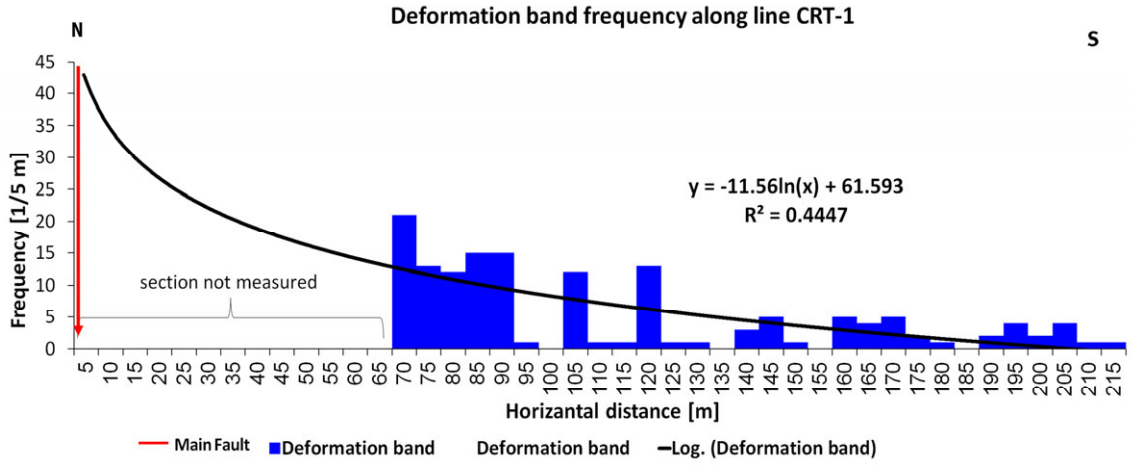

Figure 2-45 - Deformation band frequency and fitted logarithmic trend along line CRT-1.

Numerical approach also was applied to create more reliable, more precise model to describe fracture distribution around faults. Schueller et al. (2013) analysed the evolution of deformation band distribution with increasing fault throw using a numerical model. The results showed that with increasing throw both the deformation band density and the width of the damage zone increase. They proposed that the maximum deformation band density (25-60 even >120 DB/m) may be related to the critical stress at which the deformation band cluster becomes saturated with deformation band. This critical stress may be influenced by the lithology.

The changes of the deformation band frequency perpendicular to the fault might allow distinguishing internal subsets of the fault damage zone. Berg and Skar (2005) divided the fault damage zones into sub-zones based on the deformation band frequency (Figure 2-46). The inner zone is adjacent to the fault core where the deformation band frequency next to fault core is the highest i.e. the cumulative curve increases steeply from the fault core. The next zone going farther from the fault core is the outer zone where the deformation band frequency gets significantly lower i.e. the cumulative curve increases moderately. Finally, the furthest zone from the fault core is the transitional zone where the deformation band frequency is very low and become zero; the cumulative curve is nearly flat. Beyond the transitional zone the not fractured protolith or host rock can be found. Berg and Skar (2005) found that the inner zone is about 4-5 m; the end of the outer is between about 20 m to 45 m and length ranges between 15-30 m; while the length of the transitional zone is about 10 to 30 m in the footwall. In some cases, the inner zone might not be identified around the fault; an example for this is shown in Figure 2-47. Along the lines CRT-2 (Figure 2-19), the sub-zones of the damage zone cannot be identified, the characteristics of the deformation band distribution is fairly different from the most common distribution style because of the effect of the several smaller faults. The line CRT-1 shows more similar deformation band distribution characteristics to the theoretical characteristics; however, the section adjacent to fault core was not measured. The deformation band frequency was about 10 per metre in the first 5 m from the fault core. Assuming the same distribution in the start of the line CRT-1, the first 5 m is the inner zone, the outer zone is between about 5 m and 170 m and transitional zone terminates at about 210 m (Figure 2-47/A). The deformation band distribution along line KB2 is more similar to the characteristics of the second example showed in Figure 2-47/B where the inner zone is missing – no significant increase in deformation band frequency may be observed close to the fault core. This line starts with an about 175 m long outer zone where around a minor fault, the deformation band frequency increases and breaks the trend locally. At the end of the line, the transitional zone is 25 m long in this line.

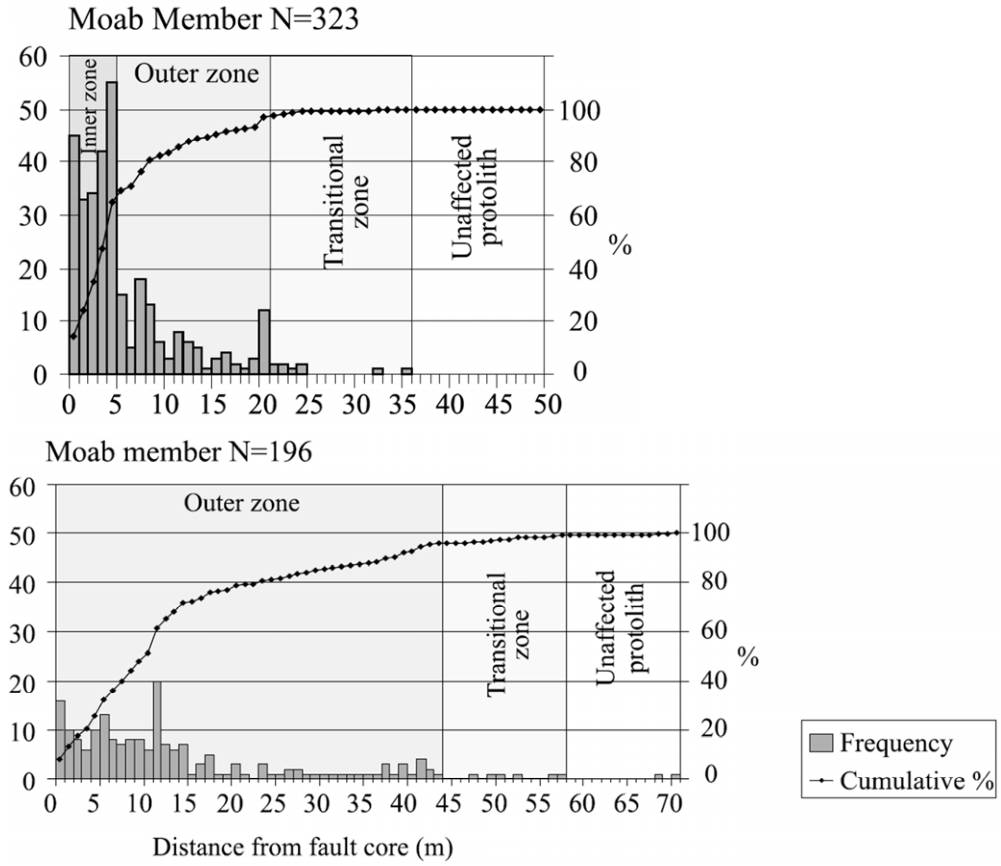

Figure 2-46 – Theoretical sub-zones (inner, outer and transitional) of the fault damage zone based on deformation band frequency and cumulative fractures density curve curvature (on the left). An example for a typical fracture distribution around a fault is shown on right hand side plot. (modified after Berg and Skar 2005)

In this study, only scan-line KB-1 at the Klondike Bluffs was measured at both the footwall and the hanging wall of the faults. Along this line on the hanging wall, the fracture density is slightly higher (by about 12%) than the footwall, having a typically logarithmically decreasing trend moving away from the fault centre. In addition, there is more fluid flow alteration and the fracture network is more complex in the hanging wall in comparison with the footwall. In the footwall, the fracture distribution is very high close to the fault centre within 12 m and does not follow a logarithmical like trend. Other authors (e.g. Berg and Skar 2005, Brogi 2008, Schueller, et al. 2013) made similar observation the fracture network is more complex on the hanging wall than the footwall at normal faults.

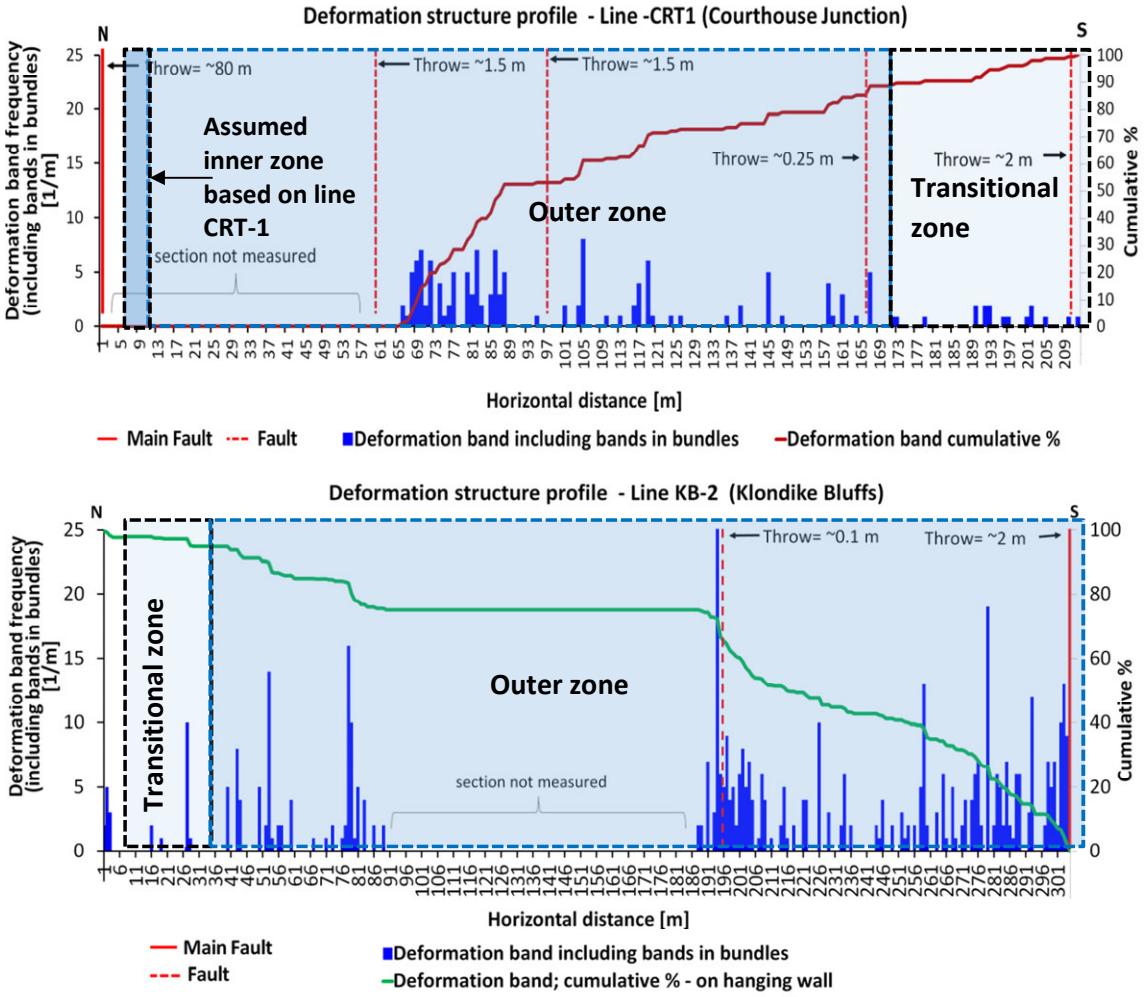

Figure 2-47 – The deformation frequency plots shows the zones of the damage zone of the line CRT-1 (Courthouse Junction, footwall) where inner, outer and transitional zones can be identified and line KB-2 (Klondike Bluffs, hanging wall) where only outer and transitional can be identified zones.

Berg and Skar (2005) observed that the hanging wall is more than three times wider than the footwall and more complex at the Bartlett fault segment of Moab fault where the fault throw is 170-300 m having a NW-SE strike. Furthermore, Berg and Skar (2005) found that in the footwall in Moab member of Curtis formation, the deformation bands orientation is NWE-ESE and their dip is 85° with a slight predominance of antithetic structures (55%) and the deformation bands are either associated with slip surfaces and joints or isolated from each other. Whereas, there are more fractures in the hanging wall in Cedar Mountain formation where the deformation band distribution is related to lithology changes, the deformation band are sub-parallel to the strike of the master fault. They have mostly (72%) antithetic dip and their dip is lower than at the footwall. In the present study, the results show that the dips of the majority of the fractures are around 80-85 degrees, are sub-parallel to the master fault; and there are more conjugate fractures at the footwall of the same fault branch at the Moab fault at Courthouse Junction, as well as in the Moab member

of Curtis formation. Furthermore, the results did not show unambiguous relationship between the occurrence of the deformation bands and other fractures.

Brogi (2008) documented that the damage zones is characteristically asymmetric around the Rapolano normal fault (Northern Apennines, Italy) in siliceous sedimentary rock. Better developed fractures can be found especially in the hanging wall where fault throw is larger than 10 m and the fracture density is increasing rapidly while approaching the fault core. In the footwall, the fracture density is more complex and there is no discernible density decrease away from the fault centre. Furthermore, mineralisation and hydrothermal alteration were found around this fault, which could be an indication of high permeability. Similarly to the results of Brogi (2008), asymmetric fracture distribution was found at the Klondike Bluffs; however, the fracture distribution was higher and more complex in the hanging wall than the footwall.

The width of the damage zone was also investigated by several studies and they found that the hanging wall is wider than the footwall in case of normal faults (Berg and Skar 2005, Brogi 2008, Schueller, et al. 2013). Berg and Skar (2005) measured about 40-60 m damage zone width on the footwall and on the hanging wall about 210 m in the Bartlett fault branch. Others' results also on the Bartlett fault branch showed that damage zone width ranges along the fault. Koestler et al. (1995) measured damage zone width of 12 m (Berg and Skar, 2005), Davatzes and Aydin (2003) measured 15-22 m, Koestler et al. (1994) measured 20-50 m and Harris et al. (2003) observed damage zone width up to 60 m. In the present work, at the Klondike Bluffs along the line KB-1, the width of the damage zone is also shorter on the footwall about 150 m than on the hanging about 180 m. However, the difference between the damage zone width of the hanging wall and the footwall is not significant. Moreover, the length of the damage zone along the line KB-2, which is farther from the junction point, exceeds 300 m on the hanging wall which is significantly longer than the damage zone width in the hanging wall at the other line.

According to Knott et al. (1996), there is a linear relationship between the fault throw and the width of the damage zone. However, based on the analysis of 106 scan-lines around normal faults in Utah and other places, Schueller, et al. (2013) found that there is a power-law relationship, with an exponent of approximately 0.5, between throw of the faults and the width of corresponding damage zones. The results of the present study do not show clear relationship between the fault throw and the width of the damage zone. At the Klondike Bluffs fault, the overall damage zone width (including the related minor fault branches) is about 180 m closer to the junction point where the fault throw is about 10 m; further from the junction point where the fault throw is significantly lower, the overall damage zone width is larger than 300 m. At the Courthouse Junction fault where the fault throw is about 80 m, the overall damage zone width was not clearly identified. Along the line CRT-1, which is closer to the junction point, fracture frequency drops significantly at about 220 m from the fault core but the line terminates at a fault cliff. In line CRT-2, the deformation band frequency is still high at the end of the line. Based on off scan-line field observations of fractures, the approximate width of damage zone of this fault segment at this outcrop is 400-500 m. In contrast, Berg (2005) observed a much smaller (about 70 m)

the damage zone width in the footwall and also in the hanging wall about 210 m at the Bartlett fault segment where the fault throw is 170-300 m then a the Courthouse Junction area.

In normal faulting regime, deformation bands in the damage zones are found to be generally sub-parallel to the master fault with synthetic and antithetic dips (Antonellini and Aydin 1994, Roznovsky and Aydin 2001, Shipton and Cowie 2001, Johansen and Fossen 2008, Kolyukhin et al. 2009, Fossen 2010). This observation is consistent with the result of this study. However, in the Jurassic Aztec Sandstone in Nevada (USA), joints, slip plains and deformation bands are oriented oblique to the master fault in strike-slip fault with 14 m of slip (Flodin, et al. 2001, Jourde, et al. 2002). Some studies found that fractures with synthetic and antithetic dip may be geologically coeval and they appear in equal proportions for faults with displacement larger than around 30 m; whereas, in case of smaller faults, the dominance of synthetic structures is found (Antonellini and Aydin 1994, Hesthammer et al. 2000, Shipton and Cowie 2001, Odling et al. 2004, Kolyukhin et al. 2009). In this study, the majority of fractures are conjugate to the main fault dip at Courthouse Junction where fault throw is about 80 metres and also at Klondike Bluffs fault where the throw is about 10 metres. Johansen et al. (2005) studied the junction point of the Moab Fault at the Courthouse Junction and found that majority of the dip of the factures are in the interval of 60–85° which is nearly the same as the result of this work where the fracture dip ranges between 60–90°. Schueller et al. (2013) also found a similar range (from 50° to 80°) for the dip of the deformation bands based on the analysis of many normal faults from different parts of the world. However, at other normal faults dip can be quite different. For example, the dominant fracture set have an angle of about 40-45° with respect to the slip surface in the Rapolano normal fault (Brogi 2008).

Stress condition plays an essential role in the development of the faults too. Faults developed under different stress conditions might have different properties. Solum, et al. (2010) compared the deformation bands formed in the Navajo sandstone reverse and normal fault environment, and found that in the case of reverse fault (contractional setting), the related deformation band network is much more areally extensive and the distribution of deformation band is not related to large faults (throw is a few metres); but it is affected by smaller faults with only a few centimetres. The fracture geometry and fracture distribution of strike slip fault show more significant difference in comparison with normal and reverse fault. Brogi (2011) analyzed fracture distribution in strike-slip faults and related damage zones in sandstone and found that the damage zones are characterized by en-échelon fractures having similar spacing and length and are concentrated in metre -wide domains. The fractures orientation is about 25–42° with respect to the master fault plane and some fractures have sigmoidal shape. Furthermore, fractures distribution decreases from the fault centre, where the maximum fracture frequency is about 12 fracture per metre and about zero to 10 m away from the centre at the faults which unaffected by pre-existing fractures; the fracture distribution is more constant, about 6 fracture per metre around the faults which are affected by pre-existing fractures (Brogi 2011).

The results of the present work shows that in normal faulting regime, deformation bands form close to the fault core and also relatively far from the fault core. The deformation band frequency has peaks as the distance grows going from the fault core. Some of the deformation bands are not related to faults. However, some peaks are related to faults but this relation is independent from the size of the fault throw. Both studied faults are normal faults; however, they are characterized by significantly different deformation band types. At Courthouse Junction, the majority of the fractures are cataclastic deformation bands which may significantly reduce the permeability of the rock. Whereas, at the Klondike Bluffs, most of the fractures are dislocation (disaggregation) deformation bands which might increase the permeability of the rock.

The two most important fault parameters are: the permeability and the extent of the fault which need to be known to better understand fluid migration processes in rock bodies. To define the extent of a fault, the length, the fault throw, the height of the faulted layers and the total width of the fault zone (core + hanging wall damage zone width + footwall damage zone width) need to be considered. The parameters of a fault e.g. width of the fault zone, fracture density, fracture distribution, fracture dips, dip direction of the fracture etc. change along the fault plane. This variation of the fault related fracture network can be seen from the studies performed along the branch fault of the Moab fault. Johansen et al. (2005) observed that the fracture network is complex, as it contains three generations of fractures with different orientations in the junction point (Courthouse Junction triangular). In this work, line CRT-1 was about 320 m from the junction point and the line CRT-2 was about 900 m from it. The fracture distribution and the width of the fault zone are fairly different along the two lines. In comparison with the Bartlett fault section, the fracture density is much higher in the inner zone but the width of the fault is significantly smaller.

Kolyukhin et al. (2009) studied the effect of the parameters of the deformation band network on the bulk permeability of the fault damage zone using stochastic model (see Figure 2-2). The following parameters of the deformation bands were considered: relative deformation band permeability (K_{DB}/K_{HR} - deformation band / host rock), deformation band density, dip angle, dip direction, heterogeneity of the deformation band permeability (i.e. holes in the fractures planes) and clustering. The clustering is expressed by the correlation dimension (Dc) i.e. fracture distribution around faults which is 1 if the distribution is uniform, about 0.1 if most of the fractures are very close to the fault core and about 0.8 if the distribution is decreasing logarithmically moving away from the fault core. The results of Kolyukhin et al. (2009) indicated that deformation band density has a constant permeability of 0.01 darcy (lower than the host rock) and by being perpendicular to the flow direction the effective permeability was reduced by about 50% related to the host rock. If the fracture density exceeds 10 deformation bands per metre. Furthermore, with the increase of the cluster parameter i.e. the increase of the width of the fault zone (where the deformation band density is increase farther from the fault core), the bulk permeability of a fault damage zone decreases where the permeability of the deformation bands are lower than the host rock regardless of other properties. In addition, the orientation of the dip of the deformation bands does not affect the effective permeability if the correlation dimension $Dc>0.8$; however, if the correlation dimension $Dc<0.8$ it might have considerably effect on the

effective permeability (Kolyukhin et al. 2009). The dip of the fractures has more significant effect on the fluid flow. For instance, the model of Kolyukhin et al. (2009) showed that in comparison with the host rock the effective permeability decreased by 50% in a damage zone where the dip of the deformation bands are ±60° if the permeability is lower relative to the host rock (K_{DB} = 0.01 darcy) and with a common decreasing deformation band distribution (Dc = 0.8) and a density of 15 deformation bands per metre. Kolyukhin et al. (2009) also showed that the discontinuities (holes) in the plains of the deformation bands, i.e. heterogeneity of the deformation band permeability, also affect the permeability of the fault damage zone. The higher the number of the holes is, the higher the permeability of the fault zone; if the holes are aligned, then the permeability is higher than if the holes are randomly distributed; with increasing clustering (Dc is decreasing), the bulk effective permeability decreases if holes are randomly distributed and it is increasing if the holes are uniformly distributed.

The geometry of the studied two faults in present work (Courthouse Junction fault and Klondike Bluffs fault) has similar parameters using model definition of Kolyukhin et al. (2009). Orientation of the deformation bands is sub-parallel to the major fault having a moderate wide variation (30-40°). The dip of the deformation bands which has about 30° variation. The distributions of the deformation bands at the Courthouse Junction and the Klondike Bluffs faults have similar logarithmically decreasing style; the correlation dimension is about 0.8. The deformation band density is also range in the same order of magnitude at both faults about 10 deformation bands per metre. Based on the field observations, the most significant difference between the studied faults is the type of deformation bands. In the damage zone of the Courthouse Junction fault, almost only cataclastic deformation bands (baffle the fluid flow) can be found and in the damage zone of the Klondike Bluffs fault almost only dislocation deformation bands (conduit to the fluid flow) can be found. Combined the results of the present field observation and the conclusion of the model of Kolyukhin et al. (2009), the relative complex fracture network geometry in the fault damage zone at the Courthouse Junction, where the relative permeability between the deformation bands and the host rock is low ($K_{DB}/K_{HR}<<1$), enhances the effect of the individual deformation bands. Consequently, the bulk permeability of the damage zone might be lower than the permeability of the individual deformation bands. At this fault, the fluid flow rate is low or zero if the pressure gradient is normal to the fault plane. If the pressure gradient is not normal to the fault plane direction is the flow rate is higher parallel to the fault plane. The fracture network geometry in the fault damage zone the Klondike Bluffs fault, where the relative permeability is probably higher than one ($K_{DB}/K_{HR}>1$), the deformation bands also might increase the effect of the permeability of the damage zone relative to the permeability of the individual deformation bands. However, this effect might be marginal if the pressure gradient is normal to the fault plane because in this case the bottleneck is the host rock itself. If the pressure gradient is not normal or parallel to the fractures the dilatant fractures might able to enhance the flow rate significantly along the fracture path ways. Based on the field observation, the majority of fluid flow occurred along the Klondike Bluffs fault.

In conclusion, the geometry of the fracture network plays an important role in the fluid migration in a reservoir which is either barrier or conduit to fluid flow. However, the most important parameter of the fault damage zone is the permeability of the individual fractures which characterize the fault zone. If the stress is greater than a certain limit (yield stress), the rock deforms irreversibly and fractures develop. The type of the developed fractures is affected by the stress condition which generated the fracture. In an extensional environment (normal faulting regime) tensile fractures may form. In a contractional environment (reverse faulting regime) compactional can form more commonly. However, the differential stress and the confining pressure play an important role in formation of the fractures. Both studied faults are in normal faulting regime and at the Courthouse Junction, the characterized by compactional, cataclastic, low permeability fractures. In contrast, the Klondike Bluffs fault zone is characterized by dislocation bands, relatively high permeability fractures. At the Courthouse Junction, as a result of the higher confining pressure and lower differential stress, cataclastic fractures developed. As a result of the stress, the microstructure of the rock deforms that result in different degree of permeability change along the deformed rock. The microstructure of different types of fractures from the two study areas investigated in the chapter 3.

2.7 Conclusion and outlook

The damage zones of the two study normal faults are characterised by different types of fractures. The Courthouse Junction fault segment is characterised by major cataclasis. This fault is a branch of the major Moab Fault, where the rocks on the surface are Moab Member of the Curtis Formation and Slick Rock Member of Entrada Sandstone. The most common fracture type is cataclastic deformation band or cataclastic deformation band bundles. In addition, slip planes with slickenside and joints can be found in the fault zone and there are only few locations where fluid flow alteration can be observed. In contrast, the Klondike Bluffs fault is characterised by extensional fractures and major fluid flow alteration. This fault is adjacent to the Salt Valley anticline, where the rock on the surface is Moab Member of Curtis Formation. The most common fracture type is dislocation (disaggregation band) deformation band or dislocation deformation band bundles. In addition, joints also can be found in the fault zone but slip planes with slickenside were not observed. Both faults formed in normal faulting regime; however, the stress condition (confining pressure, differential stress) was not the same which resulted in different fracture style.

The distribution of the type of the deformation bands is uniform around each fault: cataclastic deformation bands only can be observed at the Courthouse Junction faults and higher relative permeability dislocation deformation bands only can be observed at the Klondike Bluffs faults. This indicates that the stress condition did not changed significantly during the process of the faulting. The deformation bands formed in one generation at each fault. The orientation of the joint setting shows larger discrepancy related to the orientation of the master fault indicating that they are a different generation of the fractures formed under different stress conditions.

Orientations of the majority of fractures are sub-parallel to the master fault at both scan-lines at both study areas. The variation on the strike of the deformation bands is about 30° and dip ranges between 70 and 90° approximately 300 m far from the fault junction and the strike is about 40 degrees and dip ranges between 40 and 90° approximately about 660 m from the fault junction. The variation of the orientation of the deformation bands at the scan-line closer to the master fault is similar to the other scan-line which is farther from the junction point. This shows that both faults are far enough from the junction of the Moab fault, which is nearly perpendicular to the studied fault branch, and it does not have significant influence on the fracture system at the scan-lines. The slightly larger scatter of the deformation bund orientation at the scan-line farther from the junction point can be explained by the local variation of the complexity of the fault damage zone along the fault.

The distribution of the deformation bands shows a decreasing trend going away from the fault core in both studied fault damage zone. In general, a logarithmic function provided a good approximation to describe this decreasing trend. However, local irregularities (peaks in the deformation band density) are relatively common too which have an impact on the general trend. These local irregularities are not necessarily related to faults; several deformation band density peaks are present at both areas where there are no faults in the interval of the peaks. In conclusion, a single, simple function can provide only a rough estimate of the deformation band density of a fault damage zone. A statistical approach might provide a more realistic estimate.

The widths of the damage zones are relatively wide at both study areas. In the footwall at Klondike Bluffs, the damage zone width is about 150 m and at the Courthouse Junction 200 m and >300 m. In addition, at the Klondike Bluffs in the hanging wall, the damage zone widths are 180 m and 300 metres. The two studied faults characterised by different fracture styles (compactional and dilatational) also have significantly different fault throws but the width of their damage zones are similarly large. These results indicate that there is no clear relationship between the width of the fault damage zone and the fault throw, and between the fault damage zone width and the stress condition under the normal faults formed. Furthermore, the other dimensions of the faults need to be taken into account. The length of the Klondike Bluffs fault is about 3.5 km and the length of the Courthouse Junction fault is about 7 km long. The combined thickness of the faulted formations varies between 260 and 620 m. The size of the fault zones shows that the impacted rock body has a considerably large extension.

The average number of the deformation bands is similar at both study areas; however, about double the average number of the deformation band bundles at the Klondike Bluffs fault. There is no significant difference in the number of the deformation band within bundles at the areas. The average thickness of the cataclastic deformation bands (0.8 and 1 mm) is smaller than the average thickness of the dislocation deformation bands (2.2 and 1.3 mm). The sum of the deformation band thickness is higher at the Klondike Bluffs fault.

Some parameters of the fracture network of the fault damage zone are relatively constant along the faults; however, other parameters vary quite a lot. The type of fractures does not change along the studied faults. The dip and dip direction and also the thickness of the deformation bands, having a certain degree of general variations, do not change significantly along the faults. However, the widths of the fault damage zones, the fracture distribution and also the fracture density have significant variation along the faults.

The effect of the two studied normal faults on the permeability is different. The permeability of the deformation bands in the damage zone in Klondike Bluffs fault is higher than the permeability of the host rock and also the geometry of the fracture network can support the effect of the permeability of the individual fractures. This fault disturbs the fluid flow system creating a fluid pathway in the fault zone. The permeability of the deformation bands in the damage zone of the Courthouse Junction fault is significantly lower than the permeability of the host rock and the geometry of the fracture network supports the effect of the permeability of the individual fractures. This fault is an effective baffle to the fluid flow system which diverts the fluid migration, fluid tends to flow outside, along the fault plain.

The results of this work show that the properties of fault related fracture networks vary in different degree along the fault; some properties vary only slightly and other properties vary significantly. Therefore, it is important to collect data more frequently along the fault to analyse the structure of the fault zone in more detail. Scan-line technic has been applied by several studies. However, other technics such as 2D map (e.g. high-resolution outcrop panorama photomosaic applied by e.g. Laurich et al. (2011) or 3D structural model (applied by e.g. Kokkalas et al. 2007, Wawrzyniec et al. 2007, Jones et al. 2008, McCaffrey et al. 2008, Jones et al. 2009, Sági 2013) of the fracture network of outcrops can provide good data source for a detailed analysis. Because the structure of a fault zone is a very complex system with several parameters with great uncertainties, statistical analysis of field data can help to better understand the relationship between the different parameters of the fault zone which can improve the fault interpretation in seismic and well data.

3 Microstructure analysis of sandstone fractures

3.1 Introduction

This study focuses on fractures of the tight sandstone reservoirs such as the Rotliegend sandstone in the North Sea and in Moab, Utah. The Broad Ion Beam Scanning Electron Microscope (BIB-SEM) images allow us to study the nano-structure of the fractures. The BIB polished surface allows us to trace the pores and minerals in order to calculate statistics to gain information on the properties of the fracture porosity. Besides, the properties of the single fractures, having a large number of samples with fractures should allow us to study the spatial distribution. To better understand the fracture systems, an essentially important factor is to understand the host rocks and the stress field; which determine the type of the fractures. The knowledge of the spatial distribution and the physical properties, the types of the fractures and the properties of the host rock allow us to create a theoretical fracture model, which is able to improve the seismic interpretation. Applying these results to the seismic data, the reservoir can be better described and characterized.

The microstructure of porous rock has been widely studied since the fractal behaviour of porous rock was discovered (Mandelbrot 1983, Katz and Thompson 1985). Katz and Thompson (1985) were the first who used SEM and optical microscope to calculate the fractal dimension of the pore space of various sandstones (with pores ranging from 10 Å to 100µm). The method to determine fractal dimension of the pore size distribution in sandstones using SEM images was automated by Krohn and Thompson (1986). Since then, the fractal dimension of the size distribution of grains, pores and soil pore interface has been calculated by several authors (Krohn and Thompson 1986, Hansen and Skjeltorp 1988, Martín and Taguas 1998, Dathe et al. 2001, Li et al. 2004, Menéndez et al. 2005, Desbois et al. 2009, Yu et al. 2009, Houben et al. 2013).

The pore throat radius is an important parameter to characterize the flow through porous reservoirs (Nelson 2009). Firstly, pore throats were investigated in photo micrographic images of pore casts (Dullien and Dhawan 1974) and thin sections (Wardlaw and Cassan 1978). There is correlation between reservoir permeability and the characteristic pore throat size determined by mercury injection tests (e.g. Swanson 1981, Katz and Thompson 1986, Thompson and Raschke 1987, Ioannidis, et al. 1996). The relationship between the pore throat, permeability and porosity was shown analytically by Heid, et al. (1950) and experimentally by Windland (Kolodzie 1980) and Aguilera (2002). Based on these equations, Ziarani and Aguilera (2012) proposed a model to estimate the pore throat using the permeability and the formation factor (resistivity factor). It was also shown, that the permeability is affected by the size distribution of pore throats, the connectivity properties of the pore network and the spatial correlation of pore sizes (Constantinides and Payatakes 1989, Bryant, et al. 1993, Ioannidis and Chatzis 1993). Furthermore, the pore throat is also used to characterize the flow units of a reservoir which are stratigraphically continuous subdivisions in a reservoir and can be used to identify seals and faults. Martin et al. (1997)

worked out a classification scheme for pores based on the size of the pore throats. This classification corresponds to Oil Production Rate (OPR) for medium gravity oil. Similarly, Deng et al. (2011) proposed an initial relationship between the pore throat size and natural gas production.

Although the pore network of the porous rock is three dimensional, some studies have shown relationship between the 2D pore geometry and the permeability of the 3D pore network (Ehrlich et al. 1991, McCreesh et al. 1991, Coskun and Wardlaw 1993). Ioannidis, et al. (1996) analysed the statistical properties of microstructures of porous rock using SEM images, and they developed an empirical relationship to determine permeability from image porosity and integral correlation scale which can be calculated from the autocorrelation function of binary SEM images.

The microstructure of the deformation bands of Arches National Park, Utah have been the subjects of many studies (Aydin 1978, Antonellini, et al. 1994, Fossen and Bale 2007, Torabi et al. 2007, Eichhubl et al. 2009, Fossen et al. 2011). Aydin (1978) found, that the deformation bands in the Entrada and Navajo Sandstones are formed by a combination of various different processes, such as shear and volume change accommodated in the matrix and pore spaces, microfracturing of grains into smaller grains, shattering of smaller grains, and mixing of the fragments of grains with the matrix.

Antonellini, et al. (1994) documented two generations of deformation bands at Arches National Park. The older generation of deformation bands are characterized with little or no cataclasis, and distributed in relatively undeformed sandstone, in contrast, the younger generation of deformation bands are characterized with well-developed cataclasis, and localized in the vicinity of major structures. According to laboratory experiments, the different deformation band generations developed under different stress states, and therefore it can be assumed, that the first generation of deformation bands formed during the growth of the salt anticline while the second generation of deformation bands formed during the collapse of the salt anticline.

Fossen and Bale (2007) found that deformation bands present locally high decrease in permeability (about 4 orders of magnitude) and porosity. However, the thickness and the porosity of the bands vary rapidly, which reduce the effect of deformation bands to decrease the permeability of the reservoir. Therefore, they concluded that the deformation bands unlikely control the fluid flow, although they might influence the pattern of fluid flow (Figure 3-1).

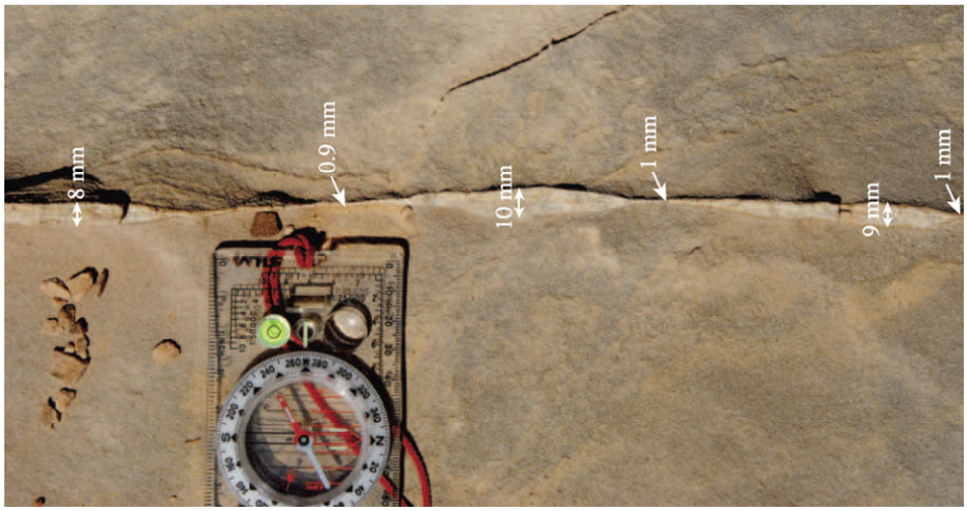

Figure 3-1 – Thickness of deformation bands shows rapid changes along the band (Entrada sandstone, San Rafael Desert, Utah) (modified after Fossen and Bale 2007).

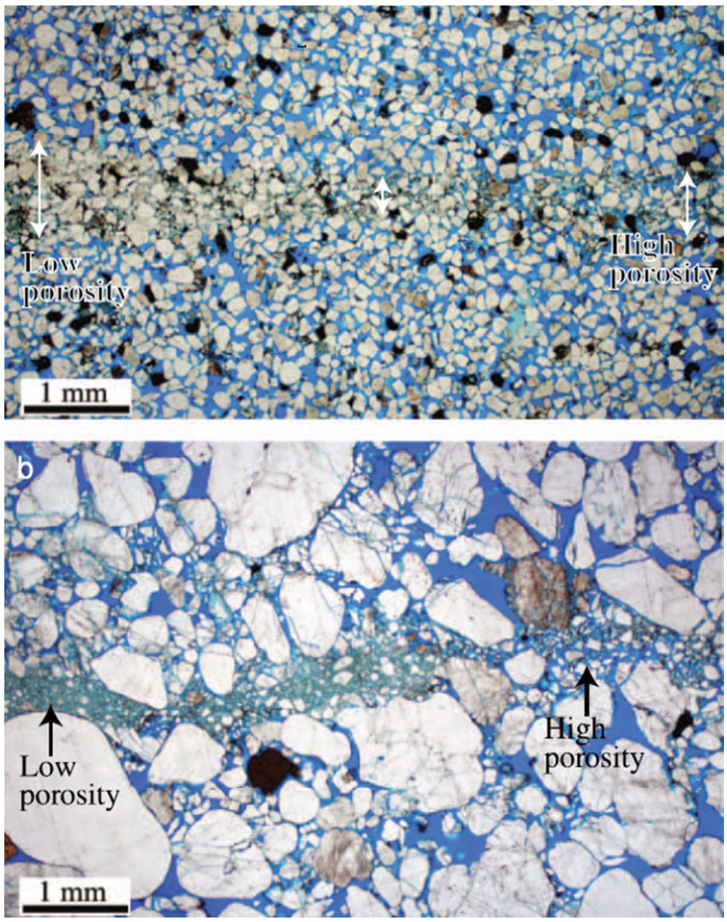

Figure 3-2 – Porosity changes rapidly in the deformation band from the left side to right side of the sample (modified after Fossen and Bale 2007).

Torabi, et al. (2007) performed ring shear experiments in order to analyse the microstructures of shear zones. They found that normal stress (burial depth) and the shear displacement are the factors which have the most important effects on the deformation of grains in the shear zone. In case of shallow depth, the boundary of the shear zone is diffuse and the major mechanisms are the reorganisation, rolling and flaking of the grains; whereas, in case of higher burial depth, the boundary of the shear zone is sharp and the major mechanism is the crushing of grains which reduce the grain size and consequently the porosity (Figure 3-3).

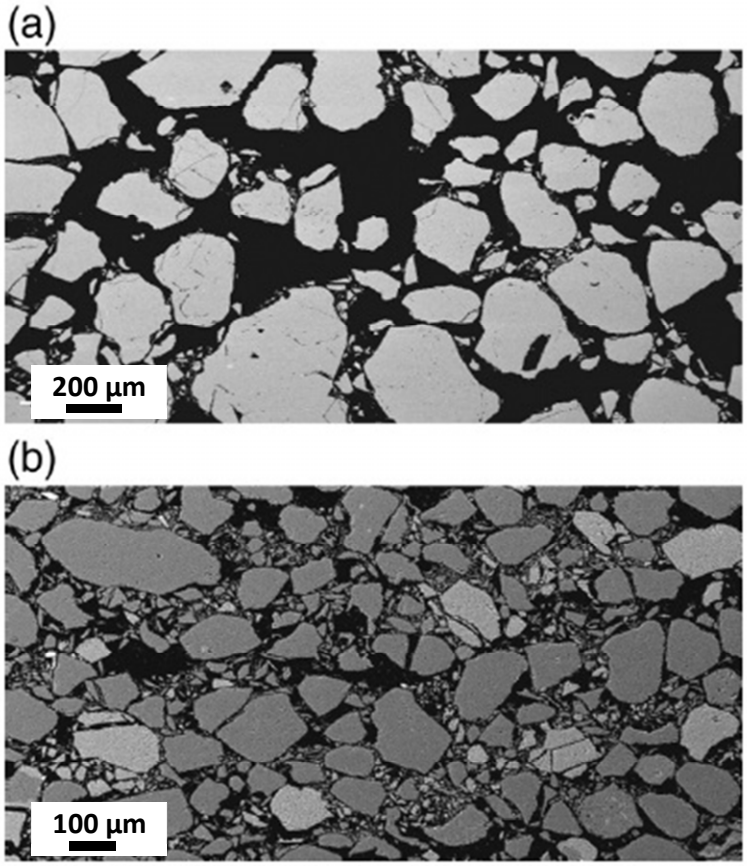

Figure 3-3 – Different types of grain breakage: a) Grain flaking is dominant at low stress b) Grain splitting is dominant at higher stress (modified after Torabi et al. 2007).

Fossen et al. (2011) found that pure compaction bands on the Navajo Sandstone in the Buckskin Gulch site (South Utah) only occur in high permeability (10±7 darcy) and porosity (29±3%) layers. With the presence of shear, in case of shear-enhanced compaction bands, the porosity and the permeability is lower and varies widely from 0 to up to 4 orders of magnitude related to the host rock adjacent to the fractures. Moreover, in the case of compactional shear bands, shear dominated over compression can also occur in low permeability and porosity layers.

Eichhubl et al. (2009) investigated the digenesis and its effect on fluid flow and cementation along the Moab fault. The Moab fault is locally characterized with extensive calcite and less quartz cement. The calcite cementation relates to structures along the Moab

fault in the Courthouse Rock – Mill Canyon area, and occurs as spherical calcite concretions and calcite veins and associated cement halos. Also, ferroan dolomite and malachite are present as fault related carbonate cement. Fe and Mn oxides are also reported in the wider Moab fault area as concretions and pipes (Chan et al. 2000). Only moderate amount of quartz was found in the area. Furthermore, minor amounts of pore filling poikilotopic barite and residual hydrocarbons were observed.

However, the deformation bands of North Sea have not been extensively analysed, the microstructure studies mainly focus on the northern part of the North Sea (Fossen and Hesthammer 2000, Hesthammer, et al. 2000, Fisher and Knipe 2001, Fossen et al. 2003). Hesthammer et al. (2000) reported three types of deformation bands from the Gullfaks area, in the northern North Sea: disaggregation bands, shear bands with clay smearing and cataclastic deformation bands. Disaggregation bands occur in sandstones with low phyllosilicate content (< 20-25%); whereas, in case of higher clay content (> 20-25%), shear bands dominate, and clay smear occur with high phyllosilicate content (> 40-50%). Cataclastic deformation bands are present in the area, they are found to be less common structures. It was shown, that disaggregation bands decrease the permeability only in minor amount. Cataclastic bands were found in the Permian Rotliegend sandstones of the southern North Sea (Fisher and Knipe 2001). Here, the cementation probably occurred after, rather than during, the formation of deformation bands causing the general decrease of permeability with depth.

The main aims of this study were to characterize the microstructure of different types of fractures of reservoir sandstones. On the analogue field, it is easily possible to collect samples from large areas of the surface of the outcrop. With a sample collection which contains samples from the most common deformation structures, the fault related fracture network can be characterized. From the prospect area, North Sea reservoir, only limited number of samples are available for fracture study; therefore, field analogues are important data source to improve our understanding of the architecture of fault zones including subseismic size fracture network. Nevertheless, the small amount of samples from North Sea area provides possibility to compare the analogue and prospect areas and to define the basic fault type on the prospect area.

3.2 Geology setting of North Sea

3.2.1 Stratigraphy

The Carboniferous basement of the North Sea is covered by Mesozoic and Cenozoic sediments. Several hydrocarbon source rocks are distributed over the entire stratigraphic sequence, such as Posidonia Shale Everik Member (Namurian) (> 10m thickness), Zechstein (100-900m thickness), Kimmeridge (11-120 m thickness) and Wealden (Coevorden) (500-700m thickness) are the major source rocks for oil, and Westphalian B (> 10m thickness) is the major source rock for gas (Gerling et al. 1999, Baldschuhn et al. 2001). The sandstones of the Permian Rotliegend and Triassic Buntsandstein are the major reservoir rocks. They both may form tight gas reservoirs as they are interbedded with clay rich layers. Carbonate reservoirs also present in the North Sea both in the Rotliegend such as the Groningen field, and in the Zechstein strata (area L8, L9, P6, Q9 and Z2). There are gas reservoirs of the Westphalian C and D starta, such as the Coevorden field.

Permian Rotliegend

The Rotliegend sandstones reservoir rocks are in a depth of approximately 2500 to 5000 m and overlain by Zechstein salt which provide a perfect seal for a reservoir. The Rotliegend sediments are divided into an upper and lower group, and the lower group is subdivided into the Slochteren and the Silverpit formation. The southern rim of the basin and the Upper Rotliegend formation mainly consist of desert type sediments (Verdier 1996); furthermore, well sorted aeolian dune sands are present in the Rotliegend sandstones which may be interbedded with wadi sandstones, sabkha siltstones and shales (Glennie and Provan 1990). Finely dispersed hematite also occurs in the Rotliegend sandstones which resposible for the red color and also a sign of an arid depositional environment. The diagenesis affected the compaction, pressure solution, clay mineral transformation and cementation of the sandstone. Therefore, the porosity and permeability also vary as an impact of diagenesis, resulting porosities between 5 % and 30 % and permeabilities between 1 mD and several hundreds of mD (Glennie and Provan 1990).

Triassic Buntsandstein

In the Lower Buntsandstein, continental, lacustrine influence is found in the western parts of the basin, which is approximately 20 to 40 m thick and can be correlated over distances of several 100 km and the strongest subsidence up to 400 m is also present in the northern and western offshore areas (Ziegler 1990, Geluk and Röhling 1997, Wong, et al. 2007). Marine influence is found in the eastern part of the basin (Roman, 2004), and several, up to 5-m-thick limestone oolite beds are present (Rogenstein Member); elsewhere in the basin these beds are much thinner. Up to 200 m of massive sandstones are present at the southern margin of the basin, in the southern Netherlands and the adjacent German area. Conglomerates also occur in the south-east part of the basin (Geluk, 1999).

3.2.2 Structural history of the North Sea area

The main tectonic events that affected the area:

1. The Caledonian and Variscan orogenies, resulting in the assembly of the Pangaea supercontinent during the Paleozoic.
2. Mesozoic rifting, accompanying the break-up of Pangaea.
3. Alpine inversion, resulting from the collision of Africa and Europa during the Late Cretaceous and Early Tertiary.
4. Oligocene to recent development of the Rhine Graben rift system

Below the Zechstein salt, at the level of Rotliegend, many structural elements show a characteristic rhomboid pattern of intersecting fault trends (Figure 3-4). The dominant family of faults trends NW-SE and probably dates from mid-Paleozoic times, when Avalonia docked against Laurussia. The second most common fault trend aligns NE-SW to ENE-WSW and became regionally established during the Early Permian (Ziegler, 1988, 1990). Since both trends were already in place prior to Rotliegend and Zechstein deposition, their presence in these younger intervals are the results from fault reactivation. The fault intersections do not indicate consistent offset geometries, and it is likely that both trends were reactivated several times more or less simultaneously. In the northern offshore of the Netherlands, the NW-SE fault trend becomes less important and N-S faults paralleling the Dutch Central Graben and Step Graben dominate.

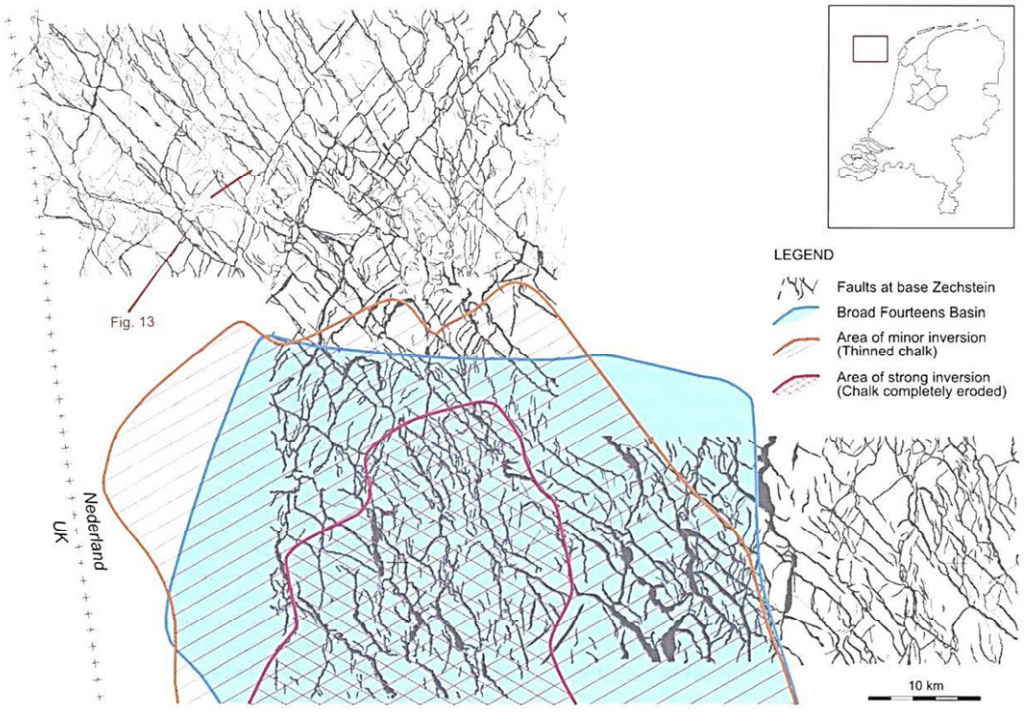

Figure 3-4 – Fault pattern at Rotliegend level in the northern sector of the Broad Fourteens Basin and adjacent Cleaver Bank High, based on good-quality 3D seismic data (modified after Wong et al. 2007).

The area of blocks of L-05 and L-06 (Terschelling Basin and the southern part of the Dutch Central Graben) is characterized by several faults. There are two dominant fault trends in this area: NNE-SSW and WNW-ESE (De Jager 2007) (Figure 3-5). The NNE-SSW trending faults were active as normal faults during the early Kimmerian tectonic phase in Late Triassic. Both NNE-SSW and WNW-ESE trending faults were active during the Late Jurassic in a trans-tensional stress field (normal faults and strike slips) and during the Late Cretaceous as strike slips (Verweij and Witmans, 2009).

The burial depths of the Rotliegend sandstones were approximately 2 km during the Late Triassic tectonic phase, approximately 3 km during the Late Jurassic tectonic phase and approximately 4 km during the Late Cretaceous tectonic phase (Verweij 2009).

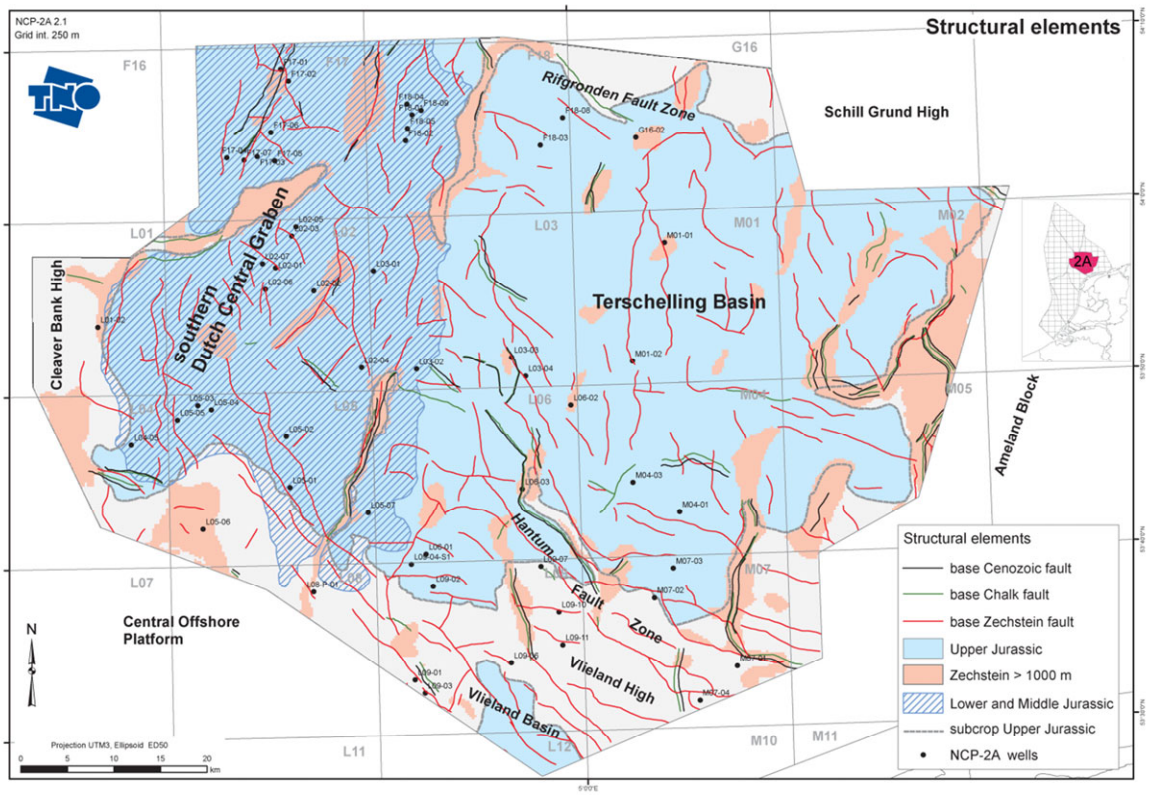

Figure 3-5 -Structural elements of offshore sub-region NCP-2A of the North Sea (Verweij and Witmans 2009).

3.3 Method

The Broad Ion Beam (BIB) sample preparation provides really fine polished sample, the Argon Ion Beam cross milling reduces the surface roughness up to about 5nm on the area of about one square millimetre (Klaver et al. 2012). Figure 3-6 shows an example for a polished SEM sample. Samples were coated with gold for SE and BSE imaging and carbon for Electron Back-Scatter Diffraction (EBSD) imaging. The samples were imaged by Zeiss Supra 55 Scanning Electron Microscopy (SEM) and BIB polished by JEOL, SM 09010 cross-section polisher. The SEM provides no true images by scanning the sample with focused beam of electrons. With BIB-polished surface, the magnification of the SEM can go up to approximately 100000 times.

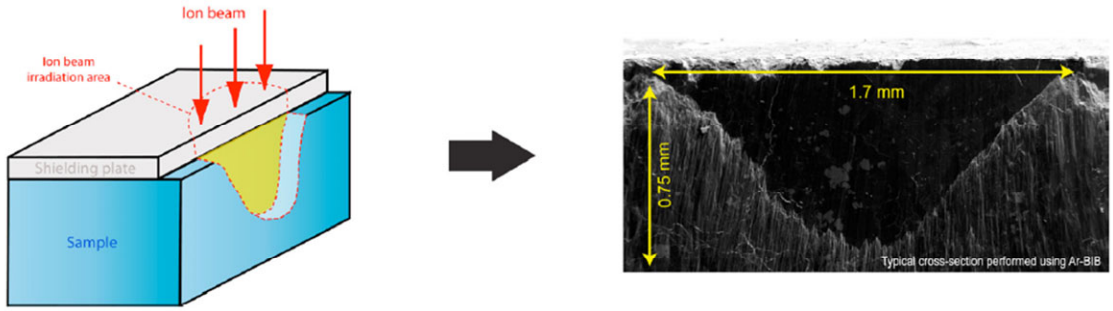

Figure 3-6 – Argon Ion Beam (BIB) cross-section on the SEM sample. The ion beam irradiates the unmasked edge of the sample (modified after Desbois et al. 2010).

In this study, SE, BSE and EBSD images were used for the analyses applying different magnifications. Overview images have about 100x-300x magnification having a resolution is 3-1 µm and for fine details of the samples were studied in higher resolution images which was taken with magnification of 1000x to up to 50000x which resolution are about 300 nm - 5 nm image resolutions. These resolution images allow studying the fine structures of the fractures and the pore filling minerals. Beside single images, also image mosaics were taken in order to gain high resolution overview images to study larger areas of the samples in high resolution. Images were merged Autopano Giga 2.6 software developed by Kolor (2012). To gain information on the mineral content, EDX were measured in lower resolution for overview and also high resolution in points.

Thin section study of the structures and the host rock

Thin sections study provides information about the microstructure of the fractures, in larger scale than the SEM microscopy. Thin sections were created on 24 mm x 36 mm glass plate without upper glass cover. The thickness of the thin sections were polished about 20-40 µm.

3.4 Results of Moab samples

Samples were collected from the most common and typical deformation structures which characterise the studied areas. From the Courthouse Junction area 30 hand specimens, from Klondike Bluffs area 10 hand specimens and from well L5-9 of North Sea 6 core samples were collected and fractures of these samples were studied by microscopy. These samples are presented in this chapter with field photos, thin section micrographs and BIB-SEM images. The description of the deformation structures of these areas based on field observations and also the geology characterisation of the areas are in chapter 2.

3.4.1 Courthouse Junction samples

This area is characterised with major cataclasis; and, only minor fluid flow alteration was observed. Samples were collected from most common types of fractures. The majority of the samples were cataclastic deformation bands. Furthermore, slip plains were found in the centre of the majority of the faults. Samples Z062 and Z064 show examples for cataclastic deformation bands and slip planes. Besides, close to the main fault core as a result of the fluid flow, mineral concretions can be observed at some spots. Samples Z030, Z040 and Z052 show examples for these features. Furthermore, close to the main fault core, a few dilatant fractures were also found (samples Z019 and Z008). Figure 3-7 shows the map of samples which were collected on Courthouse Junction area, and the colours indicate the type of the deformation structures.

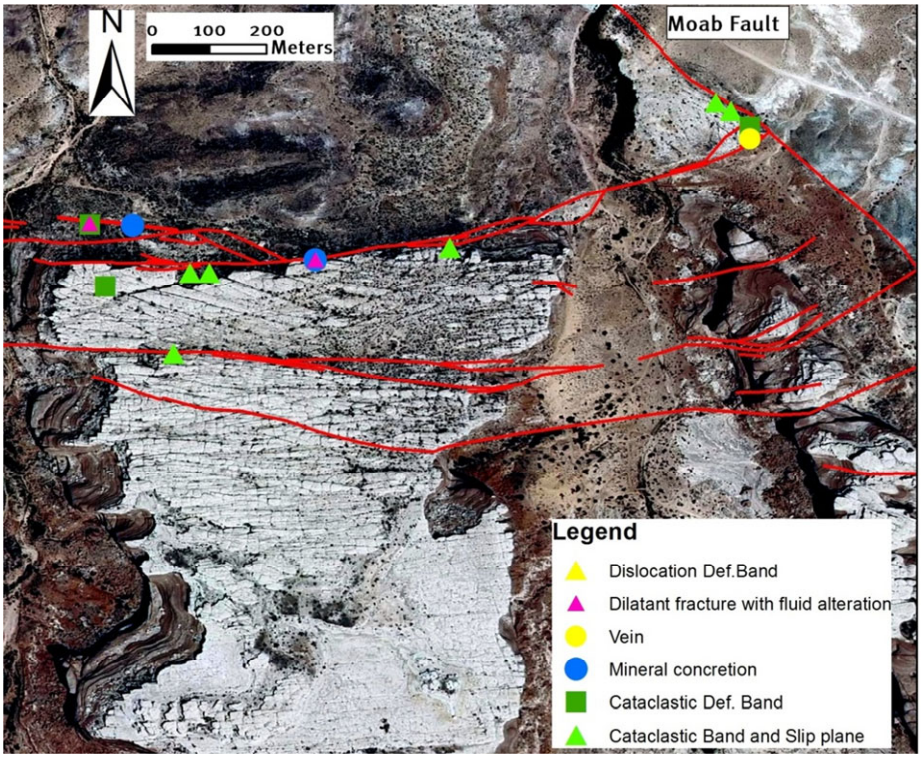

Figure 3-7 – The studied rock samples on Courthouse Junction area. (satelite image: NAIP, 2009; faults structure: Davatzes et al., 2005)

Z062 / JU130410-1

This sample represents the most common deformation structures of the Courthouse Junction area, namely the cataclastic deformation bands. Besides, slip planes are also common in the centre of the faults. This sample is from the footwall of the fault. Figure 3-7 shows the location of the sample where it was found. Figure 3-8 shows the photos of the samples pieces after cutting. Results of the microscopy analysis of the sample are listed below.

Rock type: Slick Rock Member of Entrada Sandstone
Structure in the sample: Cataclastic bands and slip plane
Grain size: out of structure: ~70-300 µm; in the structure: ~ 0.5 - 15 µm
Pore type: intergrain and intragrain porosity in K-Feldspar
Pore size: out of structure: ~25-300 µm; in the structure: ~0.2 - 3 µm
Pore throat diameter: out of structure: ~ 5-35 µm; in the structure: ~ 0.1-0.8 µm
Pore distribution: inhomogeneous
Pore orientation: random
Cementation, pore filling:

Quartz: habitus: overgrowth, growth direction: along grain surfaces

Calcite: habitus euhedral, growth direction: along grain surfaces;

Illite: habitus: fibrous, growth direction: perpendicular and tangential to grain surfaces;

K-Feldspar: habitus: along grain surfaces, growth direction: pore filling.

General observation based on BIB-SEM images:

- Granular SiO and calcite on the quartz grains reduce the pore space slightly.
- Lining clay minerals and SiO at the boundary of quartz grains.
- Calcite and clay minerals fill the pore throat.
- Randomly oriented fractures in the K-feldspar which locally fills the pore space.
- Illite significantly reduces the pore space.
- Inside the deformation structure, drastic grain size reduction can be seen.

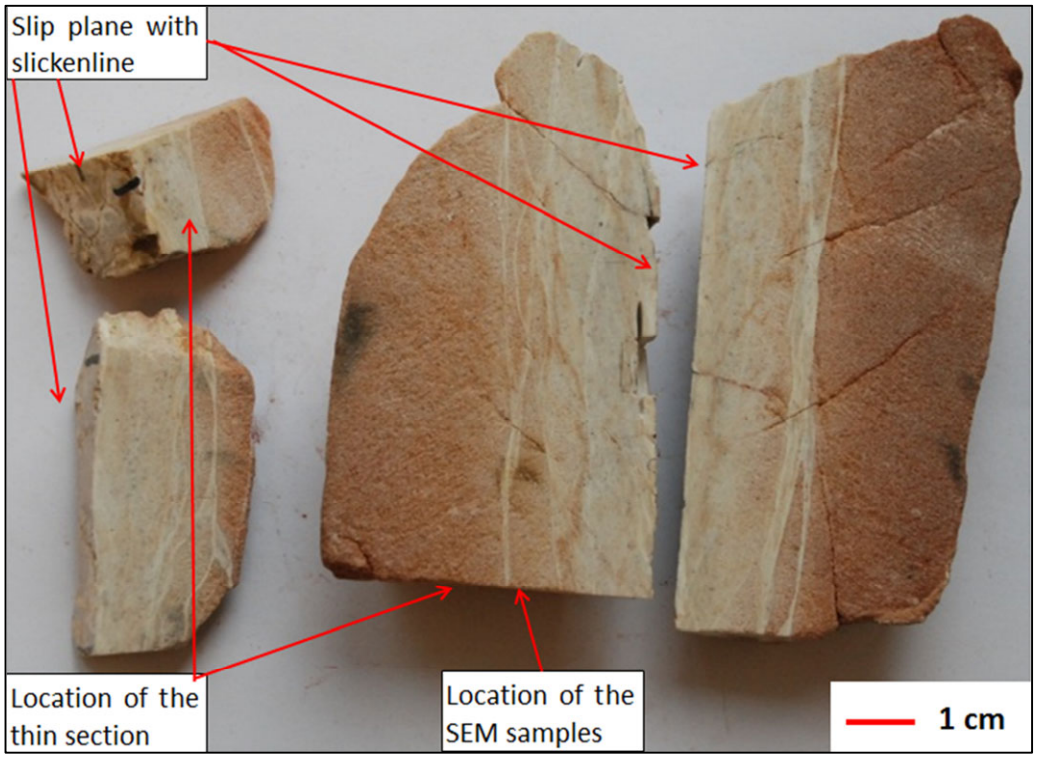

Figure 3-8 – The photo of cut parts of sample Z062 shows the location of the SEM and thin section samples.

Thin section

This is an excellent example for cataclastic deformation band bundle network which is next to a slip plane (Figure 3-8). The right hand side of the micrograph of the thin section of the sample (Figure 3-9) shows the more fractured zone of the rock which is next to the slip plane (right edge). The open fractures in the area might be the result of the sample preparation. On the left hand side of the micrograph, in the host rock, a single cataclastic band can be found. On the detailed pictures of the thin section, the strong grain size reduction can be seen (Figure 3-9). Thin sections allow us to study the shape and the size of the structures in a 2-3 cm long section. The grains inside the structure are too small to study them by optical microscope.

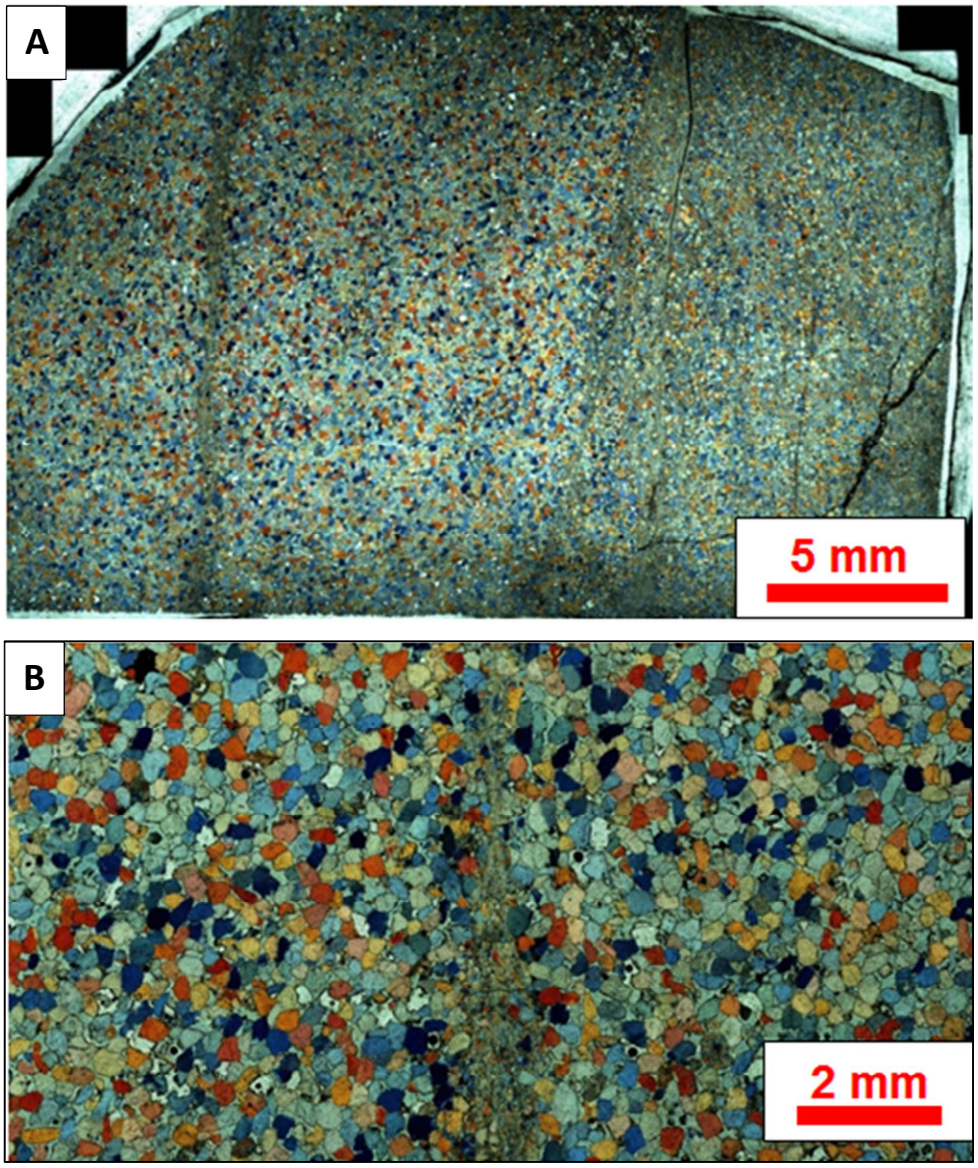

Figure 3-9 - A) Overview image of sample Z062a; B) detailed images of the structures of the sample.

SEM

BIB-SEM overview images of sample Z062c can be seen on Figure 3-10. The red dashed line indicates the deformation band in the middle of the picture. The SEM sample is taken from the same single band which can be seen on the left hand side of the thin section, too. The 1 mm long segment of the structure can be studied on the SEM sample. The width of the structure is about 0.25 mm which is in the middle of the cross section; therefore, the contrast can be seen well between the structure and undamaged rock. The size of the grains, outside of the structure, ranges from about 80 to 250 μm on the SEM cross section (Figure 3-11). The relatively large pores are partly filled with calcite and clay minerals. The pores are filled in different degree by amount of pore filling materials; some pores are filled almost totally (right part of Figure 3-11) others are only slightly. Outside of the fracture, grain crushing or damage cannot be seen. There is no transition zone observed between the fracture and the not fractured parts of the rock, where grain size reduction less than in general in the structure. Figure 3-12 shows a segment of the cataclastic band where large degree of grain size reduction can be seen; approximately 1:10 is the average ratio between the structure and the undamaged grains. On the SEM images, the grain boundaries are not visible at many places; in conclusion, it is hard to distinguish the grains. Therefore, EBSD method was used to distinguish the different grains (Figure 3-13). Inside the structure, the grain size distribution covers a relatively wide range, since some larger slightly crushed grains also remained in the deformation band. In general, inside structure large amount of pore size reduction and consequently this porosity reduction is present which can reduce the permeability of the rock significantly.

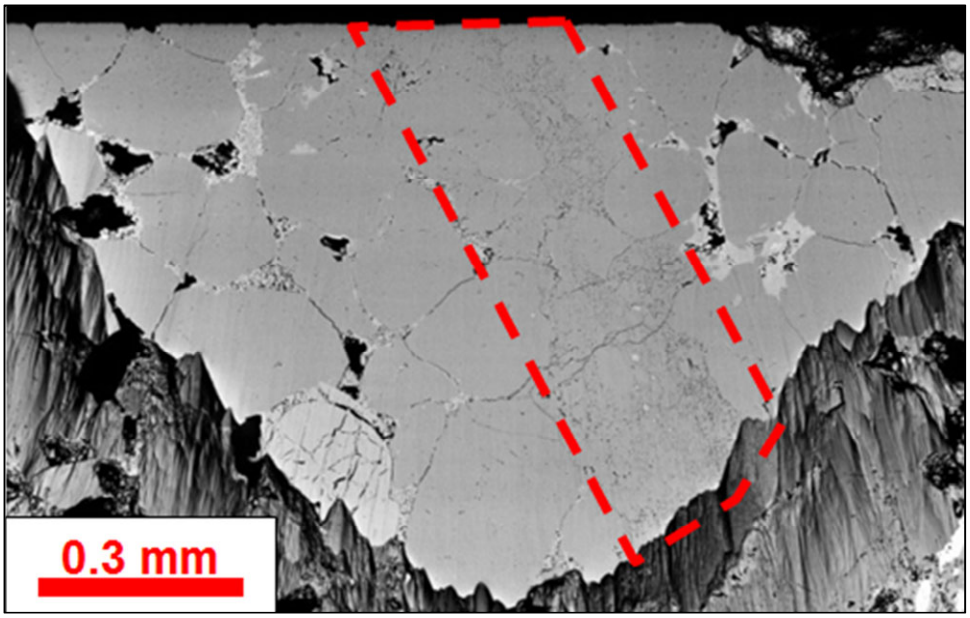

Figure 3-10 – BIB-SEM overview images of sample Z062c (originated from the Courthouse Junction fault zone). The red dashed rectangular indicates the location of a segment of a cataclastic deformation band.

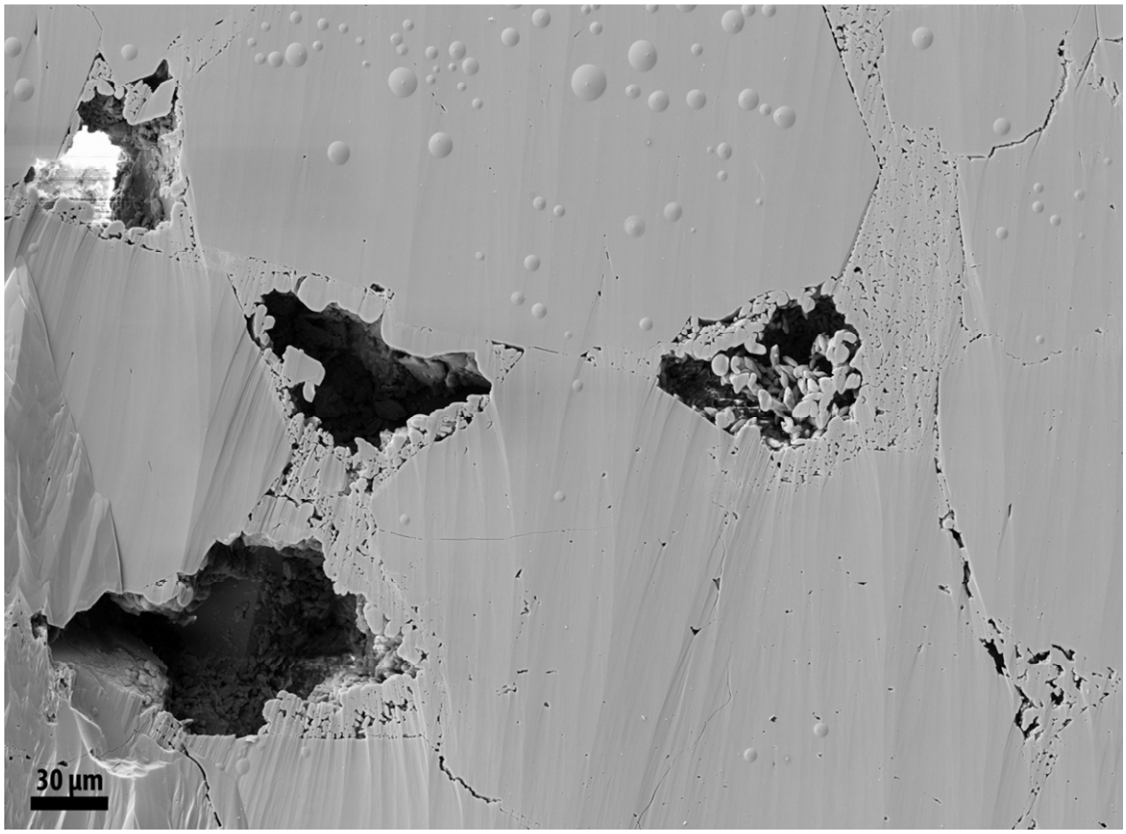

Figure 3-11 – Section of outside of the cataclastic deformation band of sample Z062c.

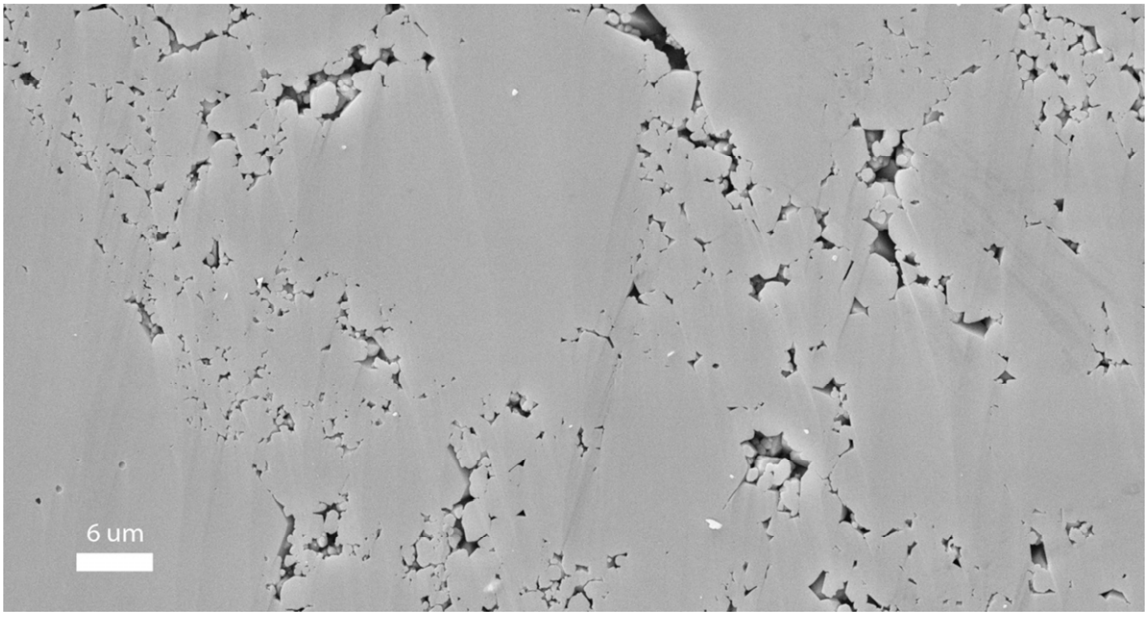

Figure 3-12 – SEM image of a segment of the cataclastic deformation band of sample Z062c.

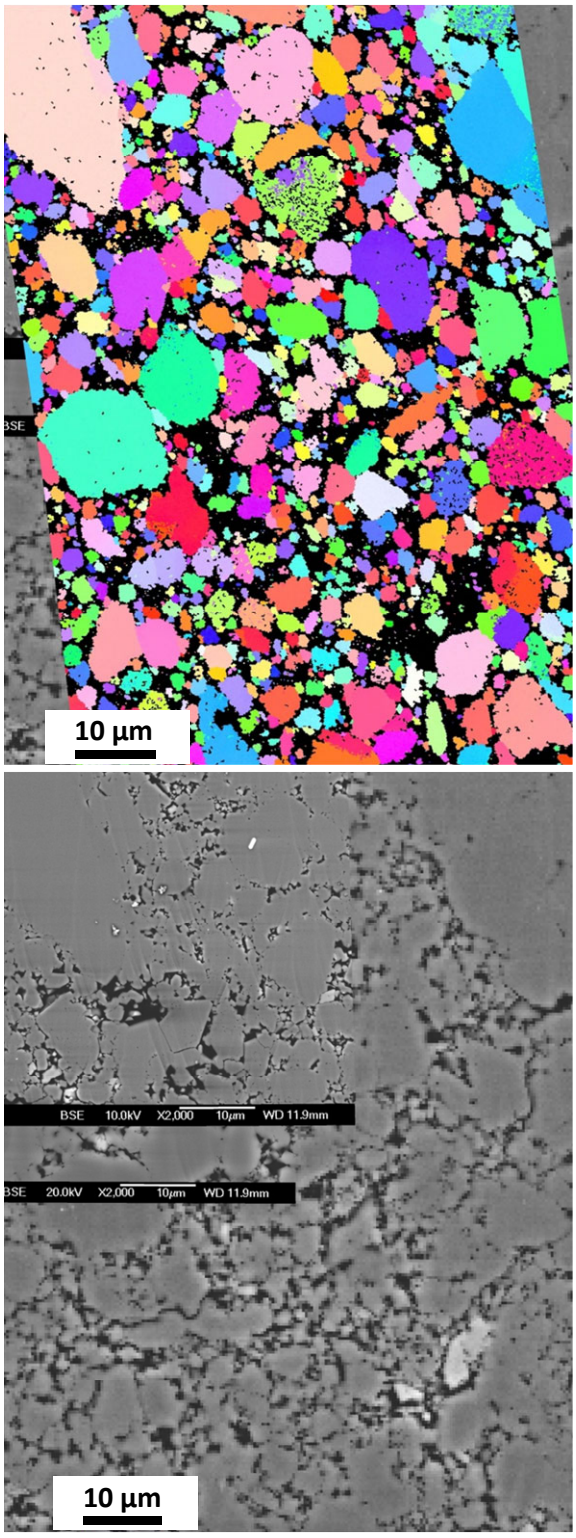

Figure 3-13 – EBSD image of a segment of the cataclastic deformation band of sample Z062c.

Z032 / ZK240410-2

Rock type: Slick Rock Member of Entrada Sandstone
Structure in the sample: Cataclastic deformation bands
Grain size: out of structure: ~60-280 µm; in the structure: ~ 0.5 - 25 µm
Pore type: intergrain, intragrain porosity in calcite and clay minerals
Pore size: out of structure: ~ 20-110 µm; in the structure: ~ 0.1 - 3 µm
Pore throat size: out of structure: ~ 5-20 µm; in the structure: ~ 0.5-2 µm
Pore distribution: inhomogeneous
Pore orientation: random
Cementation, pore filling:

Quartz: habitus: overgrowth, growth direction: along grain surfaces;
Calcite: habitus: fibrous, euhedral, granular, growth direction: along grain surfaces;
Ton-mineral: usually mixed with calcite, habitus: fibrous, euhedral, growth direction: along grain surfaces;
Illite: habitus: fibrous, euhedral, growth direction: along grain surfaces.

General observation based on BIB-SEM images:

- Clay minerals significantly reduce the pore space.
- Grain size reduction can be seen inside the deformation structure, where, in the pores, also calcite and clay minerals can be found.
- Porous calcite and clay minerals fill the pore throats and pore space.
- Significant quartz grain size reductions can be seen in the pore space and small amount of illite as well.
- Quartz overgrowth fills the pore throat, and calcite and clay minerals can be seen in the pore throat.
- Porous clay minerals and calcite fill the pore space.

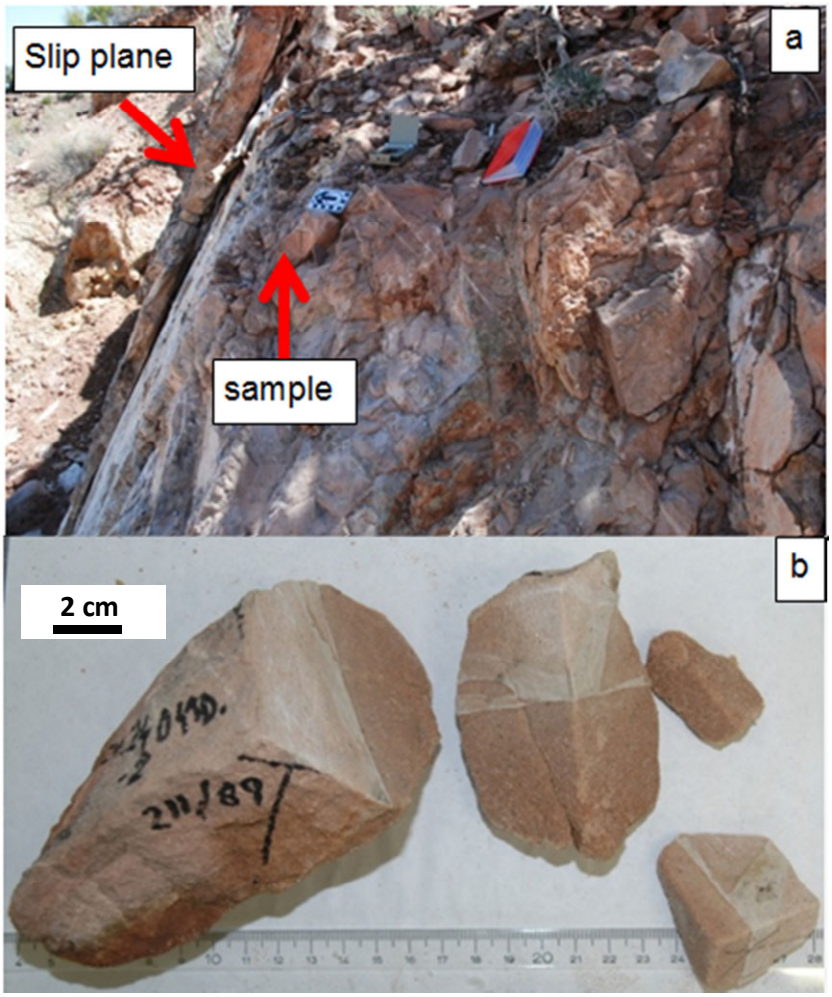

Figure 3-14 – a) original location of sample Z032; b) deformation band in the cut samples.

Thin section

This sample is located approximately 15 cm from a large slip plane which is in the core of the main fault and has an offset of about 80 m. In the footwall of the fault, a complex and relatively dense fractures network can be seen (Figure 3-14/a). This complexity can be seen in the samples as well (Figure 3-14/b). On one half of the sample, there is no fractures; however, the other half of the sample is highly fractured. The boundary between the two parts is distinct and plain. On the Figure 3-15, three different sizes of fractures can be seen. The most right hand side fracture is the boundary of this bundle. Their size changes along the structure quite lot. On the higher magnification image of the thin section (Figure 3-16) nicely considerable grain size reduction can be seen which is the result of cataclasis. The boundary of the structure might be a slip plane.

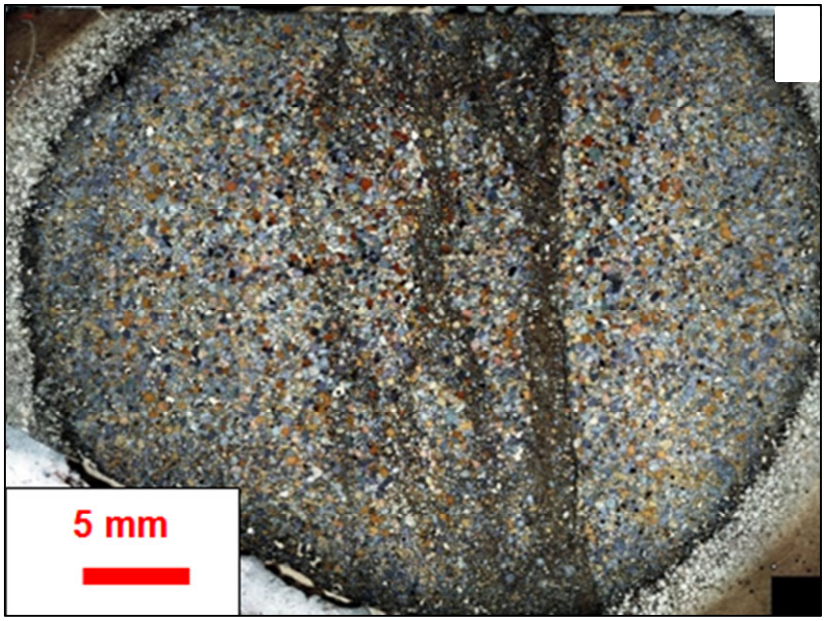

Figure 3-15 - overview of thin section of sample Z032c

Figure 3-16 - Detailed picture of thin section of sample Z032c

SEM

The SEM cross-section is taken from the boundary of the deformation structure, which is a seemingly homogenous, white coloured deformation band in red host rock. However, the overview images (Figure 3-17) there are seen large changes inside the structure going away from the host rock, which is on the right side of the image, towards the centre of the deformation band. In the middle of the BIB-SEM cross section, an approximately 0.3 mm wide band can be seen where high degree of grain size reduction can be observed. On the right side of this band, there is a transition zone where the cataclasis decreases and grain size gradually increases. The width of this zone is about 0.3 – 0.5 mm. On the left side of the highly cataclastic band, the boundary is a distinct line, which is an open fracture and seems to be a slip surface. On the left side of this fracture, the cataclasis is still relatively high; however, significantly lower than in the band in the middle of the image. Figure 3-18 shows a 65 µm by 100 µm size are (red rectangular on Figure 3-17) which is the in boundary of the two zones. An almost continuous separation can be seen between the two zones which can be an open fracture; however, no significant displacement can be observed along this line. In conclusion, this fracture is likely not a slip surface.

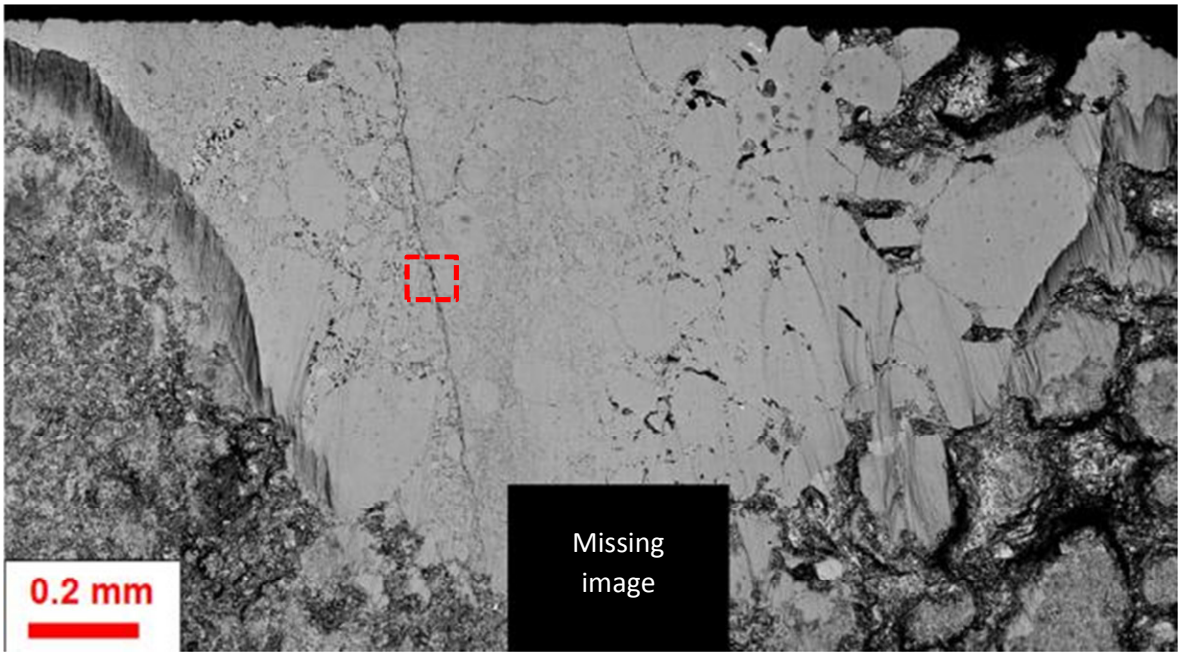

Figure 3-17 - SEM overview images of sample Z032a The red box indicates the location of the image in Figure 3-18.

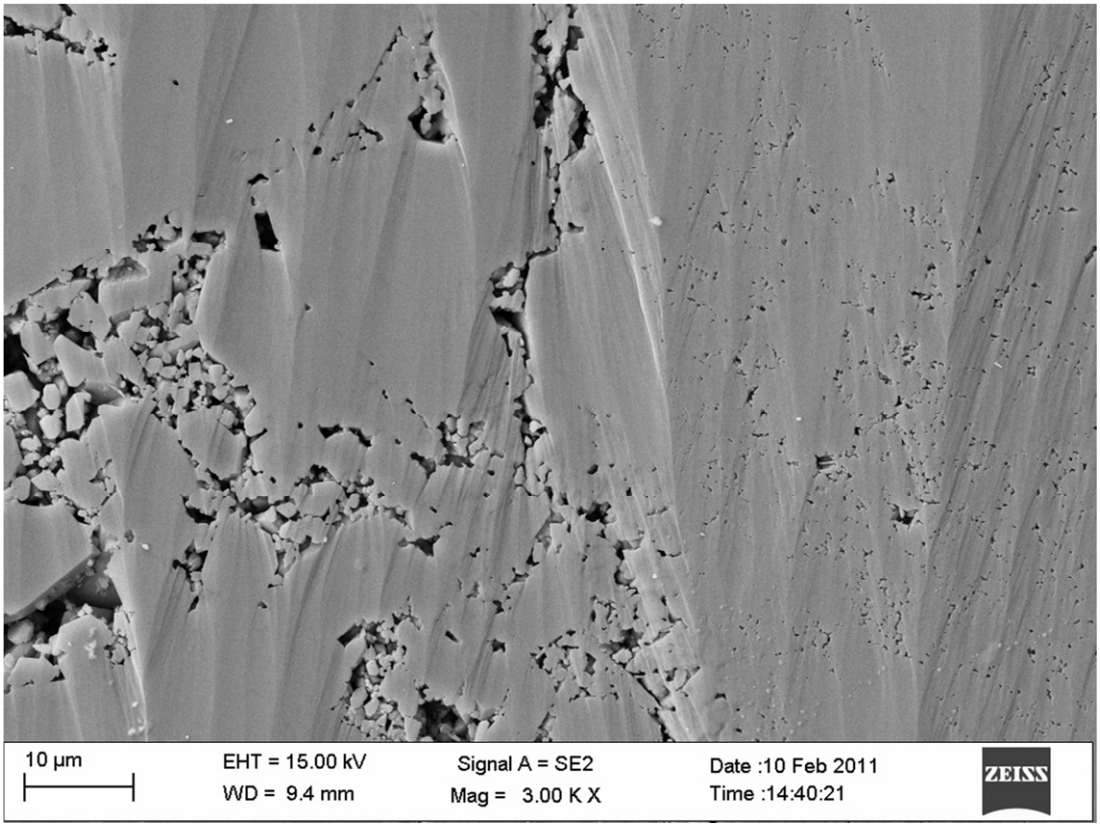

Figure 3-18 - SEM images left side of sample Z032; intermediate cataclasis

Z030_ZK240410-1

This sample was collected from the central area, in the core of the main fault segment. It was a couple of metres from the samples Z032 which contained cataclastic bands next to a slip plane. However, this sample was taken from a greenish and brownish colour, fractured part of the fault. This feature was found at 3 spots on the studied outcrop close to the fault core. On the surface, open fractures were found around the coloured rocks.

Rock type: Moab Member of Curtis Formation
Structure in the sample: Copper vein
Grain size: out of structure: ~ 50-220 µm; in the structure: ~ 10-200 µm
Pore type: intergrain
Pore size: out of structure: ~ 25-80 µm; in the structure: ~ 50-200 µm
Pore throat size: out of structure: ~ 5-20 µm; in the structure: ~ 10-30 µm
Pore distribution: inhomogeneous
Pore orientation: random

Figure 3-19 – Field photo of sample Z030 (Courthouse Junction, Mill Canyon, vicinity of the fault core). The copper coloured the rock green indicating the earlier fluid flow.

Figure 3-20 – Photo of sample Z030 before thin section preparation. The rock is coloured brown and green around the fractures.

Thin section

The photomicrograph of the structure (Figure 3-21) shows that the approximately 0.5 mm wide open fracture is filled with copper. And also in the vicinity of this copper vein, the pore space is filled with copper asymmetrically; on the left side of the vein pore space filled an only 1-1.5 mm wide zone; however, on the right the side, the filled area is 6-7 mm wide. Outside of the above described zones, copper precipitation was not observed. Figure 3-22 shows a segment of the vein in higher magnification. This image shows that the porosity and also the permeability are higher in the outer zone around vein than the porosity of the host rock. Furthermore, inside of the outer zone the grains are highly fractured; the direction of the fractures is in general parallel to the direction of the vein. Since, there was no visible displacement of the crashed grain parts parallel to the vein; this is a Mode I type, purely open fracture.

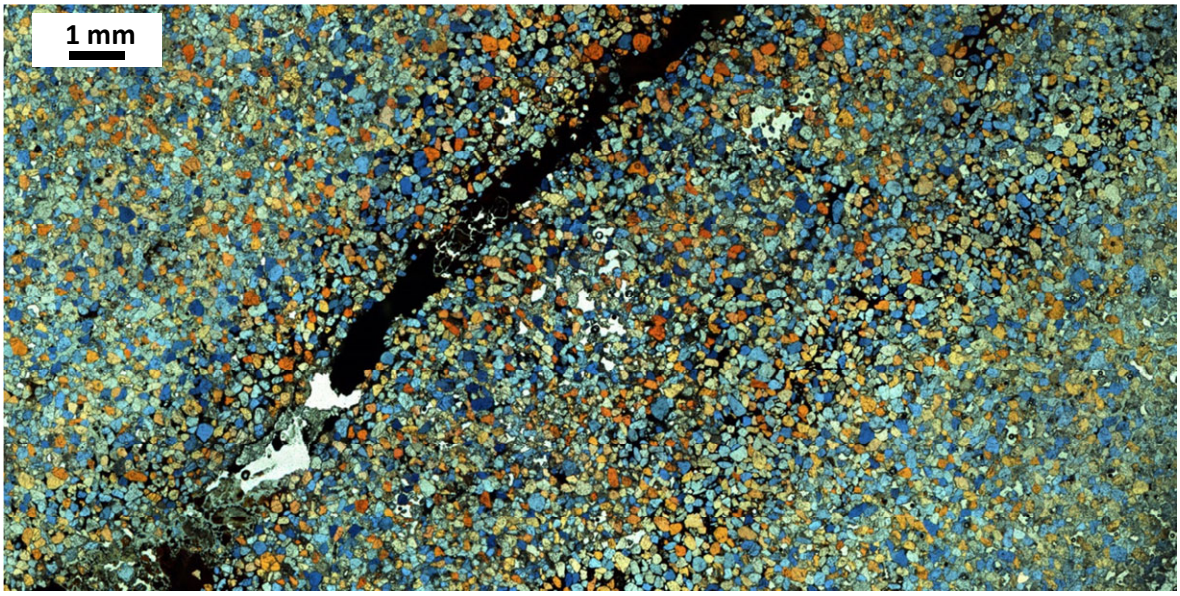

Figure 3-21 – Photomicrograph of thin section of sample Z030.

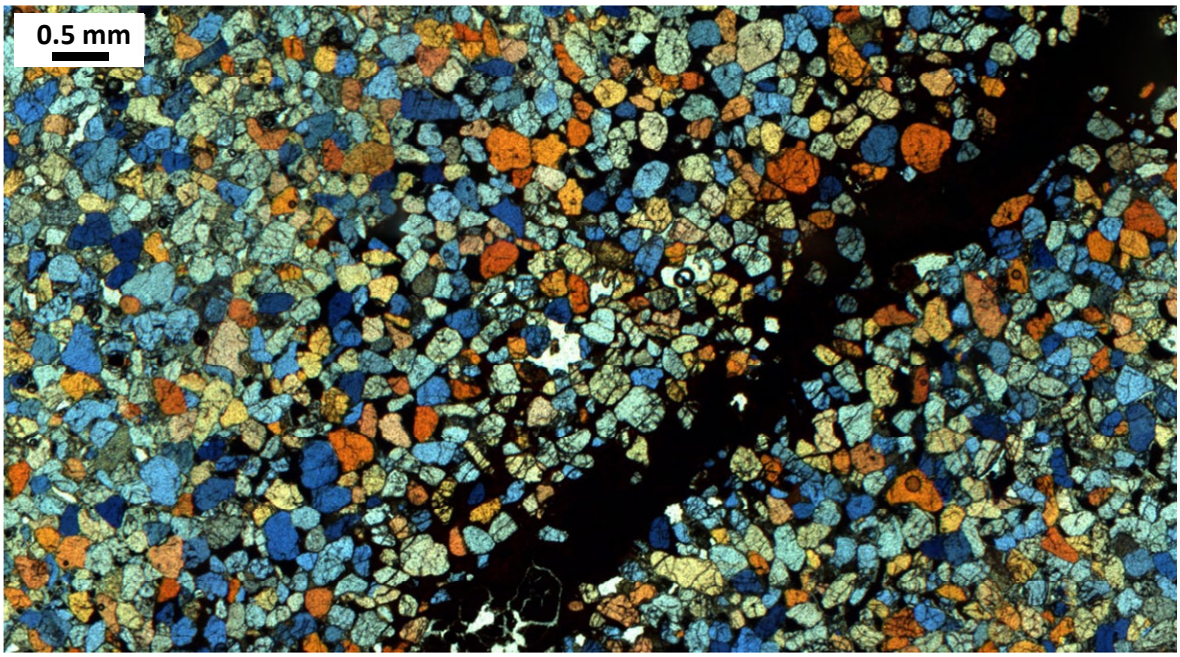

Figure 3-22 – Photomicrograph of thin section of sample Z030. Grains are fractured perpendicularly close to the copper vein.

Z040_ZK260410-3 and Z052_ZK010510-3

In the vicinity of the core of the main fault segment in addition to veins, also mineral concretions, nodules were found. One type of the concretions was copper concretions that can be seen on Figure 3-23. They were found at only some smaller, some tens of centimetres diameter spots. Photomicrograph of the sample shows the copper spots randomly scattered in the rock sample (Figure 3-24). In the concretions every pores is filled both smaller and larger; however, there are same size or larger pores outside of concretions, which have without pore filling. The diameter is not more than about 3-4 mm.

The other type of the concretions have basically white colour with some brown colour parts (Figure 3-25). Two larger, about diameter of 2-3 m spots were found very close the core of the main fault segment and also in the junction of the studied fault segment and the main Moab Fault. This type of concretions has larger approximately 0.5 – 8 cm diameters; however, the numbers of the concretions are smaller than the other type. Thin section of this sample shows that pore space of some parts of the sample is filled with calcite. Besides, at some other parts of the sample, pore space is filled with opaque minerals which are likely iron.

Figure 3-23 – Photo of sample Z040 before the thin section preparation.

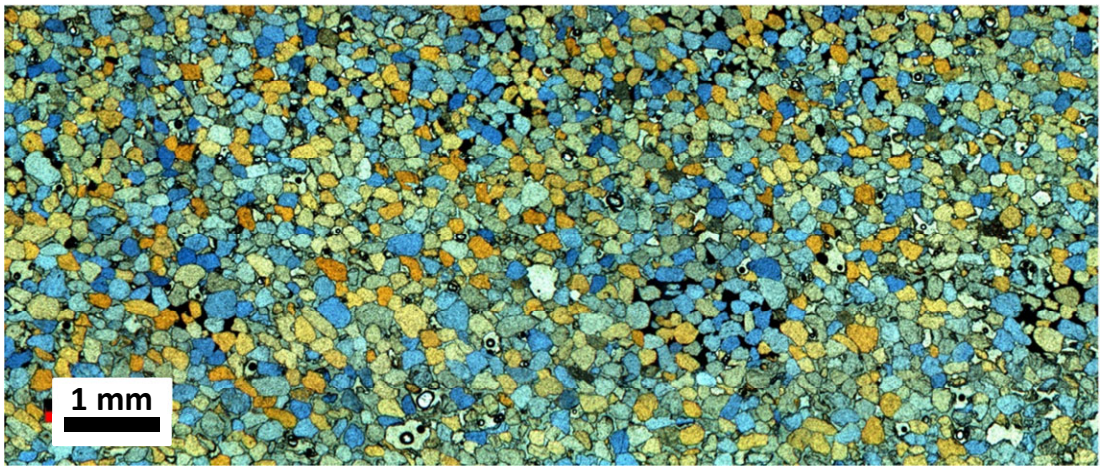

Figure 3-24 – Photomicrograph of thin section of sample Z040.

Figure 3-25 – Photo of mineral concretions which were found close to the fault (sample Z052).

Figure 3-26 – The photomicrograph of the thin section of sample Z052 shows that calcite (lighter greenish yellowish intergrain areas) and hematite (darker intergrain areas) fill the pore space.

Z008_ZK140410-1

This type of fracture was found only in the junction of the studied fault segment and the main Moab Fault. Fracture network has brown colour and they are close to a slip plane that can be seen on Figure 3-27. The pigmentation of the fractures refers to foot print of fluid flow in permeable fractures. Photomicrograph of this sample can be seen on Figure 3-28. The image shows that the fractures are cataclastic deformation bands with high degree of cataclasis. However, mineral filling can be seen in the pore space around the deformation band which is generated by fluid flow that also indicates a certain degree of increase of porosity around the fractures.

Rock type: Moab Member of Curtis Formation
Structure in the sample: Cataclastic deformation band
Grain size: out of structure: ~ 40-200 µm; in the structure: ~ 10-100 µm
Pore type: intergrain
Pore size: out of structure: N/A; in the structure: N/A
Pore throat size: out of structure: N/A; in the structure: N/A
Pore distribution: inhomogeneous
Pore orientation: random

Figure 3-27 – Photo of sample Z008 (Courthouse Junction, cataclastic band with fluid flow alteration) after cutting.

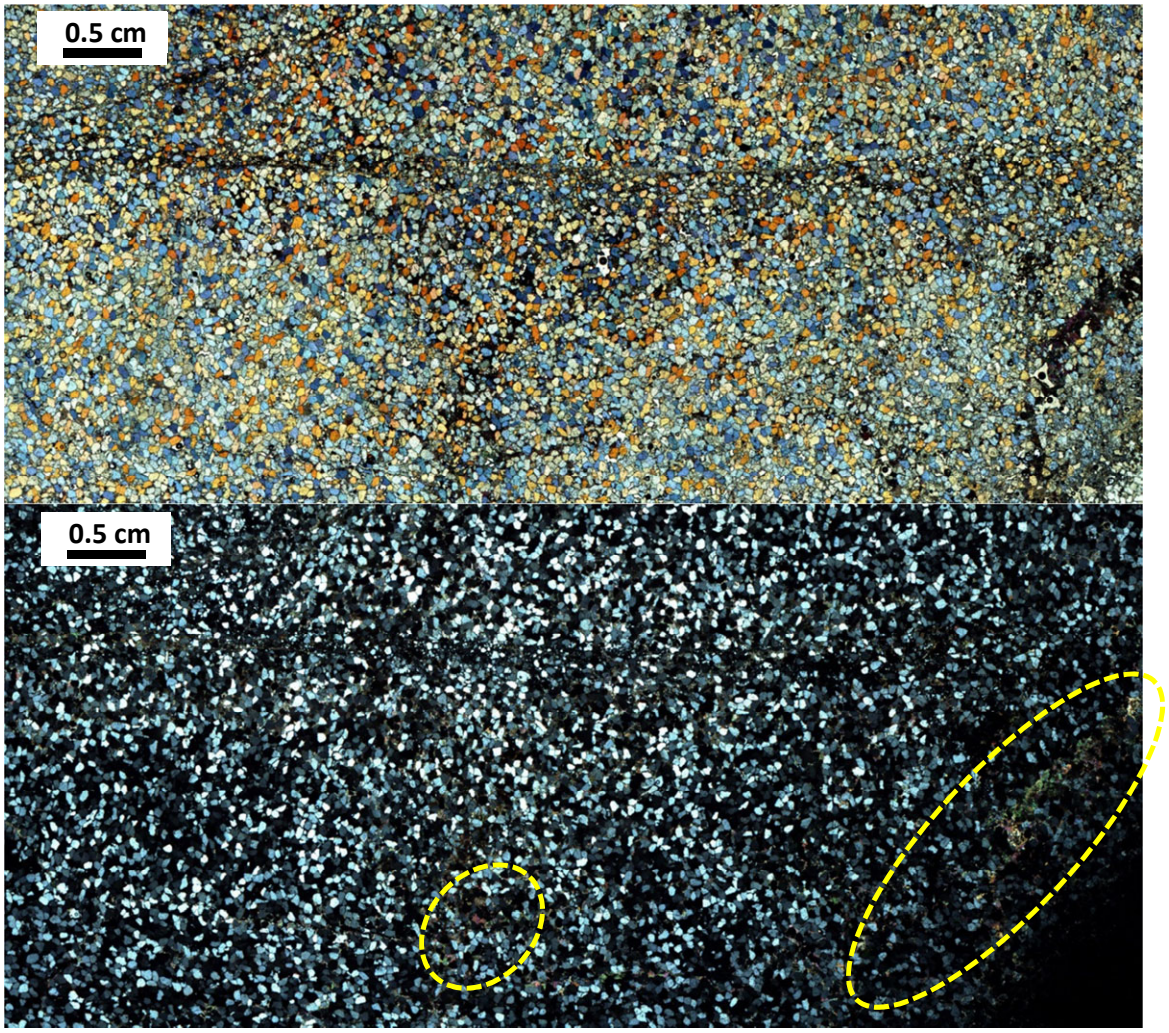

Figure 3-28 – Photomicrograph of sample Z008 (lower image is with crossed polarization). In the vicinity of a cataclastic band, calcite can be seen in the pore space (yellow ellipses).

3.4.2 Klondike Bluffs samples

The studied faults at the Klondike Bluffs area and the location of the studied samples can be seen on Figure 3-29. The majority of the fractures are dislocation, disaggregation band. Furthermore, in general, mineral precipitation was observed inside the deformation structures which indicate previous fluid migration. At several parts of this outcrop, mineral concretions were observed. The size of the individual areas featured by mineral concretions ranged from 0.5-3 m^2 and the diameter of the single nodules ranges between 0.5 and 2 mm in general. On the west part of the footwall of the fault, large size, brownish yellowish mineral concretions were found (Figure 3-30). Samples were collected from most common types of fractures. However, slip plains were not found on this area. Samples Z012, Z017 and Z045 show examples for the three more often observed types of deformation structures.

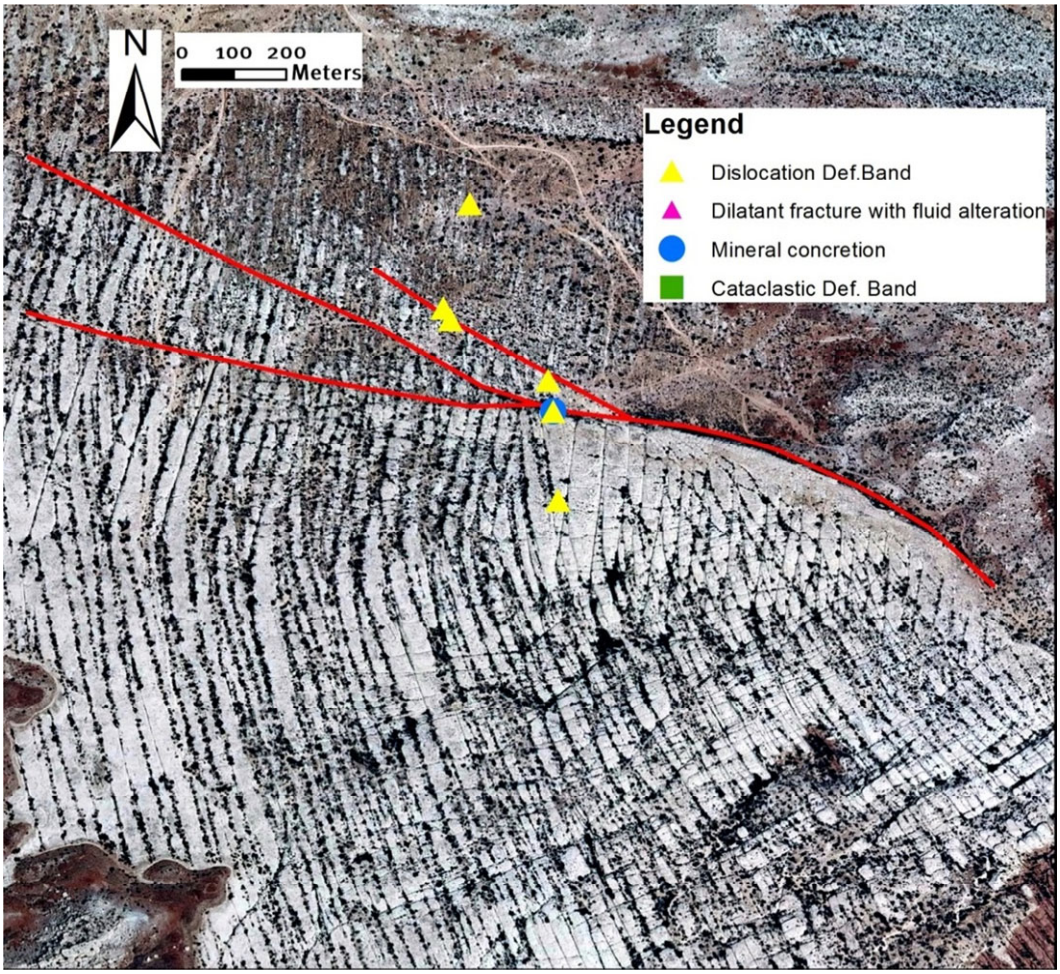

Figure 3-29 – Location of the field samples collected at the Klondike Bluffs area. (satelite image: NAIP, 2009)

Figure 3-30 – Large size mineral concretions on the west part of the footwall of the fault.

Z012_ZK150410-2

Sample Z012 represents one of the most common type deformation bands of this area, namely the dislocation band. Field photo and sample cut for thin section preparation can be seen on Figure 3-31. In general, these deformation bands have white, light grey colour and their thickness are relatively large, about 2-6 mm. These deformation bands were found about 15-20 m far from the core of the main fault, on the eastern part of the out crop, in reddish rocks.

Rock type: Moab Member of Curtis Formation
Structure in the sample: Dislocation band filled with calcite
Grain size: out of structure: ~ 30-300 µm; in the structure: ~ 30-300 µm
Pore type: intergrain
Pore size: out of structure: ~ 10-70 µm; in the structure: ~ 25-160 µm
Pore throat size: out of structure: ~ 5-35 µm; in the structure: ~ 5-50 µm
Pore distribution: inhomogeneous
Pore orientation: random

Thin section

A segment of the deformation structure can be seen on the photomicrograph of the sample on Figure 3-32. Inside the approximately 3 mm wide deformation band, the pore space is filled totally with calcite. The grains less touch each other and significantly higher permeability can be seen inside the structure. Outside of the band, grains show more crowded characteristic with less pore space. Very few grain crushing can be found both

outside and inside the structures. The orientations of the elongated grains show random orientation outside of the band; however, the orientations of the elongated grains are gently oriented within the band. This observation allows to conclude that the deformation contains both dilatancy and shear components.

Figure 3-31 – Field photo of sample Z012 from Klondike Bluffs fault zone on the left (size of the black rectangles on the scale card are 1 cm x 1 cm) and sample pieces before thin section preparation on the right.

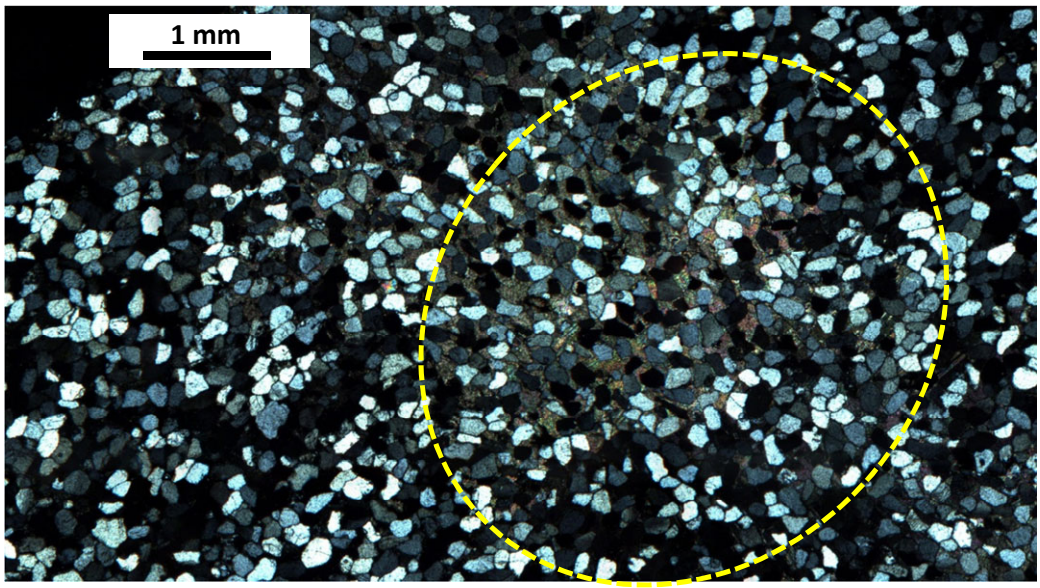

Figure 3-32 – Photomicrograph of sample Z012; calcite fills the pore space (dashed yellow ellipse) inside the dislocation band indicating the present of earlier fluid flow.

Z017_ZK190410-1

Sample Z017 shows a nice example for dislocation band, which is the most common deformation structure of the Klondike Bluffs area. These bands have very bright grey, almost white colour in general. In general, their thickness varies in relatively large range about 0.5-10 mm; mostly some mm. These deformation bands were found farther from the core of the main fault on the western part of the hanging wall of the out crop in light, whitish rocks. Around these structures, usually mm size mineral concretions can be found in the host rock.

Rock type: Moab Member of Curtis Formation

Structure in the sample: Dislocation band filled with calcite

Grain size: out of structure: ~ 40-200 µm; in the structure: ~ 40-200 µm

Pore type: intergrain: remains of small size and thin pores around the quartz grains because of the calcite growth; intragrain: porosity in calcite

Pore size: out of structure: ~ 20-75 µm; in the structure: ~ 40-130 µm

Pore throat size: 5-35 µm; out of structure: ~ µm; in the structure: ~ 5-40 µm

Pore distribution: inhomogeneous

Pore orientation: random

Cementation, pore filling:

Quartz: habitus: overgrowth, growth direction: along grain surfaces

Calcite: habitus: homogeneously fills the pores, growth direction: pore filling, deformation features: few fractures, size less than 1 µm minerals

Illite: habitus: fibrous, growth direction: perpendicular and tangential to grain surfaces

Clay mineral: habitus: euhedral; growth direction: along grain surfaces.

General observation based on BIB-SEM images:

- Inside this dislocation (shear) band, the pores are filled with calcite entirely, only mm-size gaps remained along the quartz grains in some places.
- Granular clay minerals in the remaining pore-space.
- mm or smaller size fractures can be seen in the pore filling material (calcite, illite, rutile, clay minerals).
- Empty pore throat in calcite filled deformation area.
- Locally in the pore space, illite also can be found which is fractured. Illite is grown together with calcite without any pores.
- Secondary pores between quartz grains, and calcite is filled with less than mm-size quartz, illite and calcite grains.

Figure 3-33 - Sample Z017 at the field above, and two pieces of this prepared for creating thin section.

Thin section

The pore space inside the structure is larger than in undamaged host rock area. This can be seen on the micrograph images below (Figure 3-34). Figure 3-35 shows a part of the structure in higher resolution. Within the fracture, the intergrain space is significantly higher than outside of the fracture. Only very few broken grains can be observed both in the fracture and out of the fracture. There was no distinguishable pore or grain orientation either in or out of the structure. In conclusion, this fracture is a dislocation of disaggregation deformation band; where likely no significant amount of shearing or offset is occurred. The boundary of the band (yellow dashed line on Figure 3-34) is not a straight line, more crisscross present depending on the degree of the penetration of the pore filling material. The pore space is totally filled with calcite inside the deformation band as a result of the earlier fluid flow. Next to the band, smaller calcite concretions can be seen with diameter of about 0.2-0.5 mm.

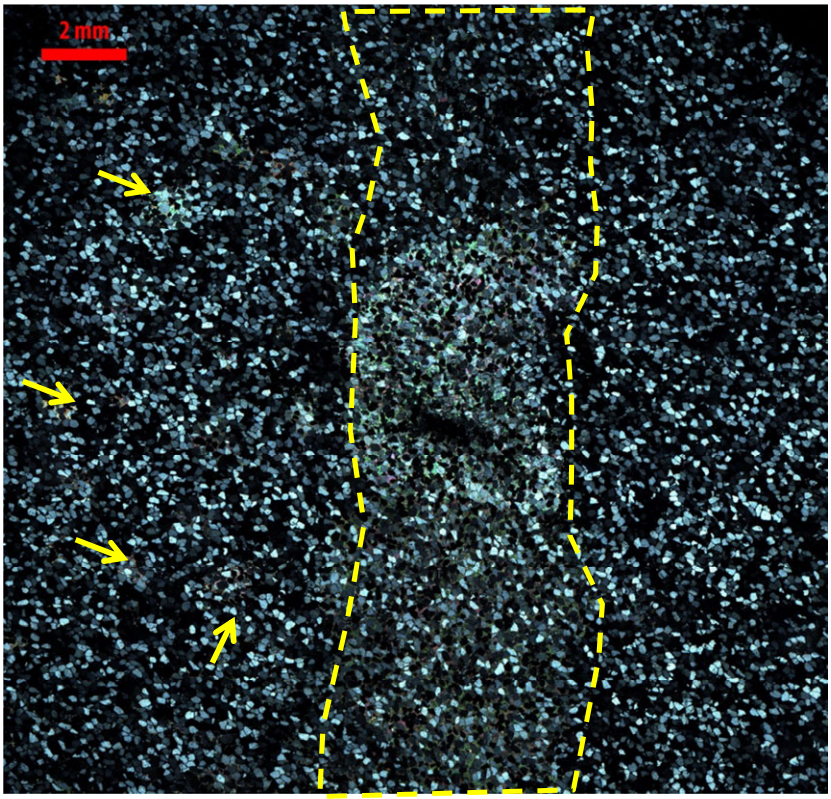

Figure 3-34 - Micrograph image of sample Z017b. Yellow arrows indicate the mineral concretions and the dashed line the location of the deformation band.

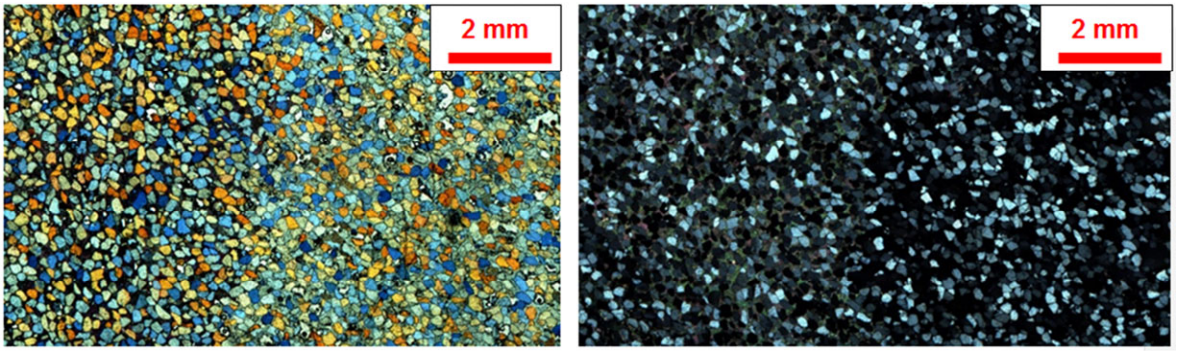

Figure 3-35 - Detailed pictures of sample Z017b. Left part of the micrographs shows the deformation band and the right part is the host rock. The picture on the left is taken with lambda filter and no polarization; picture on the right is taken without gamma filter with cross polarized light.

BIB-SEM

The overview image of the BIB-SEM sample can be seen on the Figure 2-39. The cross section was taken from the middle of the deformation band. The loose arrangement of the grains can be seen nicely on the overview image and that the intergrain space is almost entirely filled. Some fractures, cracks can be seen in grains and also in the pore filling calcite volume. The cracks of the grains outside of the BIB cross section likely occurred during the sample preparation. There are only very few intergrain cracks. The orientation and the distribution of the cracks seem to be random and the cracks do not propagate from the touching point of the grains in general. The fine structure of the sample, for example the pore throats, can be studied by BIB-SEM images. Figure 3-37 and Figure 3-38 show two examples for interaction of pore throat and pore filling material. Where the intergrain gap is lower than about 1 μm, the space is not filled by calcite. Furthermore, Figure 3-37 shows that the neighbouring grains have very similar boundary lines, so probably they had touched each other earlier; the gap opened latter and pore space got filled by calcite and finally, they both cracked slightly.

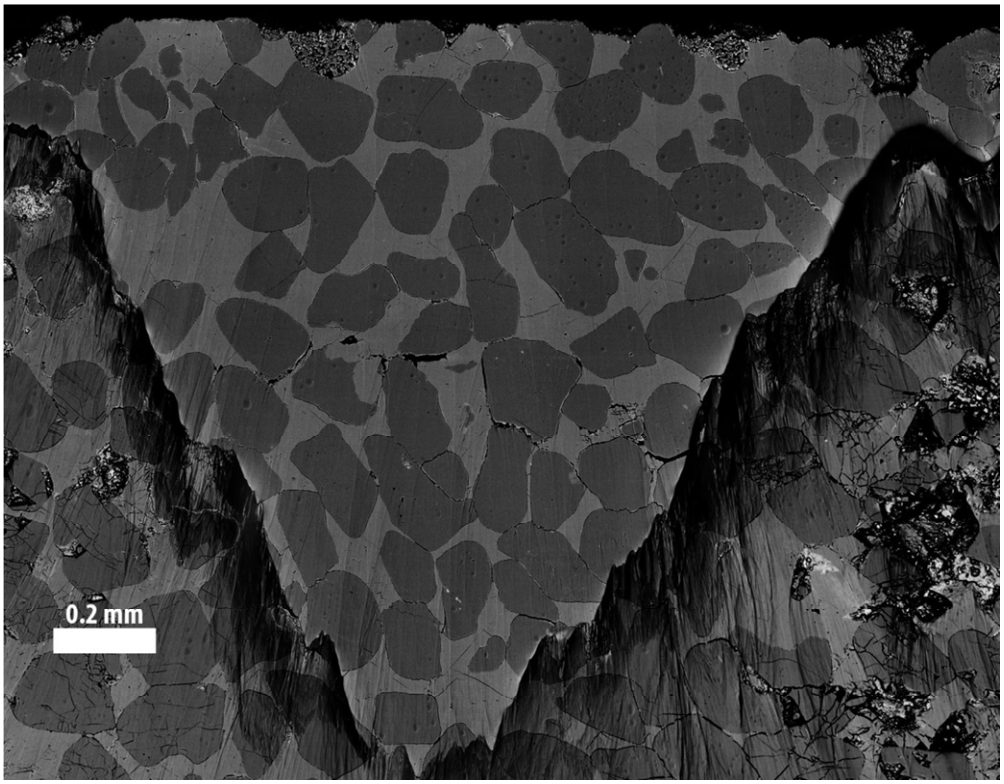

Figure 3-36 - SEM overview images of sample Z017b.

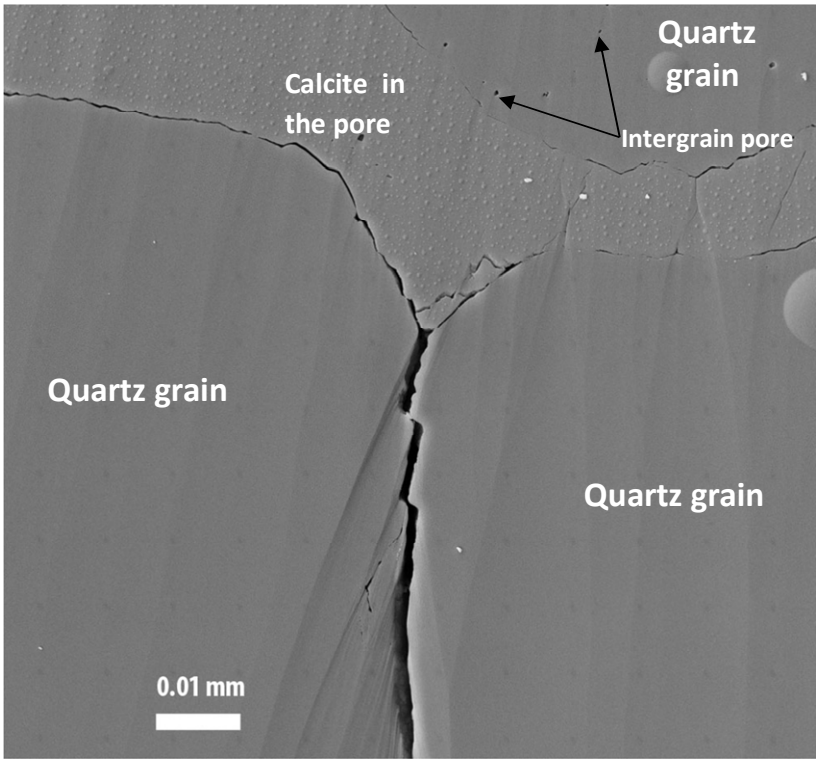

Figure 3-37 – High resolution BIB-SEM images of sample Z017 showing a few µm wide parallel gap between the grains (indicating a probably natural dislocation) pore throat and pore filling.

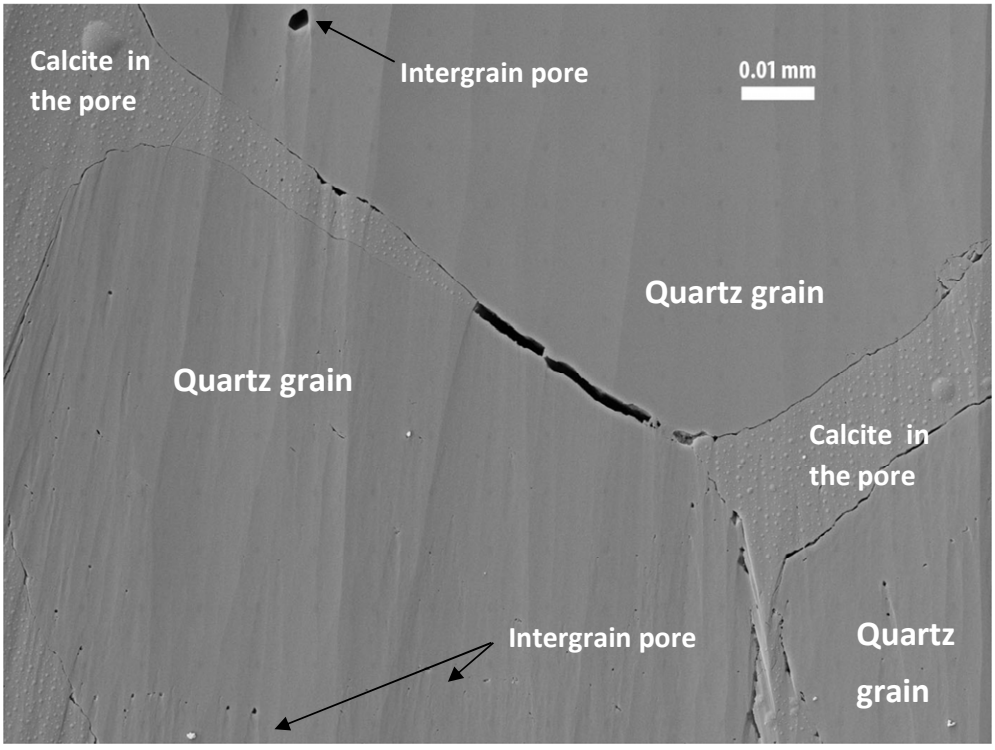

Figure 3-38 - High resolution BIB-SEM images of sample Z017 showing pore throat and a few µm wide parallel gap between the grains which pore filling material is only partly filled up.

Z045 / ZK280410-3

This sample contains a unique type of fractures because of their visual appearance. Their colour is dark reddish brown and their thickness is about 2-3 mm which slightly varying. Only some bands were found from this type of fracture and only on the middle part of the footwall wall of the fault around the south end of the line KB-1.

Rock type: Moab Member of Curtis Formation
Structure in the sample: Dislocation bands with iron precipitation
Grain size: out of structure: ~ 65-210 µm; in the structure: ~ 60-180 µm
Pore type: intergrain
Pore size: out of structure: ~ 0.5-2.5 µm; in the structure: ~ 1-3 µm
Pore throat size: out of structure: ~ 0.2-1.5 µm; in the structure: ~ 0.2-1.3 µm
Pore distribution: homogeneous
Pore orientation: random
Cementation:

Quartz: habitus: overgrowth, growth direction: along grain surfaces

Kaolinite: habitus: euhedral, growth direction: platy, face-to-face, perpendicular and tangential to detrital grains

Iron: habitus: euhedral, growth direction: along grain surfaces

General observation based on BIB-SEM images:

- Inside the deformation structure, quartz grains are covered with kaolinite and hematite.
- Zooming into the pore space, platy kaolinite and relatively large amount of iron can be seen.
- Thin layer kaolinite and less amount of iron cover the quartz grains approaching the boundary of the structure.
- Platy kaolinite covers the quartz grains, and there is no measurable amount of iron here.
- Only few minerals can be seen on the surface of the quartz grains, the pore space is almost empty.
- The contrast can be seen between the original rock matrix and iron rich structure.

Figure 3-39 - Origin of sample Z045 and Z046 from the footwall of Klondike Bluffs fault.

Thin section

The Figure 3-40 shows the photomicrograph of sample Z045. The deformation structure can be distinguished from the host rock. In the band, the pore space is filed with opaque minerals. Small amount of difference can be observed in grain- and pore size between the host rock and the band. However, this small amount of porosity increase was enough to support the fluid flow (making a fluid pathway) and as a result of the fluid flow likely iron precipitation occurred inside the band. Based on the thin section, this fracture is a dislocation deformation band in which the pore space is partially filled with hematite.

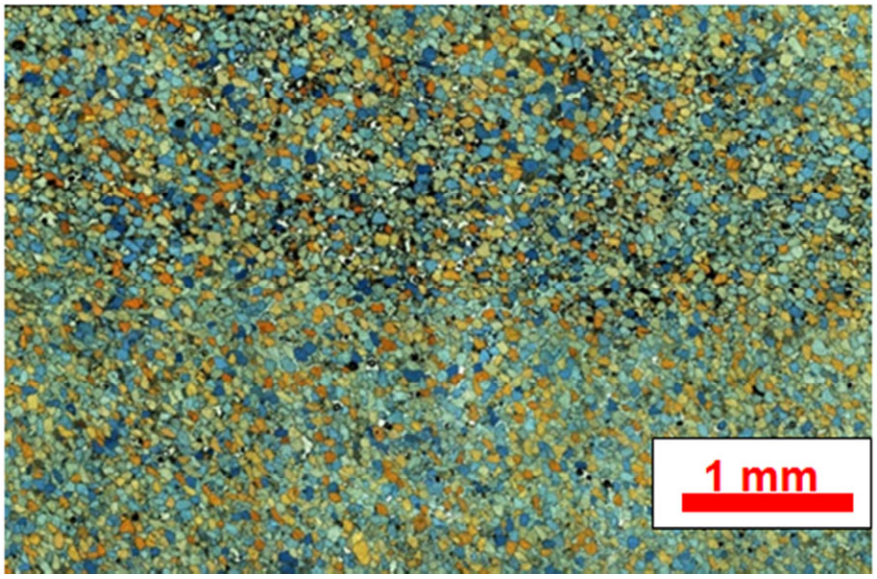

Figure 3-40 - Micrograph of sample Z045a. Top half is the deformation band, bottom half is the host rock.

SEM

Because the sample was very weak, the BIB polishing did not work out; therefore, only ordinary SEM images were taken. The SEM overview image of sample Z045 can be seen on Figure 3-41. The right side of the image shows the bright host rock and on the left side the deformation structure. On this image, it is also visible that the porosity is higher in the structure than outside of it. Furthermore, the grains seem to be clean and the pores seem to be empty in the host rock which can be seen also at the higher magnification SEM image of Figure 3-42. Figure 3-43 shows a small part of the deformation band where nicely can be seen that the pores space is partially filled with minerals. EDX measurement showed that the pore filling minerals are kaolinite (flat platy minerals) and iron.

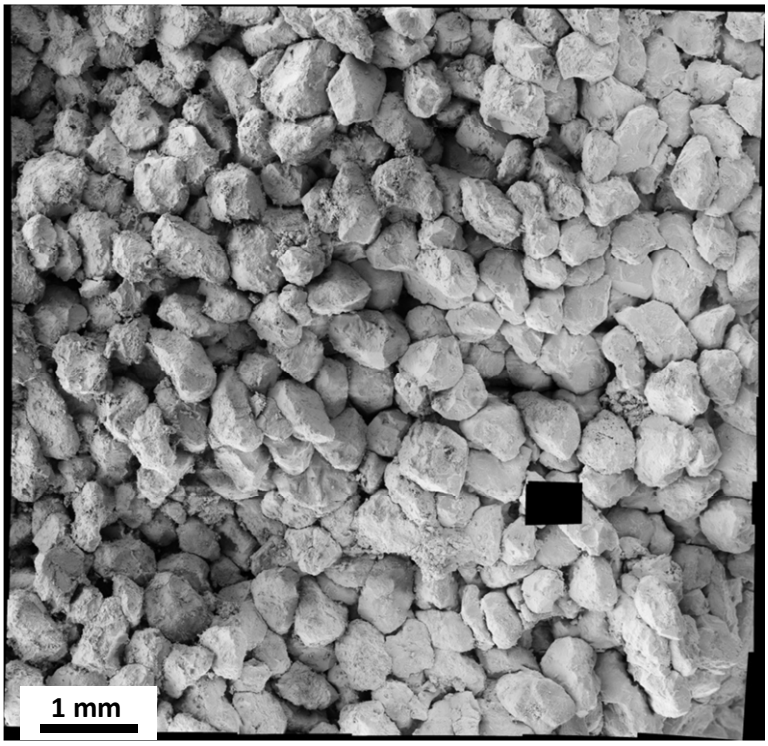

Figure 3-41 - Photomicrograph of sample Z045a where top-left half of the sample is the deformation band and bottom-right half is the host rock. (The black rectangular in the image is a missing photo mosaic.)

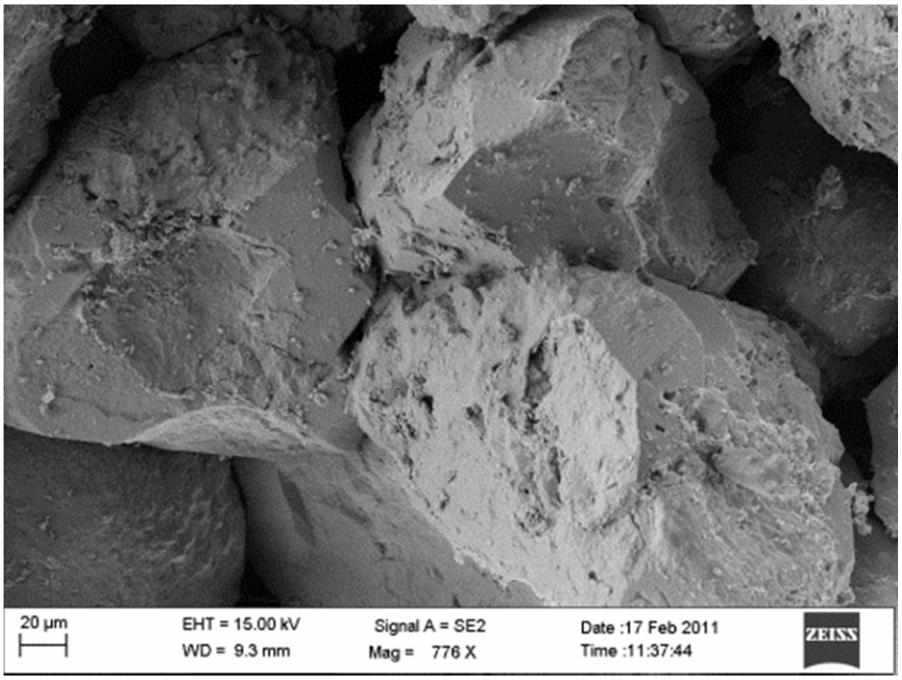

Figure 3-42 - Higher magnification photomicrograph of a part of the host rock of the sample Z045a.

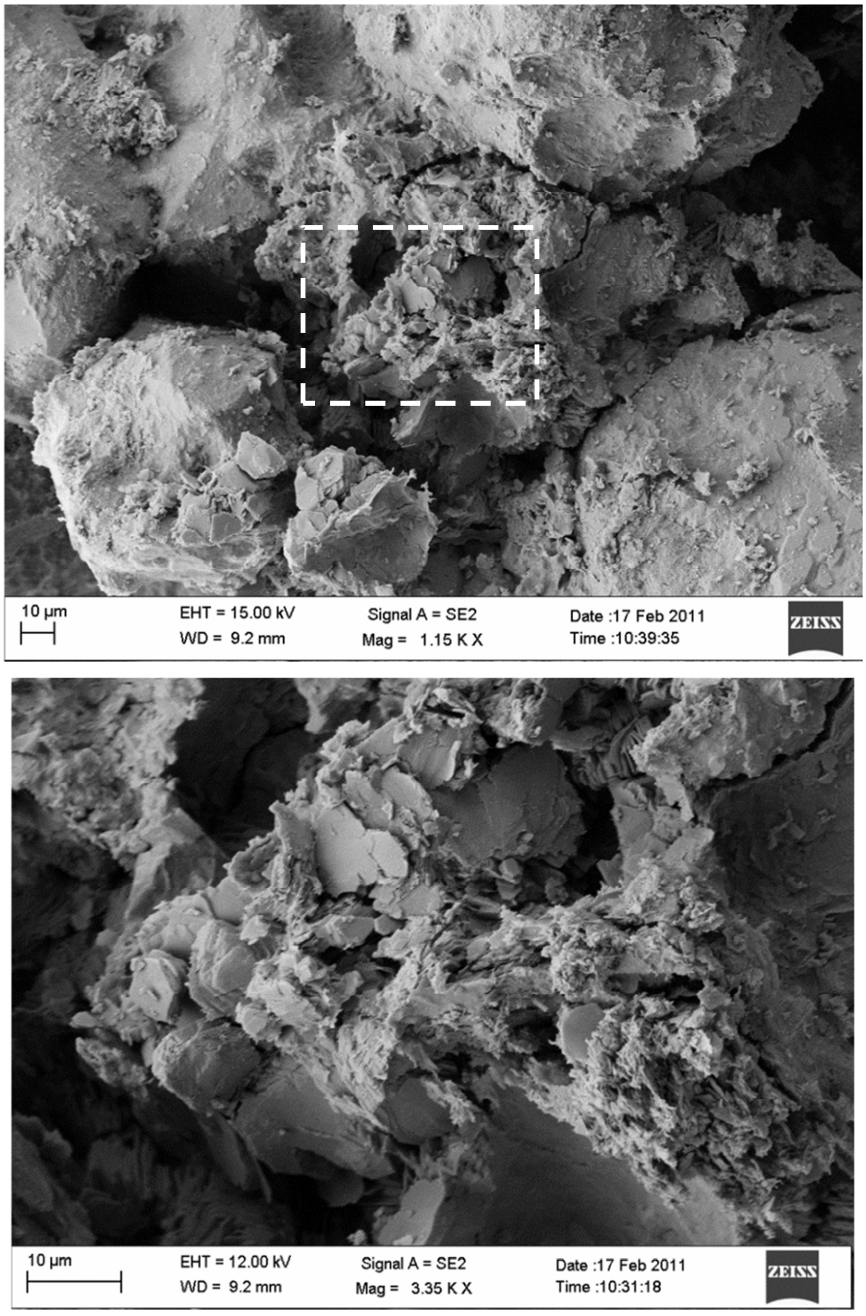

Figure 3-43 – Higher magnification photomicrograph of a part of the deformation band of the sample Z045a. The white box in the image on the top indicates the location of the image of the bottom.

3.5 Natural fractures in North Sea sandstone samples

Five core samples were studied in this work from well L5-9 of the North Sea which contain fractures. Two samples contain cataclastic deformation bands and three samples contain veins. The samples originated from about 4629-4667 metres depth (TVD) from the Permian Upper Rotliegend Group Slochteren Formation α-unit. The orientations of the cored sections were nearly vertical; black arrows on the samples show the top of the samples on the photos. The dip of the cataclastic bands were nearly vertical (80-90°), and the open fractures, and veins had the dip of 10-70 degree.

3.5.1 Sample: L5-9-1

Depth: True Vertical Depth: 4629.27 m

Rock type: Upper Rotliegend Group Slochteren Formation α-unit

Grain size: out of structure: ~ 25-230 µm; in the structure: -

Structure in the sample: vein

Dip of the structures: ~ 45 °

Pore type: intergrain

Pore size: out of structure: ~ 0.5-26 µm; in the structure: -

Pore throat size: out of structure: ~ 1-20 µm; in the structure: -

Pore distribution: inhomogeneous

Pore orientation: random

Cementation, pore filling:

Quartz: habitus: overgrowth, growth direction: along grain surfaces;

Ankerite: habitus: homogeneously fills the pores, growth direction: pore filling;

Illite: habitus fibrous, growth direction: perpendicular and tangential to grain surfaces;

Kaolinite: habitus: euhedral, growth direction: pore filling.

General observation based on BIB-SEM images:

- Ankerite filled vein contains quite complex fracture system with different orientations and different types.
- 2-3 mm thick fracture (micro joint) inside the vein material.
- Close to the vein-matrix boundary, iron poor ankerite spot.
- Illite and kaolinite fill the pores between the quartz grains.
- Rutile and anatase pore filling material on the vein-matrix boundary.
- Quartz overgrowth with sharp edges and randomly growing illite crystals on quartz grains (in the rock matrix). Kaolinite grains in the pores.

Thin section

The studied fracture can be seen on the right part of the core sample on Figure 3-44. The fracture is approximately 6 cm long in the sample. The thickness of the fracture varies relatively much (between 0.5-5 mm) and it splits into two bands in the middle of the sample. The brown colour structure is a vein which can be seen on the photomicrograph of the sample on Figure 3-45. Based on the results of EDX measurement, the vein filling material is basically ankerite and siderite. The thin section shows a nice example about the tapering and the interruption of the structure. The fracture is filled in its very thin part, and there is a grain fragment in the fracture which can be seen in the lower part of the fracture on the left image of Figure 3-45. Crystals of the pore filling mineral can be seen on Figure 3-46. Almost all the crystals are cracked but no displacement is visible; therefore, after the pore filling there was some increase in the stress.

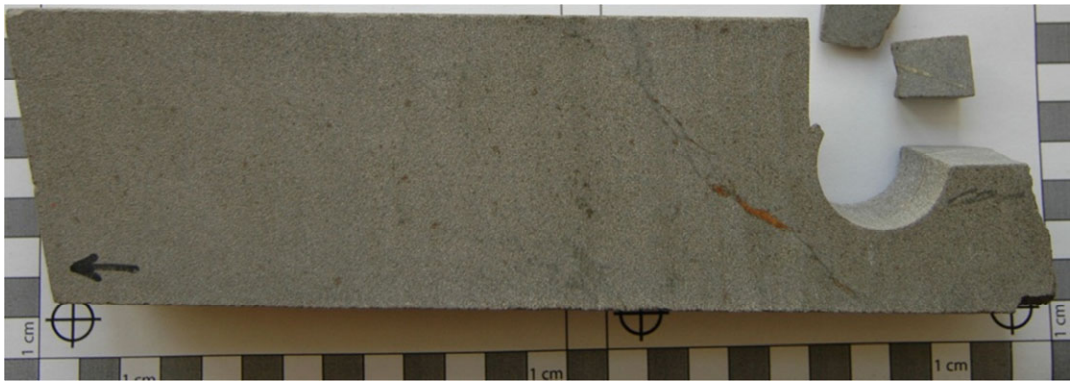

Figure 3-44 - Half core sample of sample number L5-9-1.

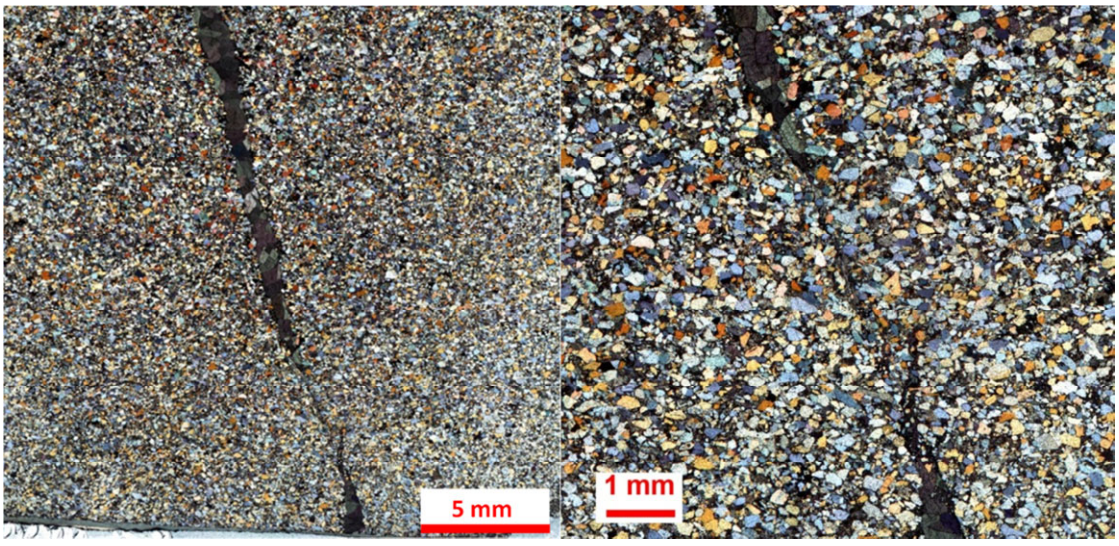

Figure 3-45 - Overview images of thin section; sample L5-9-1a (left). Break in the continuity of vein; sample L5-9-1a (right).

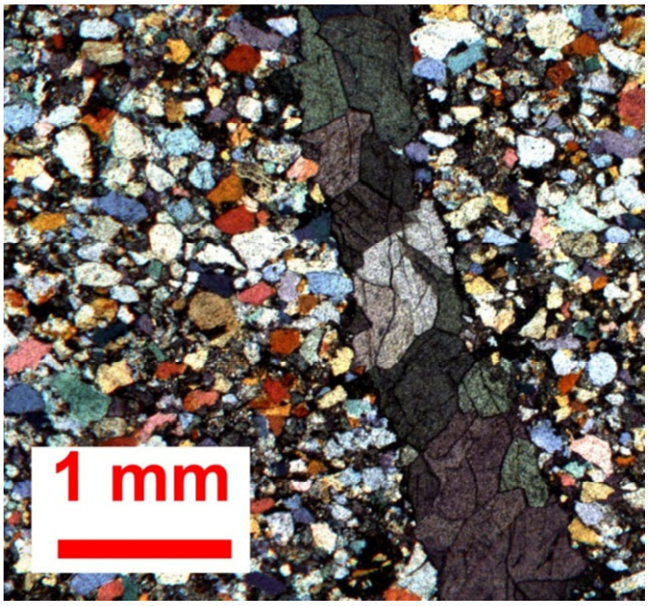

Figure 3-46 - Cracks inside the vein; sample L5-9-1a.

BIB-SEM

The BIB-SEM overview image of the sample L5-9-1a can be seen on Figure 3-47. On the left side, there is the vein (light grey) and on the top right, there are the quartz grains of the sandstone. The finer and tinier fractures and the fractures network of veins can be seen. And also inside the vein, small size (3-15 µm) pores can be observed. Close to the boundary of the vein in the host rock, material of the vein can be found in the larger (10-30 µm) pores. There is no sharp boundary between the vein and host rock. However, smaller pore spaces (less than 2-3 µm) do not contains vein material. Intergrain space (outside of the vein) is filled basically with clay minerals, such as illite and kaolinite which do not allow the ankerite to penetrate into the pores (Figure 3-48 and Figure 3-49). Based on this, presumably illite and kaolinite formed before ankerite.

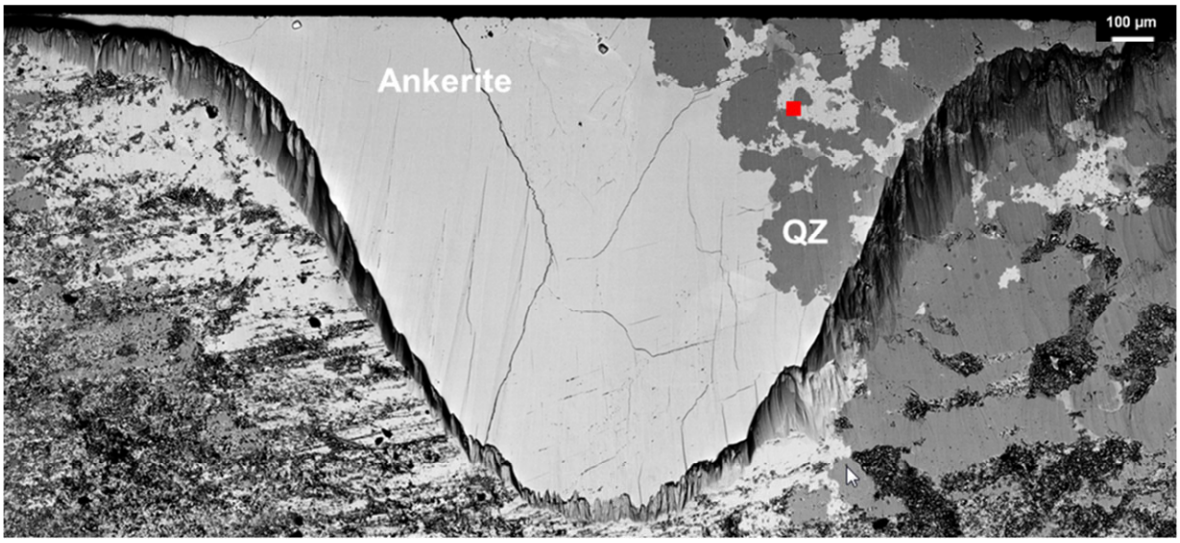

Figure 3-47 – SEM overview image of sample L5-9-1. The red dot indicates the location of image of Figure 3-48.

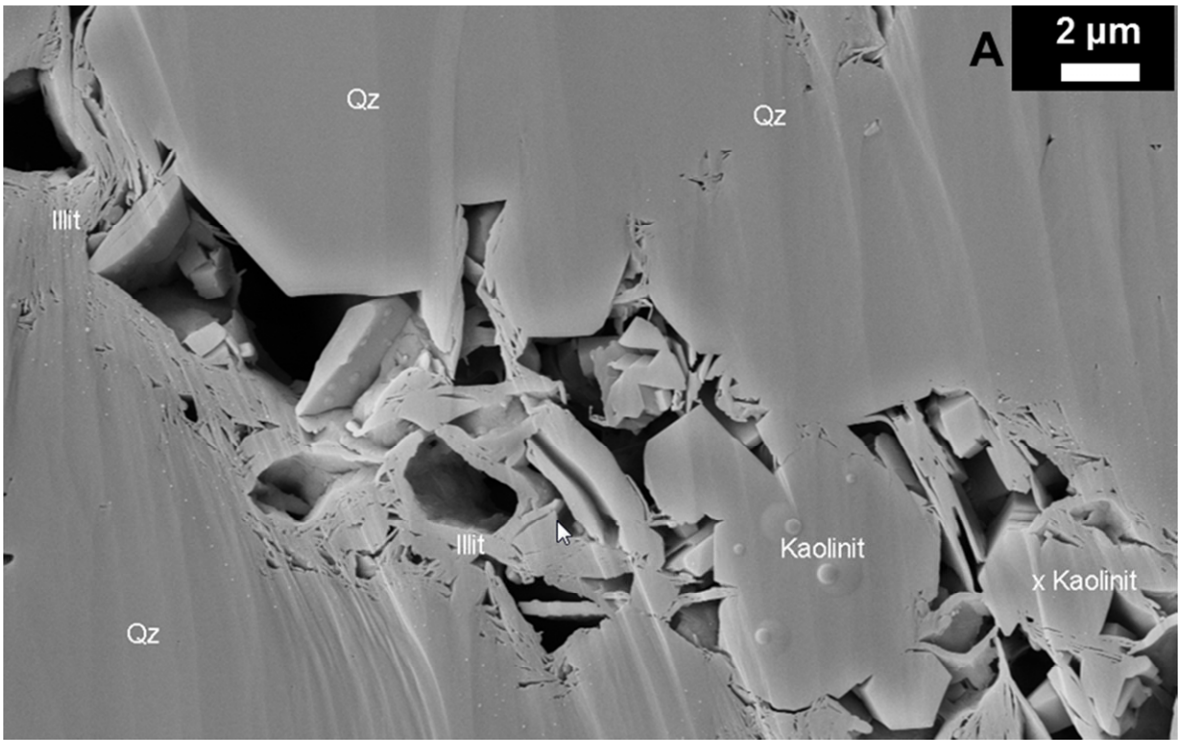

Figure 3-48 – Pore space close to the vein boundary in sample L5-9-1 where Qz is stand for quartz.

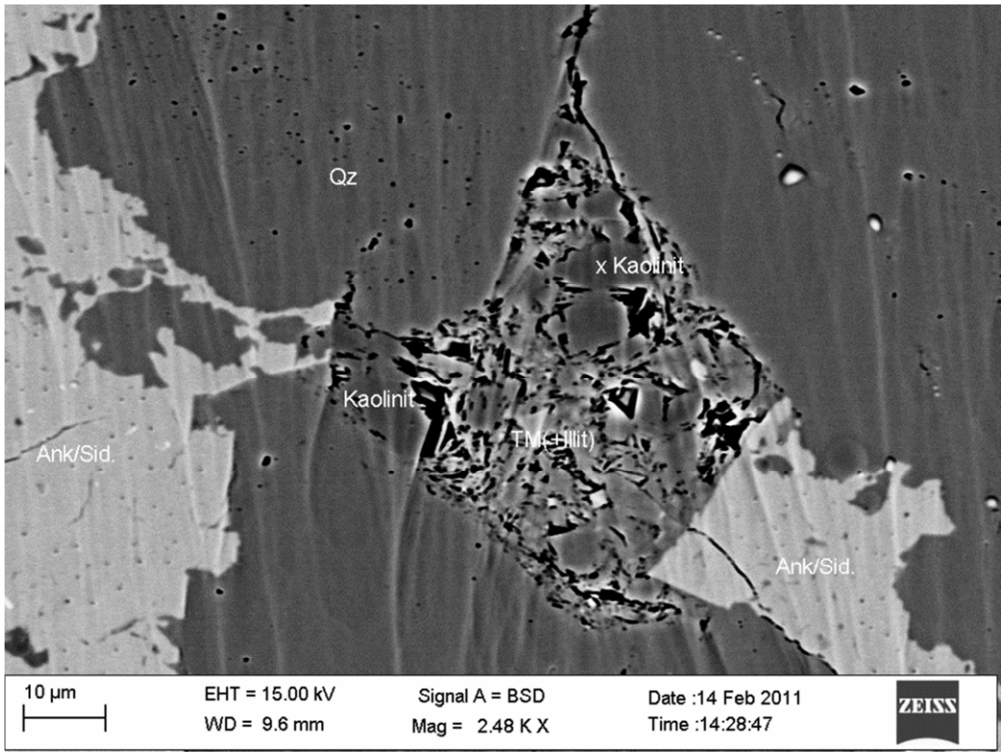

Figure 3-49 – Pore space close to the vein boundary in sample L5-9-1 where Qz: quartz, Ank/Sid: ankerite and siderite.

3.5.2 Sample: L5-9-3

Depth: Measured depth: 4691.5 m; True Vertical Depth: 4644.6 m

Rock type: Upper Rotliegend Group Slochteren Formation α-unit

Grain size: out of structure: ~ 25-250 µm; in the structure: ~ 15- 200 µm

Structure in the sample: Cataclastic deformation band

Dip of the structures: ~ 80-90 °

Pore type: intergrain, intragrain porosity in dolomite;

Pore size: out of structure: ~ 20-120 µm; in the structure: ~ 4-30 µm

Pore throat size: out of structure: ~ 5-20; in the structure: ~ 0.1-5 µm

Pore distribution: inhomogeneous

Pore orientation: random

Cementation, pore filling:

Quartz: habitus: overgrowth, growth direction: along grain surfaces

Dolomite: habitus: homogeneously fills the pores, growth direction: pore filling

Illite: habitus: fibrous, growth direction: perpendicular and tangential to grain surfaces

Kaolinite: habitus: euhedral, growth direction: pore filling

General observation based on BIB-SEM images:

- The pore space, between the quartz grains, is filled with dolomite and ankerite entirely. There are some mm-size pores in pore filling material, and mm size gaps on the grain-pore boundary.
- The general grain size is about 100 µm in the matrix, and the general pore size is 20-40 µm which is filled with randomly oriented kaolinite grains, ankerite and a small amount of gypsum.
- Illite lining on the quartz grains, and fibrous illite in the pore space.
- Original matrix on the left and deformation structure on the right, where grain and pore size reduction can be seen.
- Inside the deformation area, the pore space size, between the quartz grains, is about 5-10 µm. Randomly oriented illite can be found which reduces the pore space.
- Kaolinite grains and illite reduced the pore space.

Thin section

A bunch of deformation structures can be seen in this core sample piece which is plotted on Figure 3-50. These bands are relatively light; it is hard to distinguish the host rock from the structures even in thin sections. Photomicrograph of this structure can be seen on Figure 3-51. The fracture goes from the top-left to bottom-right. The higher magnification image of a part of the structure can be seen on Figure 3-52 which shows the structure on the bottom half of the image. Small degree of grain size reduction can be seen in the structure.

Figure 3-50 - Core piece of sample L5-9-3.

Figure 3-51 - Thin section overview image of sample L5-9-3.

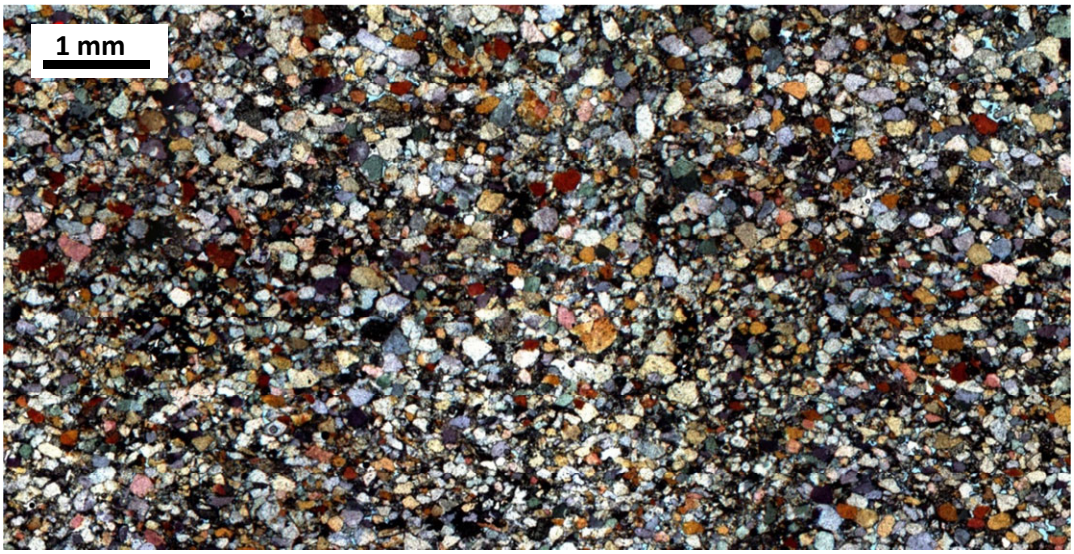

Figure 3-52 – Thin section image of structure of the sample L5-9-3. Structure is on the lower half of the image.

BIB-SEM

On the overview image of this sample a short section of the deformation structure can be seen nicely (Figure 3-53); however, the structure stops at the lower part of the cross section. Inside the structure, grain size reduction is observed. The higher resolution BIB-SEM image shows the inside of the structure (Figure 3-55). Locally, significant grain size reduction can be found in the deformation structure; and therefore, porosity is reduced. The Figure 3-54 shows the schematic drawing of the mechanism of the formation of the cataclastic deformation band (Fossen et al. 2007). Further higher magnification images of the host rock part of the sample show that kaolinite, ankerite, dolomite, illite, gypsum and halite can be found in the pore space (Figure 3-56, Figure 3-57 and Figure 3-58).

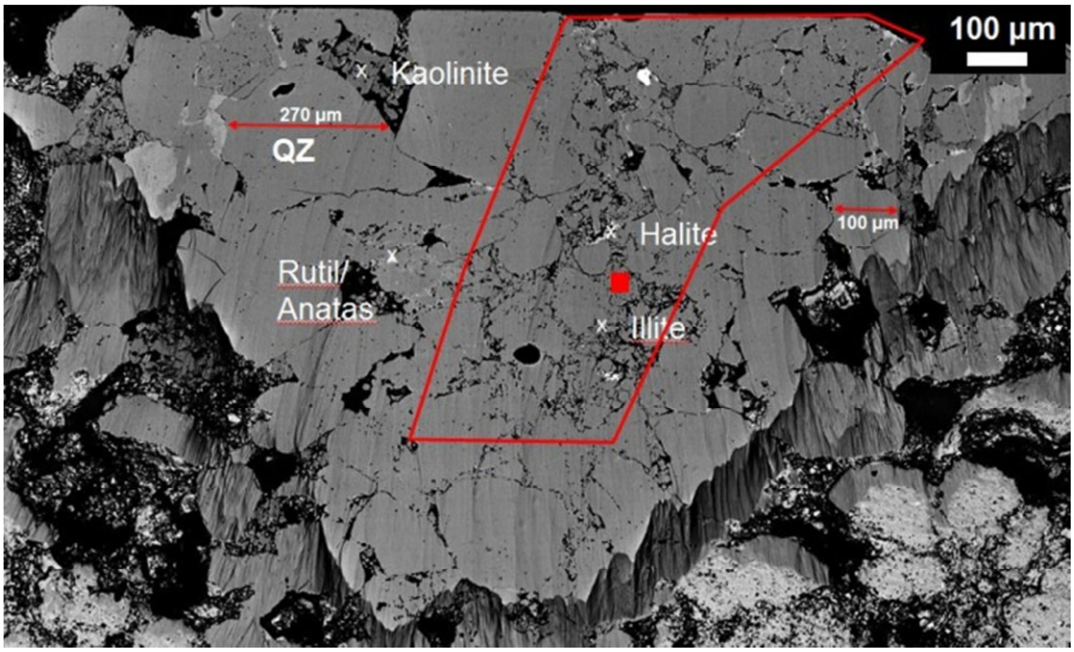

Figure 3-53 – BIB-SEM overview images of samples L5-9-3.

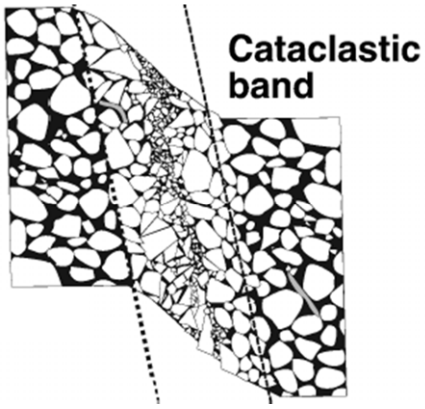

Figure 3-54 – Cataclastic types of deformation bands, based on deformation mechanism (modified after Fossen, 2010).

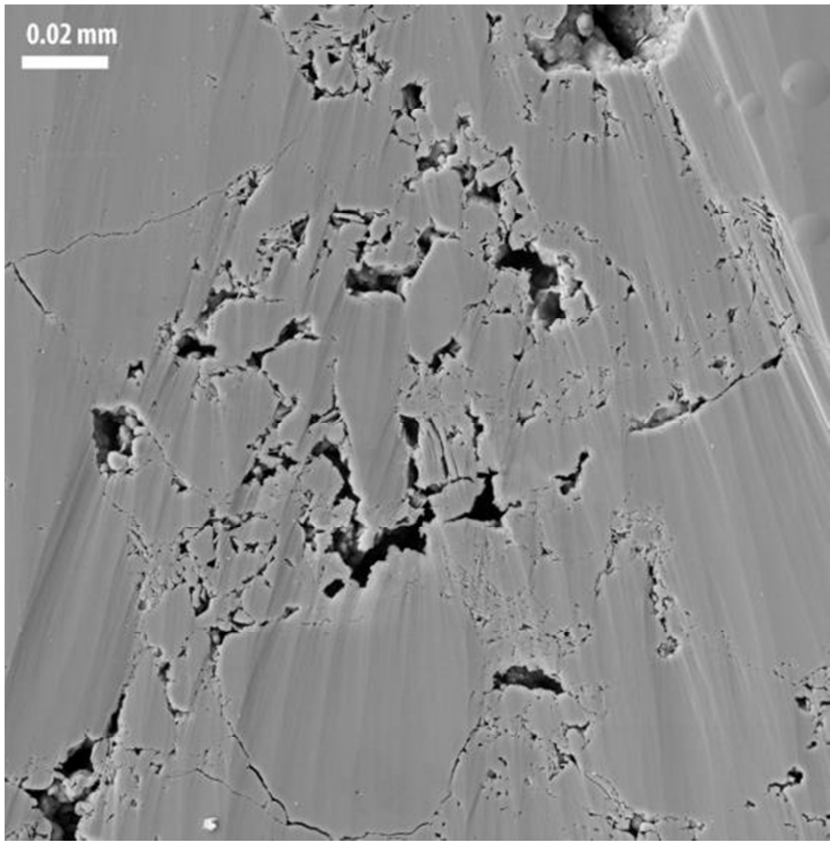

Figure 3-55 - Higher resolution images of sample L5-9-3; inside of the structure. Location of the spot is indicated by red dot on Figure 3-53.

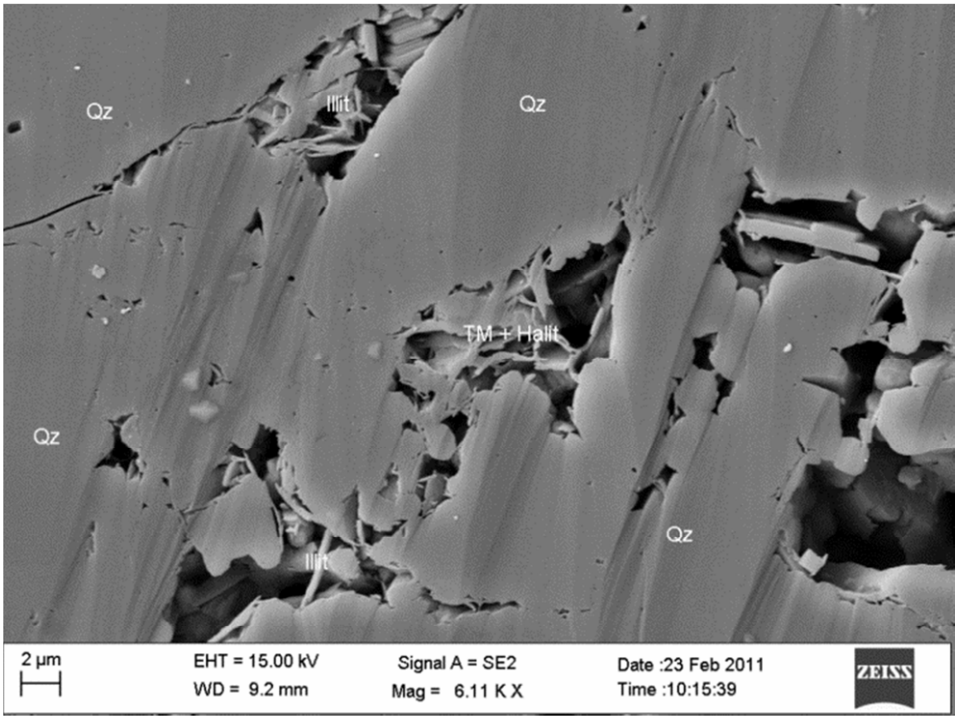

Figure 3-56 - Higher resolution images of sample L5-9-3. Outside of the structure, illite and Halite can be found in the pore space where Qz: quartz, TM: trace minerals.

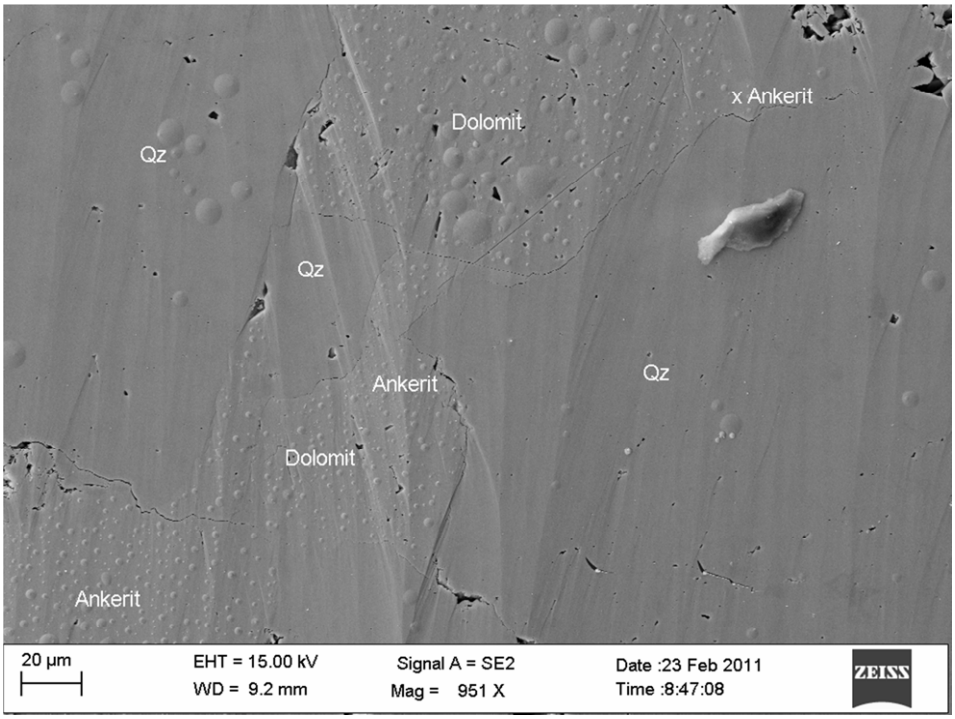

Figure 3-57 - Higher resolution images of sample L5-9-3. Outside of the structure, Dolomite and Ankerite fill the pore space where Qz: quartz.

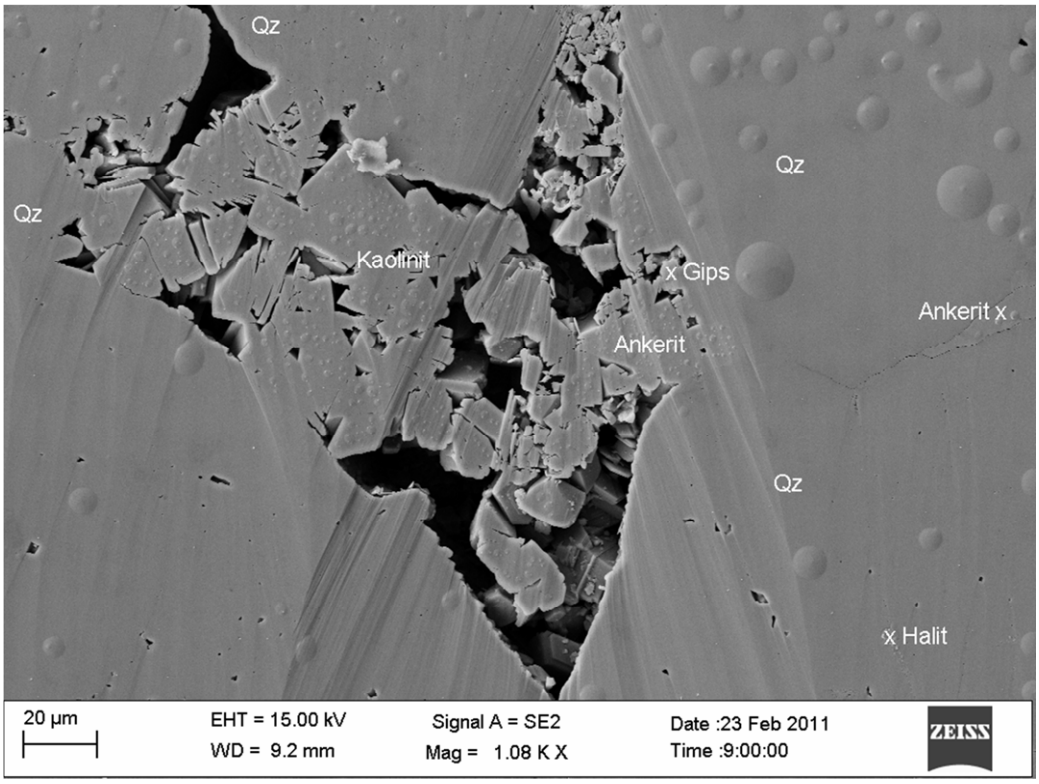

Figure 3-58 - Higher resolution images of sample L5-9-3. Outside of the structure, Kaolinite and gypsum can be found in the pore space where Qz: quartz.

3.5.3 Sample: L5-9-4

Depth: Measured depth: 4703.9 m; True Vertical Depth: 4657.0 m
Rock type: Upper Rotliegend Group Slochteren Formation α-unit
Grain size: out of structure: ~ 5-450 µm; in the structure: ~ 5-220 µm
Structure in the sample: Deformation bands, veins, open fractures
Dip of the structures: main fracture: ~ 70 °; smaller, branch fracture: ~ 10-60 °
Pore type: intergrain, intragrain porosity in dolomite;
Pore size: out of structure: N/A; in the structure: N/A
Pore throat size: out of structure: N/A; in the structure: N/A
Pore distribution: inhomogeneous
Pore orientation: random
Cementation, pore filling: N/A

Thin section

A quite complex fracture network can be seen in the half core samples on the figure above, with different types of fractures with varying thickness (Figure 3-59). The thin section was cut from the centre of the fracture network; therefore, it contains more fractures such as open cracks and also deformation bands. On the left side of the core sample, open fractures are partially filled with clay minerals. In the thin section (Figure 3-60), two cataclastic deformation bands can be found (above the open fracture) where grains sizes reduction can be seen. Besides, significant grain size reduction can be seen next to the open fracture as well. This sample represents a nice example where cataclastic bands which result of compaction and open fractures which result of dilatancy are mixed and very close to each other. Presumable, the compaction had occurred earlier than open fractures generated. Some of the open fractures might have formed during the unloading of the core sample as it was from well; however, it is sure that open fractures were present in the depth; because, some of the open fractures are filled with minerals.

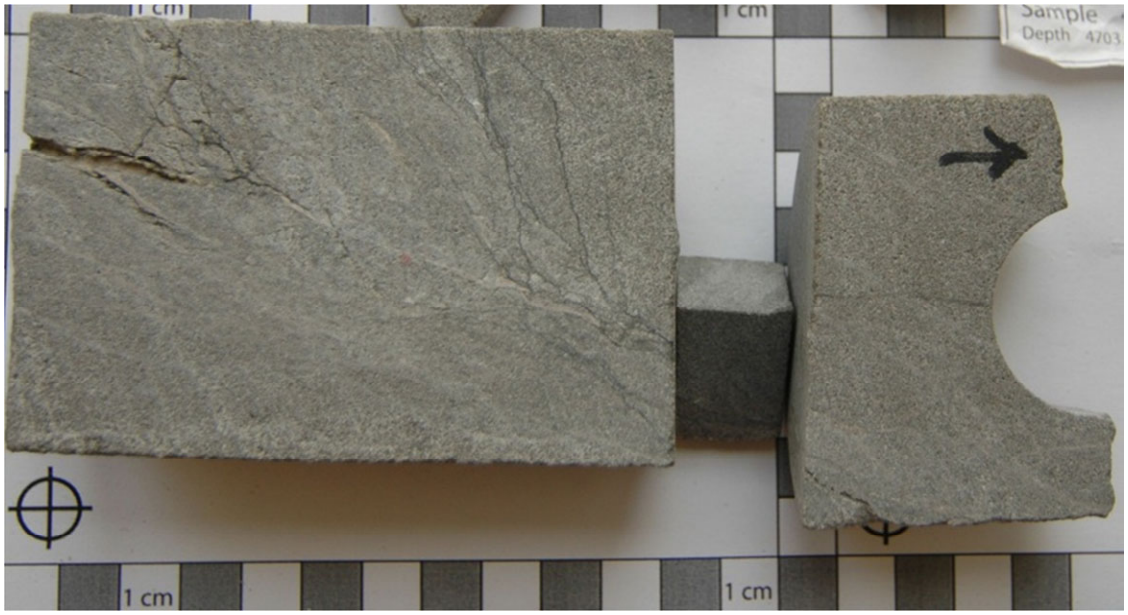

Figure 3-59 – Photo of the half core sample where sample L5-9-4 was taken.

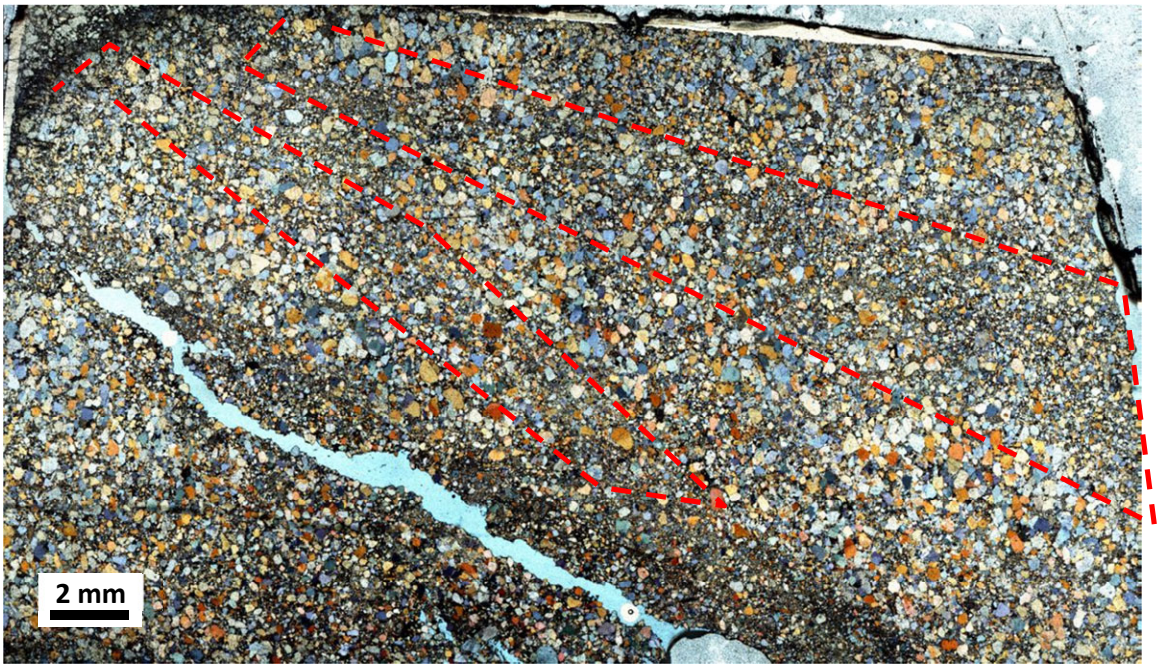

Figure 3-60 - Overview image of thin section of sample L5-9-4 is shown where dashed, red polygons indicate the deformation structure.

3.6 Discussion

In this work, the most characteristic fractures of sandstones were studied in samples of two different filed analogues in Utah and core samples of one well of the North Sea. The characteristics of the fractures of the two analogue field areas seemed to be significantly different. All the samples which were collected around the faults of Klondike Bluffs area were the same type. Ten samples were collected on the Klondike Bluffs area; they all were dilatant fractures, disaggregation bands. In addition, all of these fractures have different degree of fluid generated pore filling. In general, calcite almost fully filled the pore space in the fractures and iron filled the pore in the fractures in only a small degree. It is important to notice that there were no fractures analysed from very close to the main fault where the fracture density was high. However, there were sample analysed from close to a smaller fault branch. The properties of deformation band did not show symmetry around the main fault. In the hanging wall, the calcite filled disaggregation bands are the most common deformation structures which can be observed even 500 metres from the main fault. On the footwall of the fault, the iron filled deformation bands were found. In the Courthouse Junction area, majority of the fractures were cataclastic deformation bands in the main fault core and further from the fault as well. In addition, a few open fractures were found in the core of the main fault segment in which pore space was filled with more or less with calcite or copper likely malachite.

The North Sea samples originated from about 4629-4675 metres deep (TVD). In this relatively short vertical section, different types of fractures were found to be both dilatant and cataclastic. Veins were found with different degree of pore filling. In addition, cataclastic bands were found as well. There were dilatant and cataclastic fractures relatively close to each other in this core. In the Courthouse Junction area, there were dilatant and cataclastic fractures close to each other in or close to the fault core. In conclusion, the core samples presumably were located close to a fault core which is likely more cataclastic type of fault. Dip of the fractures varied from 10-90° where open fractures; however, dip of the cataclastic bands and dip of open type of fractures showed differences. Cataclastic bands are steeply dipping nearly vertically and open fractures have lower angle.

According to Aydin (1978), the deformation bands in the Entrada and Navajo Sandstones are formed by a combination of various different processes, including shear and volume change microfracturing of grains into smaller grains, shattering of smaller grains, and mixing of the fragments of grains with the matrix. On the one hand, the result of this study is in agreement with Aydin's statement. On the other hand, in case of the cataclastic bands, there is more shear which is the dominant type of deformation; whereas, in case of the disaggregation bands, there is less shear, and the main deformation style is slight dilatancy.

Based on the results of Antonellini et al. (1994), the studied structures in the Klondike Bluffs area belong to the older generation of deformation bands which formed during the growth of the salt anticline because they are characterised by minor or no cataclasis.

According to Fossen and Bale (2007), deformation bands present only local barrier to fluid flow, as the thickness of deformation bands changes rapidly. Similarly, the thickness of the analysed deformation bands varies in relatively wide range and thickness can change rapidly in cataclastic deformation bands (e.g. this can be seen on images of thin sections of sample Z062 and Z032) and in dilatant fractures as well, for example sample L5-9-1 a vein in Rotliegend sandstone which thinned and interrupted. However, the thickness change of disaggregation band was not observed in thin section. Besides, the veins have blocky fill (e.g. sample L5-9-1), which indicates that the rocks already had some strength when they were fractured and stayed open during fracture filling (Hilgers et al. 2001, Nollet et al. 2005).

In this study, high degree of cataclasis and in general relatively sharp gain edges can be found in the samples of Courthouse Junction which refer to the relatively large shear displacement and high stress state. However, in some cases, diffuse fracture edges can be seen in cataclastic bands close to each other in sample from the same location. In some of the cases, one of the edges of the same cataclastic band is very sharp whereas the other edge is diffuse. In general, the edge of the disaggregation bands is relatively sharp which is well visible by the mineral precipitation. However, locally some edges became more diffuse. In general, observation of this work is in agreement with results of Torabi et al. (2007), who related the type of the boundary zone to the burial depth: in case of shallow depth, the boundary of the shear zone is diffuse; whereas, in case of higher burial depth, the boundary of the shear zone is sharp.

The cementation of the studied samples is basically the same as what was described by Eichhubl et al. (2009). The Moab fault is locally characterized with extensive calcite and lesser quartz cement. The calcite cementation occurs as spherical calcite concretions and calcite veins and associated cement halos and mainly relates to fractures. Also, malachite is observed as fault related cement.

The North Sea samples of this study showed that different types of fractures such as dilatant and compaction fractures can be found in sandstone reservoirs of the North Sea. This observation is similar to the observations of Hesthammer et al. (2000). However, cataclastic band was found in low clay content sandstone (clay content by image analysis) in this study (sample L5-9-3). In this sample, the clay content is about 6.5%, the porosity in the host rock is 14% and the porosity in the fracture is about 8% (by image analysis). This result shows deviation from general observation of Hesthammer et al. (2000) who found that cataclastic bands usually occur if the clay content is higher than 20-25%.

Based on the result of the microstructure analyses of this study and other earlier results as well, the Rotliegend sandstone shows basically similar characteristics to the sandstones of the Moab area. Besides, geological characteristics of the Moab area: geological settings, tectonics events, extensive fault and fracture system, salt tectonics, show similarity to the North Sea area. Therefore, the Moab area is an appropriate analogue outcrop to better understand reservoirs of North Sea and its structures.

Basically, two different types of structures characterize these reservoir sandstones. There are dilatant, i.e. open fractures such as veins, disaggregation bands, in which the pore space larger and in conclusion the permeability as well. They help the fluid migration;

however, as a result of the fluid flow in majority of these fractures, the pore space will be filled with minerals in high degree sooner or later. And after that the open fractures will become seal. The other type of fractures is the cataclastic band where the pore and grain sizes is significantly different, sometimes by more than some order of magnitude, which have large effect on permeability. However, the thickness of these fractures varies significantly along the fracture; therefore, the sealing affectivities of these are changing very to a great extent.

3.7 Conclusion and outlook

The range of variety of the available samples covers the main type of the fractures that are common in sandstones; such as, veins, deformation bands and cracks. The amount of the available samples is relatively high from the Utah field analogue. Based on these samples, faults can be characterized relatively well, because the 2D horizontal surface around the fault was visible. However, one bore hole can provide insight in to only 1D section of North Sea sandstone reservoirs vertically.

Samples were collected from both side of the studied main fault of Klondike Bluffs area within 400 metre zone of the hanging wall and within 200 metre zone of the foot wall. Samples showed that this area is characterised by dilatant fractures consequently the minimum effective stress was relatively low at faulting. Difference can be seen between the hanging- and the foot wall of the fault in pore filling of the fractures which is resulted by fluid flow. The pore space in the fractures was filled with calcite almost totally on the hanging wall, and on the foot wall, fractures were filled only partially with hematite. This shows that different fluid flow characterised the two parts of the fault; more extensively on the hanging wall and less extensively on the foot wall. As a result of the fluid flow, mineral precipitation almost totally filled the pore space inside the fractures; therefore, the foot wall became seal for fluid flow. The fractures on the hanging wall are still filled only partially; in conclusion, this part of the fault is still conduit for fluid flow.

At the Courthouse Junction, samples were collected only on the foot wall of the main fault. In the fault core, both open and cataclastic fractures are present. This shows that the variation of the minimum principal effective stress was high at faulting close to the fault core. Further from the fault, only cataclastic bands were found that shows that the minimum principal effective stress was relatively high. Fluid flow occurred only locally in the fault core resulting in mineral (mainly copper and calcite) precipitation in the open fractures. In conclusion, this fault segment is a barrier for fluid flow basically.

Five core samples were studied from one North Sea well from block L. Two of these samples contained open fractures, veins and two cataclastic deformation bands and one sample contained both vein and cataclastic band. Based on the dip of the structures, veins and deformation bands are different generations. These samples cover an approximately 45 metre long vertical section in well L5-9. This section is approximately half of the entire throw Courthouse Junction fault (fault throw is about 80-100 metres). The fracture type

characteristics of the North Sea samples shows similarity to fractures type characteristics of the fault zone of the Courthouse Junction fault. Both fault zones have dilatant and cataclastic fractures close to each other.

In comparison, the Moab sandstones are analogue to the sandstones of North Sea prospect area; the host rock of the areas is similar, porosities and also pore throat radii of these sandstones are similar. Furthermore, fractures in Moab samples and also those of the North Sea samples are characterised by diagenesis (mainly calcite) as results of fluid migration. In addition, the characteristics of the fractures of the field analogue area show also similarities to the North Sea fractures. Furthermore, the tectonic circumstances on both areas (North Sea and Moab area) are similar: extended fault network, involved in general normal faults, and also salt tectonic characterize both areas. In conclusion, the sandstones of Moab area; such as, Slick Rock Member of Entrada Sandstone and Moab Member of Curtis Formation, are a good analogue for North Sea reservoir sandstones (Permian, Rotliegend Sandstone Group).

The deformation features in the studied samples indicate that the properties of the structures; such as thickness, pore size, grain size, pore throat radius vary along the structures. Therefore, future works should aim to study longer sections of these structures in order to measure the range of the changes of the most important properties which have influence on the fluid flow.

Besides, the BIB-SEM images showed that the very precisely polished, even rock surfaces provide possibility to study 2D microstructures of fractures and pore space in images where structures can be traced, which allow us to calculate statistics to quantify the properties of the rocks. Furthermore, serial cross section of 2D surfaces allow to study 3D architecture of rocks where fluid paths can be measured and pore throats radius, porosity and permeability can be measured more precisely.

A comprehensive fault model is necessary to better understand fluid flow properties of complex fault networks. The results of microstructure analyses, including BIB-SEM image analyses, are able to provide important information and parameters for extended fault structures and its fluid flow model. This model also can improve the seismic interpretation.

4 Correlation analysis between mechanical properties and borehole log properties in North Sea sandstones

4.1 Introduction of correlation analysis of mechanical properties

4.1.1 General introduction

In study of the fractures and fracture mechanism, it is essential to understand under what condition fractures can form. Strength is one of the most important material properties. The strength measures under what stress conditions a given material will fail. Other important material property is the elasticity that measures the relation between deformation of a material and the acting stress. Rock strength and elastic modulus are important factors in engineering and rock mechanical investigations. Rock mechanical data are used to wellbore stability to determine proper mud weight, hydraulic fracturing, pore compressibility, sand production, subsidence- and compaction calculation, well completion section or well case planning. Besides, knowledge of the rock strength also provides opportunity to predict the tendency for fracturing and the possible type of the developing fractures under a given condition. Several methods exist in order to measure mechanical properties of rocks including in-situ and in laboratory too. However, these measurements are expensive, especially if rocks are in thousands of meters depth, as they are usual in a hydrocarbon reservoir and appropriate samples are relatively rarely available for measurements from these depths. Therefore, rock mechanical property prediction methods play important roles in field of reservoir geomechanics. Wireline geophysical logs, which measure physical properties of the rock body around the borehole, are almost always measured after and/or during borehole drilling. Therefore, wireline log data often can provide possibility to predict rock mechanical properties.

Brittle failure of rock is a complex process of fracture. The fracturing process is basically a combination of microscopic tensile cracks and frictional movement on grain boundaries (Brace, et al. 1966). As stress is closing the critical point, the numbers of micro-cracks is increasing and reach the critical stress condition, the rock fails along through-going shear plane (Lockner, et al. 1991). Griggs and Handin (1960) distinguished two modes of fracture such as shear fracture and extension fracture. Later, Ramsey and Chester (2004) inferred that also hybrid fractures can form as a combination of compression and tensile state. However, mode of fracturing depends on several different properties of the rock and also on external physical parameters.

In order to predict rock strength, it is necessary to understand which factors control rock strength. Rock strength depends on structural properties of the rocks that are strongly related to the mineral composition of the rock. According to the Mohr-Coulomb theory, rock internal properties are defined as cohesion (chemical and physical bonds between grains and crystals, cementation) and internal friction. Several studies showed that porosity decreases brittle failure strength of rocks (Brace and Riley 1972, Dunn, et al. 1973, Hoshino 1974, Scott 1989, Palchik 1999). In addition, relation between petrographic properties and mechanical properties of a rock was analysed in many aspects; such as, grain shape, grain

size, mode of connection between grains, cementation or mineral composition (Fahy and Guccione 1979, Winkler 1985, Singh 1988, Shakoor and Bonelli 1991, Haney and Shakoor 1994, Ulusay, et al. 1994, Schön 1996, Bell and Culshaw 1998, Tuğrul and Zarif 1999, Hale and Shakoor 2003, Jeng, et al. 2004, Meng and Pan 2007, Pomonis, et al. 2007, Hsieh, et al. 2008). Since in sandstones, clay very often presents and clay content can change significantly, the effect of clay on rock strength was analysed in several works (Jizba 1991, Samsuri, et al. 1999, Takahashi, et al. 2007, Li and Zhang 2011). The outcome of these studies is that increasing clay content decreases the strength of sandstone and dry clay can increase strength in comparison to wet clay (Swanson et al. 2002). In addition, the type of clay content has effect on the mechanical behaviour of rocks: illite or chlorite clay is stronger than smectite-rich clay which smears easier (Lockner and Beeler 2002). Furthermore, moisture content also has effect on rock strength; numerous researches observed that increasing saturation reduces the rock strength (Colback and Wiid 1900, Simpson and Fergus 1968, Broch 1974, Ballivy, et al. 1976, Michalopoulos 1976, Priest and Selvakumar 1982, Venkatappa Rao, et al. 1985, Dyke and Dobereiner 1991, Hawkins and McConnell 1992, Hale and Shakoor 2003, Shakoor and Barefield 2009). Anisotropy also has an effect: the rock strength in compression, parallel to the foliation plane, may be greater or less than normal (Paterson and Wong 2005). Textural anisotropy can also result in significant anisotropy of tensile and compressive strength that may be associated with different failure modes and deformation mechanisms, depending on how stress is applied relative to the anisotropy planes (Li and Zhang 2011).

In addition to rock properties, rock strength depends on external factors. Rock strength monotonically increases with increasing confining pressure (Jaeger, et al. 2009) and not only the lowest principal stress, as suggested by the Coulomb-Mohr failure criteria, but also the intermediate principal stress has effect on strength (Paterson and Wong 2005). There is generally some influence of strain rate, temperature and time on brittle fracture, which may vary with the material and the experimental conditions. This observation points to there being some participation of thermally activated processes in brittle fracture. According to Sangha and Dhir (Sangha and Dhir 1972) at strain rates of 10^{-1} s^{-1} or less, the fracture stress measured by uniaxial tests increas by around 10% for 103-fold increase in strain rate and this effect is smaller in the case of triaxial tests. Donath and Fruth (Hirth and Tullis 1994) found no significant influence of strain rate on the shear fracture strength of sandstones and siltstones under a confining pressure of 100 MPa. There are several observations which show that there is some decrease in strength with increase in temperature (Fischer and Paterson 1989). The fracture strength decreases only slightly at moderate temperatures, below 300°C (Handin and Hager Jr 1958).

The previous studies clearly showed that many factors controls rock strength. Therefore, the prediction of the rock strength dependencies and influences present a challenge because of its complexity. One way to determine strength of reservoir rocks that are in thousands of meters deep, is to use geophysical well logs (Zhou et al. 2005, Chang et al. 2006).

Well logs measure several rock properties which are also related to rock strength. Different types of resistivity tools provide information on water saturation, porosity and also clay content of rock around the bore hole. Natural gamma ray measurement data mainly indicates clay content; in addition, spectral gamma ray measurement that involves Thorium (Th), Uranium (U) and Potassium (K) logs, provides further information on mineral composition of the rock. Sonic or acoustic logs allow estimating the compression and shearing wave velocity of rocks which are related to rock types, density, porosity and saturation. Furthermore, generated gamma ray based density tool measures the bulk density of the formation more accurately. Neutron log, which is the reaction of the formation to fast neutron bombardment, indicates the richness of formation in hydrocarbon; furthermore, with correction, formation density can be calculated too. (Rider 1986, Ellis and Singer 2008)

The first attempts tried to correlate only one well log to UCS in order to predict the rock strength. McNally defined an exponential relationship between the sonic log and UCS (McNally 1987). This method is a first order estimate of the rock strength. The correlation can be improved by distinguishing weak and strong strata (McNally, 1990).

Fjar et al. (2008) developed a quartic relationship between P-wave velocity and UCS for sandstones of the Gulf of Mexico. Schön (1996) described the relationship between seismic velocity and UCS as either a linear, polynomial or logarithmic relationship. Bradford et al (Bradford et al. 1998) calculated UCS from static Young's moduli, which were derived from velocity and density measurements using linear relationship and built a model for the very weak North Sea sandstones. Moos et al. (1999) used a quadratic relationship between P-wave velocity and UCS for coarse grained sandstones and conglomerates in Cook Inlet, Alaska. Lawrence developed a correlation equation between sonic log and UCS based on lithological variations (Lawrence, 1999). However, these approaches tend to show high uncertainty, due to the fundamental difference between the static (UCS) and dynamic (sonic velocity) rock strength properties.

To solve this issue, Hatherly et al. (2001) correlated the composition of well logs with UCS. Although, the variability in the strength behaviour due to; for example, cement type and the location of the cement (whether the cementation is only around the grains or also filling the pore space), cannot be investigated by such an analysis (Hatherly et al. 2004).

It is well known that stress levels affect sonic velocity magnitudes in rocks. This is one of the reasons why UCS estimates based on sonic velocity alone tend to be accurate only when determined for a specific site or lithology at that site. Whilst only marginally better, the compositional approach aims to provide a more generalized formula that allows UCS estimates to some extent account for local variations. Therefore Zhou et al. (2005) tested two new methods, the Radial Basis Function (RBF) and the Self-Organizing Maps (SOM), for predicting the rock strength from all available, geophysical logs; however, these results were valid only locally (Zhou et al. 2005).

Chang, Zoback et al. (Chang et al. 2006) summarized the empirical equations between UCS and mechanical properties derived from well logs. They stated that the reviewed relations may be useful to predict the wellbore stability, especially when there is

no other available information on the rock strength. However, they also highlighted that there is a need for the calibration of the correlation equations.

Urai et al. (1994) studied the deformation mechanism in clay and mudrocks. They developed a brittleness index to quantify the tendency of forming dilatant fractures (Urai 1995, Urai et al. 1997, Hoogerduijn-Strating and Urai 2003). The brittleness index was calculated from the UCS, which was derived from P-wave and S-wave velocity logs using a logarithmic relationship. Relation between log properties, such as, natural gamma ray, resistivity and sonic velocity, and rock mechanical properties were studied on rocks, including sandstones in the well RWTH-1, in order to gain input parameters for stress model (Trautwein-Bruns et al. 2010). Trautwein-Bruns et al. (2010) also studied the relation between rock strength and borehole breakout properties as well.

One other important parameter is the Young's modulus or elastic modulus which defines the stiffness of the rock. The Young's modulus describes the relationship between the stress and strain in elastic materials: it is the ratio between normal stress and the resulted elastic extension or shortening in the same direction (Fossen 2010).

There are many ways to determine the Young's modulus of the rock (Jizba 1991). In situ and laboratory tests can be performed to measure rock mechanical properties directly. Alternatively, it is possible to obtain the elastic moduli using methods based on wave propagation. Although, the static and dynamic moduli of a homogeneous material such as steel are identical (Fjær 1999), there can be large differences between the static and dynamic moduli of heterogeneous materials such as porous rocks, particularly at low stress levels: the static moduli of rock determined from static compression tests are characteristically lower than dynamic moduli determined from acoustic sound velocities (Simmons and Brace 1965, Cheng and Johnston 1981, King 1983, Jizba and Nur 1990, Tomosawa and Noguchi 1993, Fjar et al. 2008, Fjær 2009).

The relationship between the static and dynamic Young's moduli is affected by the lithology, especially the shale content and the degree of saturation also has an effect. (Jizba 1991) The value of the static Young's modulus depends on loading/unloading path and the level of confining pressure (Walsh 1965, Chang et al. 2006).

Young's modulus has also been used to estimate UCS, Bradford proposed a linear relationship between the static Young's modulus and UCS; although, in this study, the static Young's modulus was not measured directly, it was derived for velocity and density measurements (Bradford et al. 1998, Chang et al. 2006).

In this study, correlations between strength and static elastic moduli and wireline log properties are analysed by multivariate regression technique in two different types of sandstones of the North Sea namely Rotliegend Sandstone and Lower German Triassic Sandstone groups (Wong et al. 2007). These sandstones are found to be potential hydrocarbon reservoirs and they are important target of hydrocarbon researches. However, relatively large volume of sandstone strata is tight reservoir (Holditch 2006), where production of hydrocarbon even gas is very challenging. Therefore, knowledge and better understanding of physical and mechanical properties of sandstone reservoirs is necessary for exploitation of hydrocarbon resources. The aim of this study is to investigate the relationship

between the rock strength and different geophysical wireline well logs. Multivariate regression analyses are performed to improve the existing rock strength prediction formulas. Such analysis of North Sea sandstone samples has not been carried out before. In addition regression analysis, mechanical characterisation of the studied sandstone strata can be accomplished based on the measured rock properties.

4.1.2 Data

CORE SAMPLES

To perform the rock mechanical tests, 64 sandstone plug core samples were available. The samples were taken from four boreholes of the south and south-west part of the North Sea, from block K, P and L: K18-8, L6-8, P2-SE2 and P6-9. The samples originate from the Lower Germanic Triassic Group from the depth of about 2700 m and about 4050 m and the Rotliegend Group of sandstones from the depth of 3900 m to 4900 m. This sample collection contains 52 Rotliegend- and 12 Lower Germanic Triassic rock samples from the four wells combined (Table 4-1). In the two rock groups, there are 10 different rock members. In chapter 4.2, Table 4-3 and Table 4-4 show the list of the rock type of the samples.

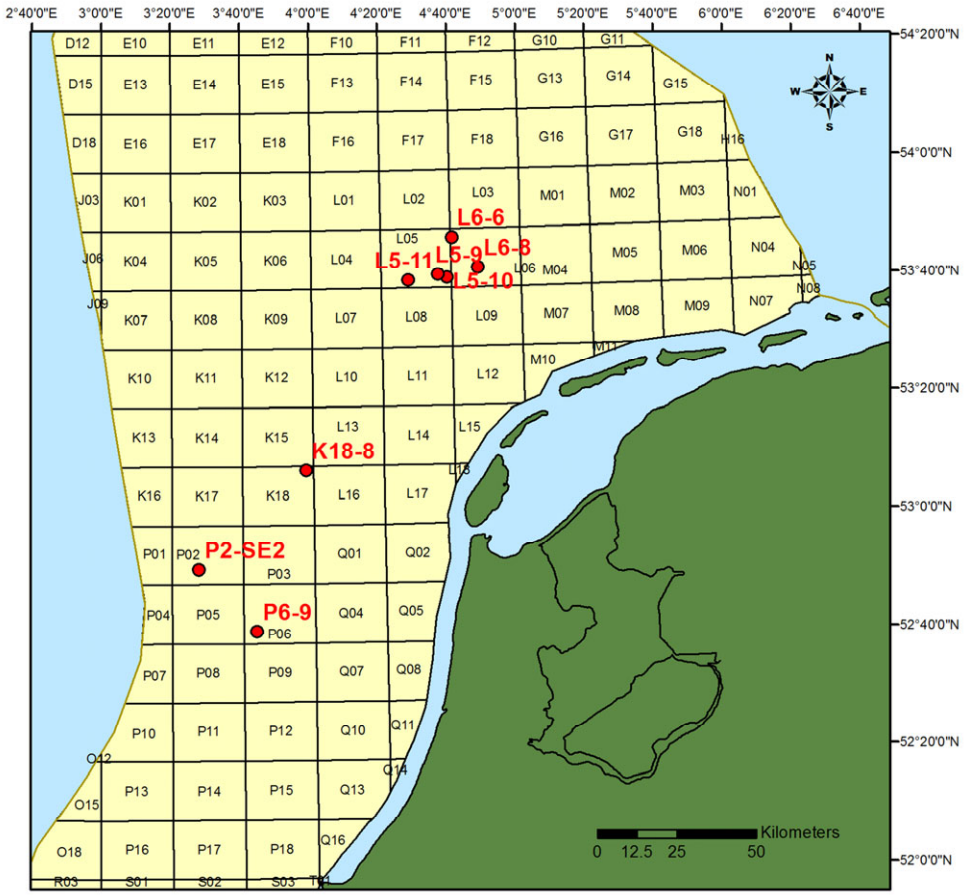

Figure 4-1 – Map of the studied wells in the North Sea

The physical size of the plug samples were 37 mm in diameter and the length of the plugs were in the range of 40 mm up to approximately 190 mm. Samples were received in good condition. There was no evidence of damage visible on the surface of the samples and also there is no visible core damage due to the core cutting and stress release. Core damage effect is a well-studied and considerable problem for mechanical test. Many aspect of the core damage effect were studied for instance by many authors (Santarelli and Dusseault 1991, Holt and Kenter 1992, Holt et al. 1993, Holt 1994). Later, synthetic rock based techniques were established to correct physical and mechanical properties of borehole samples measured in laboratory (Kenter et al. 1997, Holt et al. 2000). In the present work, these technics were not applied.

Sample orientation of 56 samples was parallel to the borehole axes from well K18-8, P2-SE2 and P6-9. Out of these 56 samples 39 plugs had inclination of less than 5 degree and 17 samples, came from almost horizontally drilled section of well P2-SE2, had inclination of 84 to 89 degree. Eight samples of the well L6-8 were cut perpendicular to the borehole axes. The inclination of this well, in the Lower German Triassic strata, is less than 2 degree, and the inclination in the Rotliegend is around 10 degree. So, these 8 samples were approximately horizontally oriented originally. Images of Figure 4-2 show an example for the originally received typical sample dedicated for mechanical tests.

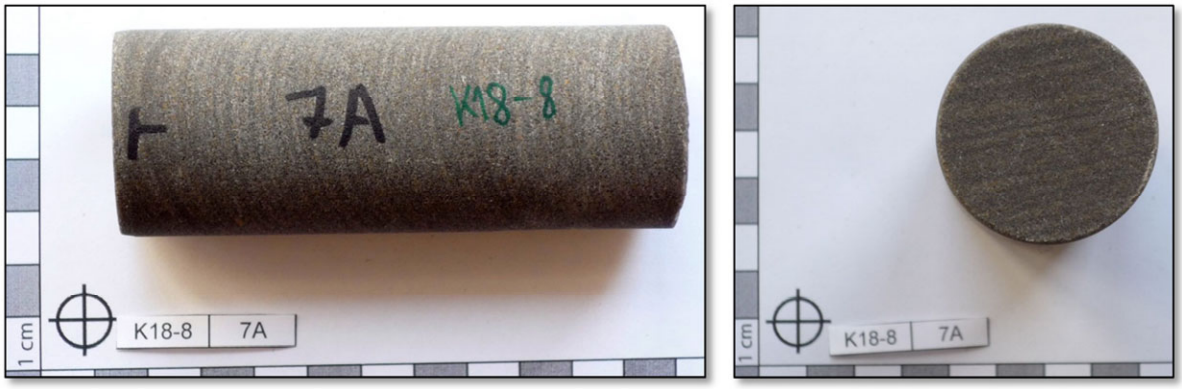

Figure 4-2 – Photo of one of the original samples from Rotliegend strata of well K18-8; side view is on the left and top view on the right.

WIRELINE WELL-LOG DATA

The other necessary data for this study are well logs. Table 4-1 shows the summary of all the used logs and the numbers of the available samples. From all the wells, gamma ray, density, sonic slowness, resistivity well-logs and also conventional core analysis reports and well-site geological reports, which contain information on core-log tie and geological strata description were available. Furthermore, spectral gamma ray, neutron porosity and sonic shear wave slowness data from only well K18-8 and L6-8. Logs above were available in digital format in ASCII, LAS file format. Most of the logs had a sampling frequency of 15 cm. Few logs had a sampling frequency of 7.5 cm. These logs were converted into 15 cm sampling frequency. Thus, the log measurement resolution in the studied log properties was 15 cm.

Table 4-1 – Table contains information on available logs and numbers of available core samples from each well and from rock types.

Well name	Rock type	P- wave Slowness (DTC)	Sonic travel time (DT)	Density (DEN)	Resistivity (RES)	Gamma Ray (GR)	Spectral Gamma Ray (K, U, TH)	Porosity (Φ)	Neutron Porosity (CNC)	Number of available samples
K18-8	Rotliegend	yes	yes	yes	yes	yes	yes	no	yes	29
L6-8	Rotliegend	yes	yes	yes	yes	yes	yes	no	yes	4
L6-8	Lower German Trias	yes	yes	yes	yes	yes	yes	no	yes	4
P2-SE2	Rotliegend	yes	no	yes	yes	yes	no	yes	no	17
P6-9	Rotliegend	yes	no	yes	yes	yes	no	yes	no	2
P6-9	Lower German Trias	yes	no	yes	yes	yes	no	yes	no	8
All	Rotliegend	yes	partly	yes	yes	yes	partly	partly	partly	52
All	Lower German Trias	yes	partly	yes	yes	yes	partly	partly	partly	12
All	All	yes	partly	yes	yes	yes	partly	partly	partly	64

4.2 Method

4.2.1 Sampling method – quality control

Measurement results were analysed by statistical calculation; such as, multivariate regression analysis. Therefore, a statistically representative sample set is critical. Histogram is one appropriate tool to check the quality of the samples set. The histogram of the log values of the studied rock is supposed to show similar characteristic to the histogram of the log values of the selected samples including the covered range (minimum and maximum values). Figure 4-3 shows example histograms for a representative sample subset (histogram on the right) out of an entire studied dataset. The covered range of the values is nearly the same as range of the entire cored section and the distribution (characteristic of the histograms) of the values is also very similar to entire section too.

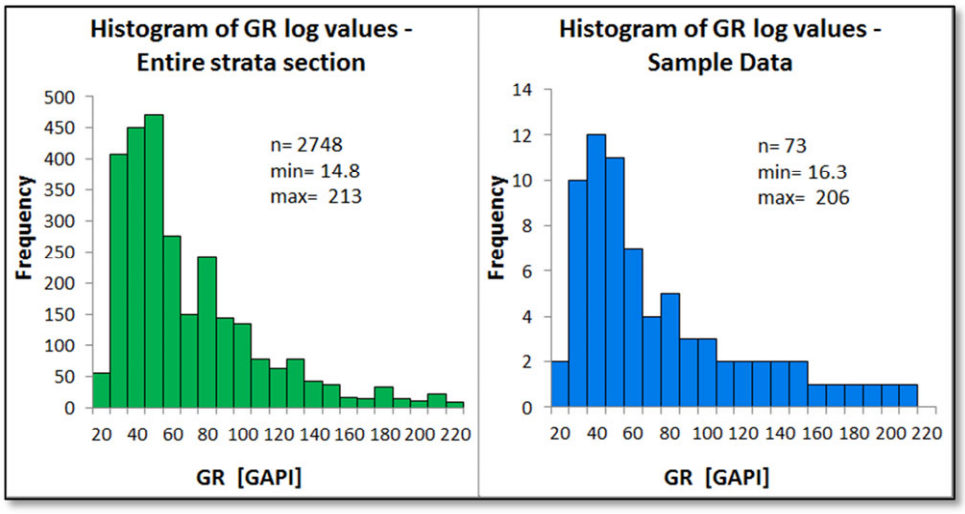

Figure 4-3 – Histogram of gamma ray log values of the entire studied rock column (left) and histogram of gamma ray log values of a sample set (right) which is an ideally representative subset of the entire dataset.

Besides the analysis of the distribution of the datasets, permutations of the values of the different log properties were created, which belong to a sample or a point of the studied strata, also a critical factor. With multivariate regression, the relation between mechanical properties and four or more log properties is analysed. For instance, what is the strength if gamma ray and density values are high while sonic slowness and resistivity values are low; or gamma ray value is low and etc. If ranges of logs are classified in three sections; such as, high, medium, low values; then, this way 64 variation of the log properties can exist. However, many of the class types do not exist, because a given class type simply does not present in the studied section or because of law of nature. In this study three and four classes were used as it can be seen in Table 4-2. Furthermore, rock type or facies also can be involved in this checking procedure if it is necessary. In this study, facies was not used for quality check. Table 4-2 shows the list of the used limits of log properties for quality check. Two limit means three classes and three limits means four classes.

Table 4-2 – Limits of the log properties listed in this table were used for quality check of selected sample set.

	Sonic slowness [μs/ft]	Density [g/cm^3]	Resistivity [Ohmm]	Gamma ray [api]	Potassium [%]	Uranium [ppm]	Thorium [ppm]	Neutron porosity [pu]
Class 1	<65	<2.45	<10	<50	<1.5	<4	<4	<8
Class 2	65-80	2.45-2.7	10-50	50-100	1.5-2-5	4-8	4-8	8-16
Class 3	80<	2.7<	50-100	100-150	2.5<	8<	8<	16<
Class 4			100<	150<				

Classes were created according to the limits (see Table 4-2) in numerical format with the following digits system for the four basic logs: ####. These artificial numbers reflect type of log properties hence they are called "log property type". The first digit stands for compression wave slowness (DTC), the second digit for density (DEN), the third digit for resistivity (RES), and the fourth digit for gamma ray (GR). And for quality check of all the used logs (spectral gamma instead of GR) the log property pattern was: DCT|DEN|RES|K|U|TH|CNC (864 theoretical variations of log properties).

Using the log property types as bins for histogram, log property type histogram(s) can be created. Based on the log property type histogram, number of required samples can be defined. Ideally, a representative data set contains around 4-6 samples from every type. However, there are types from where only very limited number of sample available. Furthermore, these rare log property types not significantly represent the studied rock; therefore, they can be neglected from the analysis.

The core-to-well tie is very important in order to know the right log values of the core samples. The core-log tie is defined by those points (markers) where correlation can be observed between log and the related core rock. However, the distance between these markers is often several meters to ten-twenty meters. Moreover, between the markers, it still has an uncertainty because of the cable stretch which is hard to predict. Figure 4-4 shows an example for log curve characteristics in gamma ray log. At some points, log values

change relatively much considerably over a short depth range – curve of the log is steep. If the log value changes very "quickly" in shorter interval then the reliability of log value belong to a given sample is low. Log values hardly change between depths of 3951 m to 3953 m. Log value of a sample from this section is much more reliable than a sample from depth of 3954 m. Log value change to more than double within 15 cm distance. This factor has to be checked and considered during data processing.

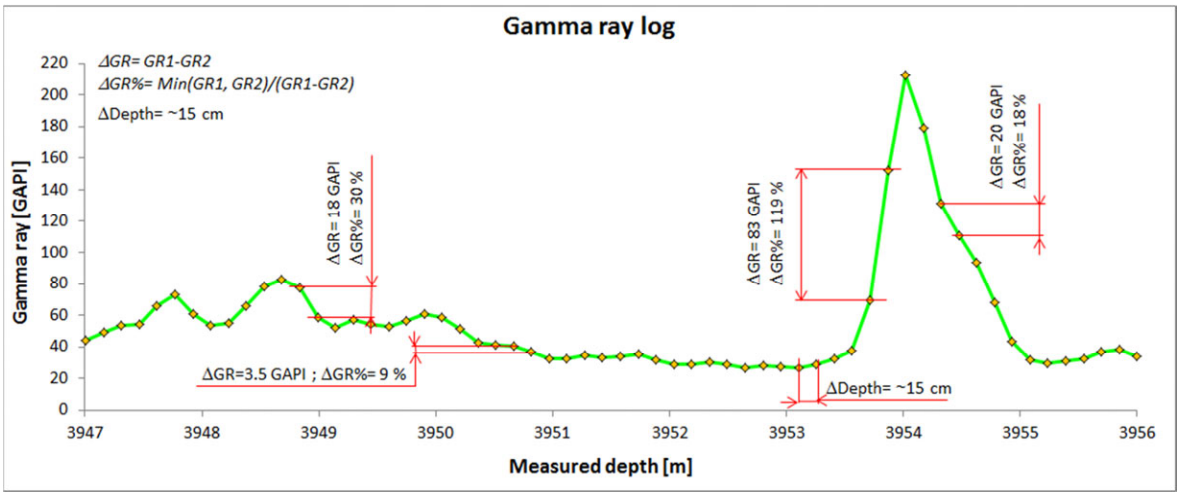

Figure 4-4 – Figure shows an eight m long section of a gamma ray log. Orange dots indicate the measured log values and the green line is log curve simply connecting the measured points. Data frequency of the log is 15 cm. Dimension lines show some examples how the value of neighbour points change relative (ΔGR %) and absolute (ΔGR), too.

Numerically, the slope of a continuous function can be analysed by first derivative of the function. For well logs, which are rather like discrete functions, the slope can be calculated by the difference of the neighbouring log values of a given range. To analyse the log curve shape, 60 cm radius was used around the given location according to (Eq. 4-1). Where, DValue% is between the minimum and the maximum log values within the given range ($MaxValue_{Radius}$-$MinValue_{Radius}$) relative to the range of the entire studied log section ($MaxValue_{Total}$-$MinValue_{Total}$).

$$DValue\% = \frac{MaxValue_{Radius} - MinValue_{Radius}}{MaxValue_{Total} - MinValue_{Total}} \cdot 100\ [\%] \qquad \textbf{(Eq. 4-1)}$$

In this part of the quality check, the cable tension logs can provide further information on the reliability of depth of logger equipment. Therefore, the total tension was involved in the quality check; the log curve shape was analysed with the same calculation.

Core-log depth shift data were available from all the wells which were used to synchronize the log data (depth measured by loggers) and core data (depth measured by the drillers). Besides, the measured depth was converted into true vertical depth for the comparison of the data from different wells.

4.2.2 Sample preparation

Sample quality check is also essential to gain reliable results. The received rock samples were intact samples, in undamaged condition. The suggestion of ISRM and ASTM (Ulusay and Hudson 2007, ASTM-D7012 2010) standards for sample preparation and UCS test measurements were followed for the rock tests. The most important parameters are the sample size and sample dimension ratio. The suggested diameter to length ratio has to be 1:2 to 1:3 and the diameter is not allowed being smaller than 10 times the diameter of the largest grain. The lengths of 10 samples (15% of all the samples) were shorter than the other samples. Therefore, all the samples were re-drilled with smaller diameter to have uniform plug sample size: diameter of 20 mm and length 40-45 mm.

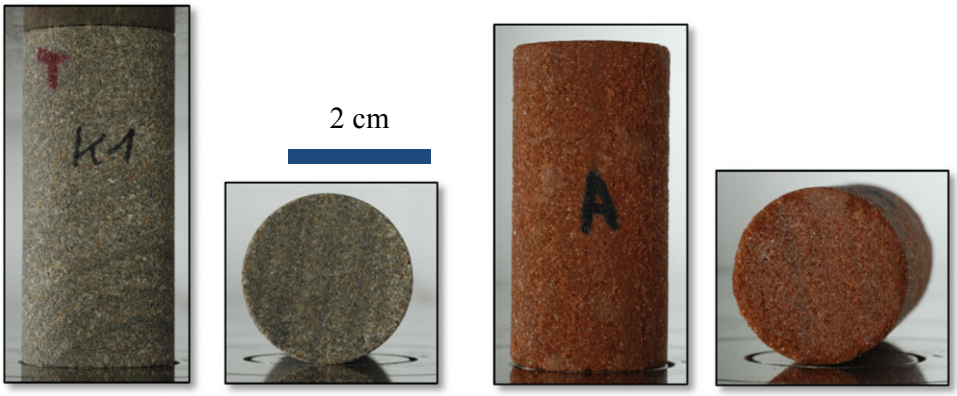

Figure 4-5 – Side and top view photos of two samples (left: K18-8/1; right: L6-8/A) which are prepared for unconfined compressive test measurement.

For the sample preparation, diamond core drill bit was used. Water cooling was used at drilling in general; however, weaker samples were cooled by air. Diamond blade was used to cut the length of the samples with water cooling. The plug ends were prepared even and perpendicular with a special grinding machine for plug samples with diamond wheel.

Combined 70 UCS plug samples were prepared from the received 64 core samples. At six samples, the length of the samples allowed us to prepare two UCS plugs from one core sample. Two of the samples (P2-SE2/7 and P2-SE2/20) were fairly weak and washed-out, therefore the required shape conditions were not been able to reach; and the plug ends were uneven and not perpendicular. In this condition, these may not provide reliable results; therefore, they were skipped from the mechanical measurements.

Some of the samples were found potential outliers. One sample (P6-9/12) broke into two parts during cutting with perpendicular to the plug ends. Two of the samples (P2-SE2/23 and P2-SE2/22) were relatively weak. Therefore, it was not possible to grind plug-ends as even as the standards require; but, deviation was not significant. Two of the samples (K18-8/12 and K18-8/13) contained larger grains than it is allowed (the ten times of the plug diameter).

4.2.3 Rock physical measurements

The second stage was the measurement of rock physical properties of the core samples. The porosity and the density of the samples was measured in the UCS plug samples or in the remains, tube shaped part of the UCS plugs. The samples were dried at 60°C until samples mass decrease were less than 0.1 % during 4 hours drying time, according to the ISRM standard (Ulusay and Hudson 2007). The mass measurement accuracy was ±0.0001 g.

In dried samples, the matrix volume was measured with helium pycnometer (machine type: AccuPyc 1330). After that, the sample bulk volume was measured by vernier caliper and also by Archimedes method. The Archimedes volume measurements were achieved on saturated samples, directly before the UCS measurements; therefore porosity had no effect on bulk volume results. Balance with accuracy of ±0.001 g was used for the mass measurements during the Archimedes measurements. The matrix- (grain) density, bulk density and porosity of the rock samples were calculated. Measurement uncertainty of porosity values are less than ±0.2 %.

4.2.4 Rock mechanical measurements

In the main stage of the work, the unconfined compressive strength of the prepared samples was measured. The UCS tests were measured with Zwick/Roell Z100 load frame using testXpert II software. This test machine is able to measures the applied force with an accuracy of ± 0.5 Newton and the frame displacement with an accuracy of ± 0.0005 mm. The measurement uncertainty values produce around ± 0.1 MPa uncertainties in UCS results.

The samples were saturated with tap water samples for UCS tests. Samples were saturated higher than 2 %, because above 2 % saturation UCS does not change much with increasing saturation (Hawkins and McConnell 1992, Barefield and Shakoor 2006, Shakoor and Barefield 2009).

Unconfined compressive strength measurements were performed in accordance with ASTM and also ISRM (Ulusay and Hudson 2007, ASTM-D7012 2010). Since the size of available core samples were limited; therefore, samples were prepared smaller than the standard suggestion in order to create uniform size plug samples. The sample diameter was 20 mm ± 0.5 mm and length 40 mm ± 1 mm. Measurement of all the samples were planned to perform with a single, relatively short unload-reload loop, as suggested by the standards. Unload-reload behaviour of rock is analysed often in pressuremeter tests (Byrne et al. 1990, Clarke 1994). The positions of the loops were defined with the applied force; ranges of the loops were from 1500 N (for lower UCS rock) to 3000 N (for higher UCS rock). Rock strengths were measured applying constant loading speed. These results were used to estimate UCS for planning loop parameters. During the tests, the tool separations were decreased with a predefined constant speed, 0.1 mm/minute, strain rate=$5 \cdot 10^{-5}$ s^{-1}. The UCS values were defined as the highest measured force divided by area of the specimen. The Young's moduli values were calculated from the longest linear section of the stress and stain curve. The

unloading moduli were calculated from linear sections of unloading part of the stress and stain curve. Figure 4-8 shows an example for the source of calculation of both moduli.

For calculation of the elastic moduli of the samples, the calibration of the measuring tool is necessary. For calibration purpose, 21 calibration tests were measured where the load frame was empty and clean in order to define the elastic behaviour of the test machine. Figure 4-6 shows the 21 measured calibration test. The strain of the load frame was defined with a third grade polygon (equation can be found in the graph) when force was lower than 25000 N. The red line on the left graph of Figure 4-6 shows the trend line of the polygon. And when force was higher than 25000 N, strain was corrected linearly that can be seen on the right graph of Figure 4-6 together with the applied equation. The measured force and strain curves of the samples were corrected with the self-strain of the load frame defined by the two equations. The real strain is the difference of the measured strain and the strain of the test machine at the given force ($\varepsilon_{machine}(F)$). On Figure 4-7, an example for calibration correction can be seen originally measured (black dashed line) and corrected (green solid line) stress and strain curve of sample K-1.

Static elastic moduli of the samples were calculated on two segments of the corrected stress and strain curves of the samples. On the one hand, the linear part of the main loading segment of the stress and strain curve was used for calculation of elastic modulus. And on the other hand, also the unload part of the unload-reload loop was used to gain unload elastic modulus. Figure 4-8 shows an example of the two sections of stress and strain curve. Static elastic modulus (Young's moduli) was calculated as the dip of the curves.

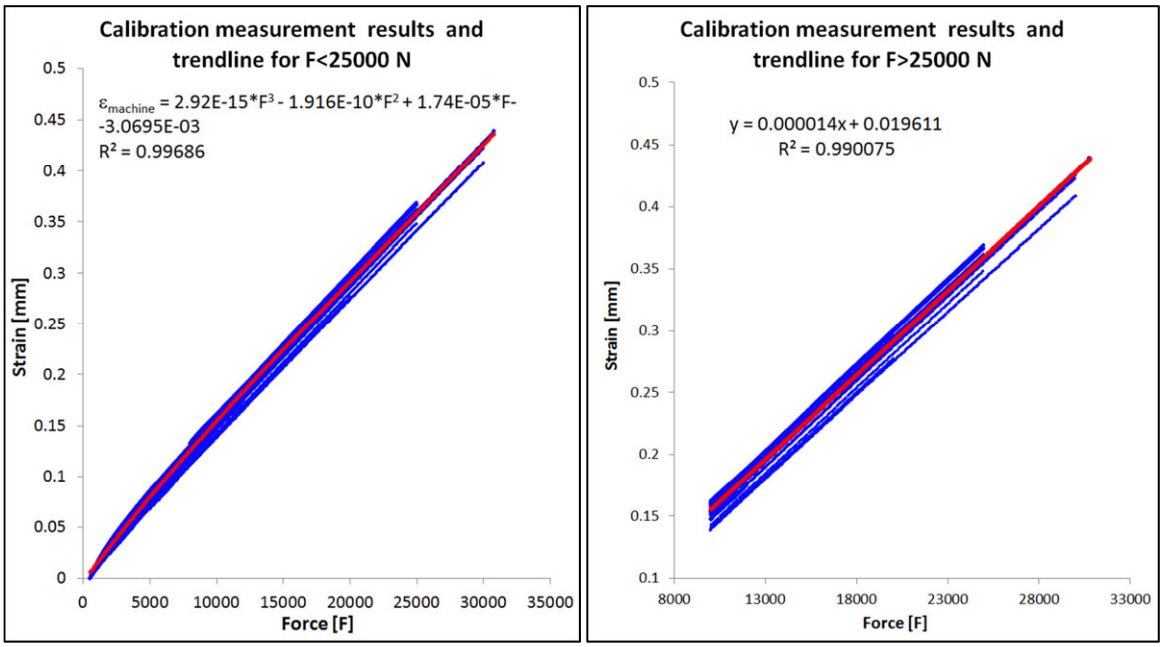

Figure 4-6 – Load frame calibration measurements results (blue lines) and the fitted trend lines (red lines) and the equation of these can be seen on the graphs. Graph on the left shows the curve that was used when force was lower than 25000 N. Graph on the right shows the curve that was used when force was higher than 25000 N.

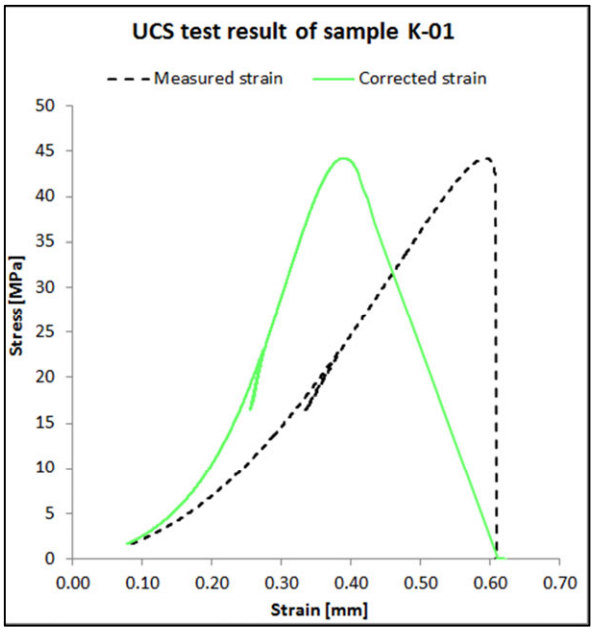

Figure 4-7 – Graph shows measured and corrected strain curve of samples K-01, self-strain of the frame was subtracted from measured strain.

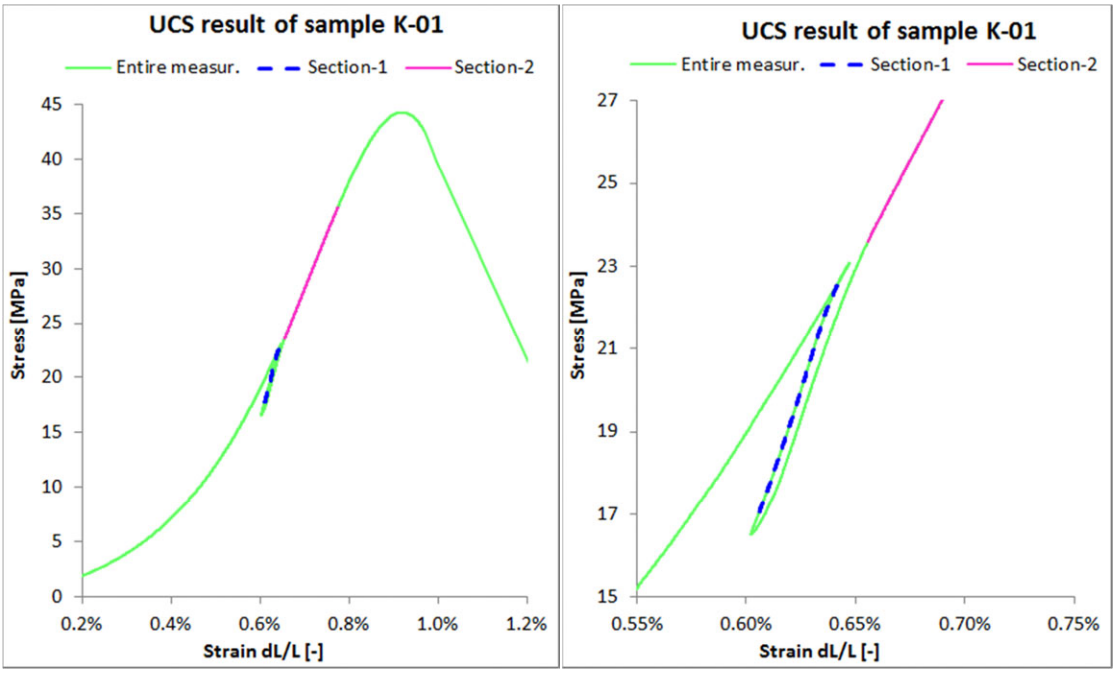

Figure 4-8 – Graphs shows on the left the entire measured stress and strain curve of samples K-01 which contains an unload-reload loop. The two sections were used for elastic moduli calculation. Purple line indicates linear part of the normal loading section and dashed blue line indicates the unloading section of the curve. Graph on the left shows the loop section of the same graph.

4.2.5 Regression analysis

In order to estimate the relationship between UCS and different log properties, regression analysis was performed. Simple and multivariate linear regression was calculated, which implies, that the dependent variable (UCS) is a linear combination of the independent variables (log properties), however it is not necessarily linear in the independent variables. In case of simple linear regression, there is one independent variable; whereas, in case of multivariate linear regression, there are more independent variables.

The simple linear regression model can be given as:

$$y = \beta_0 + \beta_1 x + u$$

The two constants, intercept (β_0) and slope (β_1) are the regression coefficients which need to be estimated from a sample of y values with their associated values of x, and u is a random variable which represents the deviation of y about its mean. (Soong, 2004)

The multivariate linear regression model with m independent variables can be described as:

$$y = \beta_0 + \beta_1 x_1 + \cdots + \beta_m x_m + u$$

where are m+1 regression coefficients (β_0, β_1, … , β_m), and u is the error with mean of 0 and variance of σ^2, which is identical to the variance of y (Soong, 2004).

The regression coefficients were calculated using the least squared method. The goal of this method is to choose the regression coefficient in a way that the sum of the squared differences between observed sample values and the estimated expected value of the model is minimized. The detailed description of this method can be found in e.g. Björck (1996) or Allen (1997).

There are some parameters to measure the "goodness" of the fit. The coefficient of the multivariate regression (R) estimates the degree to which variation in the dependent variable is associated with variations in the several independent variables taken simultaneously. The coefficient of multivariate determination (R^2), measures the percentage of the variation in the dependent variable which is explained by variations in the independent variables taken together (Schroeder et al. 1986). This can be calculated as the following:

$$R^2 = \frac{SSM}{SST}$$

where SSM is the sum of squares for regression and SST is the corrected sum of squares total, and calculated as the following:

$$SSM = \sum_{i=n}^{n} (\hat{y}_i - \bar{y})^2$$

$$SST = \sum_{i=n}^{n} (y_i - \bar{y})^2$$

Where n is the number of observation, ŷi is the estimated y value, $\bar{y}$ is the mean value of y.

Before calculating the regression coefficient, the ANOVA (Analysis of Variance) table was calculated. All the calculations were done using the Microsoft Excel Analysis ToolPak and also Matlab scripts. As a part of ANOVA, F statistic was calculated to test the hypothesis (H_0) whether all of the coefficient equal to zero.

$$H0: \beta_0 = \beta_1 = \beta_2 = \ldots = \beta_K = 0$$

If this hypothesis can be rejected, it means that there that the entire model is statistically significant.

The F statistic is the ratio of the mean squares for the model and the mean squares for the error. Based on the model, the corresponding significance F can be also calculated which gives the probability that the null hypothesis for the full model is true. If this significance F is a low value, the null hypothesis can be rejected which would mean that at least one of the regression parameters are nonzero. Thus, the regression equation does have some validity in fitting the data, so the independent variables are not purely random with respect to the dependent variable.

The residuals of the regression model are the difference between the observed value and the least square estimate. During the regression, the sum of the absolute residuals and also the sum of the absolute standard residuals (standard residual: residual divided by the standard deviation of all the residuals of a model) were supposed to be minimized.

In addition to an appropriately large R^2 value, there are some requirements regarding the residuals to verify the model. The residuals are supposed to have a normal distribution with an expected value of zero and with the same standard deviation as the original dataset. They also supposed to be independent. (Kutner et al. 2004)

The main aim of this study is to analyse the relationship between log properties and rock mechanical properties. One way is to analyse relationship between data sets is regression calculation that provides correlation equations. These equations are empirical equations because these are created only based on regression. In this case, UCS was predicted by different models and the explanatory variables of the calculation models are the different log types. The logs were also converted by non-linear functions; such as 1/x, x^2, $x^{1/2}$, log10(x), exp(x) functions. Microsoft Excel and Matlab software was used for the calculation and data visualization.

4.3 Results

4.3.1 Quality control of the log data

Firstly, the best fit resistivity log was selected from the two wells where six different logs were measured with different long receivers. The next step was to filter the outliers based on the result of the linear multivariate regressions between P-wave slowness, density, resistivity and gamma ray logs and UCS involved all the samples. Linear multivariate regressions of different models were calculated where numbers of explanatory variables were increased step by step. This way, the effect of the newly added variable on the regression quality was studied. In addition, the relation between non-linear functions (e.g. exponential-, logarithmical-, parabolic-, and hyperbolic) of the logs and the UCS were studied. Finally, the data set was separated by formations (Rotliegend and Lower German Triassic Group) and linear multivariate regressions were calculated in the same way as it was for the entire data.

The distribution of the log properties of the studied formations and samples from all the wells can be seen on histograms of Figure 4-9. The distribution and also log values of samples cover nearly the same ranges as the log values of the entire core section cover. The histograms of samples show similar characteristics values to the entire section at most frequent occurrence. Figure 4-10 shows the log type histograms of the studied rock section and core samples in order to compare the distribution of these data. Histograms shows that the sample set contains the most frequent log property types and only the very low frequent occurrence types are not represented by sample set. Hence, it allows gaining information on the dominant part of the structure.

The uncertainty of log values is showed on Figure 4-11 for four most common log properties namely: gamma ray, resistivity, sonic slowness and density on a segment of well P2-SE2. Red dots indicate the location of samples in logs. As it can be seen on the graphs, most of the samples are at relatively flat section of the log curves. Thus, uncertainties of the log value of the samples, because of the possible depth shift of the logs, are small. However, several samples are at or close to steep section of the log curve. The changes of the log values around the samples were calculated by equation (Eq. 4-1), which can be seen in right part of Table 4-3 and Table 4-4 Higher value means that the given sample has more chance for different value in case of depth shift. Besides, Table 4-3 and Table 4-4 shows all the log parameters of all the samples that were used for the calculations.

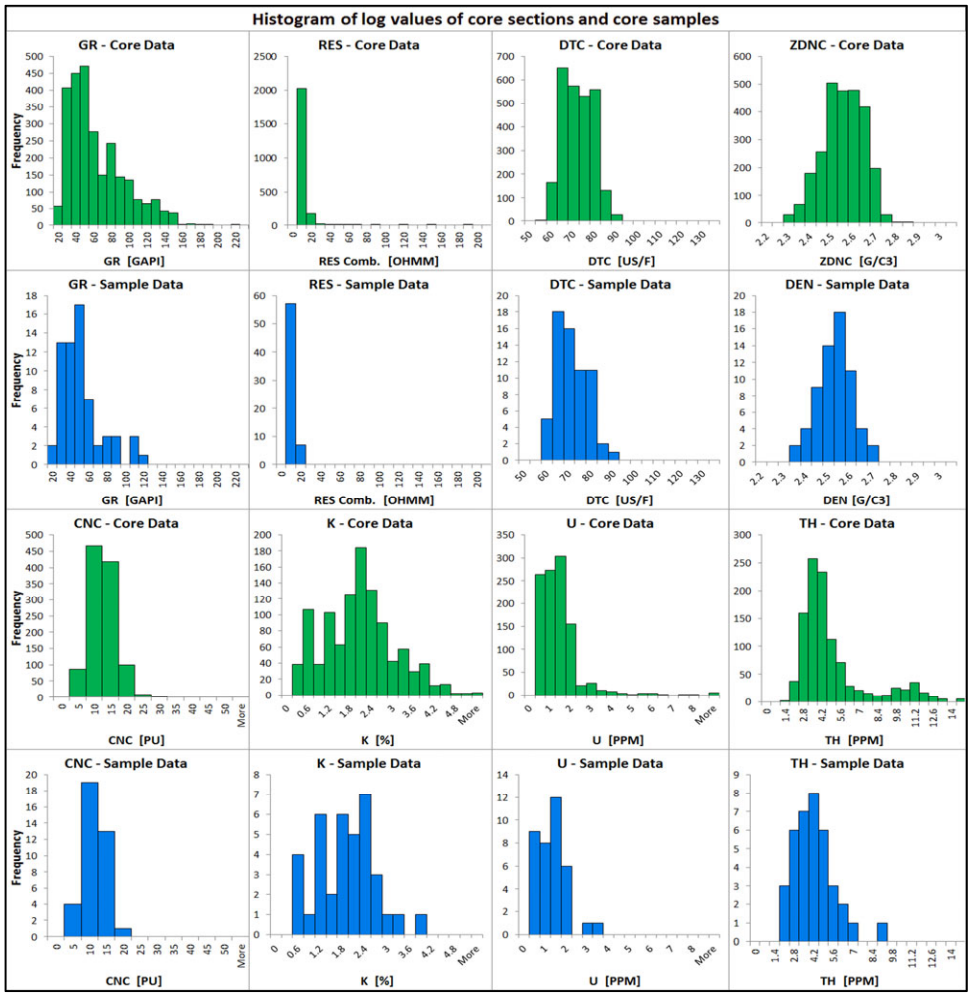

Figure 4-9 – Histograms of the log properties of the entire cored sections (first and third rows) and received samples (second and fourth rows). The distribution of the log data of the studied borehole section and core samples is compared by the histograms. (Where DTC is compression wave slowness, DEN is density, RES is resistivity, GR is gamma ray, CNC is compensated neutron porosity, K is potassium GR log, TH is thorium GR log and u is uranium GR log.)

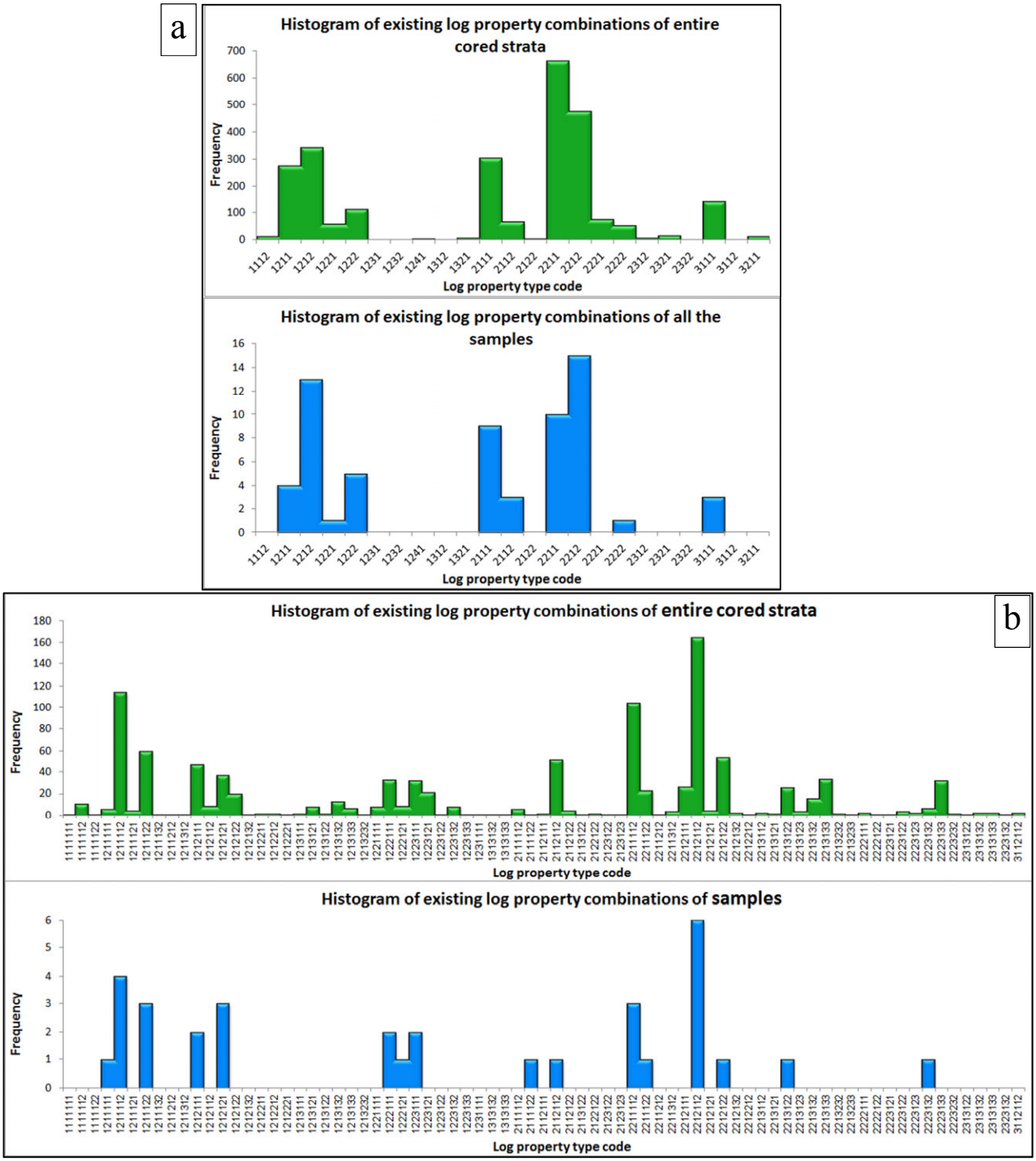

Figure 4-10 – Histogram of log property types, based on the four basic logs (DTC, DEN, RES, GR), of the entire section (upper graph) and samples (lower graph) can be seen on figure "a". On figure "b", histogram of log property types of entire section (upper graph) and samples (lower graph) can be seen based on all available log types (involved well K18-8 and L6-8).

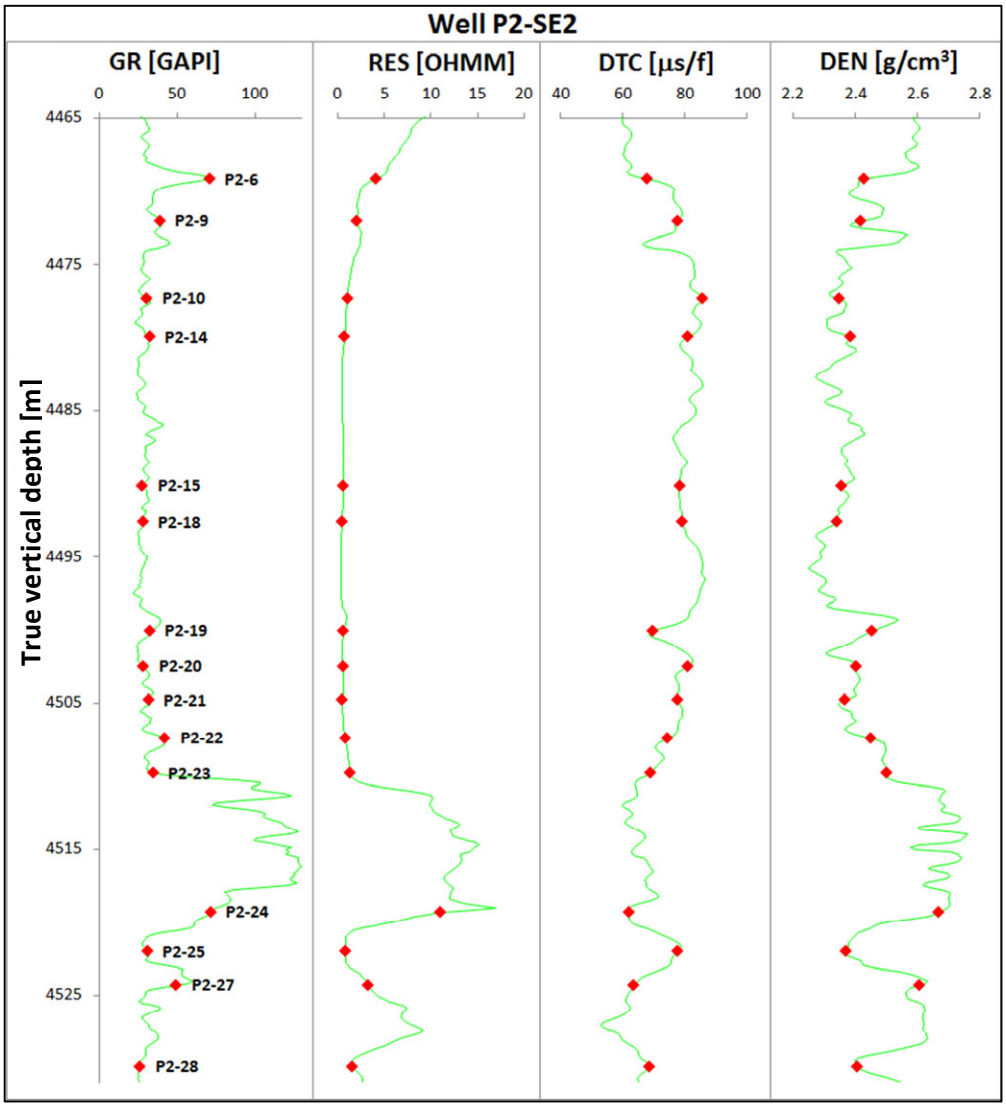

Figure 4-11 – Changes in log values around the selected samples. The red dots indicate the position (after core depth shift) of the samples that are involved in the mechanical tests. Green lines are the log values. In some cases, log values change very fast around samples; for instance in gamma ray log: sample P2-6, P2-23, P2-24, P2-27 or in the log of resistivity sample P-24. (Where DTC is compression wave slowness, DEN is density, RES is resistivity, GR is gamma ray.)

Table 4-3 –Log values of all the log types of samples from well K18-8 and L6-8. On the right part of the table, maximum of change of log values around the samples within ~ ± 60 cm relative to the total range of the cored section can be seen. Cells with "n.a." mean that there was no data available.

Basic data of the samples					Log values at depth of the samples														Log value stability around samples (~± 60 cm)								
Well name	Sample ID	Rock, Goup	Rock, Facies	DEPTH (logger) [m]	GR [GAPI]	RES Comb. [ΩM]	DT [US/F]	DTC [US/F]	DEN [G/C3]	CNC [PU]	K [%]	U [PPM]	TH [PPM]	M1R1 [ΩM]	M1R2 [ΩM]	M1R3 [ΩM]	M1R6 [ΩM]	M1R9 [ΩM]	M1RX [ΩM]	GR [%]	RES [%]	DT [%]	DTC [%]	DEN [%]	CNC [%]	K [%]	U [%]	TH [%]
K18-8	K-1	Rotl.	U Slochteren	3821.74	54.11	3.82	71.78	72.90	2.44	11.14	2.44	0.84	4.45	1.96	2.48	3.15	3.82	4.26	4.68	13.08	47.15	36.91	3.44	30.46	22.98	12.72	2.21	8.81
K18-8	K-2	Rotl.	U Slochteren	3824.33	38.96	2.97	71.13	70.94	2.48	7.76	1.67	1.40	2.01	1.90	2.19	2.50	2.97	3.37	3.84	4.76	2.61	14.77	19.83	8.11	6.37	2.03	2.99	3.24
K18-8	K-3	Rotl.	U Slochteren	3827.22	54.72	2.17	75.14	74.32	2.48	9.55	2.10	1.48	3.82	1.49	1.77	1.96	2.17	2.29	2.47	8.07	4.94	6.21	8.44	20.54	11.00	2.51	4.93	16.30
K18-8	K-4	Rotl.	U Slochteren	3830.12	59.25	1.83	72.44	71.19	2.50	12.23	2.55	0.84	6.00	1.29	1.67	1.85	1.83	1.82	1.81	5.54	1.80	6.67	4.19	8.11	6.24	5.22	6.00	6.56
K18-8	K-5	Rotl.	U Slochteren	3833.01	53.32	2.08	71.23	69.96	2.54	12.38	2.38	1.68	4.35	1.41	1.80	2.02	2.08	2.11	2.15	3.57	2.75	10.22	8.55	6.13	7.07	2.48	4.64	2.99
K18-8	K-7	Rotl.	U Slochteren	3838.50	61.72	3.73	70.48	69.71	2.52	8.09	2.65	1.25	6.23	2.41	2.97	3.40	3.73	3.95	4.23	15.95	46.68	17.59	13.55	13.70	11.89	9.47	6.82	19.89
K18-8	K-8	Rotl.	U Slochteren	3842.31	49.38	3.66	67.77	65.29	2.51	8.95	2.20	0.85	3.68	2.85	3.11	3.39	3.66	3.88	4.13	6.46	7.31	37.95	23.96	16.76	10.48	4.60	6.66	2.81
K18-8	K-9	Rotl.	L Slochteren	3940.91	48.42	3.49	64.59	63.41	2.55	7.42	2.26	0.48	3.98	2.77	3.20	3.42	3.49	3.55	3.56	6.52	1.15	7.89	3.08	10.45	6.34	3.60	9.25	3.43
K18-8	K-10	Rotl.	L Slochteren	3943.35	38.26	3.52	65.01	63.38	2.52	7.28	2.00	0.84	3.50	2.83	3.24	3.45	3.52	3.52	3.52	2.97	1.33	4.41	2.24	9.73	2.25	1.78	4.17	3.37
K18-8	K-11	Rotl.	L Slochteren	3947.01	44.43	10.88	60.24	60.22	2.60	5.39	2.21	1.17	3.77	7.87	9.81	10.53	10.88	10.71	11.10	10.90	35.15	8.74	6.70	14.78	4.61	9.14	8.22	20.32
K18-8	K-12	Rotl.	L Slochteren	3949.75	56.17	17.52	57.93	57.63	2.63	5.69	2.34	1.89	4.67	12.68	15.87	16.88	17.52	17.82	21.12	9.13	48.23	5.02	5.07	7.75	7.40	16.89	6.68	13.84
K18-8	K-13	Rotl.	L Slochteren	3951.88	31.59	8.17	57.58	57.46	2.60	4.76	1.09	1.33	3.29	7.62	8.39	8.36	8.17	8.57	9.10	3.45	53.40	40.92	25.49	33.88	22.61	2.51	1.06	12.62
K18-8	K-15	Rotl.	L Slochteren	3957.98	36.79	1.09	72.07	70.49	2.49	10.61	1.63	1.29	2.77	1.10	1.10	1.10	1.09	1.10	1.11	3.30	0.39	8.30	5.72	9.01	7.55	2.81	2.87	4.93
K18-8	K-16	Rotl.	L Slochteren	3961.03	42.99	1.00	73.10	71.57	2.45	11.70	1.73	0.98	3.26	0.97	1.03	1.03	1.00	0.99	0.98	2.40	0.24	4.54	4.08	6.31	4.96	4.37	2.63	3.39
K18-8	K-18	Rotl.	L Slochteren	3966.82	31.68	1.17	67.94	67.27	2.50	9.12	1.49	1.48	1.81	1.21	1.18	1.16	1.17	1.18	1.22	10.75	1.80	8.75	4.51	6.49	5.04	11.39	0.80	6.39
K18-8	K-19	Rotl.	L Slochteren	3969.56	43.55	2.00	68.18	67.51	2.53	9.13	1.88	1.03	3.56	1.93	1.99	2.00	2.00	2.00	2.04	4.64	0.71	4.85	2.01	7.03	11.84	1.41	0.75	1.24
K18-8	K-20	Rotl.	L Slochteren	3972.00	42.34	2.90	64.75	63.44	2.53	7.07	1.71	1.65	4.50	3.05	3.04	3.00	2.90	2.84	2.81	8.85	3.31	8.34	6.59	7.21	8.68	5.61	7.69	5.49
K18-8	K-21	Rotl.	L Slochteren	3974.90	48.07	4.01	62.16	62.19	2.52	9.30	1.32	1.29	6.70	4.07	4.16	4.14	4.01	3.96	3.99	9.09	5.34	4.15	2.51	11.17	5.95	2.12	9.73	10.46
K18-8	K-22	Rotl.	L Slochteren	3977.49	24.18	1.65	64.24	63.89	2.47	9.66	0.92	0.53	2.72	1.57	1.62	1.65	1.65	1.66	1.65	2.35	0.61	6.86	6.49	7.93	5.23	3.88	4.67	2.20
K18-8	K-23	Rotl.	L Slochteren	3978.86	29.99	1.40	66.38	65.17	2.45	10.72	1.06	0.97	4.01	1.54	1.48	1.44	1.40	1.38	1.37	5.49	1.67	8.41	7.66	8.29	8.10	5.38	1.31	5.00
K18-8	K-24	Rotl.	L Slochteren	3981.60	29.35	3.61	60.95	61.25	2.60	9.24	1.08	0.31	5.01	4.26	4.13	3.89	3.61	3.55	3.50	2.88	2.11	8.24	5.54	18.92	6.54	4.26	5.80	4.24
K18-8	K-25	Rotl.	L Slochteren	3984.50	23.44	1.14	65.09	65.43	2.46	11.33	0.79	1.16	2.40	1.18	1.19	1.17	1.14	1.14	1.13	2.91	0.19	2.49	3.34	9.91	3.83	2.59	3.00	3.86
K18-8	K-26	Rotl.	L Slochteren	3987.24	26.73	1.39	64.77	64.79	2.46	10.23	1.01	0.42	2.51	1.57	1.49	1.42	1.39	1.37	1.38	1.69	0.66	2.85	5.26	7.03	3.69	1.01	3.41	3.95
K18-8	K-27	Rotl.	L Slochteren	3989.83	27.86	1.74	65.44	64.25	2.48	10.43	1.08	1.21	2.62	1.69	1.80	1.78	1.74	1.71	1.69	2.36	1.26	2.68	2.36	7.39	3.96	1.59	2.91	9.39
K18-8	K-28	Rotl.	L Slochteren	3992.73	49.55	4.22	62.72	62.36	2.51	6.47	1.59	2.63	5.26	4.43	4.68	4.54	4.22	4.16	4.19	15.93	1.51	2.98	2.40	7.93	4.84	2.31	21.63	14.58
K18-8	K-29	Rotl.	L Slochteren	3995.47	40.14	1.19	68.42	67.45	2.53	9.61	1.58	1.58	3.00	1.15	1.20	1.20	1.19	1.20	1.20	4.99	2.83	8.86	3.35	13.34	7.17	2.89	3.63	5.43
K18-8	K-30	Rotl.	L Slochteren	3997.91	52.62	1.61	71.17	70.23	2.46	11.20	2.14	1.67	3.29	1.61	1.63	1.62	1.61	1.62	1.65	2.04	0.65	3.86	5.16	7.21	4.51	6.06	10.23	8.05
K18-8	K-31	Rotl.	L Slochteren	4000.81	46.77	4.43	65.42	65.40	2.56	10.28	2.03	1.68	3.93	4.52	4.65	4.59	4.43	4.44	4.49	4.26	4.19	24.48	16.69	10.99	21.14	10.04	2.50	5.85
K18-8	K-32	Rotl.	L Slochteren	4004.01	49.50	3.98	60.00	60.70	2.60	6.09	1.97	1.07	4.95	4.02	3.95	3.92	3.98	3.96	4.17	10.14	8.45	17.59	12.12	8.11	13.70	6.08	4.87	10.03
L6-8	L-A	LGT	Volprieh. Ss	4077.92	59.85	19.49	58.35	57.80	2.51	2.72	3.11	0.00	2.99	21.49	21.44	20.92	19.49	18.29	16.99	4.82	10.00	2.76	1.21	7.21	5.31	10.21	1.12	2.27
L6-8	L-B	LGT	Volprieh. Ss	4081.12	49.95	15.38	59.06	58.01	2.49	2.50	2.72	0.00	3.09	19.45	18.64	17.10	15.38	14.37	13.55	2.06	4.66	3.56	2.00	7.93	4.80	10.38	0.00	6.13
L6-8	L-C	LGT	Volprieh. Ss	4083.86	45.58	16.34	58.44	57.85	2.54	3.53	2.27	0.02	2.09	21.60	20.74	19.04	16.34	14.90	13.78	6.88	7.26	1.67	2.68	6.31	9.49	9.47	4.61	20.83
L6-8	L-D	LGT	Lower Bunt Ss	4087.37	115.81	11.67	67.17	65.65	2.67	15.19	3.67	3.02	9.06	15.52	18.19	16.87	11.67	9.74	7.85	27.09	10.69	13.00	5.13	8.47	28.81	7.45	22.76	6.45
L6-8	L-E	Rotl.	L Slochteren	4926.94	19.90	1.81	66.38	66.84	2.51	11.93	0.48	0.10	4.66	6.18	3.24	2.31	1.81	1.63	1.49	2.05	0.11	9.79	1.60	6.67	5.49	2.06	3.85	8.25
L6-8	L-F	Rotl.	L Slochteren	4932.27	19.33	3.27	65.56	63.77	2.54	9.57	0.44	0.76	2.42	8.96	5.13	3.90	3.27	3.08	2.95	2.14	1.35	3.06	2.73	7.57	7.03	0.99	1.23	3.56
L6-8	L-G	Rotl.	L Slochteren	4935.47	20.33	2.87	66.33	65.23	2.56	10.20	0.35	0.49	3.81	8.68	4.97	3.64	2.87	2.60	2.40	1.27	0.22	3.97	2.19	3.60	4.24	1.69	1.37	3.94
L6-8	L-I	Rotl.	L Slochteren	4940.66	20.46	4.15	66.17	64.89	2.55	9.15	0.58	0.26	4.35	11.19	6.31	4.86	4.15	3.87	3.78	5.32	1.89	6.30	1.95	3.42	2.46	4.95	12.03	19.10

Table 4-4 - Log values of all the log types of samples from well P2-SE2 and P6-9. On the right part of the table, maximum of change of log values around the samples within ~ ± 60 cm relative to the total range of the cored section can be seen. Cells with "n.a." mean that there was no data available.

Basic data of the samples					Log values at depth of the samples														Log value stability around samples (~± 60 cm)									
Well name	Sample ID	Rock, Goup	Rock, Facies	DEPTH (logger) [m]	GR [GAPI]	RES Comb. [ΩM]	DT [US/F]	DTC [US/F]	DEN [G/C3]	CNC [PU]	K [%]	U [PPM]	TH [PPM]	M1R1 [ΩM]	M1R2 [ΩM]	M1R3 [ΩM]	M1R6 [ΩM]	M1R9 [ΩM]	M1RX [ΩM]	GR [%]	RES [%]	DT [%]	DTC [%]	DEN [%]	CNC [%]	K [%]	U [%]	TH [%]
P2-SE2	P2-6	Rotl.	Sloct. Fr; Zone 3	4469.13	70.88	4.16	n.a.	68.00	2.43	n.a.	n.a.	n.a.	n.a.	n.a.	n.a.	n.a.	n.a.	n.a.	n.a.	15.46	4.83	n.a.	44.28	33.07	n.a.	n.a.	n.a.	n.a.
P2-SE2	P2-7	Rotl.	Sloct. Fr; Zone 3	4472.03	39.33	2.05	n.a.	77.54	2.42	n.a.	n.a.	n.a.	n.a.	n.a.	n.a.	n.a.	n.a.	n.a.	n.a.	4.37	0.81	n.a.	7.23	18.45	n.a.	n.a.	n.a.	n.a.
P2-SE2	P2-9	Rotl.	Sloct. Fr; Zone 3	4477.36	30.77	1.07	n.a.	85.52	2.35	n.a.	n.a.	n.a.	n.a.	n.a.	n.a.	n.a.	n.a.	n.a.	n.a.	3.78	0.34	n.a.	9.29	9.84	n.a.	n.a.	n.a.	n.a.
P2-SE2	P2-10	Rotl.	Sloct. Fr; Zone 3	4479.95	32.71	0.78	n.a.	80.94	2.39	n.a.	n.a.	n.a.	n.a.	n.a.	n.a.	n.a.	n.a.	n.a.	n.a.	2.34	0.29	n.a.	18.13	13.16	n.a.	n.a.	n.a.	n.a.
P2-SE2	P2-14	Rotl.	Sloct. Fr; Zone 3	4490.16	27.85	0.67	n.a.	78.55	2.36	n.a.	n.a.	n.a.	n.a.	n.a.	n.a.	n.a.	n.a.	n.a.	n.a.	1.90	0.07	n.a.	2.04	7.24	n.a.	n.a.	n.a.	n.a.
P2-SE2	P2-15	Rotl.	Sloct. Fr; Zone 3	4492.60	28.20	0.52	n.a.	79.28	2.34	n.a.	n.a.	n.a.	n.a.	n.a.	n.a.	n.a.	n.a.	n.a.	n.a.	2.25	0.17	n.a.	3.27	10.11	n.a.	n.a.	n.a.	n.a.
P2-SE2	P2-18	Rotl.	Sloct. Fr; Zone 3	4500.07	32.51	0.67	n.a.	69.55	2.45	n.a.	n.a.	n.a.	n.a.	n.a.	n.a.	n.a.	n.a.	n.a.	n.a.	5.95	0.67	n.a.	31.21	22.96	n.a.	n.a.	n.a.	n.a.
P2-SE2	P2-19	Rotl.	Sloct. Fr; Zone 3	4502.51	28.41	0.60	n.a.	81.08	2.40	n.a.	n.a.	n.a.	n.a.	n.a.	n.a.	n.a.	n.a.	n.a.	n.a.	3.87	0.09	n.a.	16.36	12.00	n.a.	n.a.	n.a.	n.a.
P2-SE2	P2-20	Rotl.	Sloct. Fr; Zone 3	4504.79	31.96	0.56	n.a.	77.78	2.37	n.a.	n.a.	n.a.	n.a.	n.a.	n.a.	n.a.	n.a.	n.a.	n.a.	3.64	0.14	n.a.	3.87	9.93	n.a.	n.a.	n.a.	n.a.
P2-SE2	P2-21	Rotl.	Sloct. Fr; Zone 3	4507.38	42.47	0.86	n.a.	74.45	2.45	n.a.	n.a.	n.a.	n.a.	n.a.	n.a.	n.a.	n.a.	n.a.	n.a.	7.70	0.56	n.a.	20.87	23.34	n.a.	n.a.	n.a.	n.a.
P2-SE2	P2-22	Rotl.	Sloct. Fr; Zone 3	4509.82	34.78	1.43	n.a.	69.18	2.50	n.a.	n.a.	n.a.	n.a.	n.a.	n.a.	n.a.	n.a.	n.a.	n.a.	36.86	1.97	n.a.	20.88	8.61	n.a.	n.a.	n.a.	n.a.
P2-SE2	P2-23	Rotl.	Sloct. Fr; Zone 4	4519.27	71.95	11.04	n.a.	62.09	2.67	n.a.	n.a.	n.a.	n.a.	n.a.	n.a.	n.a.	n.a.	n.a.	n.a.	10.86	18.77	n.a.	10.60	32.74	n.a.	n.a.	n.a.	n.a.
P2-SE2	P2-24	Rotl.	Sloct. Fr; Zone 4	4522.01	31.02	0.87	n.a.	77.62	2.37	n.a.	n.a.	n.a.	n.a.	n.a.	n.a.	n.a.	n.a.	n.a.	n.a.	2.30	0.06	n.a.	8.95	9.28	n.a.	n.a.	n.a.	n.a.
P2-SE2	P2-25	Rotl.	Sloct. Fr; Zone 4	4524.30	49.69	3.35	n.a.	63.67	2.61	n.a.	n.a.	n.a.	n.a.	n.a.	n.a.	n.a.	n.a.	n.a.	n.a.	15.21	2.72	n.a.	15.80	12.58	n.a.	n.a.	n.a.	n.a.
P2-SE2	P2-27	Rotl.	Sloct. Fr; Zone 4	4529.94	26.40	1.60	n.a.	68.50	2.41	n.a.	n.a.	n.a.	n.a.	n.a.	n.a.	n.a.	n.a.	n.a.	n.a.	1.82	1.97	n.a.	9.63	15.21	n.a.	n.a.	n.a.	n.a.
P2-SE2	P2-28	Rotl.	Sloct. Fr; Zone 4	4532.38	27.51	4.30	n.a.	61.74	2.56	n.a.	n.a.	n.a.	n.a.	n.a.	n.a.	n.a.	n.a.	n.a.	n.a.	9.02	5.34	n.a.	17.11	9.17	n.a.	n.a.	n.a.	n.a.
P2-SE2	P2-29	Rotl.	Sloct. Fr; Zone 4	4535.12	34.17	7.43	n.a.	60.51	2.63	n.a.	n.a.	n.a.	n.a.	n.a.	n.a.	n.a.	n.a.	n.a.	n.a.	5.77	2.26	n.a.	12.65	12.92	n.a.	n.a.	n.a.	n.a.
P6-9	P6-10	LGT	Hardegsen Frm.	2744.11	109.60	4.21	n.a.	73.93	2.62	n.a.	n.a.	n.a.	n.a.	n.a.	n.a.	n.a.	n.a.	n.a.	n.a.	12.73	27.82	n.a.	12.98	3.48	n.a.	n.a.	n.a.	n.a.
P6-9	P6-12	LGT	Hardegsen Frm.	2747.92	103.75	5.56	n.a.	75.46	2.56	n.a.	n.a.	n.a.	n.a.	n.a.	n.a.	n.a.	n.a.	n.a.	n.a.	25.13	26.46	n.a.	19.86	4.20	n.a.	n.a.	n.a.	n.a.
P6-9	P6-14	LGT	Hardegsen Frm.	2751.89	85.86	6.23	n.a.	72.99	2.55	n.a.	n.a.	n.a.	n.a.	n.a.	n.a.	n.a.	n.a.	n.a.	n.a.	29.18	17.22	n.a.	29.18	11.55	n.a.	n.a.	n.a.	n.a.
P6-9	P6-15	LGT	Hardegsen Frm.	2754.17	103.35	2.69	n.a.	78.37	2.51	n.a.	n.a.	n.a.	n.a.	n.a.	n.a.	n.a.	n.a.	n.a.	n.a.	21.32	4.22	n.a.	18.24	26.56	n.a.	n.a.	n.a.	n.a.
P6-9	P6-20	LGT	L. Detfurth Ss	2789.83	74.37	2.60	n.a.	78.92	2.42	n.a.	n.a.	n.a.	n.a.	n.a.	n.a.	n.a.	n.a.	n.a.	n.a.	7.15	2.61	n.a.	11.70	11.08	n.a.	n.a.	n.a.	n.a.
P6-9	P6-22	LGT	L. Detfurth Ss	2793.95	69.64	1.45	n.a.	77.60	2.47	n.a.	n.a.	n.a.	n.a.	n.a.	n.a.	n.a.	n.a.	n.a.	n.a.	12.71	8.66	n.a.	5.57	18.53	n.a.	n.a.	n.a.	n.a.
P6-9	P6-26	LGT	L. Detfurth Ss	2803.25	82.37	7.69	n.a.	75.35	2.52	n.a.	n.a.	n.a.	n.a.	n.a.	n.a.	n.a.	n.a.	n.a.	n.a.	2.77	7.26	n.a.	3.25	12.02	n.a.	n.a.	n.a.	n.a.
P6-9	P6-35	LGT	L Volpierh. Ss	2907.49	83.62	9.33	n.a.	70.70	2.57	n.a.	n.a.	n.a.	n.a.	n.a.	n.a.	n.a.	n.a.	n.a.	n.a.	3.45	10.18	n.a.	7.34	18.47	n.a.	n.a.	n.a.	n.a.
P6-9	P6-40	Rotl.	Slocteren Fr.	3636.26	44.26	0.95	n.a.	75.27	2.42	n.a.	n.a.	n.a.	n.a.	n.a.	n.a.	n.a.	n.a.	n.a.	n.a.	4.56	0.13	n.a.	8.83	1.75	n.a.	n.a.	n.a.	n.a.
P6-9	P6-43	Rotl.	Slocteren Fr.	3642.51	41.91	9.16	n.a.	61.04	2.56	n.a.	n.a.	n.a.	n.a.	n.a.	n.a.	n.a.	n.a.	n.a.	n.a.	7.38	2.36	n.a.	4.74	6.74	n.a.	n.a.	n.a.	n.a.

4.3.2 Rock physical and mechanical measurement results

Rock physical and rock mechanical measurement results (matrix density, bulk density and porosity (PHI), unconfined compressive strengths and elastic moduli) of the core samples can be seen on Table 4-5 and Table 4-6. Figure 4-12 shows all the measured unconfined compressive strength tests that were involved in the regression calculation. As it can be seen in the Table 4-6, strength of two samples (P2-SE2/7 and P2-SE2/20) were not measured because of their not appropriate quality. Six core samples allowed preparing two plugs. These samples located next to each other (maximum distance between these ones was 4 cm). From these sample couples, the samples with lower quality were measured first without loop. Samples P6-9/22-1 was shorter than the requirement and plug ends were broken and P6-9/26-1 had slightly broken, not even and not perpendicular ends as the requirement. Result of these can be found in the column of the tables named UCS Nr 1.

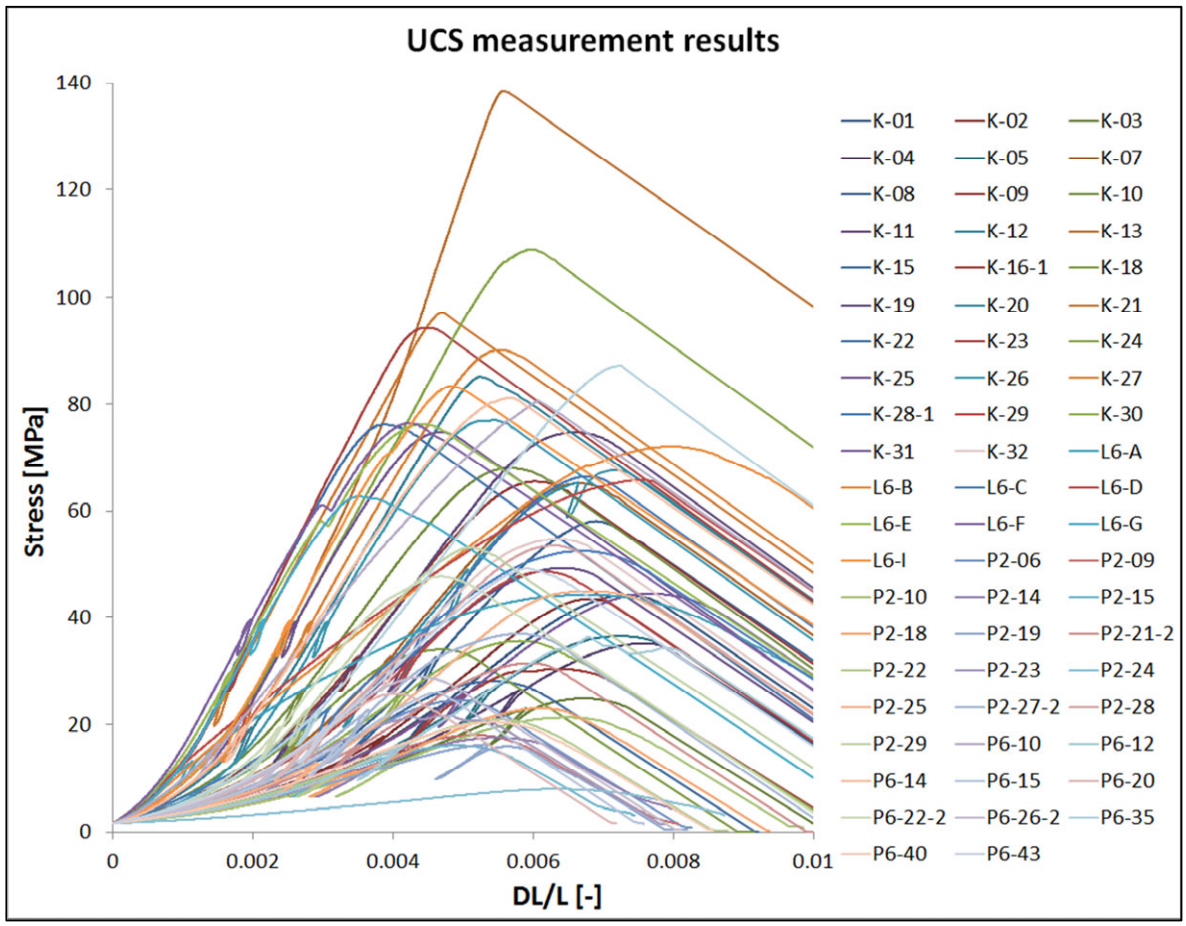

Figure 4-12 – The stress and strain curves (after calibration correction) of all the measured samples (62) with unload-reload loop. Values of UCS cover the range of 8 MPa to 138 MPa.

The UCS values of sample couples (core plugs where double samples were prepared) were compared with each other. The difference between UCS of sample couples of K-16 and K-28 is small approximately 2% (~1 MPa). Sample P2-SE2/27-1 without unloading-reloading loop had 9 % higher UCS than P2-SE2/27-2 (37 and 40 MPa) this difference is small. The differences between UCS of the sample couples of samples P6-22 and P6-26 were relatively high, approximately 35%. However, sample P6-22 measured without loop was shorter (33 mm) than the standard and broken; and, plugs of sample P6-26 were slightly different because of the clay layers. Furthermore, for both samples P6-22 and P6-26, the UCS measured without loop, were lower than UCS with loop. Sample P2-SE2/21-1, measured without loop, had significantly lower (-38 %) UCS than P2-SE2/22-2 measured with loop. The reason for this was some possible invisible damage and cracks because of the preparation.

The water saturation of the plug samples for the unconfined compressive strength tests were always higher than 2 %, except in case of three samples, namely: L6-8/A (1.4%), L6-8/D (1.7 %) and P6-9/12 (1.3%). The saturation of the samples did not increase over these values after approximately 90 minutes. During saturation, salt dissolved from samples L6-8/A, B, C and D therefore these samples were saturated longer to get rid of the salt content of the pores. After the saturation of these samples, no structural change was experienced due to the water.

The unload-reload loop was not accomplished at three samples (P2-23, P2-24 and P6-40); because the sample strength was lower than the start point of the planned unloading. The unload-reload loops were very close to the breaking point at two samples that could have effect on the strength of the samples (K-3; P2-19).

Static elastic moduli were calculated both on loading and unloading sections of stress and strain curves (see: chapter 4.2.4). The calculated elastic moduli can be found in Table 4-5 and Table 4-6.

In addition, the observed fracturing types of the samples can be found in the Table 4-5 and Table 4-6. Four different types of fractures were distinguished; such as, single shear fracture (shear/), shear fracture with its conjugate fractures (shearX), open fractures and combination of open and shear fractures (hybrid).

Table 4-5 - Rock mechanical measurements results (UCS, elastic modulus) from unconfined compression test and rock physical measurements results (matrix- and bulk density, porosity, water saturation) of the core samples from well K-18 and L6-8. In addition, the type of fracturing, as a result of UCS tests, is listed in the table.

Well Name	Plug ID.	Measred depth BRT (m)	TVDSS (m)	Lab measurement results											
				Matrix Density [g/cm3]	Bulk Density [g/cm3]	PHI [%]	UCS [MPa]	Water Saturation [%]	UCS Nr 2 [MPa]	Water Saturat. [%]	Fracturing type	E [GPa]	R^2 for E	E - unload [GPa]	R^2 for E-unload
K18-8	K-1	3822.09	3790.64	2.698	2.371	12.1	44.3	3.9%	-	-	Shear/	10.02	1.0000	15.96	0.9992
K18-8	K-2	3824.71	3799.12	2.700	2.391	11.4	43.5	3.9%	-	-	ShearX	10.25	0.9995	13.00	0.9980
K18-8	K-3	3827.65	3808.60	2.666	2.406	9.8	24.8	3.9%	-	-	Hybrid	5.38	0.9998	13.36	0.9990
K18-8	K-4	3830.49	3817.73	2.708	2.475	8.6	35.1	3.8%	-	-	Shear/	7.49	0.9987	17.08	0.9993
K18-8	K-5	3833.43	3827.21	2.694	2.511	6.8	36.5	3.5%	-	-	ShearX	8.08	0.9976	18.65	0.9986
K18-8	K-7	3838.90	3844.91	2.702	2.468	8.7	65.1	3.6%	-	-	ShearX	15.48	0.9997	26.69	0.9980
K18-8	K-8	3842.65	3856.97	2.686	2.515	6.4	58.1	3.5%	-	-	ShearX	14.25	0.9995	26.96	0.9978
K18-8	K-9	3940.52	3843.37	2.689	2.507	6.7	65.5	3.8%	-	-	ShearX	16.80	0.9999	29.25	0.9970
K18-8	K-10	3943.06	3874.51	2.692	2.505	6.9	68.0	3.8%	-	-	ShearX	18.01	1.0000	28.30	0.9974
K18-8	K-11	3946.63	3918.62	2.685	2.577	4.0	74.7	3.4%	-	-	ShearX	16.57	0.9987	21.13	0.9986
K18-8	K-12	3949.32	3951.61	2.721	2.641	2.9	85.1	2.4%	-	-	ShearX	21.53	0.9994	30.12	0.9976
K18-8	K-13	3951.65	3839.39	2.714	2.618	3.6	138.4	2.1%	-	-	ShearX	30.80	0.9943	52.94	0.9847
K18-8	K-15	3957.71	3869.15	2.675	2.329	12.9	28.1	4.5%	-	-	Hybrid	7.93	0.9989	13.37	0.9991
K18-8	K-16	3960.74	3883.99	2.659	2.357	11.4	30.4	5.6%	31.1	7.5%	Shear/	8.16	0.9990	13.41	0.9961
K18-8	K-18	3966.49	3866.17	2.689	2.434	9.5	34.0	4.4%	-	-	ShearX	11.56	0.9999	17.55	0.9991
K18-8	K-19	3969.28	3871.61	2.733	2.457	10.1	49.2	3.8%	-	-	Shear/	11.15	0.9990	23.50	0.9989
K18-8	K-20	3971.73	3876.31	2.708	2.512	7.2	67.7	3.8%	-	-	Shear/	15.78	0.9998	25.26	0.9988
K18-8	K-21	3974.61	3881.90	2.715	2.508	7.6	97.1	3.9%	-	-	Shear/	24.55	1.0000	40.10	0.9916
K18-8	K-22	3977.25	3964.87	2.685	2.377	11.5	76.1	3.5%	-	-	ShearX	26.30	0.9997	38.90	0.9890
K18-8	K-23	3978.71	3839.67	2.677	2.433	9.1	94.3	3.8%	-	-	ShearX	27.54	0.9999	43.50	0.9896
K18-8	K-24	3981.44	3853.32	2.698	2.526	6.4	108.8	3.2%	-	-	ShearX	23.69	1.0000	45.66	0.9886
K18-8	K-25	3984.38	3867.91	2.679	2.381	11.1	74.8	3.6%	-	-	ShearX	22.76	0.9997	40.60	0.9926
K18-8	K-26	3987.05	3881.12	2.692	2.425	9.9	76.9	3.6%	-	-	ShearX	21.90	0.9995	40.17	0.9935
K18-8	K-27	3989.77	3894.52	2.669	2.431	8.9	90.2	3.8%	-	-	ShearX	23.10	1.0000	38.85	0.9929
K18-8	K-28	3992.57	3908.37	2.672	2.492	6.7	66.4	3.8%	67.5	3.9%	ShearX	16.62	0.9998	27.53	0.9981
K18-8	K-29	3995.36	3922.22	2.772	2.464	11.1	48.6	3.5%	-	-	ShearX	12.71	0.9999	24.99	0.9999
K18-8	K-30	3997.92	3934.78	2.686	2.427	9.6	35.6	3.9%	-	-	Hybrid	9.42	0.9990	18.22	0.9992
K18-8	K-31	4000.77	3948.78	2.700	2.526	6.4	44.5	3.7%	-	-	ShearX	9.76	0.9995	18.85	0.9992
K18-8	K-32	4003.98	3964.80	2.709	2.588	4.4	54.8	3.6%	-	-	ShearX	14.22	0.9994	31.32	0.9958
L6-8	L-A	4077.96	4077.96	2.733	2.368	13.4	44.3	3.7%	-	-	Open	8.53	0.9978	25.33	0.9959
L6-8	L-B	4081.08	4081.08	2.693	2.477	8.0	72.1	1.4%	-	-	ShearX	10.20	1.0000	36.19	0.9973
L6-8	L-C	4083.84	4083.84	2.691	2.567	4.6	52.4	2.0%	-	-	ShearX	11.83	0.9998	35.42	0.9967
L6-8	L-D	4087.40	4087.40	2.608	2.440	6.4	65.8	1.7%	-	-	Shear/	10.02	0.9994	36.27	0.9961
L6-8	L-E	4926.44	4926.44	2.689	2.399	10.8	76.2	2.7%	-	-	Shear/	22.90	0.9995	36.91	0.9935
L6-8	L-F	4931.84	4931.84	2.687	2.450	8.8	76.4	3.0%	-	-	ShearX	22.76	0.9994	41.15	0.9903
L6-8	L-G	4935.00	4935.00	2.709	2.441	9.9	62.7	3.3%	-	-	Shear/	21.51	0.9995	40.63	0.9888
L6-8	L-I	4940.14	4940.14	2.698	2.473	8.4	83.4	3.4%	-	-	ShearX	24.39	0.9997	41.96	0.9891

Table 4-6 - Rock mechanical measurements results (UCS, elastic modulus) from unconfined compression test and rock physical measurements results (matrix- and bulk density, porosity, water saturation) of the core samples from well P2-SE2 and P6-9. In addition, the type of fracturing, as a result of UCS tests, is listed in the table.

Well Name	Plug Nr.	Measred depth BRT (m)	TVDSS (m)	Lab measurement results											
				Matrix Density [g/cm3]	Bulk Density [g/cm3]	PHI [%]	UCS [MPa]	Water Saturation [%]	UCS Nr 2 [MPa]	Water Saturat. [%]	Fracturing type	E [GPa]	R^2 for E	E - unload [GPa]	R^2 for E-unload
P2-SE2	P2-6	4459.67	3366.88	2.716	2.318	14.7	24.5	4.0%	-	-	Hybrid	7.04	1.0000	10.36	0.9975
P2-SE2	P2-7	4462.55	3367.42	2.542	2.065	18.8	-	-	-	-	-	-	-	-	-
P2-SE2	P2-9	4467.85	3367.46	2.939	2.379	19.1	18.0	4.0%	-	-	Hybrid	4.54	0.9990	7.52	0.9975
P2-SE2	P2-10	4470.50	3367.77	2.724	2.284	16.1	21.3	3.8%	-	-	Shear/	5.02	0.9993	7.84	0.9931
P2-SE2	P2-14	4480.62	3368.95	2.687	2.197	18.2	17.6	4.0%	-	-	Open	4.22	0.9981	7.33	0.9949
P2-SE2	P2-15	4483.08	3369.23	2.684	2.154	19.7	16.2	4.1%	-	-	Shear/	4.08	0.9981	7.16	0.9975
P2-SE2	P2-18	4490.73	3370.11	2.730	2.271	16.8	23.0	4.9%	-	-	Open	5.57	0.9999	7.46	0.9966
P2-SE2	P2-19	4493.15	3370.21	2.674	2.223	16.8	16.4	4.9%	-	-	Open	3.75	0.9998	8.33	0.9978
P2-SE2	P2-20	4495.64	3370.46	2.660	1.920	27.8	-	-	-	-	-	-	-	-	-
P2-SE2	P2-21	4498.22	3370.71	2.699	2.339	13.3	31.5	5.4%	22.9	5.6%	ShearX	8.17	1.0000	11.86	0.9961
P2-SE2	P2-22	4500.69	3370.95	2.700	2.358	12.7	20.9	4.3%	-	-	Open	5.48	0.9998	8.35	0.9962
P2-SE2	P2-23	4510.39	3371.90	2.718	2.615	3.8	21.6	2.2%	-	-	Shear/	6.27	0.9977	-	-
P2-SE2	P2-24	4513.19	3372.14	2.683	2.176	18.9	8.0	4.3%	-	-	Open	1.22	0.9995	-	-
P2-SE2	P2-25	4515.56	3372.41	2.679	2.445	8.8	45.0	3.8%	-	-	Shear/	10.48	0.9982	11.10	0.9932
P2-SE2	P2-27	4521.15	3372.97	2.671	2.454	8.1	36.9	4.6%	40.3	1.3%	ShearX;Sh/	11.26	0.9997	18.59	0.9951
P2-SE2	P2-28	4523.64	3373.22	2.692	2.535	5.8	53.4	2.5%	-	-	ShearX	13.63	0.9999	21.61	0.9979
P2-SE2	P2-29	4526.31	3373.49	2.722	2.587	5.0	53.1	3.1%	-	-	ShearX	16.46	0.9999	28.48	0.9972
P6-9	P6-10	2744.35	2700.78	2.831	2.605	8.0	80.6	3.1%	-	-	Shear/	16.01	0.9998	24.73	0.9986
P6-9	P6-12	2748.09	2704.50	2.727	2.535	7.1	36.3	1.3%	-	-	Shear/	8.51	0.9995	11.10	0.9956
P6-9	P6-14	2752.07	2708.50	2.705	2.367	12.5	81.1	4.1%	-	-	Shear/	19.82	0.9999	26.70	0.9966
P6-9	P6-15	2754.35	2710.78	2.713	2.361	13.0	26.0	3.6%	-	-	ShearX	8.73	0.9995	14.02	0.9972
P6-9	P6-20	2790.18	2746.57	2.683	2.331	13.1	25.7	3.5%	-	-	Open	10.14	0.9995	15.33	0.9978
P6-9	P6-22	2794.37	2750.72	2.681	2.445	8.8	47.7	3.2%	34.2	3.9%	Shear/	17.41	1.0000	20.65	0.9914
P6-9	P6-26	2803.63	2759.94	2.690	2.412	10.3	28.8	2.6%	22.1	1.1%	Open; Sh/	9.90	1.0000	13.49	0.9985
P6-9	P6-35	2906.86	2862.94	2.703	2.519	6.8	87.2	3.6%	-	-	Shear/	16.82	0.9994	23.78	0.9985
P6-9	P6-40	3633.80	3508.88	2.701	2.258	16.4	20.4	4.1%	-	-	Hybrid	4.85	0.9998	-	-
P6-9	P6-43	3640.12	3513.53	2.731	2.513	8.0	49.1	3.6%	-	-	Open	11.91	0.9997	17.56	0.9984

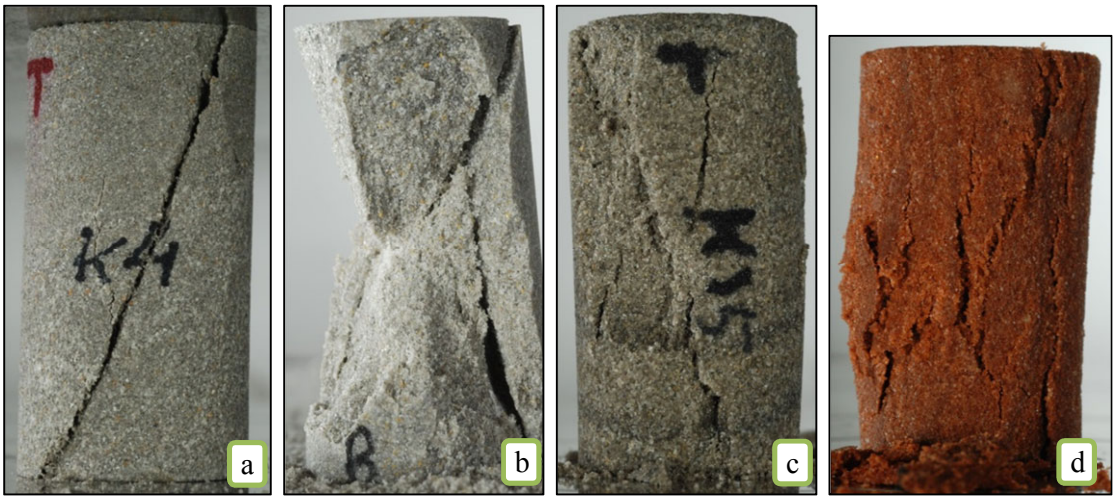

Figure 4-13 – Observed fracturing types, as a result of the compression tests. Image (a (K18-8/4): shear fracture with single fault plane (shear/) type of fracture; (b (K18-8/27): shear fracture with conjugate fault planes (shearX) type of fractures; (c (K18-8/15): shear fracture with mixed open and shear (hybrid) type of fractures and (d (L6-8/A) open (open) type of fracture.

4.3.3 Results of regression analysis of UCS versus well logs

CHECKING OF RESISTIVITY LOGS

From the four wells, two different resistivity logs were received. From well K18-8 and L6-8 "1 Foot Vertical Resolution Matched Res. – DOI" 10 (M1R1), 20 (M1R2), 30(M1R3), 60(M1R6), 90 (M1R9), 120 (M1RX) inch logs while from wells P2-SE2 and P6-9 only one log was available. Therefore, first it was checked which resistivity provides the best fit to UCS. These regression results can be seen on Table 4-7. The 60 inch log had the highest regression coefficient. This was expectable because this has middle length that means longer penetration into the rock but not too long and it can be still sensitive for "sudden" changes in rock properties. The 60 inch log combined with the other single resistivity log was used for the regression calculations.

Table 4-7 – Regression calculation results of different resistivity logs against UCS. The most right column contains the type of the resistivity.

Num. of observa-tion	Multiple R	R Square	Adjusted R Square	F	Signifi-cance F	Y	X1	X2	X3
36	0.673	**0.452**	0.401	8.808	2.1E-04	UCS	DTC	DEN	M1R1
36	0.698	**0.488**	0.440	10.150	7.5E-05	UCS	DTC	DEN	M1R2
36	0.705	**0.498**	0.451	10.566	5.5E-05	UCS	DTC	DEN	M1R3
36	0.715	**0.512**	0.466	11.177	3.5E-05	UCS	DTC	DEN	M1R6
36	0.711	**0.506**	0.460	10.924	4.3E-05	UCS	DTC	DEN	M1R9
36	0.691	**0.478**	0.429	9.760	1.0E-04	UCS	DTC	DEN	M1RX

OUTLIER CHECKING

First, the outliers were filtered. Regression of UCS was calculated against P-wave slowness (DTC), density (DEN), resistivity (RES) and gamma ray (GR). The result of these regressions can be found in Table 4-8. In the first column, the model identification numbers can be found. The second column contains the number of samples involved in the calculations. The following six columns contain statistical parameter of the regression. On the right side of the table, the calculation's variables and the involved logs are listed. Figure 4-14 shows, on the left, the predicted results against the measured data where the green dashed line is the theoretical, perfectly predicted case. On the right side of the Figure 4-14, a histogram of residuals can be seen showing the standard normal distribution of the residuals which is a requirement for a valid model. Furthermore, the histogram shows that only few samples have relatively high residuals.

Table 4-8 – Result of the multivariate regression of all the 62 samples can be seen UCS against P-wave interval travel time, density, resistivity and gamma ray values.

Mod. Id.	Num. of observa-tion	R Square	Std. Error	F	Signifi-cance F	Sum of abs. Residuals	Sum of abs Standard Residuals	Y	X1	X2	X3	X4	Rock group	Dataset informaton
1	62	0.439	20.9	11.1	9.5E-07	972.4	48.1	UCS	DTC	DEN	RES	GR	All	
2	61	0.424	19.5	10.3	2.6E-06	915.6	48.6	UCS	DTC	DEN	RES	GR	All	Excl: K-13
3	61	0.493	19.9	13.6	8.3E-08	929.2	48.4	UCS	DTC	DEN	RES	GR	All	Excl: P2-23
4	61	0.418	21.0	10.1	3.3E-06	961.3	47.3	UCS	DTC	DEN	RES	GR	All	Excl: P2-24
5	60	0.480	18.5	12.7	2.3E-07	868.5	48.7	UCS	DTC	DEN	RES	GR	All	Excl:K-13, P2-23
6	60	0.401	19.6	9.2	9.3E-06	904.7	47.9	UCS	DTC	DEN	RES	GR	All	Excl:K-13, P2-24
6a	59	0.457	18.6	11.3	9.4E-07	856.5	47.8	UCS	DTC	DEN	RES	GR	All	Excl:K-13, P2-23, P2-24

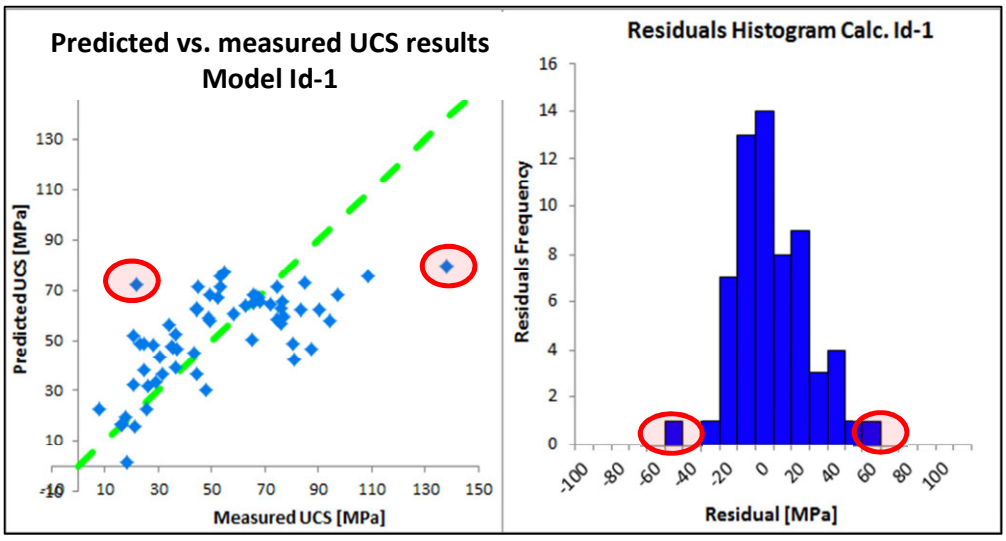

Figure 4-14 - On the left, the cross-plot shows the measured- against predicted UCS values of Model-1. Green dashed line shows the theoretical (predicted = measured) line. On the right, residual histogram of Model-1 can be seen.

Figure 4-15 shows the residuals of the regression of all the measured samples. Samples K18-8/13; K18-8/23; K18-8/24; P2-SE2/23; P6-9/10; P6-9/14; P6-9/35 were found as potential outliers, because their residuals were high (>35 MPa). Only sample K18-8/13 and P2-SE2/23 have reasons for excluding from the study. Sample K18-8/13 had much larger grains (>10 mm) than the maximum allowed size (2 mm); and consequently, its strength was higher than as it was expected. Sample P2-SE2/23 had numerous grains which had around 2 mm of diameter; its structure was quite heterogeneous with embedded clay fractions and the plug-end quality was lower than the average of the plugs; its strength was lower than the expected. In addition, sample P2-SE2/24 had significantly lower UCS. However, its residual was relatively low so this was not excluded. In conclusion, only two samples, namely K18-8/13, P2-SE2/23, were excluded from the calculation.

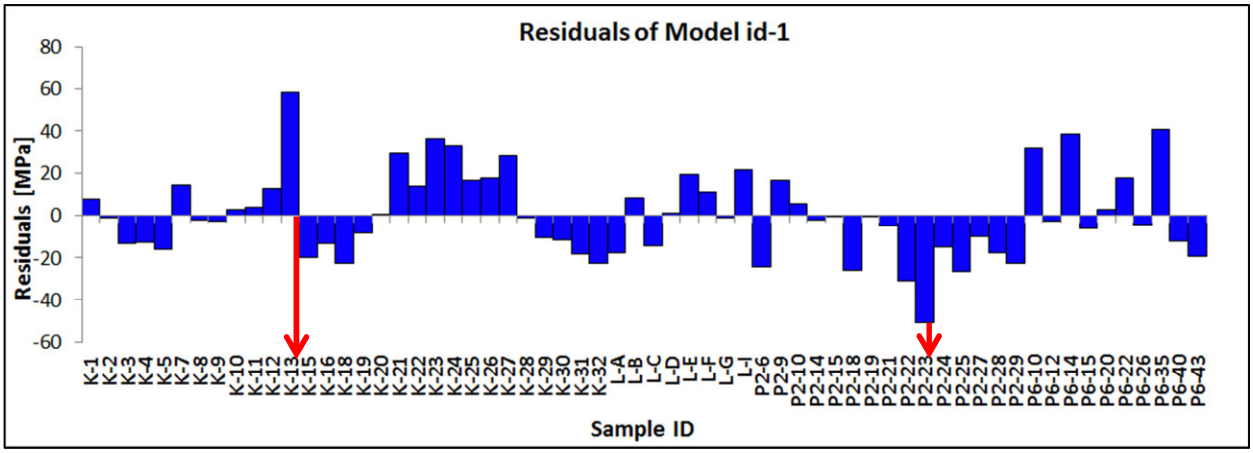

Figure 4-15 – Residuals histograms of regression of all the measured UCS results vs. DTC, density and UCS against DTC, density, gamma ray, resistivity.

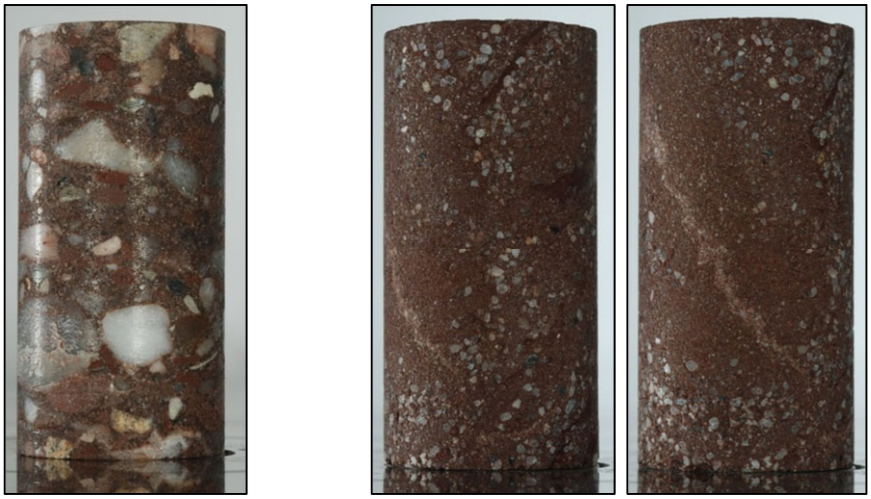

Figure 4-16 – On the left, photo of sample K18-8/13 can be seen. On the right, two photo of sample P2-SE-2/23 can be seen. These two samples were skipped from the regression calculation because of their quality (grain size, inhomogeneity).

REGRESSION ANALYSIS RESULTS COMBINED ALL THE SAMPLES

LINEAR REGRESSION OF ALL THE SAMPLES

The linear regression parameters of all the samples can be seen on Table 4-9. Sonic transit time of P-wave (DTC) showed the highest regression coefficient square (0.42) out of single regression calculations. The Multivariate regression of combined all the four logs, which were available from all the wells, gave regression coefficient square 0.48. On the left of Figure 4-17 the prediction results against the measured data are shown. Points in the cross-plot show similar tendency to the green dashed line which is the theoretical, perfectly predicted case. However, relatively large uncertainty of the prediction also can be seen. The histogram of the residuals is presented on the right of Figure 4-17. On this histogram, residual distribution shows normal distribution which proves that the relation between the predicted data (UCS, Y) and predictors (log data as X1, X2...) and it is not just as a result of accident.

Besides DT, DEN, GR, RES logs further logs were available only from wells K18-8 and L6-8; such as, neutron porosity (CNC), spectral gamma ray: Potassium (K), Thorium (TH), and Uranium (U). This means we had only 36 samples instead of 57 for these calculations. Therefore, the effect of the sample number (observations) on the regression coefficient was tested. The regression of UCS against DTC, DEN, RES, GR (Table 4-9 Model-14) was repeated but using only samples from wells K18-8 and L6-8. In the first row of (Model-14a), the result of this calculation can be seen. The regression coefficient was only slightly higher (0.51). In conclusion, there is no significant effect of sample number on regression. Table 4-10 shows the results of the linear multivariate regression with these logs.

Table 4-9 – Results of regression analysis of all the samples (two outliers excluded). UCS against P-wave transit time (DTC), density (DEN), resistivity (RES), gamma ray (GR).

Mod. Id.	Num. of observa-tion	R^2	Std. Error	F	Signifi-cance F	Sum of abs. Residuals	Sum of abs Standard Residuals	Y	X1	X2	X3	X4	Rock group
7	60	**0.424**	18.9	42.7	1.7E-08	885.8	47.2	**UCS**	DTC				All
8	60	**0.325**	20.5	27.9	2.0E-06	1001.1	49.2	**UCS**	DEN				All
9	60	**0.000**	24.9	0.0	8.8E-01	1259.6	50.9	**UCS**	GR				All
10	60	**0.096**	23.7	6.2	1.6E-02	1178.3	50.1	**UCS**	RES				All
11	60	**0.466**	18.4	24.9	1.7E-08	866.5	47.9	**UCS**	DTC	DEN			All
12	60	**0.467**	18.5	16.4	9.4E-08	867.7	48.0	**UCS**	DTC	DEN	GR		All
13	60	**0.478**	18.3	17.1	5.2E-08	867.9	48.6	**UCS**	DTC	DEN	RES		All
14	60	**0.480**	18.5	12.7	2.3E-07	868.5	48.7	**UCS**	DTC	DEN	RES	GR	All

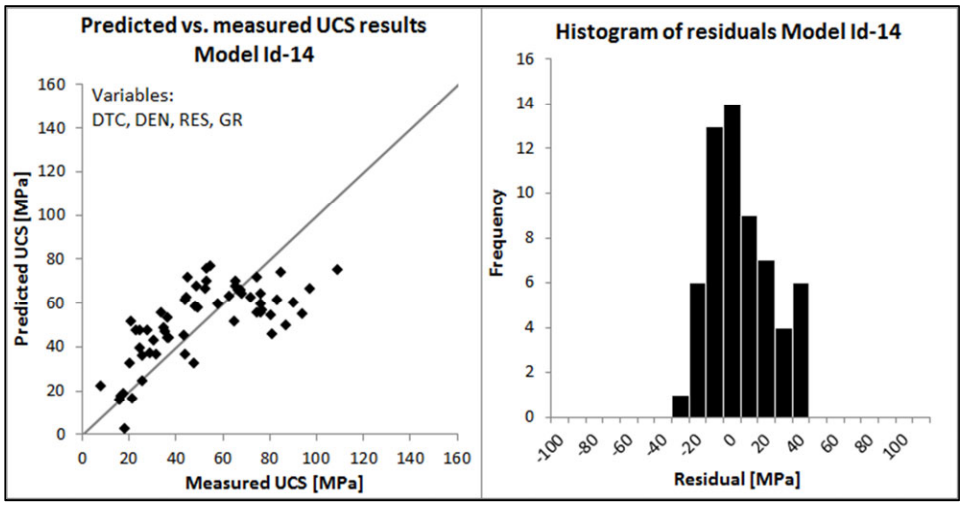

Figure 4-17 – On the left, the measured vs. predicted UCS values of Model-14; on the right, residual histogram of Model-14 can be seen. Variables listed on left graph.

Adding neutron porosity log to the Model-17, the regression coefficient increased above 0.6 (Model-18); however, here only two wells were involved in the regression. Using only one of the spectral of gamma ray, the regression coefficient did not change significantly (Model-19, 20 and -21). However, combined all of them, the regression coefficient jumped significantly above 0.7 (Model-25). Adding neutron porosity log to this variable set, the regression coefficient increased up to almost 0.75 (Model-32). Further small increase can be seen by adding also convention gamma ray log (Model-33); however, because this log does not add new information to the model, it was not used.

Figure 4-18 shows the predicted UCS vs. measured UCS check cross-plot and the residual histogram. The cross-plot shows less scattering and the histogram is normal distributed and the range of residuals narrowed from 80 MPa (-30 to 50 MPa) to 50 MPa (-20 to 30 MPa).

Table 4-10 - Regression analysis results of all the samples: Spectral gamma ray, Potassium (K), Uranium (U), Thorium (TH) and neutron porosity (CNC) logs are involved from wells K18-8 and L6-8.

Mod. Id.	Num. of observa-tion	R^2	Std. Error	F	Signifi-cance F	Sum of abs. Residuals	Sum of abs Standard Residuals	Y	X1	X2	X3	X4	X5	X6	X7	X8	Rock group
14a	36	**0.513**	15.8	8.2	1.3E-04	442.4	29.8	**UCS**	DTC	DEN	RES	GR					All
15	60	**0.457**	18.7	15.7	1.5E-07	888.2	48.7	**UCS**	DTC	RES	GR						All
16	36	**0.595**	14.1	15.7	1.9E-06	396.3	29.3	**UCS**	DTC	DEN	CNC						All
16a	36	**0.013**	21.4	0.5	5.1E-01	633.2	30.0	**UCS**	CNC								All
17	36	**0.599**	14.3	11.6	7.2E-06	390.7	*29.0*	**UCS**	DTC	DEN	RES	CNC					All
18	36	**0.608**	14.4	9.3	1.9E-05	380.3	28.6	**UCS**	DTC	DEN	RES	GR	CNC				All
19	36	**0.560**	15.0	9.9	2.9E-05	398.1	28.2	**UCS**	DTC	DEN	RES	K					All
20	36	**0.514**	15.7	8.2	1.3E-04	445.3	30.0	**UCS**	DTC	DEN	RES	U					All
21	36	**0.617**	14.0	12.5	3.7E-06	391.2	29.7	**UCS**	DTC	DEN	RES	TH					All
22	36	**0.561**	15.2	7.7	9.7E-05	398.7	28.3	**UCS**	DTC	DEN	RES	K	U				All
23	36	**0.738**	11.8	16.9	6.1E-08	320.7	29.5	**UCS**	DTC	DEN	RES	K	TH				All
24	36	**0.631**	13.9	10.2	8.4E-06	383.4	29.7	**UCS**	DTC	DEN	RES	U	TH				All
25	36	**0.738**	11.9	13.6	2.6E-07	318.7	29.3	**UCS**	DTC	DEN	RES	K	U	TH			All
26	36	**0.172**	19.6	7.1	1.2E-02	557.6	28.8	**UCS**	K								All
27	36	**0.040**	21.1	1.4	2.4E-01	631.4	30.3	**UCS**	U								All
28	36	**0.047**	21.0	1.7	2.0E-01	625.7	30.2	**UCS**	TH								All
29	36	**0.391**	17.3	6.8	1.1E-03	482.1	29.1	**UCS**	K	U	TH						All
30	36	**0.718**	12.0	19.7	3.6E-08	329.8	29.2	**UCS**	DTC	K	U	TH					All
31	36	**0.738**	11.8	16.9	6.2E-08	320.8	29.5	**UCS**	DTC	DEN	K	U	TH				All
32	36	**0.748**	11.9	11.9	6.3E-07	310.9	29.1	**UCS**	DTC	DEN	RES	K	U	TH	CNC		All
33	36	**0.757**	11.9	10.5	1.5E-06	314.5	30.0	**UCS**	DTC	DEN	RES	K	U	TH	CNC	GR	All

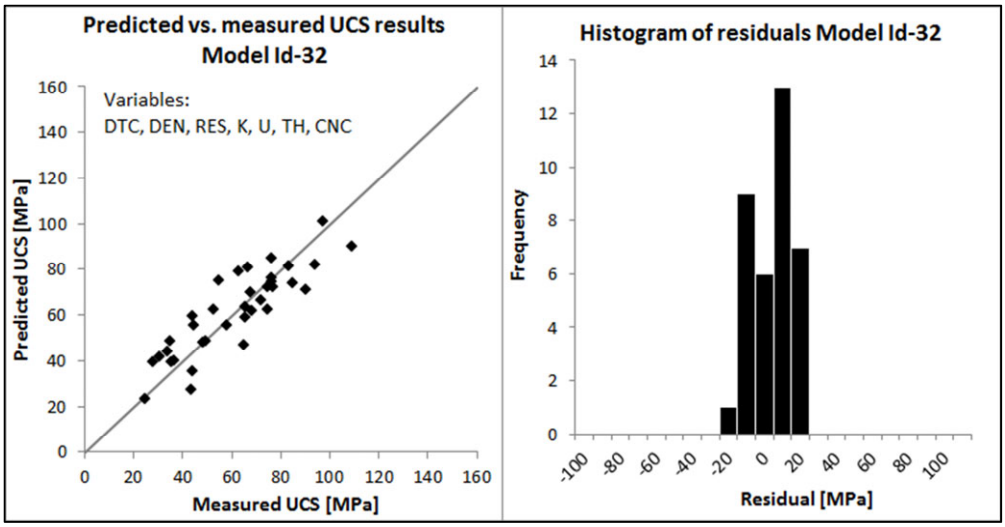

Figure 4-18 - On the left, the measured vs. predicted UCS values of Model-32; on the right, residual histogram of Model-32 can be seen. Regression was calculated with UCS against DTC, DEN, RES, K, U, TH, CNC data.

LINEAR REGRESSION OF THE ALL THE SAMPLES USING NON-LINEAR FUNCTION OF THE LOGS

First, only sonic slowness logs were converted to velocity (hyperbolic (1/x) non-linear transformation). Result of Vp (P-wave velocity in m/s) and V (1/DT in m/s) multivariate regression can be seen on Table 4-11. P-wave velocity shows always stronger correlation with UCS than 1/DT; and, P-wave velocity shows more similar correlation to UCS than P-wave slowness. Multivariate regression was calculated in the same system as in the previous case replaced DTC with Vp. The regression coefficients of UCS against Vp, DTC, RES and GR was a little higher in comparison to regression coefficient of the same calculation with slowness calculations. Figure 4-19 shows prediction check cross-plot and the residual histogram of calc. Id 39 which is the best fit model using only basic logs and all the samples.

In the next phase, the non-linear functions of the logs were used for the regression analysis. The effect of the different functions on the goodness of the model was tested step by step with each log type. The result of this can be seen on Table 4-12. In the table, variables that had the best fit are highlighted with green. Slight (0.01-0.02) increase can be seen in case of 1/DEN, 1/RES, 1/CNC and K, TH and U square. Combined these best fit transformations; model 82 had the highest coefficient and the lowest sum of absolute residuals in this stage of the analysis where all samples were used. Figure 4-20 shows prediction's cross-plot of models 82 and the residual histogram. The scattering of the points is in a narrower range around the theoretical line in the cross-plot. The histogram is still normally distributed. Sum of the absolute value of the residuals decreased while correlation coefficient increased to 0.79. Range of residuals did not show narrowing still about 50 MPa.

Table 4-11 - Regression analysis results of all samples using Vp (Vp=1/DTC) – P-wave velocity and V (V=1/DT) interval sonic velocity in m/s instead of slowness.

Mod. Id.	Num. of observa-tion	R^2	Std. Error	F	Signifi-cance F	Sum of abs. Residuals	Sum of abs Standard Residuals	Y	X1	X2	X3	X4	X5	X6	X7	Rock group
34	60	0.408	19.2	39.9	4.1E-08	895.6	47.0	UCS	Vp							All
35	36	0.324	17.7	16.3	2.9E-04	496.6	28.4	UCS	V							All
36	60	0.458	18.5	24.1	2.6E-08	866.2	47.6	UCS	Vp	DEN						All
37	60	0.478	18.3	17.1	5.3E-08	857.5	48.0	UCS	Vp	DEN	RES					All
38	60	0.460	18.7	15.9	1.4E-07	866.3	47.6	UCS	Vp	DEN	GR					All
39	60	0.481	18.5	12.8	2.1E-07	858.7	48.2	UCS	Vp	DEN	RES	GR				All
40	36	0.500	16.0	7.8	1.9E-04	449.3	29.9	UCS	Vp	DEN	RES	GR				All
41	36	0.495	16.0	7.6	2.2E-04	429.9	28.5	UCS	V	DEN	RES	GR				All
42	60	0.460	18.8	11.7	6.0E-07	868.0	47.7	UCS	Vp	DEN	LOG10 (RES)	GR				All
43	60	0.467	18.7	12.0	4.2E-07	867.9	48.1	UCS	DTC	DEN	LOG10 (RES)	GR				All
44	60	0.482	18.4	12.8	2.0E-07	838.0	47.1	UCS	DTC	DEN	1/RES	GR				All
45	36	0.550	15.1	9.5	4.0E-05	405.1	28.4	UCS	Vp	DEN	RES	K				All
46	36	0.500	16.0	7.8	1.9E-04	452.5	30.1	UCS	Vp	DEN	RES	U				All
47	36	0.606	14.2	11.9	5.5E-06	395.4	29.7	UCS	Vp	DEN	RES	TH				All
48	36	0.732	12.1	13.2	3.7E-07	326.9	29.7	UCS	Vp	DEN	RES	K	U	TH		All
49	36	0.709	12.6	11.8	1.2E-06	337.9	29.5	UCS	V	DEN	RES	K	U	TH		All
50	36	0.592	14.7	8.7	3.4E-05	391.1	28.8	UCS	Vp	DEN	RES	GR	CNC			All
51	36	0.717	12.6	10.2	2.8E-06	332.0	29.4	UCS	Vp	DEN	RES	K	U	TH	CNC	All

Table 4-12 – Results of multivariate regression of all the samples UCS against the non-linear functions of all the available logs.

Mod. Id.	Num. of observa-tion	R^2	Std. Error	F	Signifi-cance F	Sum of abs. Residuals	Sum of abs Standard Residuals	Y	X1	X2	X3	X4	X5	X6	X7	Rock group
53	60	0.490	18.3	13.2	1.3E-07	870.6	49.3	UCS	DTC	DEN	RES	GR^2				All
54	60	0.478	18.5	12.6	2.4E-07	867.2	48.5	UCS	DTC	DEN	RES	GR^ (1/2)				All
55	60	0.498	18.2	13.6	8.9E-08	846.4	48.3	UCS	DTC	DEN	RES	1/GR				All
56	60	0.482	18.4	12.8	2E-07	862.6	48.4	UCS	DTC	DEN	RES	LOG10 (GR)				All
57	60	0.478	18.5	12.6	2.4E-07	865.7	48.5	UCS	DTC	DEN	RES	EXP(GR/ 100)				All
58	36	0.749	11.9	11.9	6.1E-07	309.5	29.1	UCS	DTC^2	DEN	RES	K	U	TH	CNC	All
59	36	0.747	11.9	11.8	6.5E-07	311.7	29.2	UCS	DTC^ (1/2)	DEN	RES	K	U	TH	CNC	All
60	36	0.746	12.0	11.8	6.8E-07	312.6	29.2	UCS	LOG10 (DTC)	DEN	RES	K	U	TH	CNC	All
61	36	0.748	11.9	11.9	6.3E-07	310.8	29.1	UCS	EXP(DTC/ 1000)	DEN	RES	K	U	TH	CNC	All
62	36	0.747	11.9	11.8	6.5E-07	311.3	29.1	UCS	DTC	DEN^2	RES	K	U	TH	CNC	All
63	36	0.748	11.9	11.9	6.2E-07	310.7	29.1	UCS	DTC	DEN^ (1/2)	RES	K	U	TH	CNC	All
64	36	0.750	11.9	12.0	5.8E-07	310.0	29.2	UCS	DTC	1/DEN	RES	K	U	TH	CNC	All
65	36	0.749	11.9	11.9	6.0E-07	310.5	29.2	UCS	DTC	LOG10 (DEN)	RES	K	U	TH	CNC	All
66	36	0.746	12.0	11.8	7.0E-07	311.9	29.1	UCS	DTC	EXP (DEN)	RES	K	U	TH	CNC	All
67	36	0.752	11.8	12.1	5.1E-07	306.8	29.0	UCS	DTC	DEN	RES^2	K	U	TH	CNC	All
68	36	0.748	11.9	11.9	6.3E-07	309.8	29.0	UCS	DTC	DEN	RES^ (1/2)	K	U	TH	CNC	All
69	36	0.762	11.6	12.8	3.0E-07	297.8	28.7	UCS	DTC	DEN	1/RES	K	U	TH	CNC	All
70	36	0.752	11.8	12.1	5.1E-07	304.3	28.8	UCS	DTC	DEN	LOG10 (RES)	K	U	TH	CNC	All
71	36	0.748	11.9	11.9	6.2E-07	310.8	29.1	UCS	DTC	DEN	EXP(RES /100)	K	U	TH	CNC	All
72	36	0.758	11.7	12.5	3.7E-07	305.1	29.2	UCS	DTC	DEN	RES	K^2	U^2	TH^2	CNC	All
73	36	0.736	12.2	11.1	1.2E-06	313.1	28.7	UCS	DTC	DEN	RES	K^ (1/2)	U^(1/2)	TH^(1/2)	CNC	All
74	36	0.700	13.0	9.3	6.3E-06	329.2	28.3	UCS	DTC	DEN	RES	1/K	1/U	1/TH	CNC	All
75	36	0.732	12.3	10.9	1.4E-06	302.6	27.5	UCS	DTC	DEN	RES	LOG10 (K)	LOG10(U)	LOG10(T H)	CNC	All
76	36	0.657	13.9	7.7	3.5E-05	337.7	27.1	UCS	DTC	DEN	RES	EXP(K)	EXP (U)	EXP (TH)	CNC	All
77	36	0.742	12.1	11.5	8.4E-07	314.5	29.2	UCS	DTC	DEN	RES	K	U	TH	CNC^2	All
78	36	0.754	11.8	12.3	4.6E-07	307.1	29.1	UCS	DTC	DEN	RES	K	U	TH	CNC^ (1/2)	All
79	36	0.775	11.3	13.8	1.4E-07	290.7	28.9	UCS	DTC	DEN	RES	K	U	TH	1/CNC	All
80	36	0.762	11.6	12.8	2.9E-07	300.6	29.0	UCS	DTC	DEN	RES	K	U	TH	LOG10 (CNC)	All
81	36	0.743	12.0	11.6	8.0E-07	313.7	29.1	UCS	DTC	DEN	RES	K	U	TH	EXP (CNC/10)	All
82	36	0.791	10.9	15.1	5.2E-08	279.2	28.7	UCS	DTC	1/DEN	1/RES	K^2	U^2	TH^2	1/CNC	All
83	36	0.787	11.0	14.8	6.7E-08	279.8	28.5	UCS	Vp	1/DEN	1/RES	K^2	U^2	TH^2	1/CNC	All

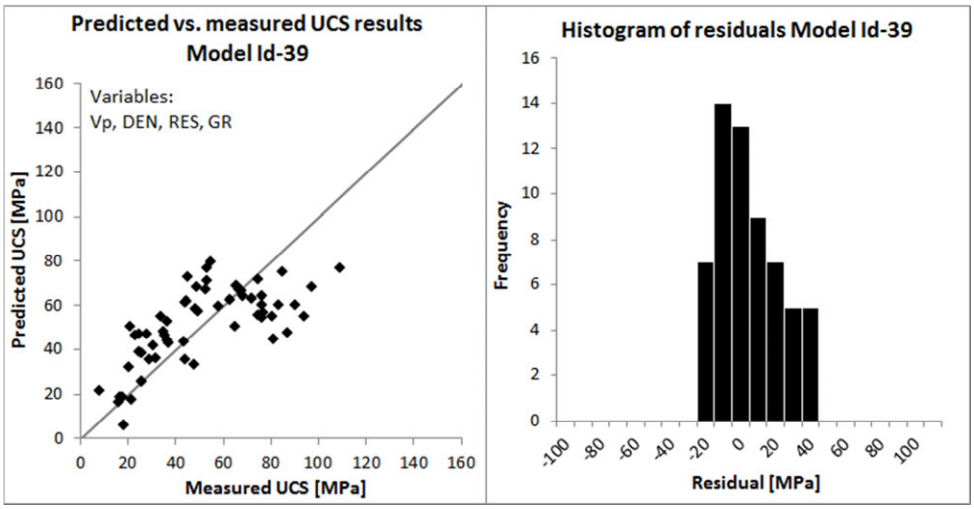

Figure 4-19 - On the left, the measured vs. predicted UCS values of Model-39; on the right, residual histogram of Model-39. Used variables are listed in the graph.

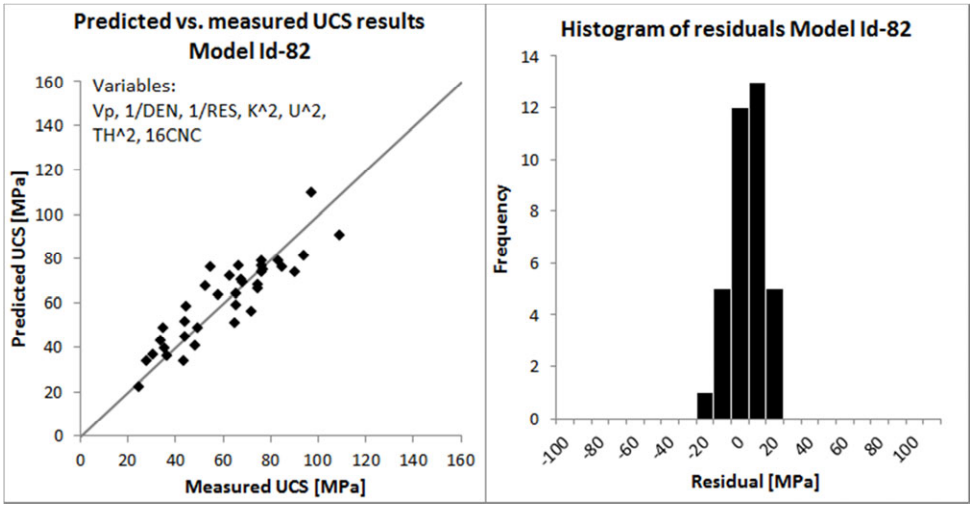

Figure 4-20 - On the left, the measured vs. predicted UCS values and; on the right, residual histogram of Model-82. Used variables are listed in the graph.

CORRELATION EQUATIONS AS A RESULT OF MULTIVARIATE REGRESSION OF ALL THE SAMPLES

Equation 14: (UCS vs. DTC, DEN, RES, GR)

$$UCS = -2.175289 * DTC + 87.855 * DEN - 0.936849 * RES + 0.0628188 * GR - 18.638$$

Equation 32: (UCS vs. UCS vs. DTC, DEN, RES, K, U, TH and CNC)

$$UCS = -4.131961 * DTC - 85.5265 * DEN - 0.179683 * RES - 13.3598 * K - 1.427968 * U + 7.22465 * TH + 1.371356 * CNC + 532.18$$

Equation 39: (UCS vs. Vp, DEN, RES, GR)

$$UCS = 0.0367799 * Vp + 88.4717 * DEN - 1.345097 * RES + 0.102739 * GR - 334.56$$

Equation 82: (UCS vs. DTC, 1/DEN, LOG10(RES), K^2, U^2, TH^2 and 1/CNC)

$$UCS = -4.74094 * \text{DTC} + 985.77/\text{DEN} - 18.520/\text{RES} - 2.9206 * \text{K}^2 - 1.9627 * \text{U}^2 + 0.76793 * \text{TH}^2 - 140.08/\text{CNC} + 6.2667$$

REGRESSION ANALYSIS RESULTS OF THE LOWER GERMAN TRIASSIC SAMPLES

Regression analyses were accomplished separately on both rock groups in order to check the effect of rock type on the correlation. Linear multivariate regression results can be seen in Table 4-13. In this case, similar tendency can be noticed that it can be seen in case of regression of all the samples. At single regression of UCS against density and sonic logs, the correlation coefficient is low; furthermore, at UCS against gamma ray and resistivity logs, the correlation is almost zero. Model-92 had higher regression coefficient than the other models with less variables. Besides, F decreased and significance F increased. Thus, the probability of the hypothesis, reliability of the result decreased since the number of the samples relatively low. The regression coefficient did not increase by applying non-linear functions of the parameters (Table 4-14). Figure 4-21 shows cross-plot and the residual histogram of Model-92. The scattering of the point is in a relatively narrow range around the theoretical line in the cross-plot. The residual histogram shows normal distribution.

Table 4-13 - Result of multivariate regression using the non-linear functions of the logs of Lower German Triassic samples.

Mod. Id.	Num. of observa-tion	R^2	Std. Error	F	Signifi-cance F	Sum of abs. Residuals	Sum of abs Standard Residuals	Y	X1	X2	X3	X4	Rock group
85	12	0.111	22.5	1.3	2.9E-01	216.4	10.1	UCS	DTC				LGT
86	12	0.278	20.3	3.8	7.8E-02	192.8	10.0	UCS	DEN				LGT
87	12	0.052	23.2	0.6	4.7E-01	226.5	10.2	UCS	RES				LGT
88	12	0.002	23.8	0.0	8.8E-01	230.6	10.2	UCS	GR				LGT
89	12	0.342	20.4	2.3	1.5E-01	196.2	10.6	UCS	DTC	DEN			LGT
90	12	0.477	19.3	2.4	1.4E-01	145.6	8.9	UCS	DTC	DEN	RES		LGT
91	12	0.447	19.8	2.2	1.7E-01	165.7	9.8	UCS	DTC	DEN	GR		LGT
92	12	0.547	19.2	2.1	1.8E-01	145.5	9.5	UCS	DTC	DEN	RES	GR	LGT

Table 4-14 – Result of multivariate regression of Lower German Triassic samples using non-linear functions of the parameters.

Mod. Id.	Num. of observa-tion	R^2	Std. Error	F	Signifi-cance F	Sum of abs. Residuals	Sum of abs Standard Residuals	Y	X1	X2	X3	X4	Rock group
93	12	0.081	22.9	0.9	3.7E-01	222.1	10.2	UCS	Vp				LGT
94	12	0.333	20.5	2.2	1.6E-01	197.1	10.6	UCS	Vp	DEN			LGT
95	12	0.409	20.5	1.8	2.2E-01	164.5	9.4	UCS	Vp	DEN	RES		LGT
96	12	0.520	19.7	1.9	2.2E-01	151.1	9.6	UCS	Vp	DEN	RES	GR	LGT
97	12	0.519	19.8	1.9	2.2E-01	152.0	9.6	UCS	Vp	1/DEN	RES	GR	LGT
98	12	0.469	20.8	1.5	2.9E-01	161.4	9.7	UCS	Vp	DEN	LOG10 (RES)	GR	LGT
99	12	0.461	20.9	1.5	3.0E-01	160.8	9.6	UCS	Vp	DEN	1/RES	GR	LGT
100	12	0.417	21.7	1.3	3.7E-01	162.3	9.4	UCS	Vp	DEN	RES	1/GR	LGT
101	12	0.379	22.5	1.1	4.4E-01	178.2	10.0	UCS	DTC	1/DEN	LOG10 (RES)	1/GR	LGT
102	12	0.374	22.5	1.0	4.5E-01	179.1	10.0	UCS	Vp	1/DEN	LOG10 (RES)	1/GR	LGT

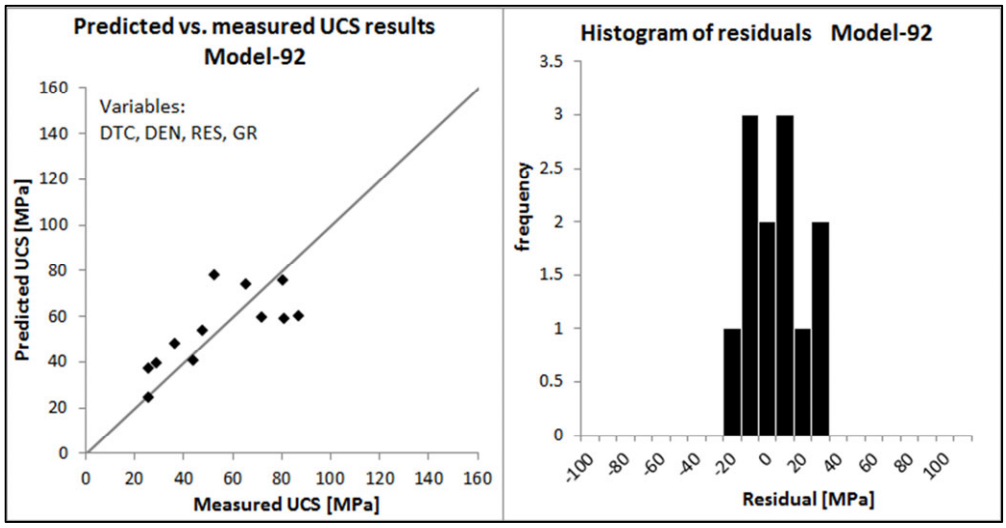

Figure 4-21 - On the left, the measured vs. predicted UCS values and; on the right, residual histogram of Model-92 can be seen. Used variables can be seen on the top of the left graph.

CORRELATION EQUATIONS AS A RESULT OF REGRESSION OF LOWER GERMAN TRIASSIC SAMPLES

Equation 92: (UCS vs. DTC, DEN, RES, GR)

$$UCS = -2.65213 * DTC + 351.7 * DEN - 4.85015 * RES - 0.74691 * GR - 549.02$$

REGRESSION ANALYSIS RESULTS OF THE ROTLIEGEND SAMPLES

Linear multivariate regression results can be seen on the Table 4-15. Using single variables for regressions (Model id: 103, 104), regression coefficient is much higher (0.59) for DTC than in the case of Model-7 without rock type separation. However, only small increase can be seen at coefficient of regression UCS versus density. The value of R^2 increased above 0.64, with Vp R^2 increased to 0.65 (Table 4-16) in case of multivariate regression with four general logs. The regression coefficient square increased more significantly by applying spectral gamma ray logs; however further increase was not experienced by adding CNC to spectral gamma ray logs. Model-112 and Model-115 have almost the same statistical properties, both can be acceptable. The graph and the histogram of the prediction can be seen on Figure 4-22.

The multivariate regression results using non-linear function of the logs can be seen on the Table 4-16. The regression results had nearly the same correlation coefficient in most of the cases using Vp instead of P-wave slowness. Furthermore, several combinations of non-linear transformation of logs were used for multivariate regression results of Rotliegend samples (UCS against well logs).

Table 4-15 – Linear multivariate regression results of Rotliegend samples (UCS against well logs).

Mod. Id.	Num. of observa-tion	R^2	Std. Error	F	Signifi-cance F	Sum of abs. Residuals	Sum of abs Standard Residuals	Y	X1	X2	X3	X4	X5	X6	X7	Rock type
103	48	0.588	16.5	65.6	2.1E-10	615.9	37.8	UCS	DTC							Rotl.
104	48	0.339	20.9	23.6	1.4E-05	800.6	38.8	UCS	DEN							Rotl.
104a	48	0.162	23.5	8.9	4.5E-03	925.1	39.8	UCS	RES							Rotl.
104b	48	0.025	25.4	1.2	2.8E-01	988.5	39.4	UCS	GR							Rotl.
104c	32	0.072	21.7	2.3	1.4E-01	556.3	26.0	UCS	CNC							Rotl.
105	48	0.603	16.4	34.2	9.4E-10	604.0	37.7	UCS	DTC	DEN						Rotl.
106	48	0.604	16.5	22.3	6.1E-09	608.4	38.0	UCS	DTC	DEN	RES					Rotl.
107	48	0.640	15.8	26.0	7.7E-10	561.1	36.8	UCS	DTC	DEN	GR					Rotl.
108	48	0.640	15.9	19.1	4.2E-09	558.1	36.6	UCS	DTC	DEN	RES	GR				Rotl.
109	32	0.699	13.1	15.7	9.5E-07	284.8	23.4	UCS	DTC	DEN	RES	K				Rotl.
110	32	0.722	12.6	17.5	3.4E-07	299.3	25.6	UCS	DTC	DEN	RES	U				Rotl.
111	32	0.685	13.3	14.7	1.7E-06	306.2	24.6	UCS	DTC	DEN	RES	TH				Rotl.
112	32	0.825	10.3	19.6	2.4E-08	216.0	23.2	UCS	DTC	DEN	RES	K	U	TH		Rotl.
113	32	0.803	11.0	17.0	9.8E-08	238.2	24.2	UCS	DT	DEN	RES	K	U	TH		Rotl.
114	32	0.692	13.5	11.7	5.5E-06	294.6	23.9	UCS	DTC	DEN	RES	GR	CNC			Rotl.
115	32	0.825	10.6	16.2	1.1E-07	216.1	23.2	UCS	DTC	DEN	RES	K	U	TH	CNC	Rotl.

Table 4-16 – Multivariate regression results using the functions of the logs of of Rotliegend samples (UCS against well logs).

Mod. Id.	Num. of observa-tion	R^2	Std. Error	F	Signifi-cance F	Sum of abs. Residuals	Sum of abs Standard Residuals	Y	X1	X2	X3	X4	X5	X6	X7	Rock type
117	48	0.5995	16.2	68.9	1.1E-10	604.4	37.6	UCS	Vp							Rotl.
118	32	0.5445	15.2	35.9	1.4E-06	372.9	24.9	UCS	V							Rotl.
119	48	0.6208	16.0	36.8	3.4E-10	583.3	37.3	UCS	Vp	DEN						Rotl.
120	48	0.6300	16.0	25.0	1.4E-09	581.4	37.6	UCS	Vp	DEN	RES					Rotl.
121	48	0.6530	15.6	20.2	2.0E-09	551.9	36.9	UCS	Vp	DEN	RES	GR				Rotl.
122	32	0.6744	13.6	14.0	2.7E-06	294.5	23.2	UCS	Vp	DEN	RES	GR				Rotl.
123	32	0.6673	13.7	13.5	3.5E-06	300.7	23.5	UCS	V	DEN	RES	GR				Rotl.
124	32	0.6974	13.1	15.6	1.0E-06	285.3	23.4	UCS	Vp	DEN	RES	K				Rotl.
125	32	0.7193	12.6	17.3	3.8E-07	297.7	25.3	UCS	Vp	DEN	RES	U				Rotl.
126	32	0.6776	13.5	14.2	2.3E-06	306.5	24.3	UCS	Vp	DEN	RES	TH				Rotl.
127	32	0.8214	10.5	19.2	3.0E-08	216.6	23.1	UCS	Vp	DEN	RES	K	U	TH		Rotl.
128	32	0.6919	13.5	11.7	5.5E-06	291.9	23.7	UCS	Vp	DEN	RES	GR	CNC			Rotl.
129	32	0.8214	10.7	15.8	1.4E-07	216.8	23.1	UCS	Vp	DEN	RES	K	U	TH	CNC	Rotl.
130	32	0.8347	10.3	17.3	5.8E-08	222.9	24.7	UCS	DTC	1/DEN	1/RES	K^2	U^2	TH^2	1/CNC	Rotl.
131	32	0.8392	10.1	17.9	4.2E-08	217.9	24.5	UCS	Vp	1/DEN	1/RES	K^2	U^2	TH^2	1/CNC	Rotl.
132	32	0.8430	10.0	18.4	3.2E-08	215.9	24.5	UCS	DTC	1/DEN	LOG10 (RES)	K^2	U^2	TH^2	1/CNC	Rotl.
133	32	0.8415	10.0	18.2	3.6E-08	214.1	24.2	UCS	Vp	1/DEN	LOG10 (RES)	K^2	U^2	TH^2	1/CNC	Rotl.
134	32	0.8428	10.0	18.4	3.2E-08	216.2	24.5	UCS	DTC	LOG10 (DEN)	LOG10 (RES)	K^2	U^2	TH^2	1/CNC	Rotl.
135	32	0.8416	10.0	18.2	3.5E-08	214.5	24.3	UCS	Vp	LOG10 (DEN)	LOG10 (RES)	K^2	U^2	TH^2	1/CNC	Rotl.

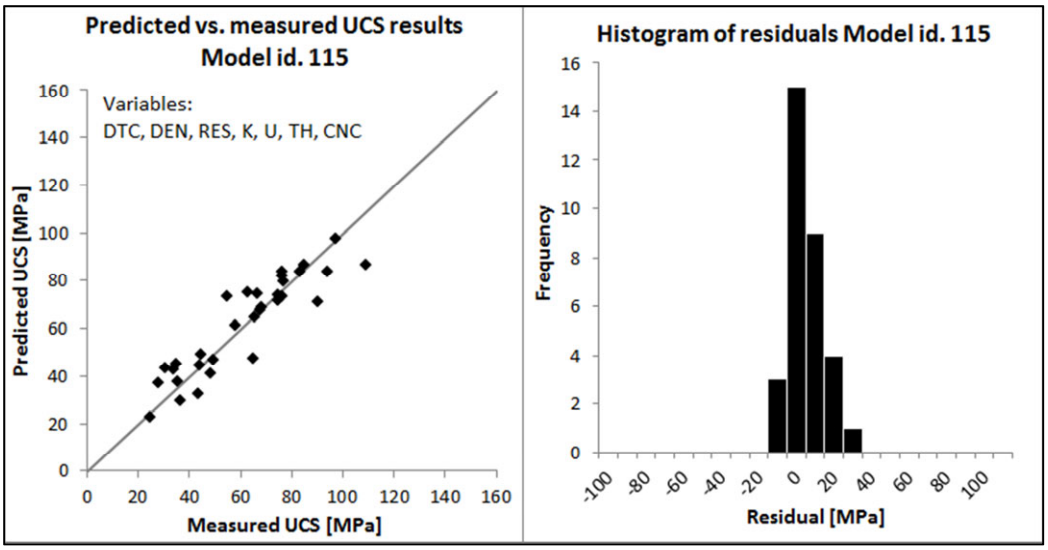

Figure 4-22 - On the left, the measured vs. predicted UCS values and; on the right, residual histogram of calc. of Id 115 can be seen. Used variables can be seen on the top of the left graph.

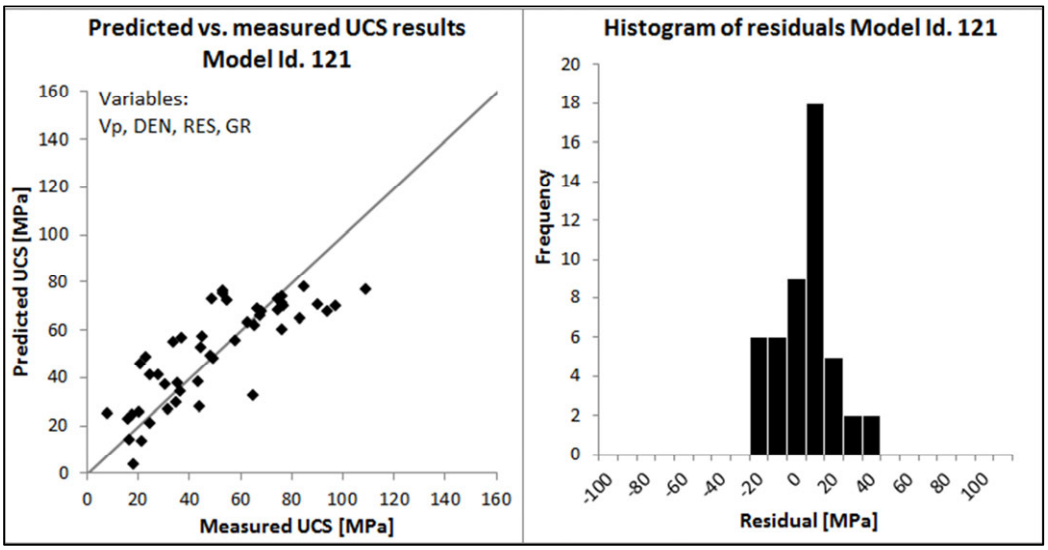

Figure 4-23 - On the left, the measured vs. predicted UCS values and; on the right, residual histogram of Mode-121 can be seen. Used variables can be seen on the top of the left graph.

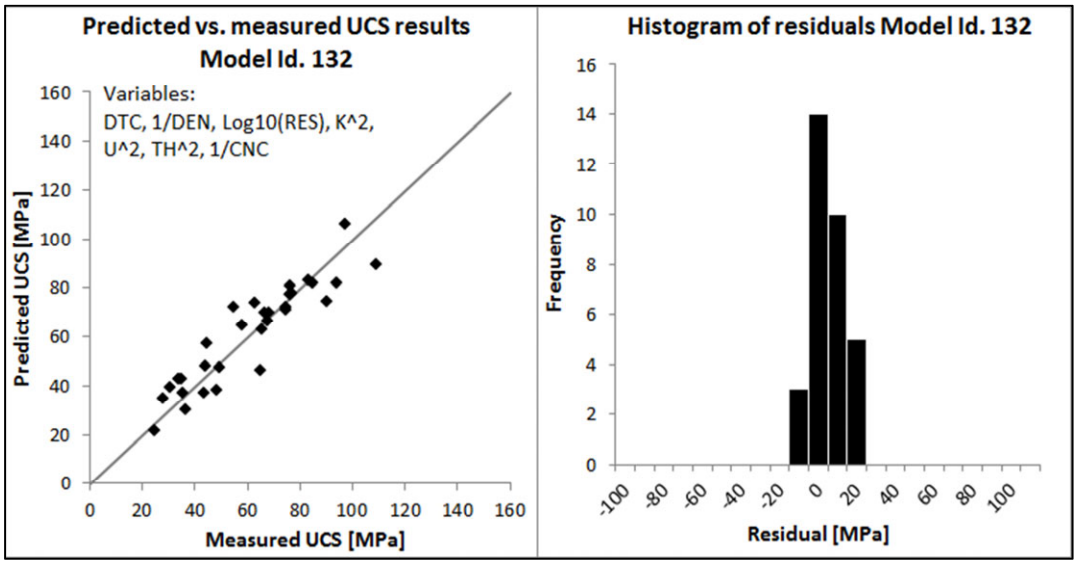

Figure 4-24 - On the left, the measured vs. predicted UCS values and; on the right, residual histogram of Model-132 can be seen. Used variables can be seen on the top of the left graph.

CORRELATION EQUATIONS AS A RESULT OF MULTIVARIATE REGRESSION OF ROTLIEGEND SAMPLES

Model 115: (UCS vs. DTC, DEN, RES, K, U, TH and CNC)

$$UCS = -4.23955 * DTC + -183.21 * DEN + 1.4045 * RES - 11.0135 * K - 8.43636 * U + 5.91520 * TH + 0.011687 * CNC + 802.02$$

Model 121: (UCS vs. Vp, DEN, RES and GR)

$$UCS = 0.062393 * \mathrm{Vp} - 58.42 * \mathrm{DEN} - 0.50098 * \mathrm{RES} - 0.34318 * \mathrm{GR} - 70.286$$

Model 132: (UCS vs. DTC, 1/DEN, LOG10(RES), K^2, U^2, TH^2 and 1/CNC)

$$UCS = -4.47508 * \mathrm{DTC} + 1144/\mathrm{DEN} + 28.798 * \mathrm{LOG10(RES)} - 3.6 * \mathrm{K\hat{}2} - 3.1547 * \mathrm{U\hat{}2} + 0.60285 * \mathrm{TH\hat{}2} - 149.51/\mathrm{CNC} - 87.043$$

4.3.4 Results of regression analysis of elastic moduli versus well logs

OUTLIER CHECKING

First, regressions were calculated between Young's moduli and log properties with all the samples in order to check outliers (Model-201). Then, the potential outliers defined earlier in the UCS study (K-13, P2-23, P2-24, P614, P6-35) were excluded from the calculations (Model-202 to Model-207, Table 4-17). Figure 4-25 and Figure 4-26 show statistical graphs of results of regression of Model-201. Residuals of this model did not show extreme values. Besides, no significant effect was seen on regression coefficients because of the skipped samples, even in the case when all the five potential outlier samples were excluded (Model-207). Therefore, no sample was excluded as outlier from regression calculations between Young's moduli and log properties.

Table 4-17 - Table shows the result of regression outlier tests for elastic moduli regression analysis. Results where, outlier(s) were skipped, was compared with result were all the samples were involved (Model-201).

Mod. Id.	Num. of observation	R^2	Std. Error	F	Significance F	Sum of abs. Residuals	Sum of abs Standard Residuals	Y	X1	X2	X3	X4	Rock group	Notes
201	62	**0.406**	5577	9.7	4.4E-06	2.81E+05	52.1	E	DTC	DEN	RES	GR	All	
202	61	**0.384**	5425	8.7	1.5E-05	2.67E+05	51.0	E	DTC	DEN	RES	GR	All	Excluded: K-13
203	61	**0.434**	5446	10.7	1.6E-06	2.70E+05	51.3	E	DTC	DEN	RES	GR	All	Excluded: P2-23
204	61	**0.387**	5571	8.9	1.3E-05	2.77E+05	51.4	E	DTC	DEN	RES	GR	All	Excluded: P2-24
205	61	**0.437**	5438	10.9	1.3E-06	2.70E+05	51.5	E	DTC	DEN	RES	GR	All	Excluded: P6-14
206	61	**0.422**	5538	10.2	2.7E-06	2.74E+05	51.2	E	DTC	DEN	RES	GR	All	Excluded: P6-35
207	57	**0.442**	5105	10.3	3.2E-06	2.36E+05	47.9	E	DTC	DEN	RES	GR	All	Excluded:K-13, P2-23, P2-24, P6-14, P6-35

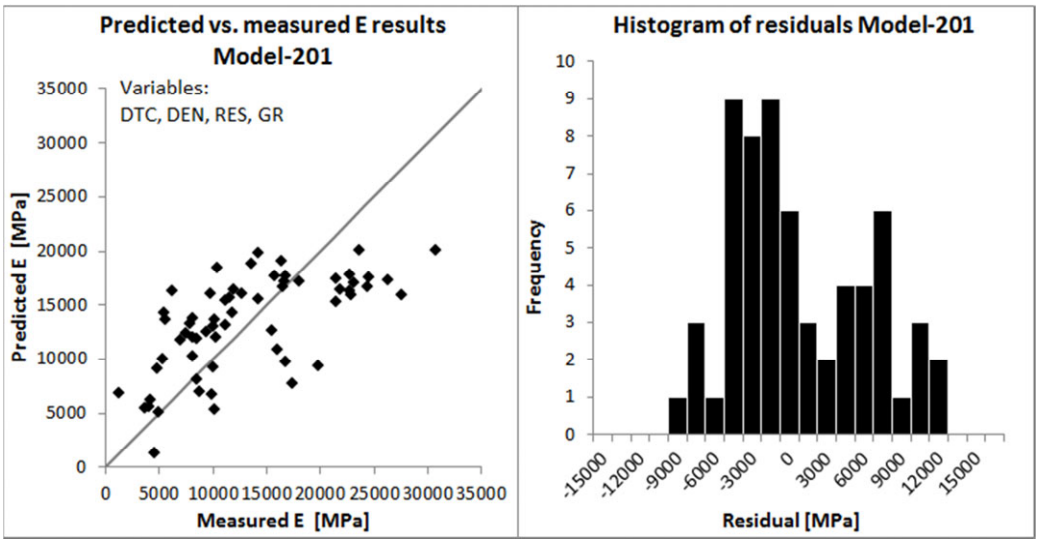

Figure 4-25 - On the left, the measured elastic modulus against predicted elastic modulus (E) values of Model-201; on the right, residual histogram of Model-201 can be seen. Used variables can be seen on the top of the left graph.

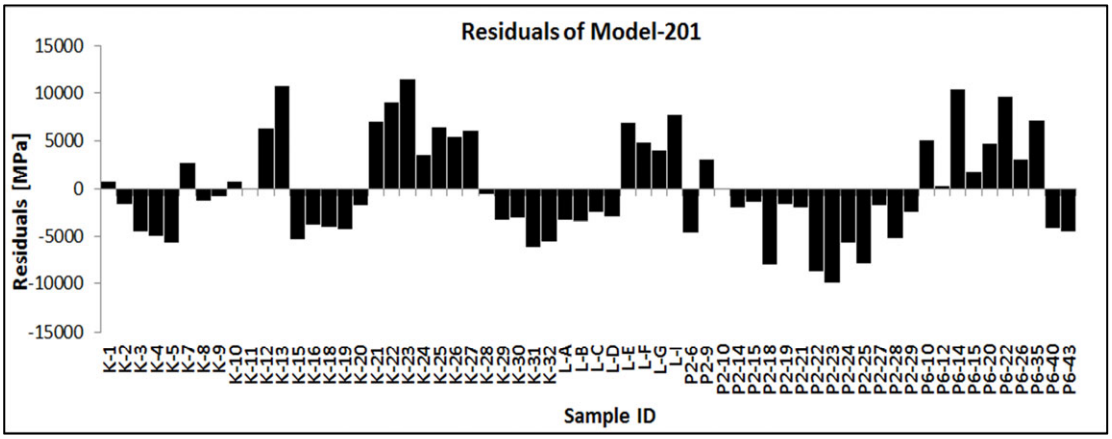

Figure 4-26 - Residuals histograms of regression of Model-201 can be seen. In which all the measured elastic moduli (E) results was used against DTC, density and UCS against compression wave velocity, density, gamma ray and resistivity properties.

REGRESSION ANALYSES OF ELASTIC MODULI AGAINST LOG PROPERTIES OF ALL THE SAMPLES

The regression analyses of the elastic moduli were performed in the same system as the UCS results. Young's moduli and unload moduli, measured in the loading and unloading sections of stress-stain curve, were involved in the analyses. The result of the regression analysis between elastic moduli and well logs can be seen in Table 4-18 where the different rock types were not separated. In general, these results show similar main tendencies to the result of UCS-log regressions. The regression coefficients were low in models where single variable was used (e.g. E vs. DTC or E vs. DEN). The regression of Potassium gamma log (K) against Young's modulus resulted in the highest R^2, values was almost 0.5. While, compression wave slowness against Young's modulus had 0.36 of R^2 and against compression wave velocity even lower (0.31). The regression of density versus Young's modulus had only 0.16 of R^2 and the rest of the log properties had lower R^2 values. Combined the four basic logs (DTC or Vp, DEN, GR, RES), the squared regression coefficients increased to 0.41 (Model 216 and Model 242). Model 217 has the same parameter, but only samples from well K18-8 and L6-8 were involved in regression in order to check the effect of reduction of sample number. The squared regression coefficient of Model 217 (R^2= 0.62) is significantly higher than the coefficient of Model 216. Involving neutron log (CNC) increased the value R^2 of the regression to 0.7 (Model-221). From spectral gamma logs, the potassium showed the larges effect on the regression, R^2 increased to 0.72 (Model-222); while, adding uranium and thorium logs to the model, the regression coefficient slightly decreased (Model-223 and Model-224). Models in which all the available log properties were involved had the highest regression coefficients R^2=0.81. These models were Model-235 which involved compression wave slowness and Model-254 which involved compression wave velocity. The difference between the regression coefficients of these two models is

negligible. Linear regression analysis using the functions of the logs, resulted in higher regression coefficient with the setting of Model-286 where hyperbolic (for DEN, RES, CNC) and parabolic (for K, U, TH) transformations were applied. Besides, the regression results of unload moduli showed very similar correlation coefficients to the regression results of Young's moduli. Figure 4-27 and Figure 4-28 show the measured vs. predicted plots and the residual histogram of Model-242 (based on the four basic logs) and Model-286 (based on all the available logs). Histograms show close normally distributed residuals.

Table 4-18 - Figure shows result of regression analysis of Rotliegend samples, Young's moduli (E) unloading modulus (E-UL) against well logs: compression wave slowness (DTC), density (DEN), resistivity (RES), spectral gamma ray, Potassium (K), Uranium (U), Thorium (TH) and neutron porosity (CNC) logs are involved from wells K18-8 and L6-8.

Mod. Id.	Num. of sampl.	R^2	Std. Error	F	Signifi-cance F	Sum of abs. Residuals	Sum of abs Standard Residuals	Y	X1	X2	X3	X4	X5	X6	X7	Rock group	Notes
208	62	0.325	5795	28.9	1.3E-06	2.90E+05	50.5	E	DTC							All	Excl: none
209	62	0.159	6471	11.3	1.3E-03	3.19E+05	49.6	E	DEN							All	Excl: none
210	62	0.012	7012	0.7	4.0E-01	3.62E+05	52.1	E	RES							All	Excl: none
211	62	0.046	6890	2.9	9.4E-02	3.54E+05	51.8	E	GR							All	Excl: none
216	62	0.406	5577	9.7	4.4E-06	2.81E+05	52.1	E	DTC	DEN	RES	GR				All	Excl: none
217	37	0.616	4492	12.8	2.5E-06	1.31E+05	31.0	E	DTC	DEN	RES	GR				All	Excl: none
218	37	0.004	6915	0.1	7.2E-01	2.17E+05	31.8	E	CNC							All	Excl: none
221	37	0.702	4020	14.6	2.3E-07	1.06E+05	28.4	E	DTC	DEN	RES	GR	CNC			All	Excl: none
222	37	0.723	3812	20.9	1.5E-08	1.09E+05	30.4	E	DTC	DEN	RES	K				All	Excl: none
223	37	0.570	4752	10.6	1.4E-05	1.43E+05	32.0	E	DTC	DEN	RES	U				All	Excl: none
224	37	0.581	4692	11.1	9.5E-06	1.39E+05	31.5	E	DTC	DEN	RES	TH				All	Excl: none
228	37	0.803	3322	20.4	2.4E-09	9.31E+04	30.7	E	DTC	DEN	RES	K	U	TH		All	Excl: none
229	37	0.495	4924	34.3	1.2E-06	1.44E+05	29.6	E	K							All	Excl: none
230	37	0.048	6761	1.8	1.9E-01	2.10E+05	31.5	E	U							All	Excl: none
231	37	0.001	6926	0.0	8.9E-01	2.17E+05	31.8	E	TH							All	Excl: none
235	37	0.808	3332	17.5	7.7E-09	9.02E+04	30.2	E	DTC	DEN	RES	K	U	TH	CNC	All	Excl: none
235a	37	0.801	5374	16.6	1.3E-08	1.39E+05	28.9	E-UL	DTC	DEN	RES	K	U	TH	CNC	All	Excl: none
237	62	0.312	5852	27.2	2.4E-06	2.90E+05	49.9	E	Vp							All	Excl: none
242	62	0.416	5531	10.2	2.8E-06	2.79E+05	52.1	E	Vp	DEN	RES	GR				All	Excl: none
242a	59	0.497	8748	13.4	1.2E-07	4.09E+05	48.4	E-UL	Vp	DEN	RES	GR				All	Excl: none
243	37	0.610	4523	12.5	3.1E-06	1.33E+05	31.3	E	Vp	DEN	RES	GR				All	Excl: none
251	37	0.803	3323	20.4	2.4E-09	9.45E+04	31.2	E	Vp	DEN	RES	K	U	TH		All	Excl: none
253	37	0.709	3968	15.1	1.5E-07	1.05E+05	28.4	E	Vp	DEN	RES	GR	CNC			All	Excl: none
254	37	0.811	3306	17.8	6.2E-09	9.11E+04	30.7	E	Vp	DEN	RES	K	U	TH	CNC	All	Excl: none
254a	37	0.806	5307	17.2	9.4E-09	1.40E+05	29.4	E-UL	Vp	DEN	RES	K	U	TH	CNC	All	Excl: none
286	37	0.862	2832	25.8	8.0E-11	6.80E+04	26.8	E	Vp	1/DEN	1/RES	K^2	U^2	TH^2	1/CNC	All	Excl: none
286a	37	0.774	5728	14.2	7.8E-08	1.46E+05	28.3	E-UL	Vp	1/DEN	1/RES	K^2	U^2	TH^2	1/CNC	All	Excl: none

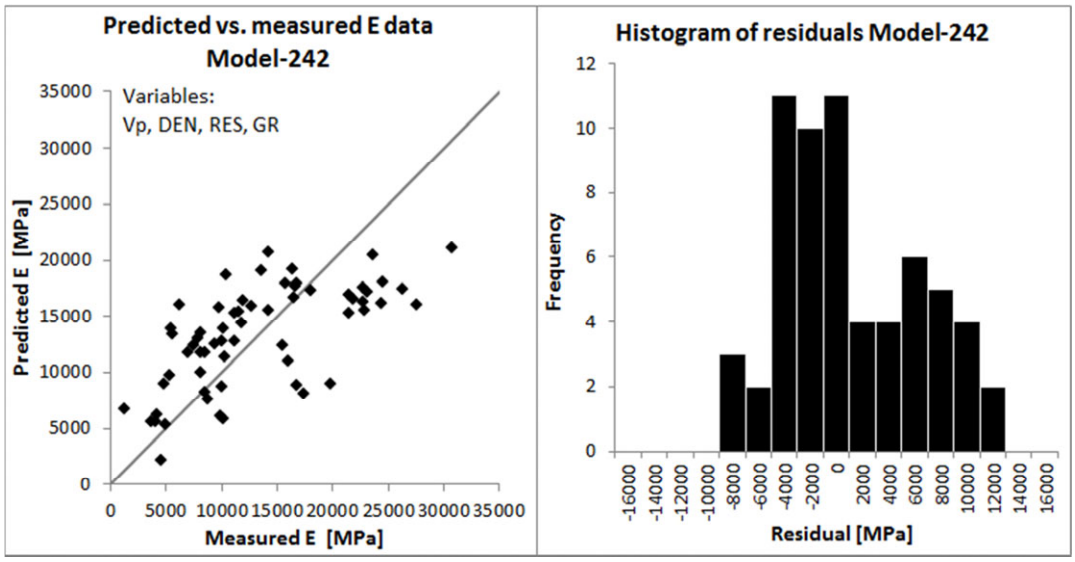

Figure 4-27 - On the left, the measured against predicted elastic moduli (E) values of Model-242; on the right, residual histogram of Model-242 can be seen.

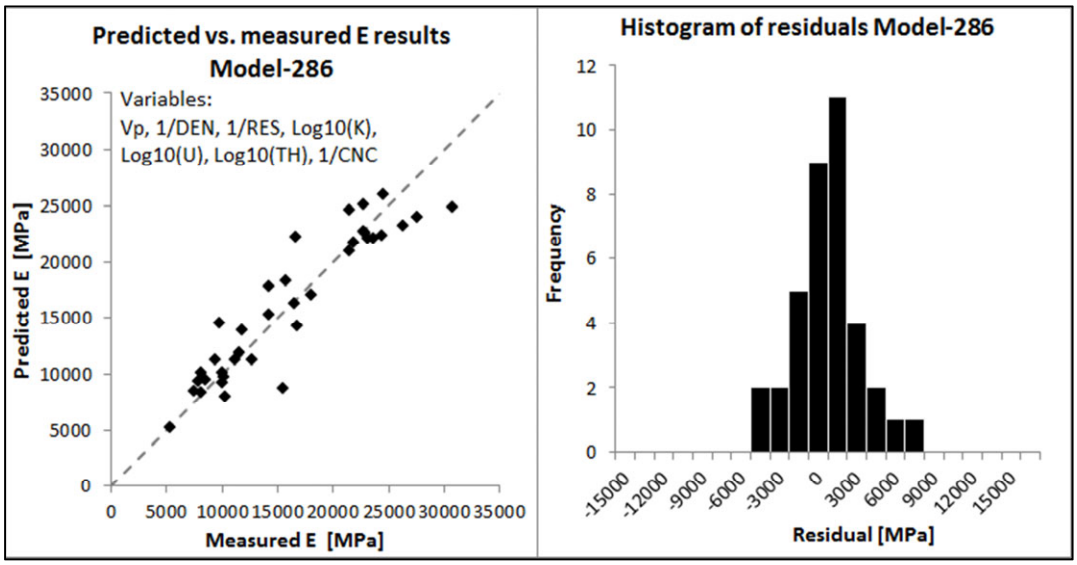

Figure 4-28 - On the left, the measured against predicted elastic moduli (E) values of Model-286; on the right, residual histogram of Model-286 can be seen.

REGRESSION ANALYSES OF ELASTIC MODULI AGAINST LOG PROPERTIES OF TRIASSIC SAMPLES

Table 4-19 shows the result of regression analysis between elastic moduli and well log where only Lower German Triassic samples were involved and only the four basic logs were available. The regression coefficients of single variable models were very low for all the four five models. The correlation of resistivity versus Young's modulus had the highest R^2 value. In the case of linear multivariate regression of Model-295 where all the logs were included R^2 was almost 0.6. Model-299 with Vp had nearly the same R^2. Model-304 had almost 0.7 of square correlation coefficient where square of gamma ray values were applied for the calculation. The relatively low F values indicate that the reliability of the results is low. Regressions with unload moduli had significantly higher R^2 values above 0.8. However, the standard error and also the sum of absolute value of Model- 299a and Model-304a are higher than the values of the regression of Model-299 and Model-304. Therefore, these results of unload moduli are less reliable than Young's moduli models.

Table 4-19 - Figure shows the result of regression analysis of Rotliegend samples, Young's moduli (E) unloading modulus (E-UL) against well logs: compression wave slowness (DTC), compression wave velocity (Vp), sonic velocity (V), density (DEN), resistivity (RES), spectral gamma ray, Potassium (K), Uranium (U), Thorium (TH) and neutron porosity (CNC) logs are involved from wells K18-8 and L6-8.

Mod. Id.	Num. of sampl.	R^2	Std. Error	F	Signifi-cance F	Sum of abs. Residuals	Sum of abs Standard Residuals	Y	X1	X2	X3	X4	Rock group	Notes
288	12	0.052	4113	0.5	4.8E-01	4.01E+04	10.2	E	DTC				LGT	Excl: none
289	12	0.015	4192	0.2	7.0E-01	4.06E+04	10.2	E	DEN				LGT	Excl: none
290	12	0.105	3997	1.2	3.1E-01	3.82E+04	10.0	E	RES				LGT	Excl: none
291	12	0.001	4222	0.0	9.4E-01	4.13E+04	10.3	E	GR				LGT	Excl: none
295	12	0.580	3271	2.4	1.5E-01	2.36E+04	9.0	E	DTC	DEN	RES	GR	LGT	Excl: none
296	12	0.066	4083	0.7	4.2E-01	3.98E+04	10.2	E	Vp				LGT	Excl: none
299	12	0.591	3229	2.5	1.3E-01	2.33E+04	9.0	E	Vp	DEN	RES	GR	LGT	Excl: none
299a	12	0.833	4635	8.7	7.5E-03	3.48E+04	9.4	E-UL	Vp	DEN	RES	GR	LGT	Excl: none
304	12	0.693	2798	3.9	5.5E-02	1.88E+04	8.4	E	Vp	DEN	RES	GR^2	LGT	Excl: none
304a	12	0.838	4563	9.1	6.7E-03	3.37E+04	9.3	E-UL	Vp	DEN	RES	GR^2	LGT	Excl: none

REGRESSION ANALYSES OF ELASTIC MODULI AGAINST LOG PROPERTIES OF ROTLIEGEND SAMPLES

Table 4-20 shows the results of regression analysis between elastic moduli and well log where only Rotliegend samples were involved. And all type of logs was available for 33 samples out of 50 samples. There was no outlier skipped. When only single variable was used (e.g. E vs. DTC or E vs. DEN), square regression coefficients were low. Regression of potassium spectral gamma log (K) and slowness (DTC) regressions against Young's modulus resulted the highest R^2, its value was almost 0.5. The regression of density versus Young's modulus had only 0.2 of R^2 and the rest of the log properties resulted in significantly lower R^2 values. Combined the four basic logs (DTC or Vp, DEN, GR, RES), square correlation coefficients increased to above 0.7 (Model 315 and Model 329). Square regression coefficient of Model 316 (R^2= 0.7) is significantly higher than the coefficient of Model 315. Related to Model-317, R^2 increased to about 0.8 adding neutron log to the regression. And, regression coefficient increased further to about 0.9 extending the model with spectral

gamma ray logs. Using the non-linear function of the logs in the models, the regression coefficients did not increased significantly. The regression of unload moduli resulted in lower square regression coefficients than regression of Young's moduli. Multivariate regression models which have three or more variables are reliable: value of F is high and significance of F is very low. However, the standard error is high even at the best fitting model (Model-337).

Table 4-20 - Figure shows result of regression analysis of Rotliegend samples, Young's moduli (E) unloading modulus (E-UL) against well logs: compression wave slowness (DTC), compression wave velocity (Vp), sonic velocity (V), density (DEN), resistivity (RES), spectral gamma ray, Potassium (K), Uranium (U), Thorium (TH) and neutron porosity (CNC) logs are involved from wells K18-8 and L6-8.

Mod. Id.	Num. of sampl.	R^2	Std. Error	F	Signifi-cance F	Sum of abs. Residuals	Sum of abs Standard Residuals	Y	X1	X2	X3	X4	X5	X6	X7	Rock group	Notes
310	50	0.521	5280	52.2	3.3E-09	2.10E+05	40.3	E	DTC							Rotl.	Excl: none
311	50	0.209	6786	12.7	8.5E-04	2.69E+05	40.1	E	DEN							Rotl.	Excl: none
311a	50	0.087	7290	4.6	3.8E-02	2.95E+05	41.0	E	RES							Rotl.	Excl: none
311b	50	0.111	7191	6.0	1.8E-02	2.92E+05	41.0	E	GR							Rotl.	Excl: none
311c	33	0.475	5072	28.0	9.3E-06	1.33E+05	26.6	E	K							Rotl.	Excl: none
311d	33	0.138	6495	5.0	3.3E-02	1.74E+05	27.1	E	U							Rotl.	Excl: none
311e	33	0.000	6996	0.0	9.2E-01	1.94E+05	28.2	E	TH							Rotl.	Excl: none
314	50	0.705	4236	36.6	3.1E-12	1.64E+05	39.9	E	DTC	DEN	GR					Rotl.	Excl: none
315	50	0.705	4281	26.9	2.0E-11	1.64E+05	39.9	E	DTC	DEN	RES	GR				Rotl.	Excl: none
315a	47	0.619	8146	17.1	2.2E-08	3.00E+05	38.5	E-UL	DTC	DEN	RES	GR				Rotl.	Excl: none
316	33	0.792	3360	26.6	3.5E-09	8.23E+04	26.2	E	DTC	DEN	RES	GR				Rotl.	Excl: none
317	33	0.828	3049	33.8	2.4E-10	7.37E+04	25.8	E	DTC	DEN	RES	K				Rotl.	Excl: none
318	33	0.773	3511	23.8	1.2E-08	9.35E+04	28.5	E	DTC	DEN	RES	U				Rotl.	Excl: none
319	33	0.672	4215	14.4	1.7E-06	1.07E+05	27.0	E	DTC	DEN	RES	TH				Rotl.	Excl: none
320	33	0.893	2497	36.2	2.0E-11	5.59E+04	24.8	E	DTC	DEN	RES	K	U	TH		Rotl.	Excl: none
322	33	0.799	3363	21.4	1.2E-08	7.78E+04	25.2	E	DTC	DEN	RES	GR	CNC			Rotl.	Excl: none
323	33	0.894	2536	30.1	1.2E-10	5.52E+04	24.6	E	DTC	DEN	RES	K	U	TH	CNC	Rotl.	Excl: none
323a	33	0.847	4972	19.8	9.8E-09	1.12E+05	25.5	E-UL	DTC	DEN	RES	K	U	TH	CNC	Rotl.	Excl: none
323b	33	0.874	2713	30.0	1.7E-10	6.24E+04	25.5	E	DT	DEN	K	U	TH	CNC		Rotl.	Excl: none
325	50	0.530	5228	54.2	2.1E-09	2.05E+05	39.6	E	Vp							Rotl.	Excl: none
326	33	0.492	4985	30.1	5.4E-06	1.34E+05	27.4	E	V							Rotl.	Excl: none
329	50	0.717	4195	28.4	8.2E-12	1.62E+05	40.3	E	Vp	DEN	RES	GR				Rotl.	Excl: none
329a	47	0.636	7969	18.3	8.9E-09	2.94E+05	38.7	E-UL	Vp	DEN	RES	GR				Rotl.	Excl: none
330	33	0.796	3329	27.2	2.7E-09	7.99E+04	25.7	E	Vp	DEN	RES	GR				Rotl.	Excl: none
335	33	0.896	2469	37.2	1.5E-11	5.43E+04	24.4	E	Vp	DEN	RES	K	U	TH		Rotl.	Excl: none
336	33	0.805	3313	22.3	8.3E-09	7.48E+04	24.6	E	Vp	DEN	RES	GR	CNC			Rotl.	Excl: none
337	33	0.896	2513	30.8	9.2E-11	5.43E+04	24.4	E	Vp	DEN	RES	K	U	TH	CNC	Rotl.	Excl: none
337a	33	0.856	4829	21.2	4.8E-09	1.10E+05	25.8	E-UL	Vp	DEN	RES	K	U	TH	CNC	Rotl.	Excl: none

Model 242: (E vs. Vp, DEN, RES, GR)

$$E = 11.213 * Vp + 16551 * DEN - 665.86 * RES - 1.4628 * GR - 75960$$

Model 242a: (E-unload vs. Vp, DEN, RES, GR)

$$\mathrm{E-unload} = 20.817 * Vp + 17625.6 * DEN - 641.11 * RES + 8.38138 * GR - 112014$$

Model 286: (E vs. Vp, 1/DEN, 1/RES, LOG10(K), LOG10(U), LOG10(TH), 1/CNC)

$$E = 21.726 * Vp + 366979/DEN - 3276.4/RES - 15287 * LOG10(K) + 1925.9 * LOG10(U) + 7888.9 * LOG10(TH) - 45891/CNC - 225470$$

Model 286a: (E-unload vs. Vp, 1/DEN, 1/RES, LOG10(K), LOG10(U), LOG10(TH), 1/CNC)

$$\mathrm{E-unload} = 30.991 * Vp + 219860 * DEN - 1178.2 * RES - 19492.6 * LOG10(K) - 3717 * LOG10(U) + 15927.8 * LOG10(TH) - 80363.8/CNC - 198469$$

Model 299: (E vs. Vp, DEN, RES, GR)

$$E = -304.55 * GR - 681.9 * RES + 85351 * DEN - 3.5608 * Vp - 157645$$

Model 299a: (E-unload vs. Vp, DEN, RES, GR)

$$\mathrm{E-unload} = 28.512 * Vp + 82768 * DEN - 2021 * RES - 146.148 * GR - 282524$$

Model 304: (E vs. Vp, DEN, RES, GR)

$$E = -0.2085 * Vp + 94753 * DEN - 944.52 * RES - 1.9404 * GR\text{^}2 - 204966$$

Model 304a: (E-unload vs. Vp, DEN, RES, GR)

$$\mathrm{E-unload} = 30.085 * Vp + 87717.4 * DEN - 2147.6 * RES - 0.941529 * GR\text{^}2 - 306104$$

Model 329: (E vs. Vp, DEN, RES, GR)

$$E = 20.0046 * Vp - 29519 * DEN - 226.4 * RES - 175.53 * GR + 4263.2$$

Model 329a: (E-unload vs. Vp, DEN, RES, GR)

$$\mathrm{E-unload} = 30.324 * Vp - 23336.7 * DEN - 865.03 * RES - 275.57 * GR - 42153$$

Model 337: (E vs. Vp, DEN, RES, K, U, TH, CNC)

$$E = 17.002 * Vp - 62332 * DEN + 390.8 * RES - 5206.3 * K - 2555.4 * U + 1133.6 * TH - 111.57 * CNC + 101076$$

Model 337a: (E-unload vs. Vp, DEN, RES, K, U, TH, CNC)

$$\mathrm{E-unload} = 28.8946 * Vp - 43158 * DEN - 291.5 * RES - 7752.4 * K - 4010.6 * U + 2031.8 * TH + 417.44 * CNC + 9378.96$$

4.3.5 Analysis of the relation between the rock properties measured in laboratory

The last stage of the data analysis was to analyse relations between rock properties that were measured in laboratory; such as: unconfined compressive strength (UCS), elastic modulus, both loading (E) and unloading (E-unload), porosity (PHI), matrix density (DEN-MX), bulk density (DEN). The result of the simple linear regression of UCS against the above listed rock properties and Young's modulus against unloading modulus can be seen in the Table 4-21. Calculations were done on the total sample set and separately by the different rock types as well.

No correlation was found between UCS and matrix density (Model-404) which indicates that the studied samples consist of very similar density minerals. Low correlations (R^2= 0.2 to 0.4) were found between UCS and porosity. And also similar low correlation was found between UCS and density. Separating the rock groups, only little bit higher correlations can be seen in Rotliegend sample set. And lower correlation can be seen in the Triassic sample set. Very strong correlation was found between UCS and elastic moduli for Rotliegend sample set, R^2 is about 0.9 (Model-412, Model-413). Line fit plot of Model-412 can be seen on Figure 4-29. However, the correlation between UCS and elastic moduli was much lower by Lower German Triassic samples. R^2 was about 0.46 at Model-216 and R^2 is about 0.42 at Model-417. The Triassic sample set was separated further by wells in order to check whether the low correlation is related to the location of the source. Model-420 and Model-421 were calculated based on samples of well P6-9. These models had significantly higher correlations than the models where the two wells were combined. Two models were created based on samples of well L6-8: Model-421 and Model-423. There was almost zero correlation found between UCS and Young's modulus. While Model-423 had higher correlation (R^2=0.64) between UCS and unload moduli. However, here the calculation based on only four samples therefore reliability of this result is low. Graphs of Model-416, Model-420 and Model-422 furthermore Model 417, Model-421 and Model-423 are plotted in Figure 4-30. In general, correlation between UCS and unload elastic modulus was found slightly lower than correlation between UCS and Young's modulus.

Table 4-21 – Result of linear multivariate regression, UCS against rock physical and mechanical properties: elastic modulus, loading (E) and unloading (E-loop), porosity (PHI), matrix density (DEN-MX), bulk density (DEN).

Mod. Id.	Num. of observa-tion	R^2	Std. Error	F	Signifi-cance F	Sum of abs. Residuals	Sum of abs Standard Residuals	Y	X1	Rock type	Dataset informaton
401	62	**0.853**	10.5	347.6	1.2E-26	458.2	44.2	UCS	E	All	Skipped: none
402	59	**0.799**	11.9	226.8	1.6E-21	534.4	45.2	UCS	E-UL	All	Skipped: none
402a	59	**0.797**	3101	224.3	2.0E-21	124882.3	40.6	E	E-UL	All	Skipped: none
403	62	**0.376**	21.5	36.1	1.2E-07	1016.2	47.6	UCS	PHI	All	Skipped: none
404	62	**0.005**	27.2	0.3	5.8E-01	1368.6	50.8	UCS	DEN-MX	All	Skipped: none
405	62	**0.354**	22	32.9	3.4E-07	1043.3	48.1	UCS	DEN	All	Skipped: none
406	62	**0.286**	5962	24.0	7.7E-06	281290.1	47.6	E	PHI	All	Skipped: none
407	62	**0.010**	7018	0.6	4.3E-01	363520.8	52.2	E	DEN-MX	All	Skipped: none
408	62	**0.256**	6085	20.6	2.7E-05	291297.6	48.3	E	DEN	All	Skipped: none
412	50	**0.921**	8.0	562.0	3.8E-28	274.8	34.8	UCS	E	Rotl.	Skipped: none
413	47	**0.866**	10.2	290.3	3.0E-21	361.1	35.9	UCS	E-UL	Rotl.	Skipped: none
413a	47	**0.936**	1888	655.2	1.8E-28	66551.2	35.6	E	E-UL	Rotl.	Skipped: none
414	50	**0.408**	21.9	33.0	6.1E-07	806.3	37.2	UCS	PHI	Rotl.	Skipped: none
415	50	**0.375**	22.5	28.8	2.3E-06	845.3	38.0	UCS	DEN	Rotl.	Skipped: none
416	12	**0.458**	17.5	8.5	1.6E-02	161.0	9.6	UCS	E	LGT	Skipped: none
417	12	**0.416**	18.2	7.1	2.4E-02	164.5	9.5	UCS	E-UL	LGT	Skipped: none
418	12	**0.172**	21.7	2.1	1.8E-01	208.6	10.1	UCS	PHI	LGT	Skipped: none
419	12	**0.221**	21.0	2.8	1.2E-01	199.2	9.9	UCS	DEN	LGT	Skipped: none
419a	12	**0.030**	4159	0.3	5.9E-01	41268.2	10.4	E	E-UL	LGT	Skipped: none
420	8	**0.727**	15.2	16.0	7.2E-03	87.2	6.2	UCS	E	LGT	Well: P6-9
421	8	**0.836**	11.8	30.6	1.5E-03	69.8	6.4	UCS	E-UL	LGT	Well: P6-9
422	4	**0.061**	14.9	0.1	7.5E-01	41.5	3.4	UCS	E	LGT	Well: L6-8
423	4	**0.641**	9.2	3.6	2.0E-01	20.4	2.7	UCS	E-UL	LGT	Well: L6-8

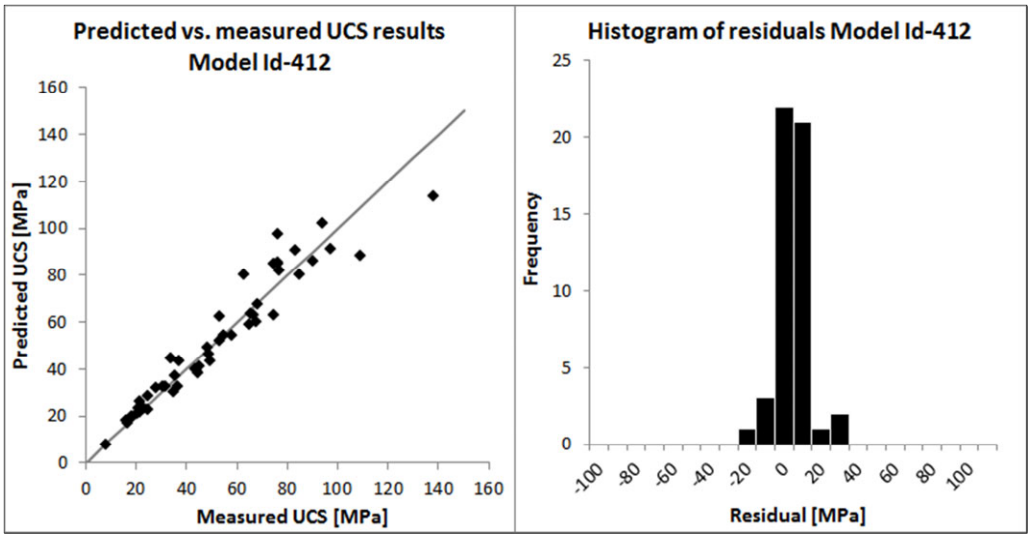

Figure 4-29 – Line fit plot and residual histogram of Model-412.

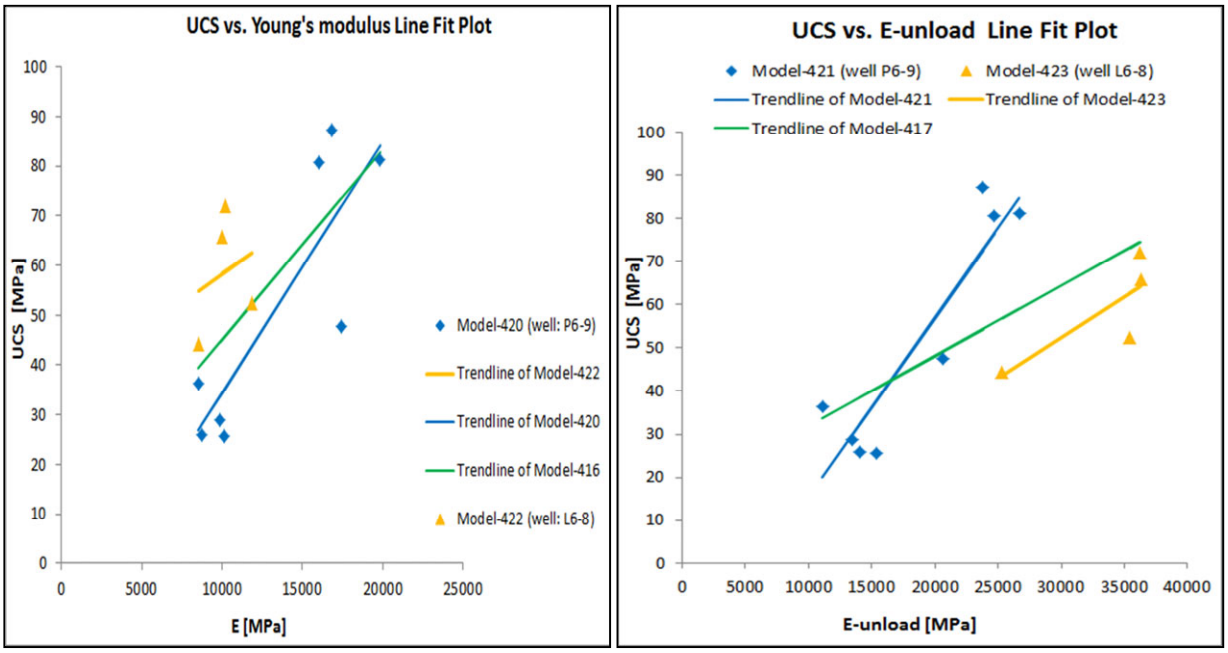

Figure 4-30 - Line fit plot and residual histogram of Model-416, Model-420 and Model-422 UCS vs. Young's moduli can be seen on the left and Model-417, Model-421 and Model-423 UCS vs. unload moduli can be seen on the right. Models based on Lower German Triassic samples.

CORRELATION EQUATIONS BETWEEN UCS AND ELASTIC MODULUS

Model 401: (UCS vs. E) $UCS = 0.003565 * E + 4.79557$

Model 402: (UCS vs. E-unload) $UCS = 0.001981 * E\_unload + 6.61862$

Model 402a: (E vs. E-unload) $UCS = 0.51231 * E\_unload + 1514.166$

Model 412: (UCS vs. E) $UCS = 0.003577 * E + 3.38239$

Model 413: (UCS vs. E-unload) $UCS = 0.00202684 * E\_unload + 5.3753$

Model 413a: (E vs. E-unload) $E = 0.564886 * E\_unload + 575.03$

Model 416: (UCS vs. E) $UCS = 0.003821 * E + 6.90317$

Model 417: (UCS vs. E-unload) $UCS = 0.00162 * E\_unload + 15.784$

4.4 Discussion

4.4.1 Mechanical characterisation of Rotliegend and Lower German Triassic Sandstone Groups

In this study, rock physical properties (porosity, matrix density and bulk density) and rock mechanical properties (unconfined compressive strengths, Young's modulus and unloading modulus) of two sandstone groups of the North Sea were measured: Lower German Triassic Sandstone samples (from five members) originating from a depth of about 2700 to 2800 m and about 4090 m TVDSS, and Rotliegend Sandstone samples (from four members) originating from depth of 3800 m to 4900 m TVDSS.

Based on the results, the mechanical properties of the studied sandstones can be characterized. Table 4-22 contains the basic statistics of the rock's physical and mechanical results for both sandstones separately. The average and the median of all mechanical and physical properties of both the Rotliegend and Lower German Triassic sandstones are nearly the same. Combining the two groups of sandstones, average values are: porosity≅ 9%; bulk density≅ 2.44 g/cm^3; UCS≅ 52 MPa; Young's modulus≅12.9 GPa; unloading modulus ≅23 GPa and ration of Young's modulus and unloading modulus E/E_{UL}= 0.54 (based on the averages). The effect of moisture content on the rock strength was considered and corrected when the present results were compared with others test results measured in dry samples. Several studies have described the relationship between strength of dry and wet rocks (see chapter 4.1.1). Hawkins and McConnell (1992) showed that the effect of the moisture content might generate up to 70% loss in strength for British sandstone. The magnitude of this effect depends on material properties of the rock material and the degree of saturation. In the present work, the strength of wet samples was measured. These strength results were then corrected to take into account the effect of the moisture content so as to compare them with strength measured in dry samples. The strength of the samples was reduced by 30%. Many researchers have investigated the relation between log data and rock strength and the elasticity of different sandstones. Chang et al. (2006) and Zoback (2007) studied the mechanical properties of sandstone which originated from different parts of the world based on 260 sandstone test results by six authors. The unconfined compressive strengths in this database range widely from 5 MPa to about 360 MPa for dry samples. The unconfined compressive strengths of the studied samples range between 8 and 138 MPa for Rotliegend sandstones and 26 and 87 MPa for Lower German Triassic sandstone. Young's moduli of sandstones range from 1 to 70 GPa in Chang et al.'s (2006) and Zoback (2007) data and, in this work, from 1 GPa to 30 GPa for Rotliegend sandstones and from 8 GPa to 20 GPa for Lower German Triassic sandstone.

Table 4-22 – Basic statistics of rock physical and mechanical measurement results of Rotliegend Group (50 samples) and Lower German Triassic Group (12 samples) samples.

	Rotliegend Group n= 50						Lower German Triassic Group n= 12					
Rock property	Poro-sity [%]	Matrix Density [g/cm3]	Bulk Density [g/cm3]	UCS [MPa]	E [GPa]	E-unload [GPa]	Poro-sity [%]	Matrix Density [g/cm3]	Bulk Density [g/cm3]	UCS [MPa]	E [GPa]	E-unload [GPa]
Minimum	2.9	2.66	2.15	8.0	1.22	7.16	4.6	2.61	2.33	25.7	9	11
Maximum	19.7	2.94	2.64	138.4	30.80	52.94	13.4	2.83	2.60	87.2	20	36
Range	16.8	0.28	0.49	130.4	29.58	45.78	8.8	0.22	0.27	61.5	11	25
Average	10.0	2.70	2.43	51.8	13.55	24.03	9.3	2.70	2.45	54.0	12	24
Median	9.3	2.70	2.44	48.9	11.74	21.61	8.4	2.70	2.44	50.0	10	24
Stand. Dev.	4.3	0.04	0.11	28.1	7.55	12.61	3.0	0.05	0.09	22.7	4	9

The values of all the measured properties of Rotliegend sandstone cover a relatively wider range than that of the Lower German Triassic sandstones. This indicates that the properties of the Rotliegend sandstone vary widely in general. The lower variation of the results of the Triassic sandstones may indicate that the properties of the Triassic sandstone change moderately in general. However, the reason also could also be that the relatively low number of samples (12 pieces of sample) does not cover the entire range. To study the properties of the subunits of the rock groups, statistical analysis was calculated. Table 4-23 shows the basic statistics of the four members of the Rotliegend Group separately, Upper and Lower Slochteren Members of the Rotliegend Group. Zone 3 and 4 are reservoir zones of Upper-Slochteren Member in the area of well P2-SE2 in block P2 of the North Sea. Based on the average of the four members, the Upper Slochteren member has a slightly lower strength and elastic modulus than the average of the entire group. The average porosity and density of the Upper Slochteren Member is similar to the average of the entire group. The Zone 3 of the Upper Slochteren Member (the shallowest strata) has twice as high porosity (indicated in red in the table) as the average of the whole member; and has significant lower (lowest of all the members; 21 MPa) strength and elastic modulus than the average of the entire group. Furthermore, Zone 4 of Upper-Slochteren shows slightly lower porosity than the average of the group. However, the average strength of this zone (36 MPa) is higher than that of Zone 3, but significantly lower than the average strength of the group, while values of elastic moduli are slightly lower than the overall average. In contrast, the strength and elastic moduli of the Lower Slochteren Group are much higher than the average of the group, while its average porosity is nearly the same as that of Slochteren Zone 4 (8%). The ratios of the elastic moduli of the four Rotliegend members are close to the average of the group. Only Zone 3 has higher E/ EUL value (0.64) than the average of the group, where the strength and the elastic moduli were the lowest in comparison with all the members. The unconfined compressive strength of Slochteren Zone 3 and Zone 4 sandstones in well P2-NE, measured by Collins (2002), is very similar to the UCS results from well P2-SE2 (this work). However, Young's modulus in well P2-SE2 is lower than in well P2-NE (E≈8-16 GPa).

Table 4-24 shows the basic statistics of the sandstones of the Lower German Triassic Group (Hardegsen Formation, Lower Detfurth Sandstone Member and Lower Volpriehausen Sandstone Member) separately. The porosity of all three Triassic sandstones is around the same as the overall average. Only the Volpriehausen Sandstone, which is the deepest strata,

has a slightly lower porosity. The Lower Detfurth Sandstone showed lower strength (34 MPa) than the other Triassic sandstones and also lower than the average of all the measured sandstone. However, the elastic modulus of this rock is average, while its E/E_{UL} value (0.76) is the highest of all the rock members. Furthermore, the Lower Volpriehausen Sandstone Member has significantly higher strength and also unload-modulus, but its Young's modulus is average, and it has significantly lower E/E_{UL} value (0.39) than the average of all the samples.

Table 4-23 - Basic statistics of rock physical and mechanical measurement results of rock members of Rotliegend Group samples.

Member	Slochteren Fr; Zone 3 n=9						Slochteren Fr; Zone 4 n=6					
Rock property	Poro-sity [%]	Matrix Density [g/cm3]	Bulk Density [g/cm3]	UCS [MPa]	E [GPa]	E-unload [GPa]	Poro-sity [%]	Matrix Density [g/cm3]	Bulk Density [g/cm3]	UCS [MPa]	E [MPa]	E-unload [MPa]
Minimum	12.7	2.67	2.15	16.2	3.75	7.16	3.8	2.67	2.18	8.0	1.22	11.10
Maximum	19.7	2.94	2.38	31.5	8.17	11.86	18.9	2.72	2.62	53.4	16.46	28.48
Range	7.1	0.27	0.22	15.3	4.42	4.70	15.1	0.05	0.44	45.5	15.25	17.38
Average	16.4	2.73	2.28	21.0	5.32	8.47	8.4	2.69	2.47	36.3	9.89	19.94
Median	16.8	2.70	2.28	20.9	5.02	7.84	7.0	2.69	2.49	40.9	10.87	20.10
Stand. Dev.	2.5	0.08	0.08	4.9	1.46	1.60	5.5	0.02	0.16	18.3	5.44	7.20

Member	Upper Slochteren n=9						Lower Slochteren n=26					
Rock property	Poro-sity [%]	Matrix Density [g/cm3]	Bulk Density [g/cm3]	UCS [MPa]	E [GPa]	E-unload [GPa]	Poro-sity [%]	Matrix Density [g/cm3]	Bulk Density [g/cm3]	UCS [MPa]	E [GPa]	E-unload [GPa]
Minimum	6.4	2.67	2.26	20.4	4.85	13.00	2.9	2.66	2.33	28.1	7.93	13.37
Maximum	16.4	2.73	2.51	65.1	15.48	26.96	12.9	2.77	2.64	138.4	30.80	52.94
Range	10.0	0.07	0.26	44.7	10.63	13.95	10.0	0.11	0.31	110.3	22.87	39.57
Average	9.8	2.70	2.43	41.9	9.75	18.66	8.3	2.70	2.47	69.5	18.55	31.70
Median	8.7	2.70	2.47	43.5	10.02	17.32	8.9	2.69	2.46	71.4	19.76	30.72
Stand. Dev.	3.1	0.02	0.09	14.5	3.69	5.40	2.7	0.02	0.08	25.5	6.47	10.83

Table 4-24 - Basic statistics of rock physical and mechanical measurement results of rock members of Lower German Triassic Group samples.

Member	LGT Hardegsen Fr. n=4						LGT Lower Detfurth Ss. Fr. n=3						LGT Volpriehausen Ss. Fr. n=5					
Rock property	Poro-sity [%]	Matrix Density [g/cm3]	Bulk Density [g/cm3]	UCS [MPa]	E [GPa]	E-unload [GPa]	Poro-sity [%]	Matrix Density [g/cm3]	Bulk Density [g/cm3]	UCS [MPa]	E [GPa]	E-unload [GPa]	Poro-sity [%]	Matrix Density [g/cm3]	Bulk Density [g/cm3]	UCS [MPa]	E [GPa]	E-unload [GPa]
Minimum	7.1	2.70	2.36	26.0	8.51	11.10	8.8	2.68	2.33	25.7	9.90	13.49	4.6	2.61	2.37	44.3	8.53	23.78
Maximum	13.0	2.83	2.60	81.1	19.82	26.70	13.1	2.69	2.44	47.7	17.41	20.65	13.4	2.73	2.57	87.2	16.82	36.19
Range	5.9	0.13	0.24	55.2	11.31	15.60	4.3	0.01	0.11	21.9	7.51	7.16	8.8	0.13	0.20	42.9	8.29	12.41
Average	10.1	2.74	2.47	56.0	13.27	19.14	10.8	2.68	2.40	34.1	12.48	16.49	7.8	2.69	2.47	64.4	11.85	30.18
Median	10.2	2.72	2.45	58.5	12.37	19.38	10.3	2.68	2.41	28.8	10.14	15.33	6.8	2.69	2.48	65.8	11.02	30.38
Stand. Dev.	3.0	0.06	0.12	29.0	5.59	7.73	2.2	0.00	0.06	11.9	4.27	3.72	3.3	0.05	0.08	16.8	3.58	6.53

4.4.2 Discussion of regression analysis of UCS data

In the regression analysis, 64 North Sea sandstone samples were involved. The correlation between log data and both UCS and elastic moduli were studied. From the statistical point of view, sample number is an important factor. The number of Lower German Triassic sandstone samples is relatively low considering that they originate in three facies. However, as the standard deviations of the results are not significantly high (in comparison with those of the Rotliegend results), the results of Triassic samples may provide a good representation of the Lower German Triassic Sandstone members. The number of Rotliegend samples is relatively high, even the number of those samples that have spectral gamma and neutron log data, which were available only from two wells. Two outlier samples were excluded from the regression analysis of UCS versus log. Both originated from the Rotliegend Sandstone Group. The sample set of Rotliegend sandstone provides a more representative and more reliable result.

The results of single variation regression analysis of UCS against well logs showed significant differences between the Rotliegend and the Triassic sandstone groups. The results of the Rotliegend sandstone are in agreement with observation of results in other studies: strength shows the highest correlation with sonic velocity (Vp) (R^2= 0.6) and R^2 is just slightly lower between UCS and compressive wave slowness (DTC) (R^2= 0.58). The correlation of the UCS and the bulk density (DEN) is slightly lower (R^2= 0.34). In general, the correlation between the acoustic wave slowness (velocity) of the compressive wave and UCS is relatively high. The acoustic wave slowness is an often used parameter in UCS correlation equations. In contrast, single variation regression of UCS of the Lower German Triassic Sandstone Group showed a lower correlation between UCS and acoustic slowness (R^2= 0.11). The single regression coefficient of Triassic samples was the highest between UCS and bulk density (R^2= 0.28). This observation already indicates a certain degree of difference between the two studied rock groups. The linear regression results of UCS combined both rock groups and resulted in lower regression coefficients. UCS against DTC had the highest regression coefficient (R^2= 0.42) combining the two rock groups. The exponential approach provided the highest R^2 values using non-linear function of logs for the regression. Figure 4-31 shows the line-fit plot of UCS versus DTC data combined and separated by rock groups. This tendency is in accordance with others' observation, as can be seen in Table 4-25 where many correlation equations (UCS-DT) are exponential. The regression coefficients of the models with the function of single variables are low. Figure 4-32 shows the UCS-sonic velocity cross plot by Chang et al. (2006), which contains the results of three previous works from different sandstones (Lama and Vutukuri 1978, Carmichael 1982, Jizba 1991). The cross plot shows a much larger scatter in the data and large deviation from the fitted curves. Therefore, the application of multiple physical rock properties, i.e. more variables, is reasonable.

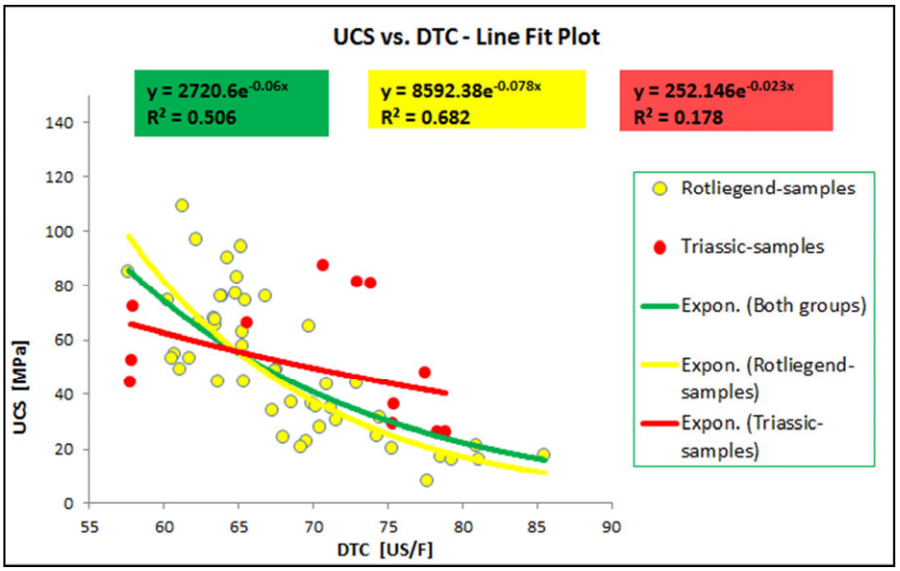

Figure 4-31 – UCS versus sonic velocity cross plot and fitted exponentially fitted curves of samples sets.

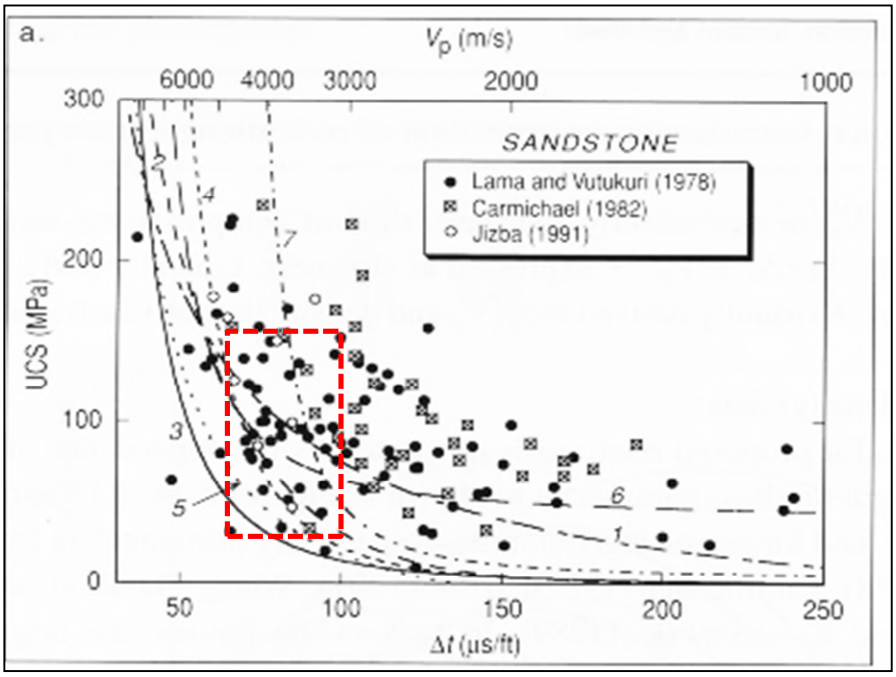

Figure 4-32 – UCS (dry) versus sonic velocity cross plot by Chang et al. (2006) where the seven curves indicate the curve of equation 1-7 of Table 4-25. Red polygon indicates the approximate range of the results of this study (water saturation is considered –> higher UCS).

The correlation between UCS and sonic velocity, together with bulk density, has been studied by several authors (e.g. Moos et al. 1999, Chang et al. 2006) (see equation 5, 6, and 7 in Table 4-25. In chapter 4.1.1, it was shown that many factors control the strength of a rock. The regression coefficient of the Triassic Group shows a significant increase with multiple variables (UCS vs. DTC, DEN and GR) in comparison with the single regression results: R^2 increased from 0.28 (Model-86 UCS vs. DEN) to 0.55 (Model-92). Model-89, Model-90 and Model-91 show that each log property played a role in the increase of the correlation coefficient. The resistivity and the natural gamma ray log data increased the R^2 from 0.34 (Model-89 UCS vs. DTC, DEN) to 0.55 (Model-92). The square of the regression coefficient of the Rotliegend Group increased slightly, 0.6 (Model-117) to 0.65 (Model-121). This shows that the strength of this rock group more depends on sonic velocity-related factors.

The effect of the mineral composition on rock's mechanical properties was observed in previous studies (see chapter 4.1.1). However, only very few works have been published on correlation analysis between rock's mechanical properties and multiple log properties, apart from the combination of sonic velocity and density. There is only one correlation equation in which clay content and Poisson's ratio is also involved (Equation 4 in Table 4-25). In addition, a few works applied resistivity, spectral gamma and/or neutron porosity logs for rock strength prediction (e.g. Hatherly, et al. 2001, Hatherly, et al. 2004, Zhou, et al. 2005). Zhou et al. (2005) used Prompt Gamma Neutron Activation Analysis (Borsaru et al. 2001) logs to gain mineral composition and also some other log properties which were also applied in this study. They used Radial Basis Function and Self-Organizing Maps (Kohonen 2001) to predict the strength of sandstone and siltstone samples. The strength prediction of the Self-Organizing Maps had a correlation coefficient of 0.65 and the Radial Basis Function had a correlation coefficient of 0.72. In addition, they reviewed the equation of McNally (Equation 2 in Table 4-25 UCS vs. DTC) with the same samples, which resulted in a squared regression coefficient of 0.62. The Radial Basis Function showed that additional logs, such as resistivity and spectral gamma logs, provide further information for strength prediction, which increased the correlation. In this study, each component of the spectral gamma log was tested rather than the general gamma ray log with the Rotliegend samples (Model-109, Model-110 and Model-111). Each of these models has higher regression coefficients than the Model-108 with the GR log only. In addition, the model with the uranium log had a slightly higher regression coefficient (R^2=0.69) than the other two spectral gamma models. The combined application of all the three spectrums increased the correlation significantly in Model-112, where R^2 was 0.83. Regression results of all the samples showed similar tendencies with spectral gamma ray logs (Model-19, Model-20, Model-21 and Model-25). However, here, the model with the thorium log had slightly higher correlation than these three models. The results of the regressions, where the two rock groups were combined, gave slightly lower correlation coefficients than the correlation coefficients for the Rotliegend Group.

Figure 4-33 shows the predicted UCS logs by the five best correlation equations along a 200 m long segment of Rotliegend strata of well K18-8. Figure 4-34 shows the predicted UCS log by the three best correlation equations along a 70 m long segment of Lower German Triassic strata of well P2-SE2. The predicted UCS logs (Figure 4-33 and Figure 4-34) are

relatively hectic with very quick and large changes. The extreme values are not realistic. The predicted results are unrealistic at several points, such as zero, negative or very high values. Nevertheless, the main characteristics and tendencies of the UCS log fit well to the measured points. The reasons for this kind of behaviour of the predicted logs could be: on the one hand, the source data (the wireline logs) already have this kind of behaviour, and, on the other hand, the multivariate regression itself may produce some artificial waviness to create a better fit out of the variables. Figure 4-35 shows the predicted UCS logs of the Rotliegend strata of all the four wells. In general, the measured UCS values fit the predicted logs well. However, some parts of the logs show very low values. For instance, in the top part of the log of well P6-9, the predicted values are very close to zero in an approximately 50–60 metres long section. The reason for the unrealistic prediction could be either unreliable log data or significant different characteristics of the rock there. There is no sample taken from this part of the well, so the regression does not involve this section; therefore, the prediction might not provide reliable results. This section needs to be calibrated by using additional samples.

4.4.3 DISCUSSION OF REGRESSION ANALYSIS OF ELASTIC MODULI DATA

The following three figures show the logs of the same well and the rock strata for Young's modulus. Figure 4-36 shows the predicted Young's modulus logs of the Rotliegend layer in well K18-8, Figure 4-37 shows the Young's modulus logs of the Lower German Triassic sandstone and Figure 4-38 shows the Young's modulus logs of the Rotliegend layers in all the four wells. Since, there is strong correlation between UCS and Young's modulus, the UCS logs and Young's modulus logs show very similar characteristics.

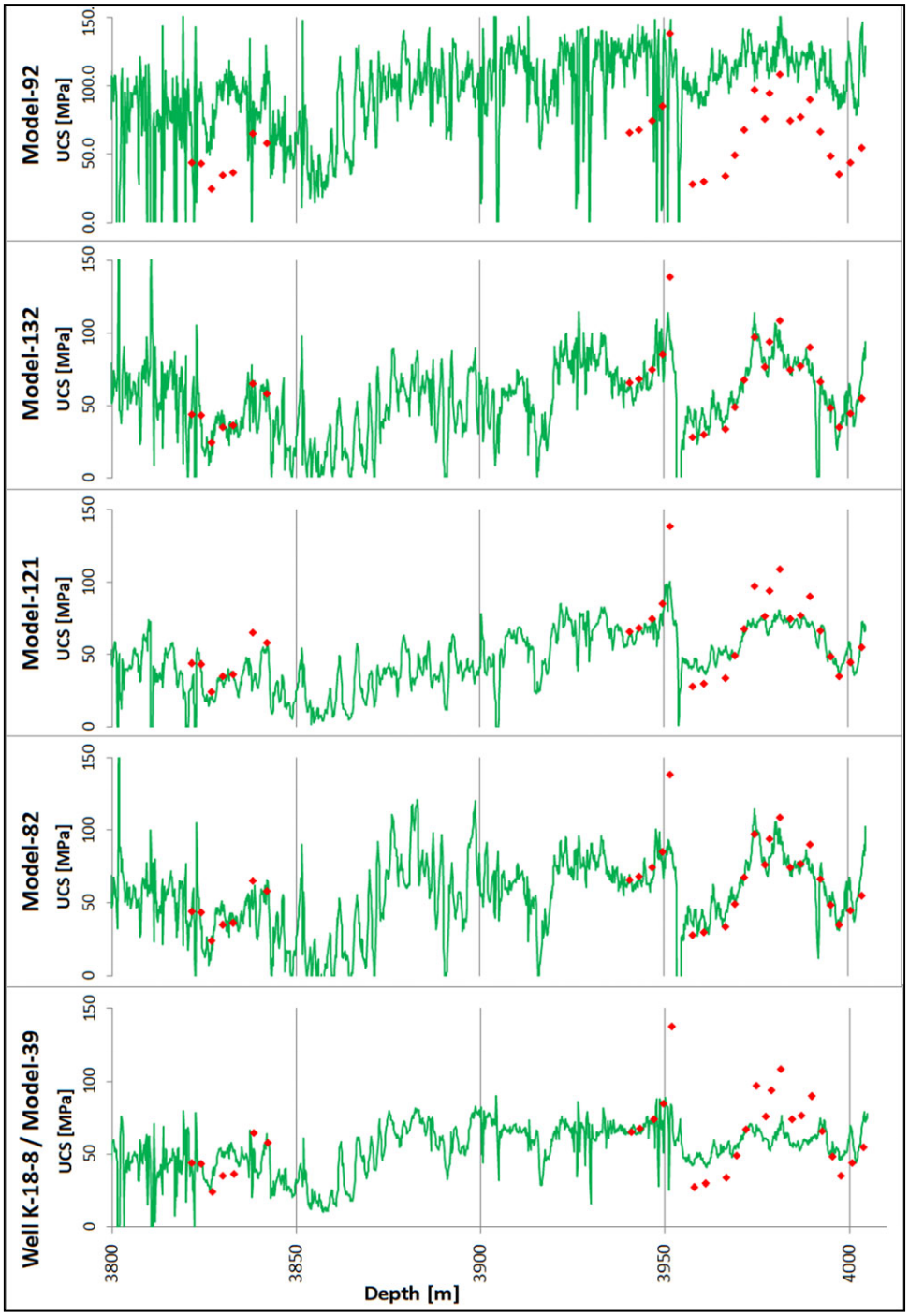

Figure 4-33 – Predicted UCS logs calculated by present correlation equations in the Rotliegend section of well K18-8. The red dots indicate the measured UCS values. Boxes on the right show the basic data of the given model.

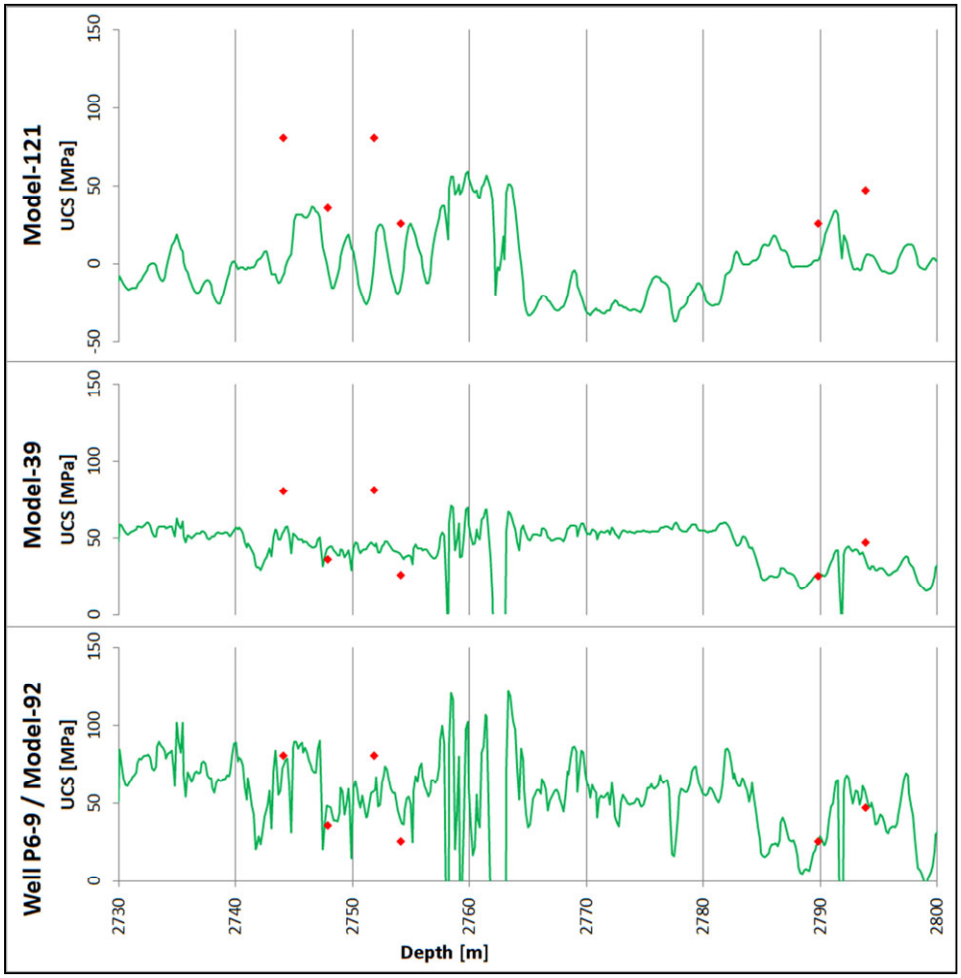

Figure 4-34 - Predicted UCS logs calculated by present correlation equations in the Lower German Triassic strata of well P6-9. Red dots indicate the measured UCS values. Boxes on the right show the basic data of the given model.

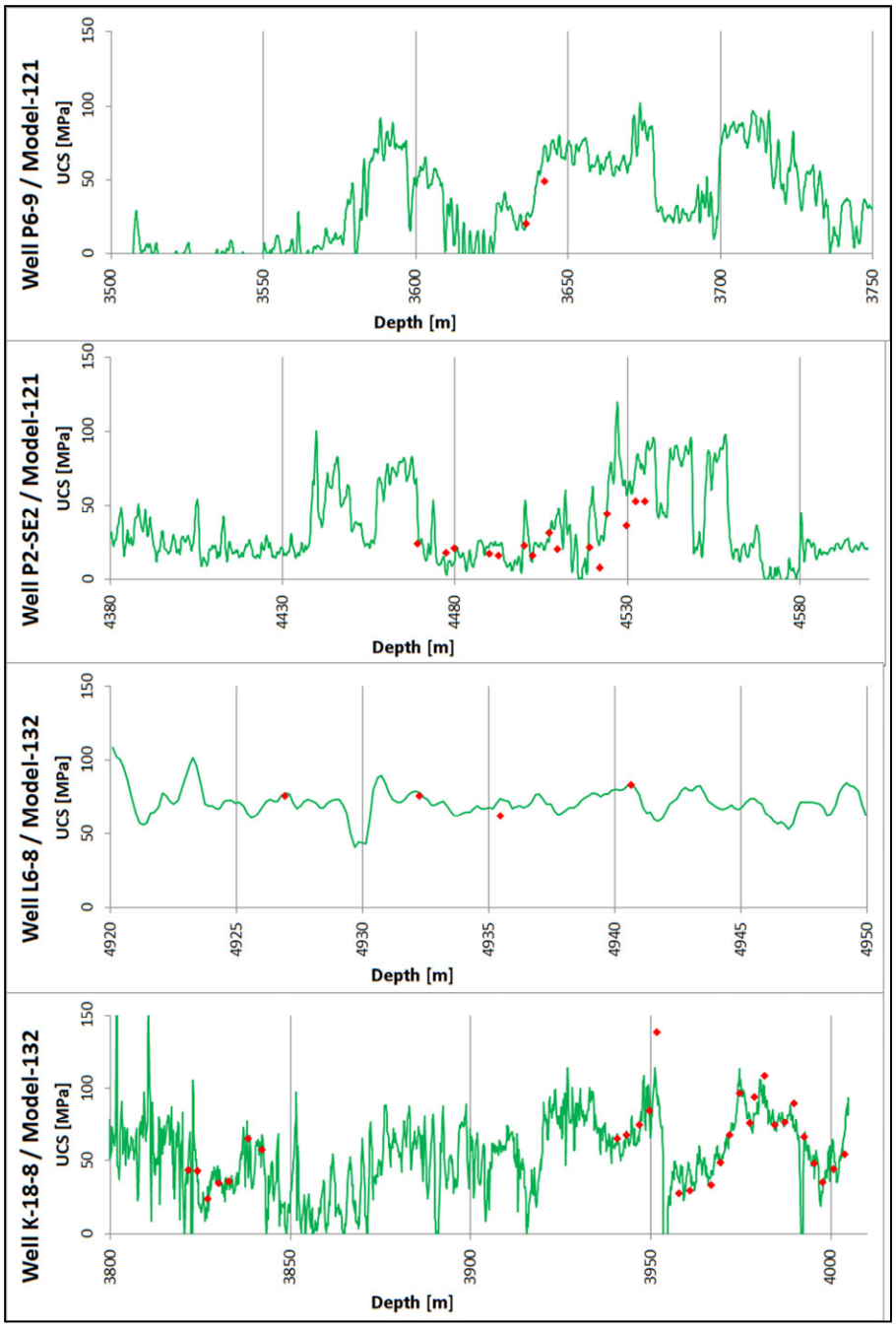

Samples: Rotliegend
Variables:
Vp, DEN,
RES, GR

Samples: Rotliegend
Variables:
Vp, DEN,
RES, GR

Samples: Rotliegend
Variables:
DTC, 1/DEN,
LOG10(RES),
K^2, U^2,
TH^2, 1/CNC

Samples: Rotliegend
Variables:
DTC, 1/DEN,
LOG10(RES),
K^2, U^2,
TH^2, 1/CNC

Figure 4-35 - Predicted UCS logs calculated by present correlation equations in the Rotliegend strata of all the four wells. Logs were calculated by the best fitting models. Red dots indicate the measured UCS values. Boxes on the right show the basic data of the given model.

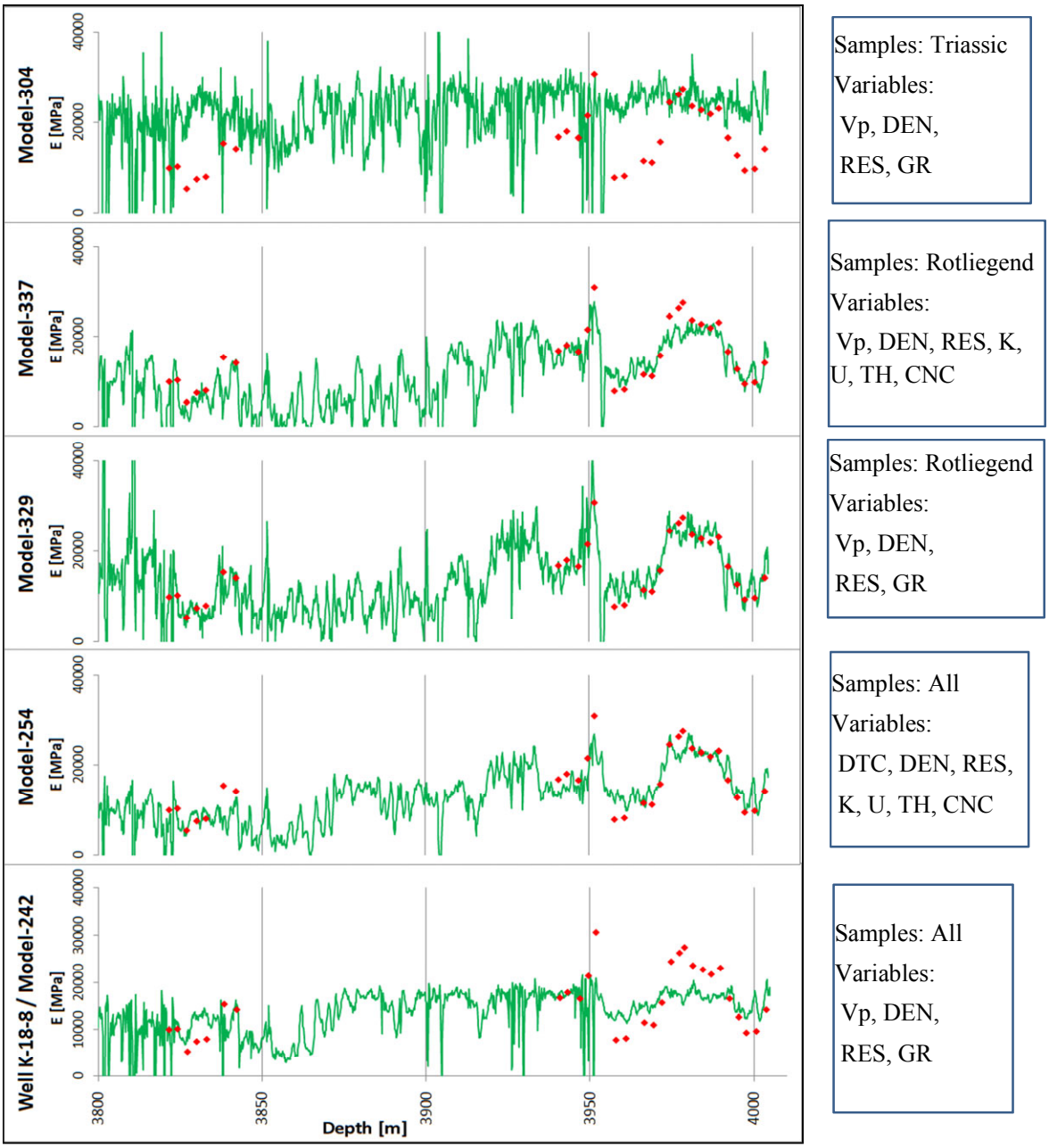

Figure 4-36 - Predicted Young's logs calculated by present correlation equations in the Rotliegend section of well K18-8. The red dots indicate the measured Young's modulus values of the samples. Boxes on the right show the basic data of the given model.

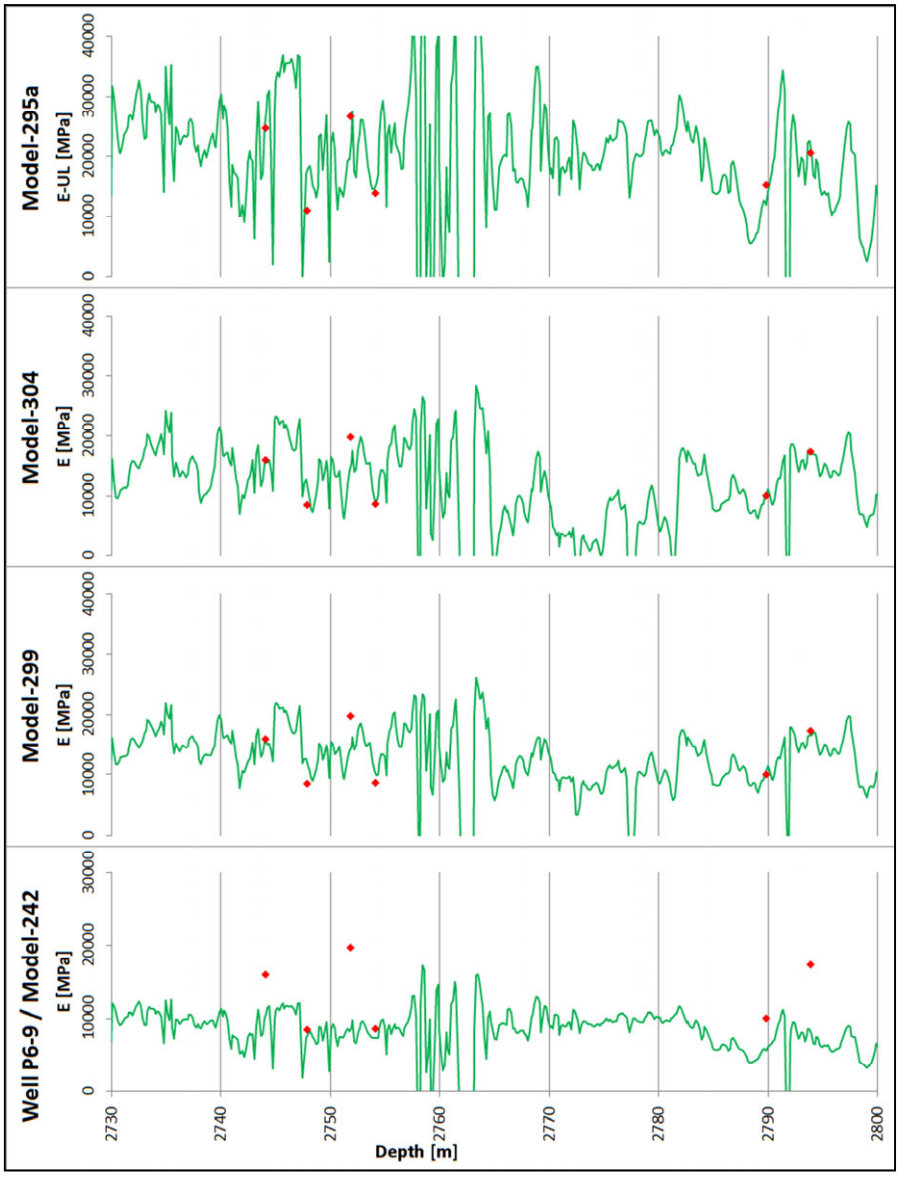

Figure 4-37 - Predicted Young's logs calculated by present correlation equations in the Lower German Triassic strata of well P6-9. The red dots indicate the measured Young's modulus values of the samples. Boxes on the right show the basic data of the given model.

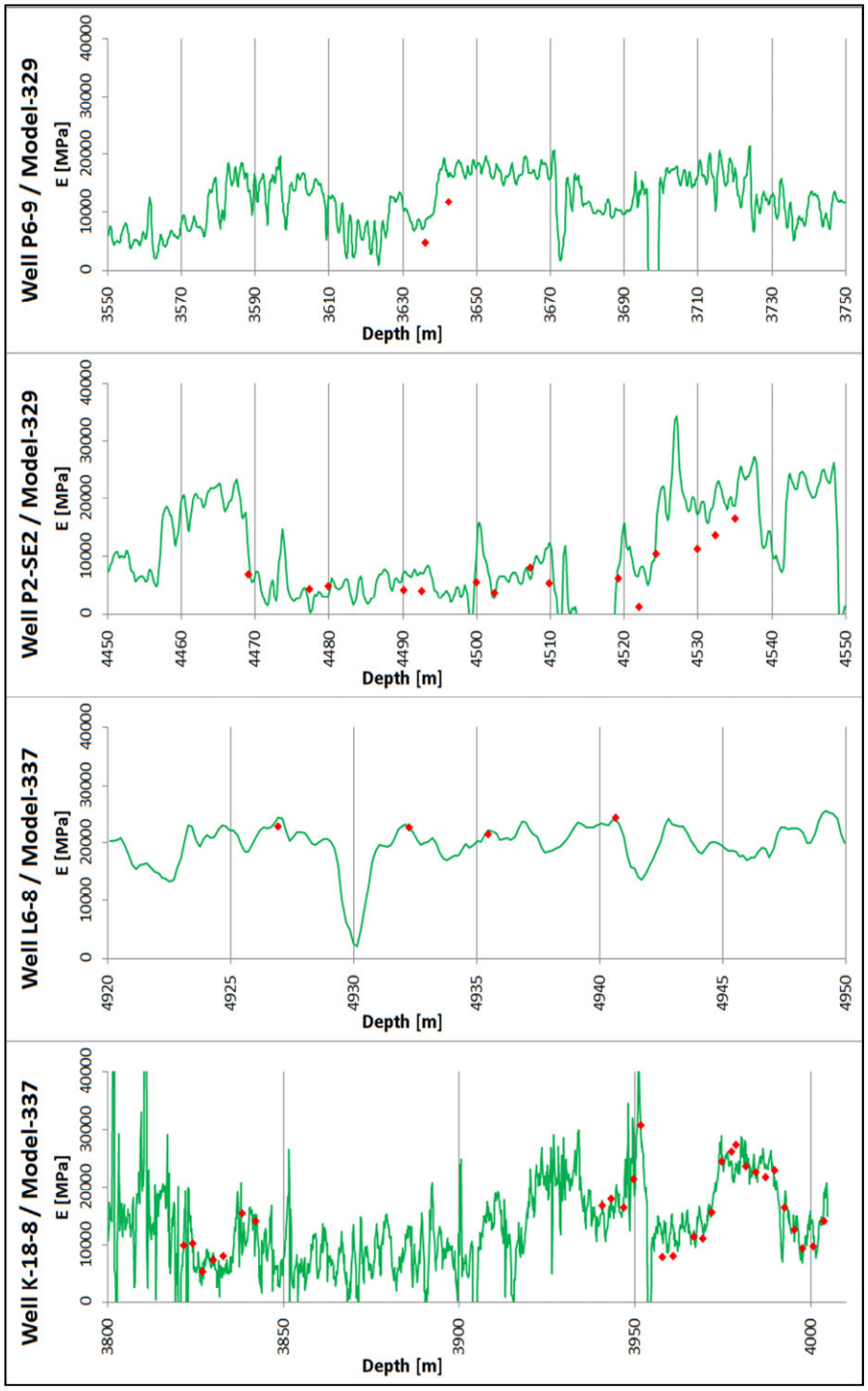

Samples: Rotliegend
Variables:
Vp, DEN, RES, K, U, TH, CNC

Samples: Rotliegend
Variables:
Vp, DEN, RES, K, U, TH, CNC

Samples: Rotliegend
Variables:
Vp, DEN,
RES, GR

Samples: Rotliegend
Variables:
Vp, DEN,
RES, GR

Figure 4-38 - Predicted Young's logs calculated by present correlation equations in the Rotliegend strata of all the four wells. Red dots indicate the measured Young's moduli values. Boxes on the right show the basic data of the given model.

4.4.4 INTERPRETATION OF THE PREDICTED LOGS

As can be seen in the UCS and Young's moduli logs, there are very high and very low peaks in the logs. The UCS of rock cannot be negative; however, high values might be valid. Nevertheless, the reason for the peaks in predicted UCS logs is probably an artificial effect of the function or source log data. Therefore, a meaningful interpretation of the predicted log is necessary to filter the unrealistic data. An interpretation of a 60 metre long section of well K18-8 can be seen in Figure 4-39.

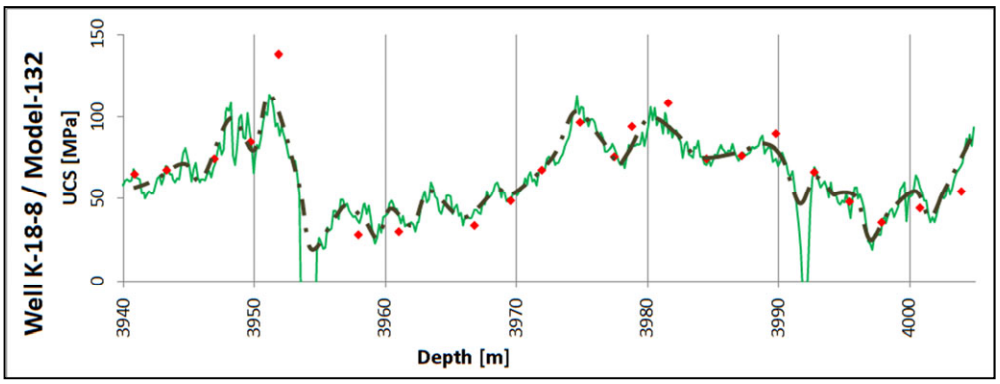

Figure 4-39 – Graph shows only a 60 m long section of the Rotliegend strata from well K-18-8; where the black dash dot line indicates an interpretation of the predicted UCS log. Red dots indicate the measured UCS values.

4.4.5 COMPARISON OF OUR RESULTS WITH OTHER CORRELATION MODELS

Numerous empirical equations have been developed to estimate rock strength from wireline log data. In this study, eleven UCS-log correlation equations for sandstones, listed in Table 4-25, were applied using the data of the present work and compared with the present results. Seven out of the eleven equations (Equation-1 to Equation-7) were based on measured log properties (Vp, DTC, DEN) and the rest were based on elastic modulus and porosity, which can be derived from log data or measured in a laboratory. The UCS logs were calculated by these equations using the log data. Six equations were modified in order to gain better fit. The names of these modified equations have an extension: "v2". The measured versus predicted UCS graphs of the results can be seen in Figure 4-40 and Figure 4-41. The basic statistics of the residuals of these predictions are listed in Table 4-25. The sum of the absolute differences between the calculated and the measured values are relatively large. Therefore, the equations were corrected with a constant shift. As a result of the correction, the sum of absolute difference decreased significantly. The Young's modulus based on Equation 9 provided the best prediction. The graph of the UCS log created by the best log property based on equations can be seen in Figure 4-42. The plot shows that these equations provide relatively good prediction only in short sections of the log – each equation in a different part of the log. Only Equation 4, which involves multiple variables (DT, DEN and Vclay), provides a relatively good prediction in the long sections of the log. This supports that the more variables that are involved in the correlation equation, the better prediction can be achieved.

	Equation Id.	Source	Equation	Residual minimum	Residual maximum	Residual range	Sum of absolute difference
Based on wireline log data	Equation 1	Freyburg (1972)	UCS=0.035*Vp-31.5	32.2	108.8	76.6	4459
	Equation 1 v2	Eq-1 modified	UCS=(0.035*Vp-31.5)-78	-45.8	30.8	76.6	890
	Equation 2	McNelly (1987)	UCS=1200*exp(-0.036*DTC)	3.2	105.5	102.3	3203
	Equation 2 v2	Eq-2 modified	UCS=1200*exp(-0.036*DTC)-55	-51.8	50.5	102.3	953
	Equation 3	source: Chang (2006)	UCS=1.4138*10^7*DTC^-3	-47.3	28.9	76.2	940
	Equation 4	Fjaer (1992)	UCS=3.3*10^(-20)*DEN^2*Vp^4**[(1+v)/(1-v)]^2*(1-2*v)*[1+0.78*Vclay]	7.4	174.0	166.6	4242
	Equation 4 v2	Eq-4 modified	UCS=3.3*10^(-20)*DEN^2*Vp^4*[(1+v)/(1-v)]^2*(1-2*v)[1+0.78*Vclay]-60	-52.6	114.0	166.6	1770
	Equation 5	Moos (1999)	UCS=1.745*10^-9*DEN*Vp^2-21	-30.1	50.9	81.0	1242
	Equation 5 v2	Eq-5 modified	UCS=1.745*10^-9*DEN*Vp^2-5	-46.1	34.9	81.0	855
	Equation 6	source: Chang (2006)	UCS= 42.1*EXP(1.9*10^(-11)*DEN*Vp^2))	16.7	114.0	97.3	3720
	Equation 6 v2	Eq-6 modified	UCS=42.1*EXP(1.9*10^(-11)*DEN*Vp^2))-63	-46.3	51.0	97.3	932.9
	Equation 7	source: Chang (2006)	UCS=3.87*EXP(1.14*10^(-10)*DEN*Vp^2)	103.1	17538	17435	135203
Based on other properties	Equation 8	source: Chang (2006)	UCS=46.2*EXP(0.027*E)	-21.3	39.8	61.0	1098
	Equation 9	Bradford at al. (1998)	UCS=2.28+4.1089*E	-27.9	34.2	62.1	514
	Equation 10	Vernik (1993)	UCS=254*(1-2.7*FI)^2	30.450492	142.350319	111.9	5147
	Equation 10 v2	Eq-10 modified	UCS=(254*(1-2.7*FI)^2)-81	-50.549508	61.3503189	111.9	1473
	Equation 11	source: Chang (2006)	UCS=277*EXP(-10*FI)	-1.683697	123.041201	124.7	3414

Table 4-25 – List of the equations were used to predict UCS from well log properties. On the right side of the table, the residual statistics are listed as a result of the equations with data of this study. (RHO= density, Vclay=volume of clay from gamma ray log, v=0.21=Poisson's ratio, FI=porosity)

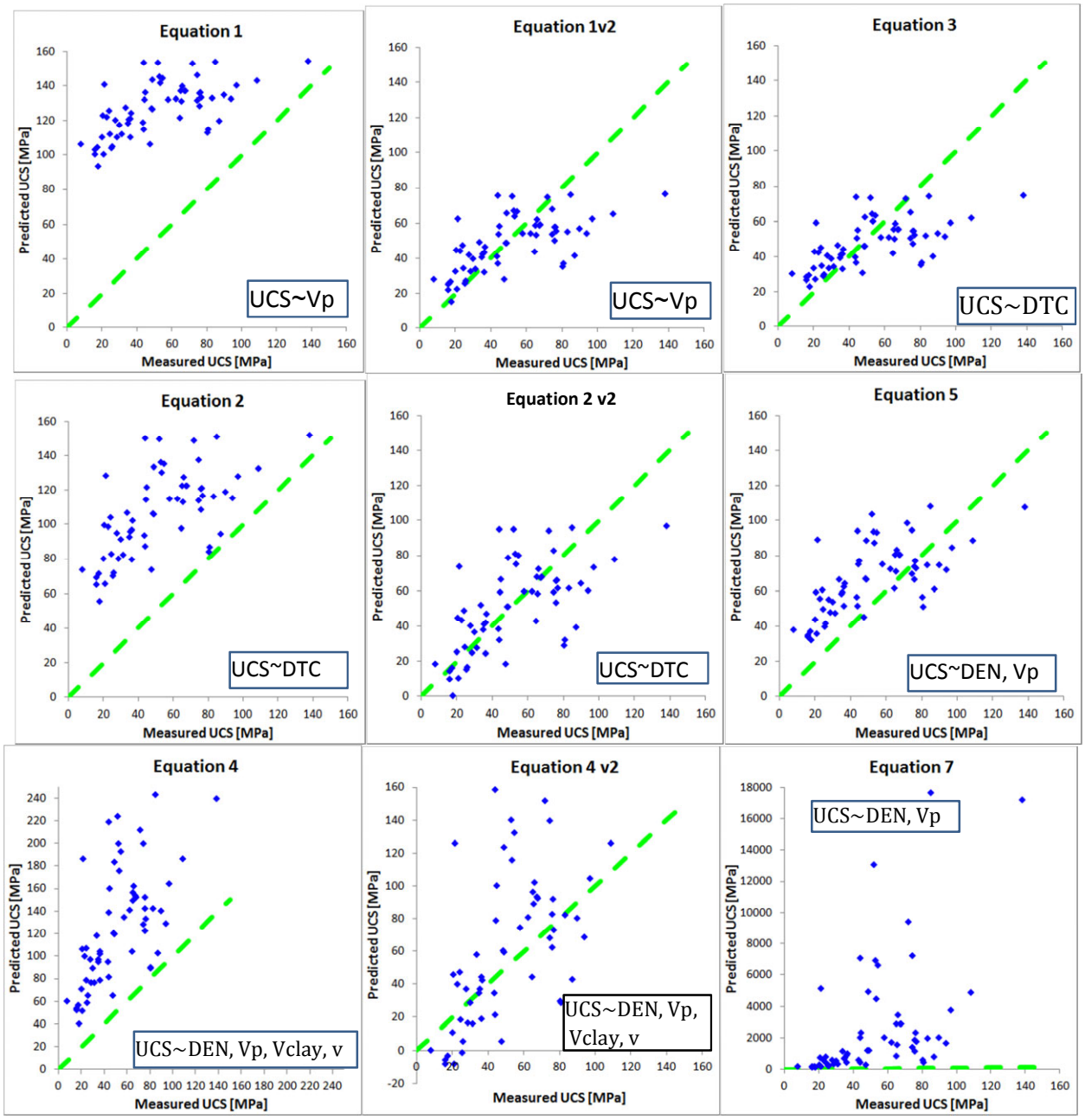

Figure 4-40 – Measured versus predicted data cross plot of the UCS calculations by equations listed in Table 4-25.

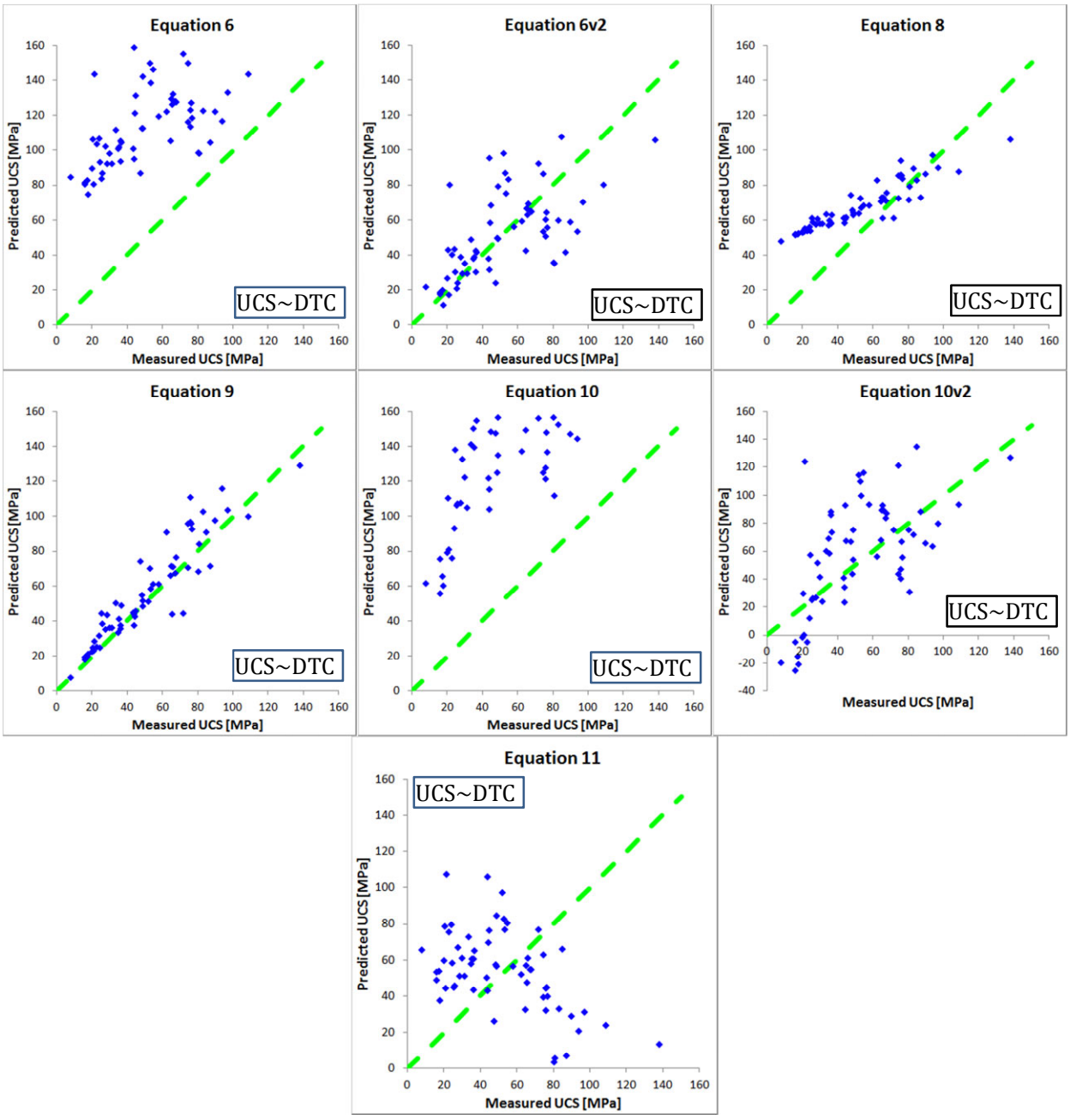

Figure 4-41 - Measured versus predicted data cross plot of the UCS prediction calculations by equations listed in Table 4-25.

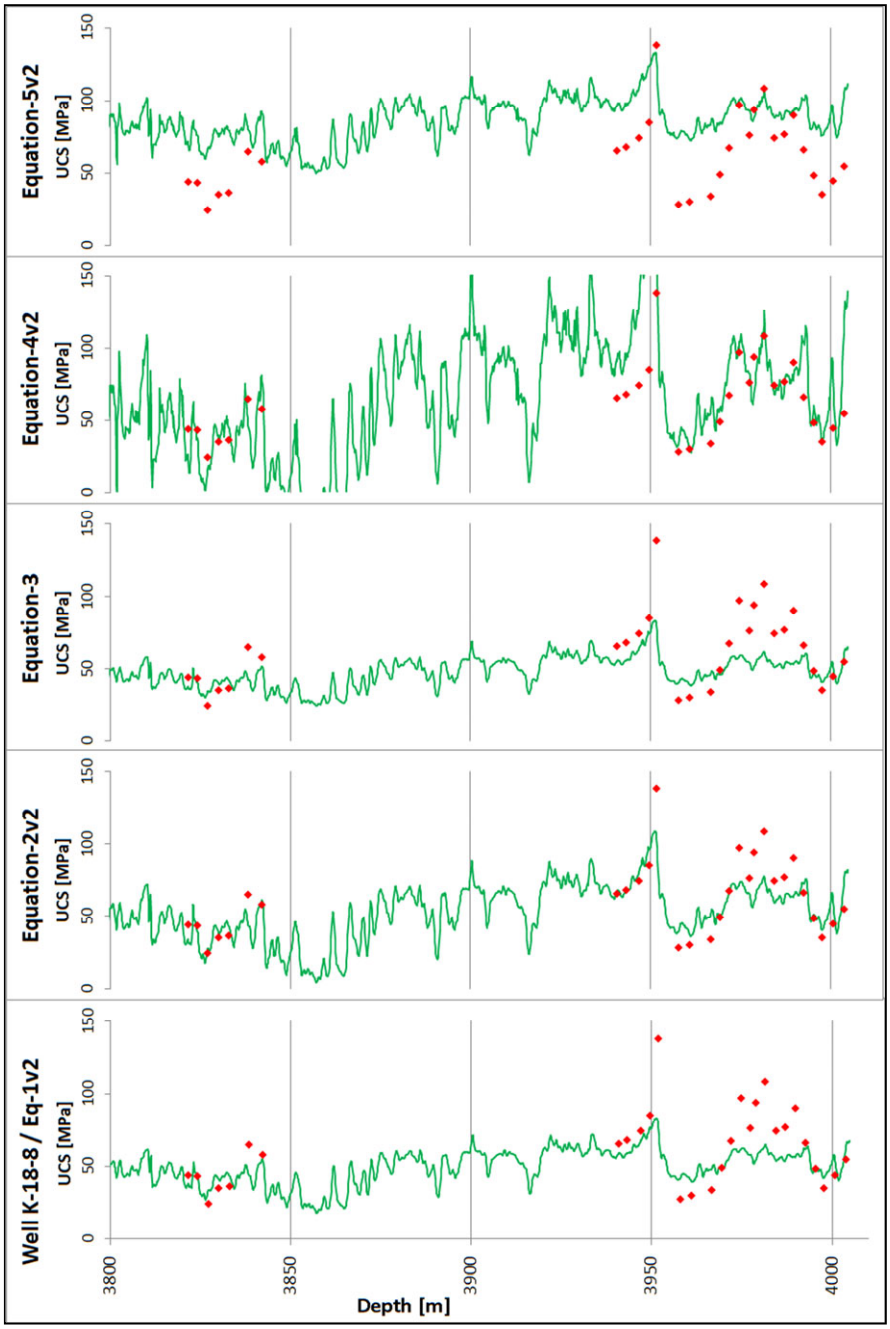

Figure 4-42 – Graphs show predicted UCS logs by equations 1-5 (Table 4-25) where "v2" indicates that the equation was modified. The red dots indicate the measured UCS values.

4.5 Conclusion

In conclusion, the results of this study showed that better fit and more reliable wireline log-based rock strength and elastic modulus correlation equation can be created using more log properties as predictor variables for multivariate regression. Much better fit was provided by models where four or more log properties were involved in the model. A relatively strong relation was found between rock strength and spectral gamma ray logs (and also between elastic modulus and spectral gamma ray logs). A detailed investigation of this relation may provide additional information to better understand rock strength. The sonic velocity, the density and the spectral gamma ray logs had a significant effect on the goodness of the models. The other types of logs had less significant effect; nevertheless, the best predictions are obtained by applying these logs too (resistivity, neutron porosity logs): it was possible to achieve a squared regression coefficient higher than 0.8. In the Rotliegend sandstone, the best correlation was found between the acoustic slowness log and UCS (R^2=0.59). However, in the Lower German Triassic sandstone, the correlation between the logs and the UCS was lower in general than in the Rotliegend; the best correlation was found between the density log and UCS (R^2=0.28).

The UCS logs predicted by the correlation equations show artificial or unrealistic behaviour at some short sections, such as negative UCS values or very sudden and large changes in values. This unrealistic behaviour may originate, on the one hand, from the log data, because logs can also contain artificial values, and, on the other hand, the multivariate regression could also create unrealistic values as a side-effect of the line fitting in a multidimensional space. Therefore, quality control of the predicted logs is important to filter these features and create a more realistic predicted log.

In addition to quality control of the log data (e.g. to apply corrections, filter the unrealistic values), the goodness-of-prediction can also be improved by applying a more appropriate sample selection method. A more comprehensive data set can be gained if an arbitrary sampling method is applied for the sample selection. The arbitrary sampling is supposed to be based on all the relevant log data to gain a samples set which involves all the permutations of the log properties (e.g. gamma ray, density, resistivity, etc.) and values (by defined classes). With a more comprehensive sample set, the prediction model may be more reliable and valid for the more expansive (large) sections

A strong correlation was found between the elastic moduli and the rock strength in the measured results. The regression coefficient between the elastic moduli and the rock strength is higher in the Rotliegend sandstone (R^2=0.92) than in the Lower German Triassic sandstones (R^2=0.46). The difference between the regression coefficient of the Triassic sandstones in well P6-9 (R^2=0.73) and L6-8 (R^2=0.06) is significant. The correlation is good between the elastic modulus and unloading modulus, applying all the samples to the model, and even better for the Rotliegend sandstones only. However, the correlation between the elastic modulus and unloading modulus was found to be very low in the Triassic sandstones in only well L6-8.

A comprehensive study on the relation between log properties and rock mechanical properties, which includes, for example triaxial rock mechanical tests, mineral composition analysis and microstructure analysis, can produce more general equations. The better understanding of the factors which influence rock mechanical properties can improve the log-based rock mechanical property prediction models.

5 Brittleness Index for North Sea sandstones

5.1 Introduction and background

Brittleness is an important property of a reservoir rock, especially for tight reservoirs, where open fractures contribute considerably to the hydrocarbon production. The brittleness of the rock is related to the fracture behaviour and sand production of a reservoir. In a more brittle rock, considerably more open fractures can develop; moreover, in less brittle sandstones the sand production can increase significantly.

Although brittleness is an important and widely used parameter, there is no conventional definition of it. The brittleness of a rock has been defined in many ways. Morley (1944) and Hetenyi (1950) described the brittleness as the lack of ductility. According to Ramsay (1967), a rock is brittle when the internal cohesion of the rock is broken. Obert and Duvall (1967) and Fossen (2010) defined the brittle material as the one which deforms by fractures at or only slightly beyond the yield stress. A rock is brittle if its strength becomes zero or nearly zero after the failure and there is no significant elastic, defined Jaeger, et al. (2009). According to Yagiz and Gokceoglu (2010), a rock is brittle when it breaks at very little deformation.

Some studies, such as Paterson and Wong (2005) and Heard (1960) elaborated on the brittle-ductile characteristics of rocks (listed in Table 5-1). They analysed different types of rocks under different conditions; nevertheless, some of their observations are similar. Paterson (1978) studied the Wombeyan Marble under compression with changing confining pressure. Heard (1960) analysed Solnhofen Limestone samples which were deformed under compression or extension with changing confining pressures and temperatures. According to the results of Paterson and Wong (2005) and Heard (1960), in case of brittle rocks, the permanent strain before failure is less than 3%, and between 3-5% rocks are semi-brittle. In case of ductile rock, they all measured more than 5% permanent strain before failure. Also, all of these studies showed, that; on the one hand, in brittle rocks, there is loss of cohesion and strong dilatancy, the strain is localized, one of the major deformation mechanisms is microcracking, stress drop related to failure; and on the other hand, in ductile rocks, there is no loss of cohesion, and the strain and the distribution of macroscopic deformation features are homogenous and there is no stress drop at failure. However; there are also differences in the results due to the different rock types and different conditions. For example, in the cases of marble and limestone, axial splitting was observed in the brittle samples, conjugate shear fractures were described in the semi-brittle samples; whereas, in the case of brittle sandstone, single shear fractures were reported. Further differences are that in the brittle marble and the brittle limestone besides microcracking there was also minor twinning; while in ductile marble, crystal plasticity, twinning and microcracking were observed; however, in ductile limestone (at 700 °C and 700 MPa) there was no microcracking, but crystal plasticity and grain boundary sliding. In contrast, in both brittle and ductile sandstones, particulate sliding and grain size reduction were observed in addition to microcracking. Pressure dependence of strength was also analysed in the studies above. Patterson (1978) found that

the strength of brittle marble is strongly affected by the pressure, the strength of the semi-brittle marble decreases with increasing pressure; and, also in ductile marble, the strength is influenced by the confining pressure. Furthermore, Heard (1960) found that the strength of ductile limestone is strongly affected by both the temperature and the confining pressure, whereas in brittle limestone the effect of temperature on strength is low. Holt et al. (2015) described the importance of the effect of the stress condition, the pore pressure, the temperature and also the bedding plane on the brittleness.

Table 5-1 – Definitions of brittle – ductile characteristics of rocks by Paterson and Wong (2005) and Heard (1960).

Reference	Paterson, M.S. (2005)			Heard, H.C. (1960)		
Definition	The capacity for substantial change of shape without gross fracturing			The capacity for more than 5% permanent deformation before failure		
Example	Wombeyan Marble (initially non-porous) deformed in compression			Solnhofen Limestone deformed in compression or extension (ductility in extension starts at higher pressure than in compression		
Parameter changed	Confining pressure			Effective confining pressure and temperature (Terzaghi's principle does not hold at high strain rates)		
	Brittle	Semibrittle	Ductile	Brittle	Semibrittle	Ductile
P, T				25 °C, 1 MPa		700 °C, 700 MPa
Permanent strain before failure	<3%	>3%	>5%	<3%	>3%	>5%
Work hardening	-		+	very strong	strong	no
Stress drop associated with failure	Y		N	Y		N
Loss of cohesion	Y		N	Y		N
Microcracking	extensive, localized		extensive, delocalized	strong		absent
Acoustic emission	++(?)		+(?)	strong (?)		none
Pressure dependence of strength	++	decreasing	+	strong		none
Temperature dependence of strength	N/A	N/A	N/A	weak		strong
Deformation mechanism	microcracking, minor twinning		crystal plasticity, twinning, microcracking	microcracking, minor twinning		crystal plasticity, grain boundary sliding
Dilatancy	++		+	strong		minor or absent
Strain homogeneity	strongly localized	localized	macroscopi-cally homogeneous	localized		macroscopi-cally homogeneous
Macroscopic features of deformed samples	axial splitting	conjugate shear fractures	delocalized deformation	axial splitting	conjugate shear fractures	delocalized deformation

In the literature, several empirical equations are available which estimate the brittleness of the rock with different approaches. The brittleness indices and equations referenced in this thesis are listed in. Protodyakonov (1962) calculated the brittleness as the product of the UCS and percentage of fines formed in Protodyakonov impact test. Coates and Parsons (1966) defined the brittleness as the ratio of reversible strain and total strain. The same concept was used by Baron et al. (1962) and reviewed by Hucka and Das (1974), as the brittleness is the ratio of the reversible energy and the total energy. Furthermore, they also suggested more equation to calculate the brittleness. Firstly, the brittleness can be expressed as the ratio of the difference of the UCS and tensile strength and the sum of the UCS and tensile strength. Secondly, brittleness can be calculated using the Mohr's envelope as the sinus of the angle of the internal friction. Thirdly, the brittleness can be estimated as the difference of macro and micro indentation hardness. An absolute index was created based on the absolute irreversible longitudinal strain at failure (George 1995, Yagiz and Gokceoglu 2010). If the strain was lower than 3%, the rock was said to be brittle, between 3% and 5% strain, the rock was brittle-ductile and if the strain of the rock at failure is higher than 5%, then the rock is said to be ductile. Holt et al. (2015) analysed several brittleness indices by laboratory experiences in shales and found that the quantification of the brittleness is challenging even for well-defined approaches like B_2 and B_3. They also found that the B_2 index strongly depends on the applied method to estimate it (stress-strain curves, unload–reload cycles or elastic moduli from ultrasonic velocity measurements) (Holt et al. 2015). Altindag (2002) estimated the brittleness as the arithmetic mean of the UCS and Brazilian tensile strength. Heidari et al. (2013) calculated the brittleness index as the ratio of the UCS and the Brazilian tensile strength and also as the half of the product of the UCS and the Brazilian tensile strength. In addition, Rickman et al. (2008) suggested a brittleness index based on the Young's modulus and Poisson's ratio (B_8) which can be gain by mechanical laboratory tests or log based empirical equations. Brittleness index B_8 considering effect of the stress of the compression wave velocity (i.e. compression wave velocity increases with increasing stress and thus depth) has an inverse relation with the magnitude of brittleness index B_8 (Holt et al. 2015). Some researches (e.g. Varga 2012 and Gray 2012) applied this approached to find brittle sections (sweet spots) in shale reservoirs. Sahloo (2013) proposed an integrated mineralogy based method to classify lithofacies to find sweet spots in Eagle Ford shale. Later, Lie and Sun (2015) (B_9) proposed a brittleness index as the ratio of the Young's modulus and the Poisson's ratio and proposed to take into consideration the mineral composition of the rock by the volume fraction of the brittle and plastics minerals.

Others have used punch penetration or impact tests to measure the brittleness of the rock (Protodyakonov 1962, Blindheim and Bruland 1998, Copur, et al. 2003, Yagiz 2009, Yagiz and Gokceoglu 2010). Blindheim and Bruland (1998) measured the brittleness as the percentage of fines formed in an impact test for NTNU model (Blindheim and Bruland 1998, Yagiz and Gokceoglu 2010). According to Yagiz, the brittleness can be expressed as the ratio of maximum force applied on the rock and the corresponding penetration during punch penetration tests (Yagiz 2009). Copur et al. (2003) estimated the brittleness as the ratio of force decrement and force increment in punch penetration tests.

Several studies have focused on the parameters that influence the brittleness of the rock (Göktan 1991, Copur et al. 2003, Yagiz 2009, Yagiz and Gokceoglu 2010). Yagiz and Gokceoglu (2010) developed two models to estimate the brittleness of rock by constructing fuzzy inference system and nonlinear regression analysis. They measured several rock properties, such as punch penetration, uniaxial compressive strength, Brazilian tensile strength and unit weight of rock on different types of rock samples retrieved from tunnel cases, and predicted the brittleness of these rocks by these parameters. Heidari, et al. (2013) investigated 8 different types of rocks and they found no relationship between the porosity and the brittleness of the rock. However, they noted that the brittleness of the rock was reduced due to saturation. They also predicted the brittleness using point load tests results, and calculated brittleness indices (B_4, B_5, B_6) using three different combinations of the UCS and the Brazilian tensile strength, and they found good correlation between these brittleness indices and the point load index (Is50).

Fracture toughness is an often used rock mechanical property in civil engineering, mining or tunnel boring. Fracture toughness measures the required stress or energy for fracturing and propagation of pre-existing fractures. A special laboratory test was developed to obtain fracture toughness of materials (Srawley and Brown Jr 1965). Kahraman and Altindag (2004) studied the relationship between fracture toughness and brittleness. They studied two brittleness indices: B_5 Hucka and Das (1974) and B_6 Altindag (2002), more details Table 5–2. A strong relation was found between the brittleness index B_5 and fracture toughness; however, there was no correlation found between brittleness index B_6 and fracture toughness.

The majority of the above-mentioned definitions of the brittleness indices consider only the rock mechanical properties, such as strength, internal friction angle, elastic properties that are constant for a material. These are independent of stress condition (more details in chapter 1.2 and chapter 4.1) which has a significant effect on the in situ brittleness (e.g. Jaeger et al. 2007). Others defined the brittle-ductile behaviour of rock materials considering many properties, for example stress drop, strain distribution, measure of permanent strain, deformation mechanism or microcracking. The qualitative brittleness definition of Heard (1960) considers several significant factors, such as temperature or stress condition. Qualitative definitions can provide valuable information on the phenomena; however, it is difficult to apply them in practice without a quantitative approach.

Urai and Wong (1994) and Urai (1995) defined the brittle mudrock as the one that dilates during deformation and allows fracture permeability to develop. According to Ingram and Urai (1999), as the strain starts to localize at peak differential stress, the shear fracture starts to undulate. And due to the curvature of the fracture, the permeability of the fracture can increase or decrease depending on whether the confining pressure is low or high (Figure 5-1). Using this brittleness concept, Ingram and Urai (1999) quantified the brittleness of mudrocks as the ratio of the UCS of the given rock and the UCS of a normally consolidated rock in non-overpressured domains (UCS_{NC}) (BRI_1 in). They found that if this brittleness index is higher than two, the risk of embrittlement and the risk of developing open fractures increases as the brittleness index increases. They proposed to apply this brittleness index to

predict the leakage of mudrock top-seals on a regional scale by constructing a brittleness index map of a formation using the UCS values estimated from sonic velocity logs (Ingram and Urai 1999). This approach was used by Ishii et al. (2011) to analyse the relationships between brittleness and transport properties in mudstones. They measured triaxial tests to gain rock mechanical data of the mudstone including the brittle-ductile transition. Ishii et al. (2011) found that if the brittleness index is lower than two, the mudstone failed in a ductile way, in agreement with statement of Ingram and Urai (1999). Furthermore, they found that the mudstone fails in a semi-brittle way if the index is between two and eight, and it will fail in ductile way if the index is larger than eight.

These above-mentioned indices are not able to express the brittle behaviour of rock strata located in the deeper region of the brittle Earth crust; for instance, hydrocarbon reservoirs or related seal layers that are usually in thousands of meters of depth. Hoogerduijn-Strating and Urai (2003) presented a brittleness index that considers - beside rock properties such as unconfined compressive strength - the stress conditions as well. Their proposed index (BRI_2) can be found in Table 5–2. This index was developed for prediction of brittleness of shale top seals in order to predict the sealing capability and chance of the leakage of reservoir top seals. The index was developed for Pierre shale (about Pierre shale e.g. in Olgaard et al. (1997)). For calculation of brittleness index, they apply the earlier developed correlation equation for Pierre shale to predict UCS from sonic well log (Urai 1995, Ingram and Urai 1999) and the internal friction angle was predicted based surface area. Hoogerduijn-Strating and Urai (2003) studied the brittle behaviour of Paleozoic and Mesozoic mudrock top seals in North Oman. They were able to distinguish different characteristic top seals from excellent to poor based on their brittleness index.

Table 5-2 - List of the empirical brittleness indices.

Id.	Equation	Base	Description	Considered parameters	Reference
B_1	$B_1 = q \cdot UCS$	impact test	q=is the percentage of fine formed in Protodyakonov impact test	rock properties	Protodyakonov (1963)
B_2	$B_2 = \frac{\varepsilon_{rev}}{\varepsilon_{total}}$	strain	ε rev: ratio of reversible strain and ε rev: total strain	rock properties	Hucka and Das (1974)
B_3	$B_3 = \frac{E_{rev}}{E_{total}}$	energy	E_{rev}: ratio of reversible-energy and E_{total}:total energy	rock properties	Hucka and Das (1974)
B_4	$B_4 = \frac{UCS}{TS}$	strength	Ratio of unconfined compressive strength (UCS) and tensile strength (TS).	rock properties	Hucka and Das (1974)
B_5	$B_5 = \frac{UCS - TS}{UCS + TS}$	strength	Ratio of unconfined compressive strength and tensile strength.	rock properties	Hucka and Das (1974)
B_6	$B_6 = \frac{UCS \cdot TS}{2}$	strength	UCS: unconfined compressive strength; TS: tensile strength	rock properties	Altindag (2002)
B_7	$B_7 = \frac{\tau_p - \tau_r}{\tau_p}$	shear strenght	τp: peak shear strength; τr: residual of shear strength	rock properties	Bishop (1967)
B_8	$B_8 = \frac{E_{brit} + \vartheta_{brit}}{2}$	E_{stat}; υ_{stat}	E_{brit}= 100*(Estat-1)/(8-1) E_{stat}: static Young's modulus; υ_{brit}= 100*(υ_{stat}-0.4)/(0.15-0.4) υ_{stat}: static Poisson's ratio	rock properties	Rickman et al. (2008)
B_9	$B_9 = \frac{Y_{BRIT}}{P_{BRITZ}}$	E; υ	YBRIT=0.1*E; PBRITZ=2.5(υ − 0.4), E: Young's modulus; υ: Poisson's ratio	rock properties	Liu and Sun (2015)
B_{10}	$B_{10} = 45 + \frac{\varphi}{2}$	internal friction angle	φ= angle of rock internal friction	rock properties	Hucka and Das (1974)
B_{11}	$B_{11} = \sin\varphi = \frac{\frac{\partial R}{\partial \sigma_n}}{1 + \left(\frac{\partial R}{\partial \sigma_n}\right)^2}$		The brittleness is determined from Mohr envelop; φ= angle of rock internal friction, σ_n: normal stress on the plane of failure; R: resistance to deformation	rock properties	Hucka and Das (1974)
B_{12}	$B_{12} = \varepsilon_{1i}$ 100, %	strain	absolute index based on the absolute irreversible longitudinal strain (ε_{1i}) at failure: ε_{1i} < 3% brittle, 3% < ε_{1i} < 5% brittle–ductile, ε_{1i} > 5% ductile,	rock properties	George (1995)
B_{13}	$B_{13} = S_{20}$	impact test	S_{20} = the percentange of fines (<11.2 mm) formed in an impact test for NTNU model	rock properties	Blindheim and Bruland (1998)
B_{14}	$B_{14} = \frac{F_{max}}{P}$	punch penetration test	F_{max} = maximum force applied on the rock P = corresponding penetration	rock properties	Yagiz (2009)
B_{15}	$B_{15} = \frac{P_{dec}}{P_{inc}}$	punch penetration test	P_{inc} and P_{dec} = force increment and decrement in test	rock properties	Copur et al. (2003)
B_{16}	$B_{16} = \frac{H_m - H}{K}$	hardness	H and Hm: macro and micro-hardness; K: bulk modulus	rock properties	Honda and Sanada (1956)
B_{17}	$B_{17} = \frac{H}{K_{IC}}$	H,K_{IC}	H: hardness; K_{IC}: fracture toughness	rock properties	Lawn and Marshall (1979)
B_{18}	$B_{18} = \frac{H \cdot E}{{K_{IC}}^2}$	H, E, K_{IC}	H: hardness; K_{IC}: fracture toughness; E: Young's modulus	rock properties	Quinn and Quinn (1997)
B_{19}	$B_{19} = \frac{W_{qtz}}{W_{Tot}}$	mineralogy	Wqtz: weight of quartz; Wtot: total minarl weight	rock properties	Jarvie et al. (2007
B_{20}	$B_{20} = \frac{W_{qtz} + W_{dol}}{W_{Tot}}$	mineralogy	Wqtz: weight of quartz; Wtot: total minarl weight; Wdol: weight of dolomit	rock properties	Wang and Gale (2009)
B_{21}	$B_{21} = \frac{W_{QFM} + W_{carb}}{W_{Tot}}$	mineralogy	WQFM: weight of quartz, feldspar and mica; Wtot: total mineral weight; Wcarb: weight of carbonate mineral	rock properties	Jin et al. (2014)
BRI_1	$BRI_1 = \frac{UCS}{UCS_{NC}}$	strength	UCS=unconfined compressive strength; UCS_{NC}=unconfined compressive strength of a nonoverpressurized normally consolidated rock	rock properties and vetical stress	Ingram, G. M. and Urai, J. L. (1999)
BRI_2	$if\ \sigma'_1 \geq UCS;$ $BRI_2 = \frac{(\sigma'_1 - \sigma'_3)}{(0.1 \cdot UCS + \sigma'_3)}$ $if\ \sigma'_1 < UCS$ $BRI_2 = 0.1 \cdot (\sigma'_1 - \sigma'_3) - \sigma'_3$	strength and stress	Ratio of differential stress and unconfined compressive strength.	rock properties and stress condition	Hoogerduijn-Strating, E. and Urai, J. L. (2003)

Brittle-ductile transition

In order to interpret the brittleness index, it is important to know at which conditions a rock is brittle or the ductile. It has been shown, that during triaxial tests, with increasing the confining pressure, higher stress is required to break the sample. Moreover, with higher confining pressure, the rock shows higher tendency for ductile behaviour (Kármán 1911, Adams 1912, Jaeger, et al. 2009). However, in some cases, the rock showed a transitional type of behaviour, so it can undergo large strain (~7%) and still fail in a brittle way (Kármán 1910). Therefore, it is really hard to find a value of confining stress to distinguish the brittle and the ductile behaviour. According to Heard (1960), the brittle-ductile transition can occur at that given confining stress, at which the strain at failure is 3-5%.

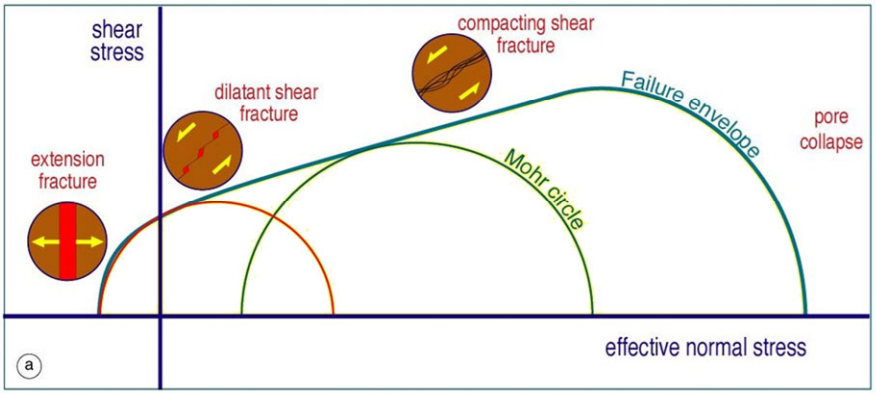

Figure 5-1 - In Mohr diagram three main types of fracture type are shown. (modified after Hoogerduijn-Strating and Urai 2003)

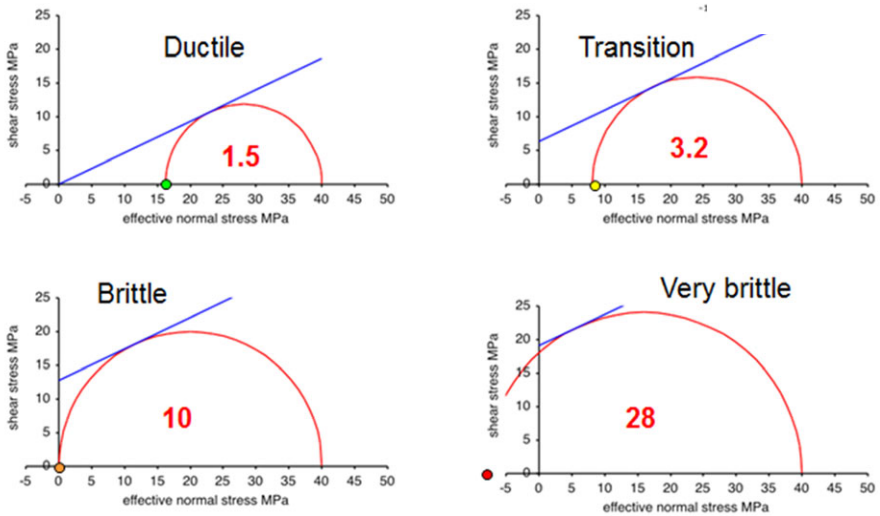

Figure 5-2 – Brittleness index diagrams of Hoogerduijn-Strating and Urai (B_{12}) for four different rock with different UCS values. Brittleness index value is around 3.2 in the transition zone. (modified after Hoogerduijn-Strating and Urai 2003)

There are several theoretical models to describe the brittle or ductile behaviour of the rocks. Both in the brittle part and in the ductile part, the critical stress of the rocks is influenced by the confining pressure, however in a different way. In the brittle regime, the

peak differential stress is linearly proportional to the effective mean stress according to the Mohr-Coulomb theory. Contrarily, in the ductile regime, the relationship between the critical differential stress and the effective mean stress can be estimated by an elliptical model, such as the Cam clay model (Wood 1990), Carroll's critical state model (1991) or the DiMaggio-Sandler model (1970) cap model (Wong and Baud 2012). These models are affected by the porosity and the grain size of the rock, and also the strain rate of the deformation. According to Wong and Baud (2012), we can identify the stress state of a given rock at the brittle-ductile transition with the intersection of the Mohr failure envelop and the elliptical yield cap.

In this work, the aims of the study of brittleness are; on the one hand, to develop an improved brittleness index equation which quantifies the brittleness of rocks under a given stress similarly to the brittleness index of Hoogerduijn-Strating and Urai (B_{12}). However, this work aims to find a single equation instead of combination of two equations. On the other hand, to calculate a brittleness index log for the studied sandstone reservoir strata in order to characterise the brittle behaviour of these rocks and predict the type of possibly occurring fractures.

5.2 Proposed new brittleness index equation (BRI_3):

In the development of new brittleness index (BRI) equation, the following objectives were considered:

- The brittleness index is supposed to quantify a property of rock materials related to the tendency of the type of fractures at failure. The condition of rock failure can be approached by Mohr-Coulomb equation, where the relevant rock properties are the internal friction angle, the cohesion or the UCS.
- Different types of fractures can be formed in the same type of rock under different stress conditions (in chapter-1 Figure 1-3). Therefore, it is necessary to consider stress condition at failure at brittleness prediction of a rock. The two dominant factors are the maximum and the minimum effective stress values (σ'_1 and σ'_3). The intermediate principle stress, σ'_2 has an effect on the rock strength; but, less significantly than the others; therefore, σ'_2 was not involved in this approach.
- The parameters of the transition zone are also necessary to consider. The transition zone between brittle and ductile status where a rock is semi brittle located in a certain distance from the origin of the Mohr diagram and it also covers a range of normal stress of the Mohr diagram.
- The temperature plays an important role in rock strength and fracturing and in the study of the brittle behaviour of rocks. However, the temperature does not reach that level where the brittle behaviour of rock material significantly changed in the depth region of reservoir strata. Therefore, the temperature was not considered parameter either in the brittleness index equation.
- Parameter n is supposed to be an even round number.

The above-mentioned objectives are in agreement with the concept of Hoogerduijn-Strating and Urai equation the BRI_2 in Table 5-2. Graph of BRI_2 equation can be seen on Figure 5-3 for a given rock with changing stress conditions. As it can be seen, equation BRI_2 contains two

different type of equation one for the case if $\sigma'_1 > UCS$ and another equation for the case if $\sigma'_1 < UCS$. The value of BRI_2 is equal to 10 if $\sigma'_1 = UCS$; and, at this point there is a break in the graph and it jumps suddenly in the negative, brittle part of the graph. However, the behaviour does not fit the behaviour of the rock very well in general.

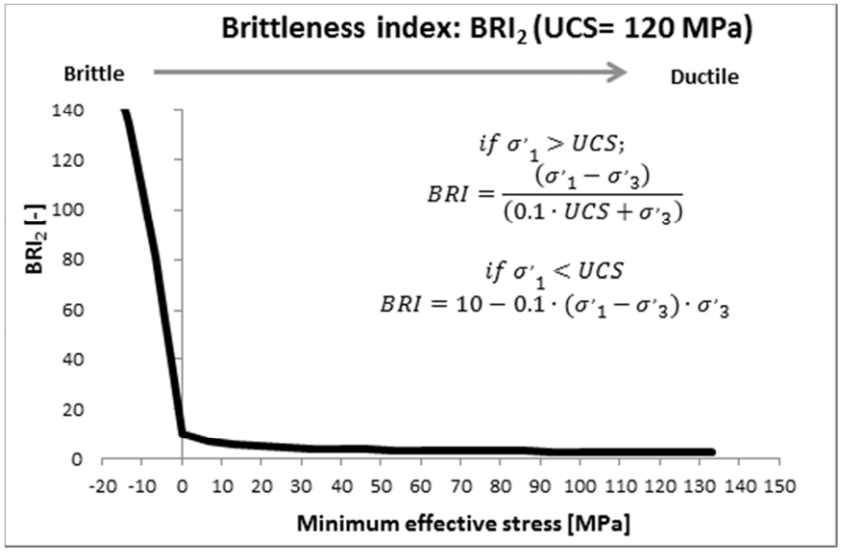

Figure 5-3 – Graph of brittleness index of BRI_2 by Hoogerduijn-Strating and Urai 2003 (Table 5–2).

The basic idea of the newly proposed brittleness index equation (BRI_3) is to use the UCS of the rock as a reference value and compared with the stress conditions. This is demonstrated in a Mohr diagram in Figure 5-4 where the blue Mohr circle indicates the UCS stress state. If the diameter of a Mohr circle at failure is smaller (green circle in Figure 5-4) than the diameter of the Mohr circle of UCS, then the analysed rock is more brittle. The larger the diameter of a Mohr circle relative to the UCS case, the more ductile the material is under that stress condition. In the proposed brittleness index equation, the UCS is divided by the differential stress (Eq. 5-1). The characteristic of the function without of these parameters is very similar to BRI_2 as it can be seen on Figure 5-5. Therefore, to modify the behaviour of the function, two parameters named m and n were applied. The equation (Eq. 5-1) is the proposed new brittleness index equation (BRI_3). Where n is a power index which can change the curvature of the function which related to width transition zone. In addition, n is a multiplication factor for UCS which can shift function along the X axis. Figure 5-6 shows the effect of these parameters. The location of the brittle-ductile transition zone of the rock on the X axis can be set with n parameter i.e. what the stress condition range is where the rock is semi brittle.

Because there is no available exact method to define the brittle-ductile transition of a given rock; therefore, the applied parameter values were estimated based on the result of previous studies. The m and n parameters of the brittleness index equation were defined based on Kármán's sandstone triaxial measurement results (Kármán 1910). Based on this stress and strain curves of triaxial series of sandstone, the brittle zone ends at approximately 15 MPa confining pressure because the stress and strain curve with 28 MPa confining

pressure breaks after relatively large strain after the yield point. The unconfined compressive strength of the rock was approximately 60 MPa. In this analysis, BRI_3 logs m= 2 and n= 6 parameters were used to calculate brittleness index logs as it fit Kármán's results well. Figure 5-7 shows the relation between UCS and internal friction angle (φ) and brittleness index function.

The UCS to the brittleness index equation can be calculated from wired line well log values (see Chapter 4). The vertical stress (σ_1) can be calculated from the density log as the integral of the mass of vertical rock column (Eq. 5-2). If the pore pressure is known effective stress can be calculated. To calculate the minimum principal stress of rocks at failure, the failure criteria has to be known i.e. the failure envelop of the rock. In the negative field of the normal stress of the Mohr space, the failure envelop can be defined by Griffith's parabola (Eq. 5-3) where C is the cohesion and assumed that $C=2\cdot\sigma_T$ where σ_T is the tensile strength. In the positive filed of the normal stress of the Mohr space, it can be defined by the linear Coulomb's failure criteria (Eq. 5-4) φ is the internal friction angle. The internal friction angle based on Kármán's (1911) results is approximately 40°, for brittleness index log calculations φ=40° value was used. Knowing the UCS and the internal frictional angle of the rock, the cohesion can be calculated (Eq. 5-5). With these data, the failure envelop can be defined and the minimum principal effective stress can be calculated at failure if the maximum principal effective stress is given.

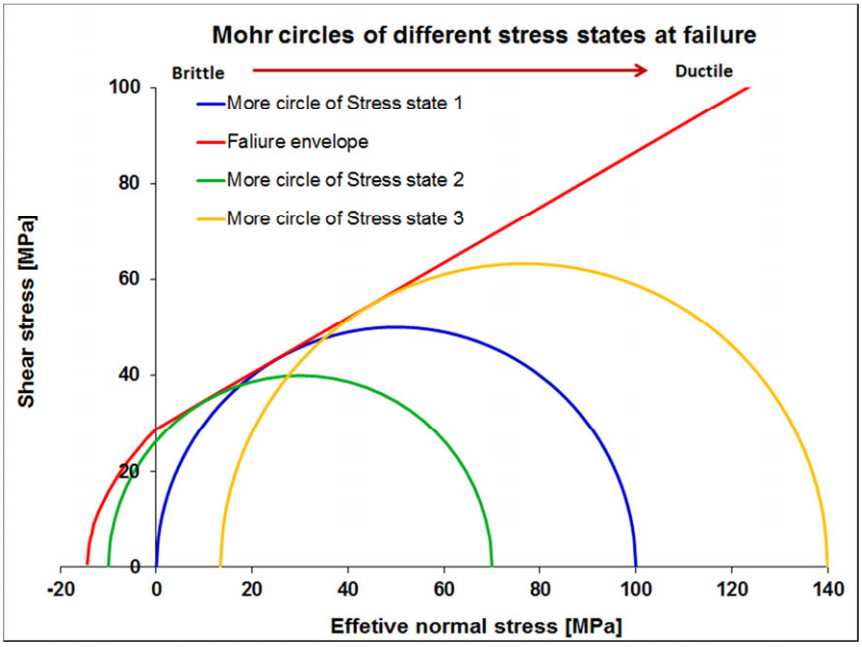

Figure 5-4 – Mohr circle of different stress condition at failure. Diameter of the circles are smaller towards to the brittle part of the Mohr space.

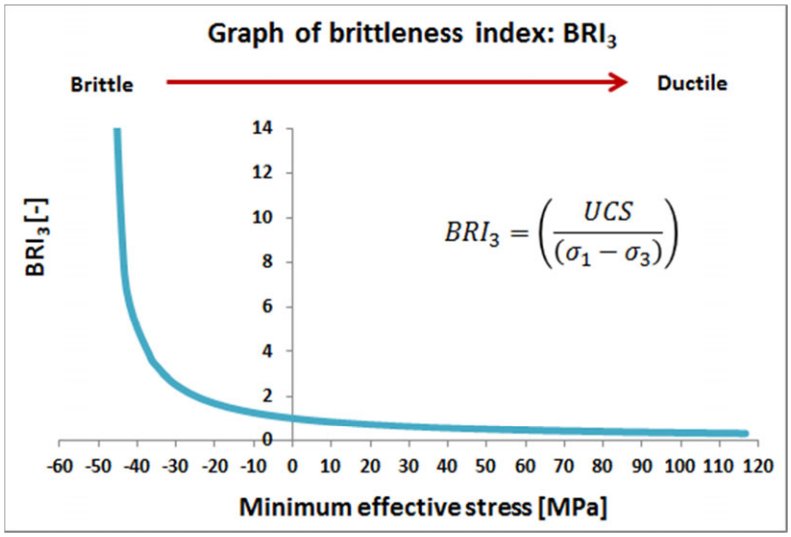

Figure 5-5 –BRI_3 function without parameters (or in case m=1 and n=1) (UCS=100, φ=30°).

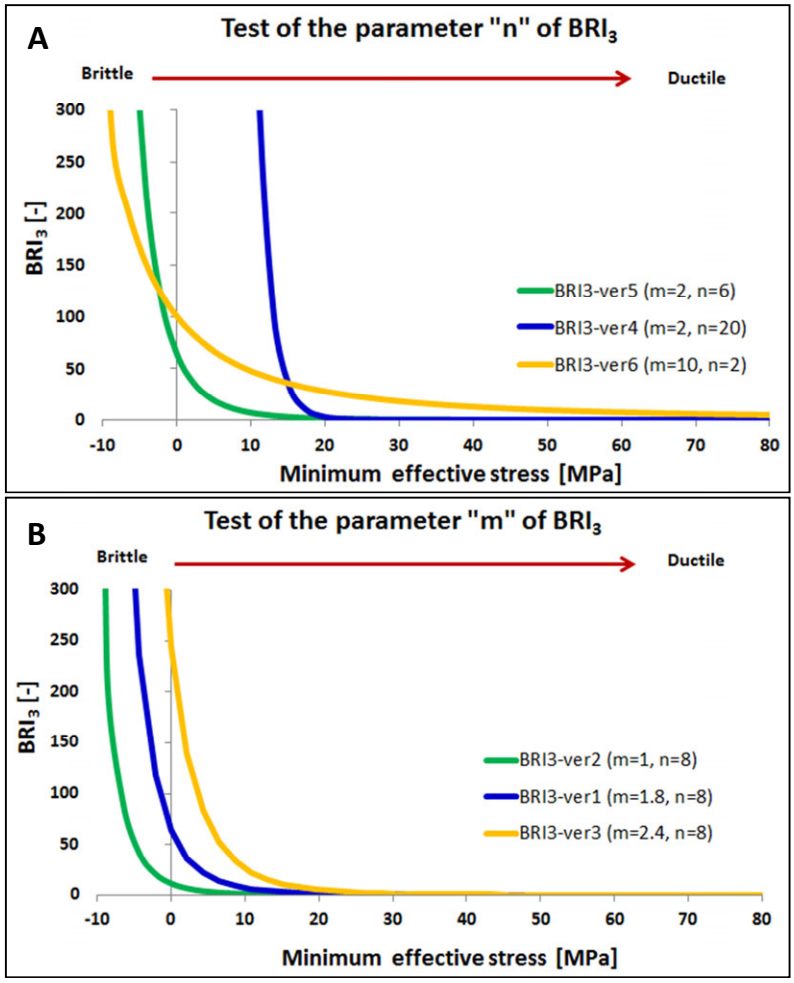

Figure 5-6 –BRI_3 function with different functions (UCS= 80 MPa, φ=40°); figure A: effect of parameter "n"; figure B: effect of parameter "m".

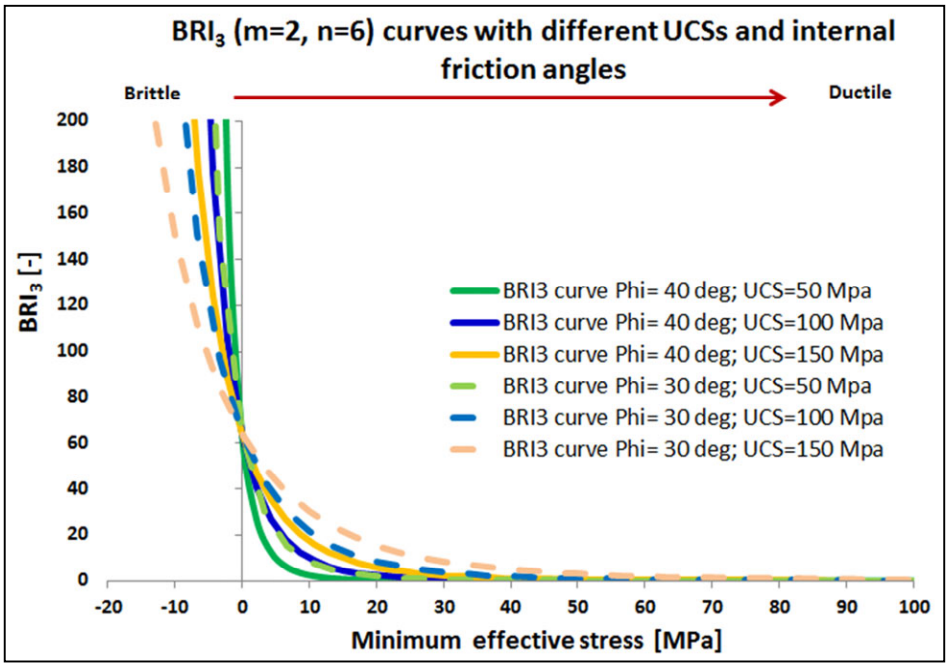

Figure 5-7 – Brittleness index function with parameter m= 2 and n= 6 for rocks with UCS and internal fiction angel.

$$\mathrm{BRI} = \left(\frac{m \cdot UCS}{(\sigma_1 - \sigma_3)}\right)^n \quad \textbf{(Eq. 5-1)}$$

$$\sigma_{1eff} = \sigma'_1 = \left(\int_0^z \rho_{rock}(z) \cdot g \, dz\right) - p_{pore} \quad \textbf{(Eq. 5-2)}$$

$$\sigma_s + 4 \cdot \sigma_T \cdot \sigma_s - 4 \cdot \sigma_T = 0 \quad \textbf{(Eq. 5-3)}$$

$$\sigma_s = \mathrm{C} + \tan(\varphi)\sigma_n \quad \textbf{(Eq. 5-4)}$$

$$\mathrm{C} = \frac{UCS \cdot (1 - \sin\varphi)}{2 \cdot \cos\varphi} \quad \textbf{(Eq. 5-5)}$$

$$\sigma_{3eff} = \sigma'_3 = \sigma_{1eff} \cdot \frac{1 - \sin\varphi}{1 + \sin\varphi} - \frac{UCS \cdot (1 - \sin\varphi)}{1 + \sin\varphi} \quad \textbf{(Eq. 5-6)}$$

5.3 Results: Brittleness Index logs

Brittleness index logs were calculated for the Rotliegend Sandstone in 4 wells and the Lower German Triassic Sandstone in 2 wells. To calculate the proposed new brittleness index equation (BRI_3, Eq. 5 1), m=2 and n=6 parameters were applied. The logs were calculated with three pore pressure conditions: 1.) no pore pressure (black line), 2.) pore pressure is equal to the hydrostatic pressure (blue line) and 3.) pore pressure is higher than the hydrostatics pressure by 10 MPa (green line). The maximum effective principal stress was calculated using an average overburden density of 2.5 g/cm^3 above the top of the logs since density logs were not available in the shallower hole section. In the plots of the logs, red dashed lines indicate the brittleness index under zero minimum effective stress condition (i.e. UCS). The BRI_3 is always equal to 64 if m=2 and n=6 and the maximum principal effective stress is equal to UCS independently from the magnitude of the rocks unconfined compressive strengths. Therefore, this is a constant line in the BRI_3 plots. This line can provide a guideline which indicates the brittle the condition where rock most likely fails in a brittle way. If the value of the BRI_3 is higher than this limit, the rock breaks in a brittle way certainly. The assumed boundary of the brittle zone, based on Kármán's (1910) results (see chapter 5.2), is 15 MPa minimum effective principal stress. The brittleness index is 1.4 at this stress state for the rock that has UCS of 60 MPa (Figure 5-8). If the boundary of the brittle zone is lower, then the BRI_3 value increases significantly. Therefore, the knowledge of the boundary of the brittle zone is important. The BRI logs cover a wide range from 0 up to more than 10000, the brittleness index is plotted in logarithmic scale.

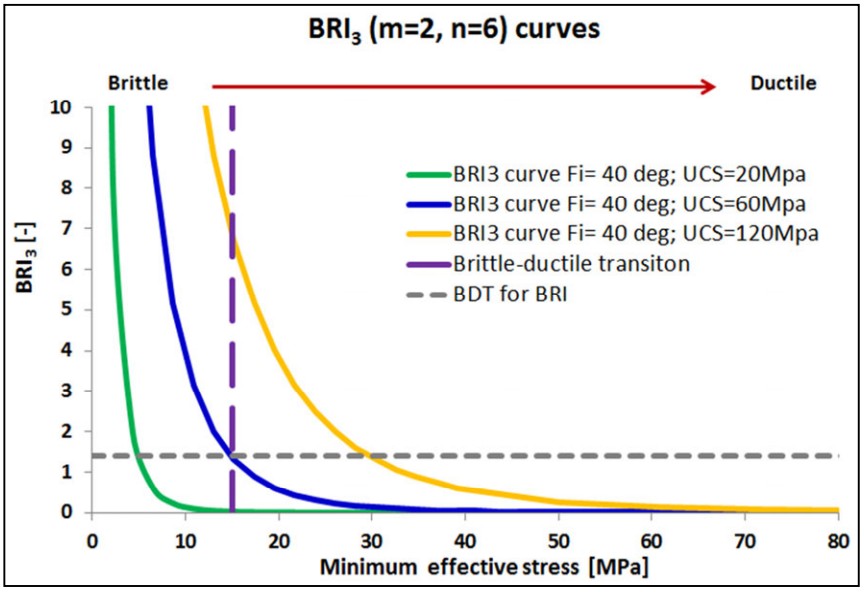

Figure 5-8 – Brittleness index graphs (n= 1.8 and m= 8) with varies UCS. The dashed lines show the assumed brittle-ductile transition (BDT). BRI is 4 at σ'_3 = 30 MPa.

Figure 5-9 shows the brittleness index graphs of Rotliegend sandstone strata of wells P2-SE2 and K18-8. In the approximately 250 m section of the well P2-SE2, nine facies can be separated which are indicated by the coloured column on the right side of the graph. A strong correlation between rock facies and brittleness index log can be seen. This correlation can be seen even at a relatively layer thin e.g. around a depth of 3360 m in well P2-SE2. Four facies can be considered as brittle: Zone-2A, Zone-2C, Zone-4 and Zone-6. The brittleness indices in these rocks are relatively high (they are in the brittle range) with hydrostatic or higher pore pressure. Without pore pressure the brittleness indices slightly lower than the UCS line. Besides, brittleness indices of other facies in this log are low even higher pore pressure.

The brittleness index log in Rotliegend strata in well K18-8 can be seen on right side of Figure 5-9. In the approximately 240 metres long section in this well, four facies was distinguished. The correlation is lower between brittleness log and rock layers than in well P2-SE2. The brittleness index values higher are in the Silverpit Ameland Member almost in the entire section; the BRI_3 without pore pressure is slightly lower than the UCS limit but with pore pressure it is unambiguously higher. Only several metres of Silverpit Ten Boer Member are available; therefore, the brittleness of this sandstone might be not reliable. In this short section, the brittleness index values are higher than the UCS limit on the upper part of it. In more than 100 metre long Upper Slochteren strata, the BRI_3 log contains subsequences of more brittle and non-brittle sections. One longer and one shorter brittle section can be found in this facies where the rock is definitely in the brittle range but only with at least hydrostatic pore pressure. Furthermore, in a relatively long section of this facies, the brittleness index values are much lower (close to zero even with overpressure) than in the other parts of the log. The approximately 100 metre long Lower Slochteren Member has also brittle and less brittle subsequence. In the top and the middle part of the rock, non-brittle sections can be found locally (several metres). This member contains the most brittle section of the entire log of this well. The Rotliegend sandstones are more brittle in well K18-8 than in well P2-S2 even though rocks are located deeper in well K18-8.

Figure 5-10 (on the left) shows the brittleness index logs of Rotliegend Lower Slochteren Sandstone Alpha Member of wells L6-8. This log, which is only 30 metres long, shows relatively homogeneous characteristic. Only a few, local (approximately one metre long sections) higher and lower peaks can be seen in this section. In general, this sandstone is brittle if the pore pressure exceeds the hydrostatic pore pressure. If the pore pressure is lower than the hydrostatic pore pressure then it is in the brittle-ductile transitional zone and with zero pore pressure it might fail in a ductile way.

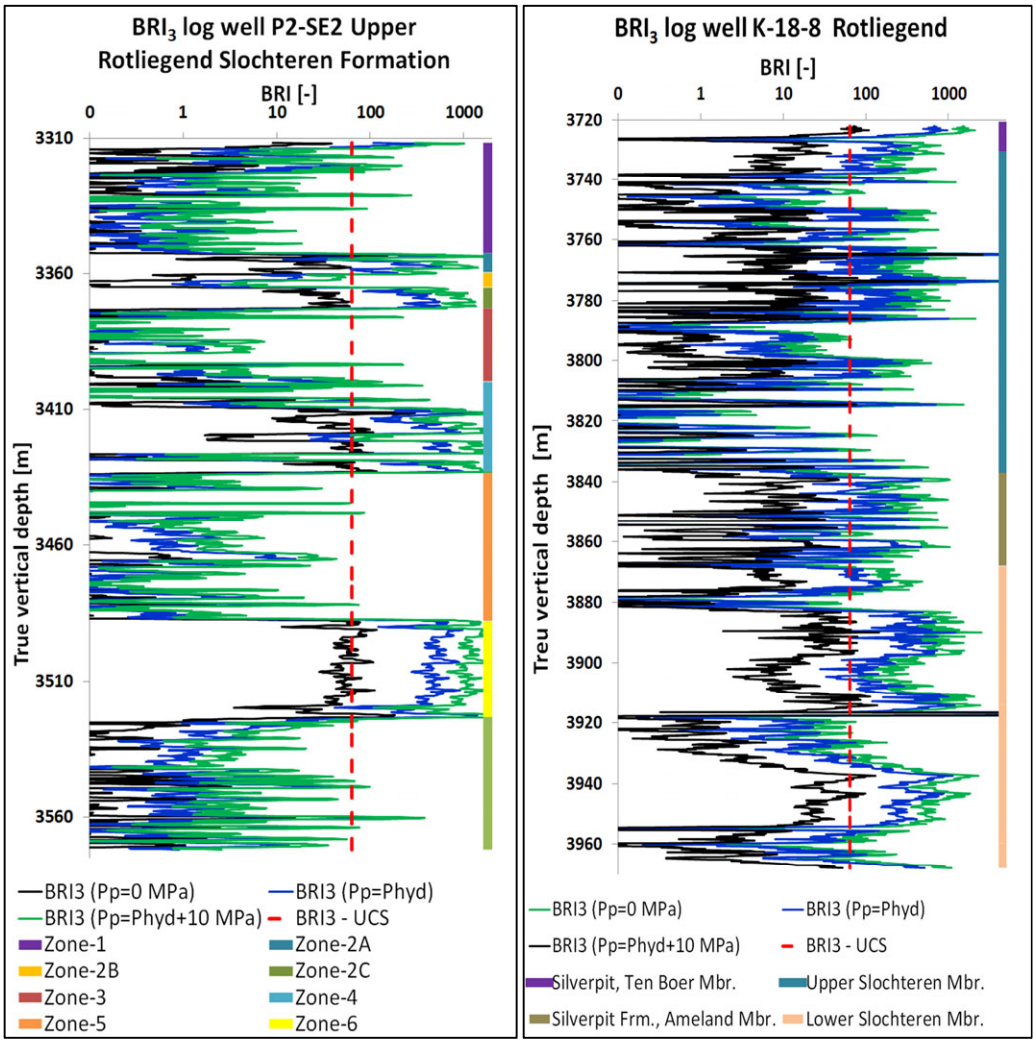

Figure 5-9 – Brittleness index (BRI_3) where m=2; n=6 logs of sections of Rotliegend Sandstone of well P2-SE2 (on the left) and well K18-8 (on the right) with zero, hydrostatic (Phyd) and hydrostatic + 10 MPa pore pressures (Phyd + 10 MPa). The dashed red line indicates the BRI_3 for zero minimum principal effective stresses condition (UCS).

Figure 5-10 shows (on the right) the brittleness index logs of Upper Rotliegend Slochteren Sandstone Formation in wells P6-9. This about 100 metres long section shows a heterogeneous characteristic. There are three approximately 10 metres long sections where the brittleness index values are higher. The logs only locally reach the UCS line without pore pressure. However, the log gets into the brittle range with hydrostatic pressure. Besides, those sections of the log where the brittleness index is low, the logs stay in the ductile range even with higher pore pressure. These sections most likely fail in a ductile way. Only in the very bottom of the log, there is a several metre long section where the relatively low brittleness index values can increase above the UCS line with at least hydrostatic pore pressure. In this formation, the brittle and ductile sections can be separated based on the brittleness index inside the formation. In the upper about 50 m section, the very low brittleness index is likely related to the lithology. This section is a clay reach section based on the geological log. The low brittleness index section at 3550 m is related to the clay reach

lithology. However, there is no lithological change reported between 3490 m and 3510 section where the brittleness index low too.

Figure 5-11 shows the brittleness index logs of the Main Buntsandstein Subgroup of the Lower German Triassic Sandstone Group in wells P6-9 and L6-8. In the approximately 350 metres long section of log of well L6-8, two sandstone layers are present. The upper 25 metres relatively thin section is part of 40 metres thick Volpriehausen Sandstone Member. In this member, the brittleness index is low except two very short peaks which might be not reliable. Below the layer boundary (approximately from 4040 m to 4100 TVDSS), there is an transition zone where brittleness index log without pore pressure jumps up to the UCS line and it stays there in the top 60 metres of the Lower Buntsandstein Formation. At a depth of 4110 TVDSS metres, the brittleness index log jumps up over the UCS line even with no pore pressure. In the very bottom of the strata at 4360 m TVDSS, the log jumps up significantly which might be related to lithological changes. The Lower Buntsandstein Formation can be separated into three sections by brittleness.

In the approximately 140 metres long section of log of well P6-9, the Hardegsen Formation, Lower Detfurth Sandstone Member and Lower Volpriehausen Sandstone Member of the Lower German Triassic Group are present (on the right of Figure 5-11). Between these sandstone members and formation, clay and siltstone can be found. In general the brittleness index logs are above the UCS line in the Hardegsen Formation even with no pore pressure. The brittleness index logs are lower in the Lower Detfurth Sandstone Member and Lower Volpriehausen Sandstone Member. The brittleness index is higher than the brittleness index of UCS only with at least hydrostatic pore pressure. All the logs are relatively hectic which might be related to the quality of the source log or less likely related to lithological variation. The brittleness index logs have a slight decreasing tendency with the depth.

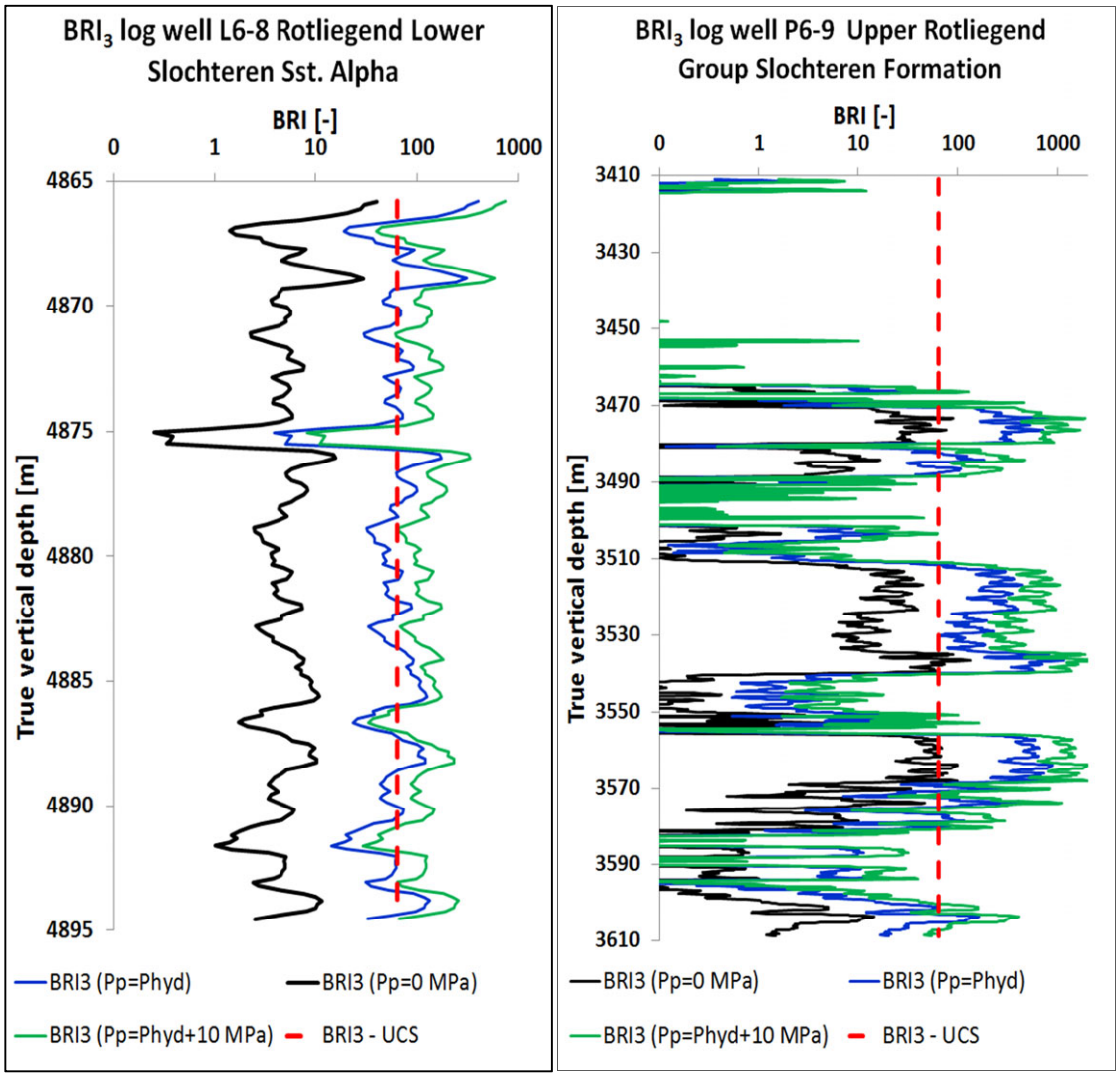

Figure 5-10 - Brittleness index (BRI_3) where m=2.5; n=6 logs of sections of Rotliegend Sandstone of well L6-8 (on the left) and well P6-9 (on the right) with zero, hydrostatic (hyd) and hydrostatic + 10 MPa pore pressures (Pp). The dashed red line indicates the BRI_3 for zero minimum principal effective stresses condition (UCS).

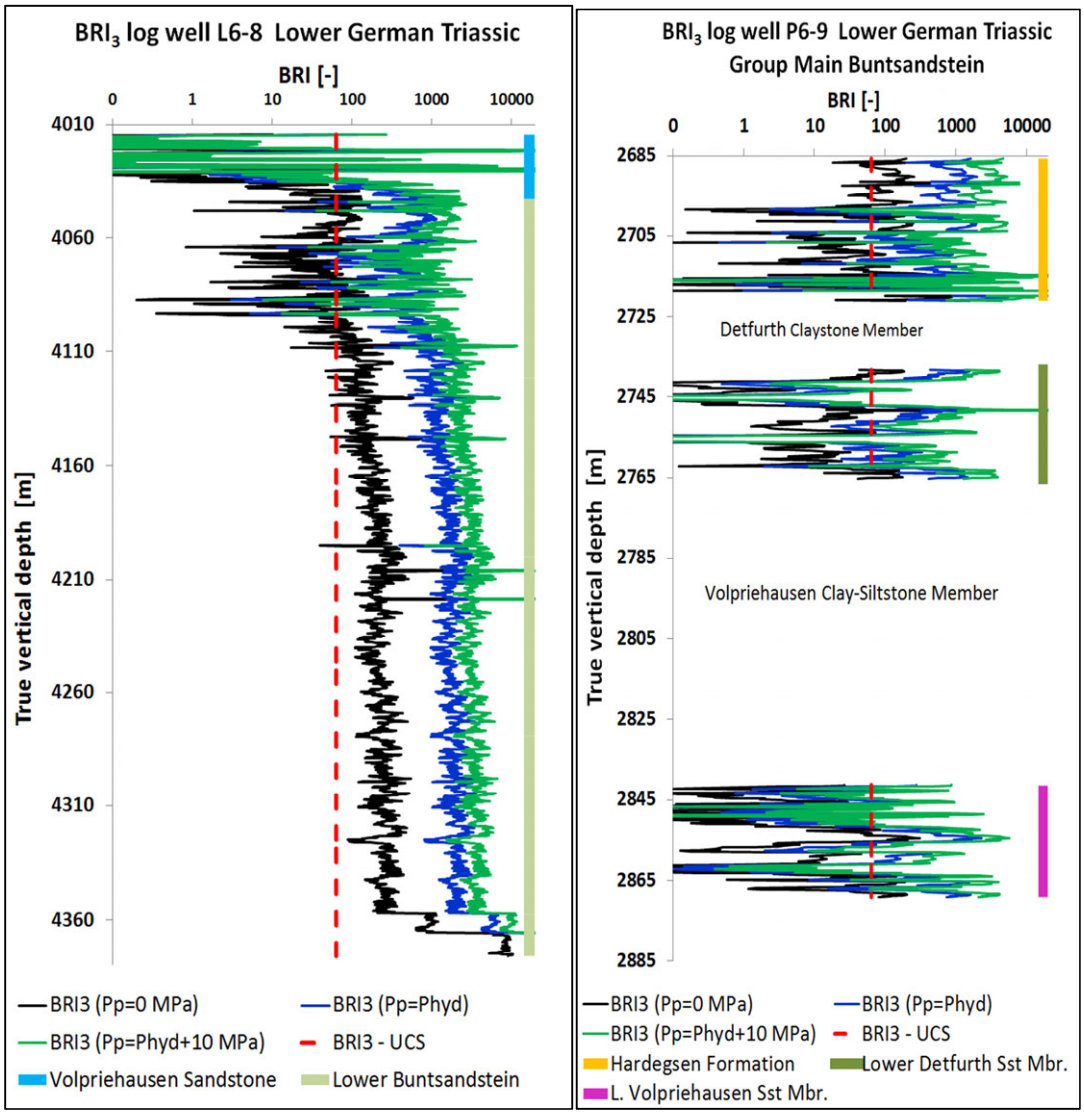

Figure 5-11 -Brittleness index (BRI_3) where m=2.5; n=6 logs of sections of Lower German Triassic Sandstone of well L6-8 (on the left) and well P6-9 (on the right) with zero, hydrostatic (hyd) and hydrostatic + 10 MPa pore pressures (Pp). The dashed red line indicates the BRI_3 for zero minimum principal effective stresses condition (UCS).

5.4 Discussion

There were two aims to develop a new brittleness index equation (BRI_3) which works according to the idea of the equation of Hoogerduijn-Strating and Urai. One of the aims was to make the existing equation simpler by using only one equation. The other aim was to have an option to setup the brittle-ductile transition by parameters and make the equation adjustable. As can be seen in Figure 5-12, the BRI_2 brittleness index (Hoogerduijn-Strating and Urai 2003), increases rapidly if $\sigma_3 < 0$ MPa. The BRI_2 function varies in a relatively narrow range, between 10 and about 3, if the σ_3 is between 0 and 50 MPa. This kind of function characteristic is not ideal because the brittle-ductile transition boundary may be in this 0 and 50 MPa σ_3 range. Since there are no parameters in the BRI_2 function, it is not allowed to change the characteristic of the function to become more appropriate for a studied rock.

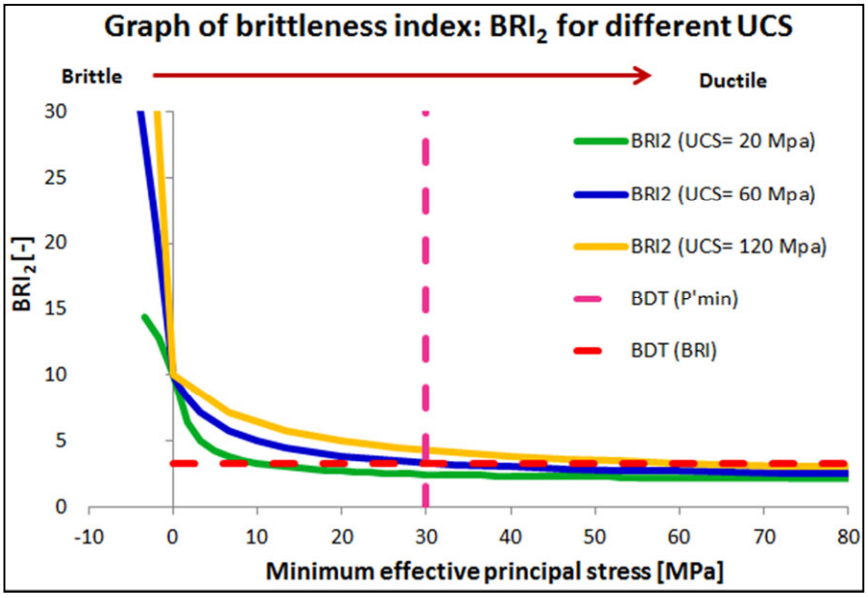

Figure 5-12 - Brittleness index graphs of Hoogerduijn-Strating and Urai (BRI_2) with varies UCS. The dashed lines show the assumed brittle-ductile transition (BDT). BRI is 3.3 at σ'_3 = 30 MPa.

The results showed that the BRI_3 brittleness index log revealed good correlation with lithology (see Chapter 5.3). In general, the variation of these brittleness indices is relatively low within a formation in well P2-SE2 Rotliegend Sandstone, well L6-8 Rotliegend and Lower German Triassic Sandstone and well P6-9 Lower German Triassic Sandstone. However, there were some layers where significant changes could be noticed, such as wells K18-8 and P6-9 Rotliegend Sandstones. Furthermore, Lower Buntsandstein (LGT) of well L6-8 or Lower German Triassic Sandstone of well P6-9 or Zone 2A, 2C, 4, 6 of Rotliegend Sandstone were found to be relatively brittle. Several semi-brittle layers become brittle if the pore pressure is above the hydrostatic pressure (here the applied overpressure=10 MPa). Since the definition of the brittle-ductile transition is only approximate, the brittleness logs might not provide reliable results in this range. Nevertheless, the BRI_3 log can provide a good prediction to identify major changes in the brittleness.

Figure 5-13 shows brittleness index logs for the Rotliegend section of well P2-SE, calculated by the equations as follows: BRI_3 with parameters m=8 and n=1 and with the parameters m=2 and n=10; BRI_2; BRI_1; and B_3 (see Table 5-2). The B_3 index is based on internal friction angle, which was calculated by gamma ray (Eq. 5-8; Chang et al. 2006) and acoustic velocity-based empirical equations (Eq. 5-7; Lal 1999). The behaviour of the BRI_3 logs with the two different parameter setting is very different in the brittle-ductile zone (i.e. below the UCS line). These logs show an example of how the parameters allow the change in BRI_3 function in the lower minimum stress range. The BRI_2 logs give high values if σ'_3 is lower than zero and, if it is higher, i.e. below the UCS line, the index remains relatively high, here about 4. The BRI_1 index values are lower; here they range between 0-5. The brittle-ductile boundary for the BRI_1 index is two (2) defined empirically for shale by Hoogerduijn-Strating and Urai (2003) and, more recently, Ishii et al. (2011) found the same brittle-ductile boundary for shale. The position of this boundary relative to log with no pore pressure is very similar to those of the BRI_3 and BRI_2 logs. This indicates that the UCS curve might be a good estimate of the brittle-ductile boundary in sandstone too. The main trends (position of the high brittleness index section) are the same for the BRI_3, BRI_2 and BRI_1 logs. However, only the rock property-based B_3 logs are significantly different. There is no correlation between the gamma ray-based log and the BRI logs. The acoustic velocity-based log shows a relatively good correlation with trends of the BRI logs; however, not everywhere, for example at about 3440 m. The reason of the similarities is that the UCS log calculation involves the velocity, which is a dominant parameter of the UCS calculation. The gamma ray-based log brittleness index (B_1) has no correlation with lithology. This log provides very different brittleness prediction in comparison with the other logs. It is nearly constant, except two short sections where it has low values.

$$\varphi = \sin^{-1}\frac{V_p - 1000}{V_p + 1000} \qquad \textbf{(Eq. 5-7)}$$

$$\varphi = \tan^{-1}\left(\frac{(GR - GR_{sand})\cdot\mu_{shale} - (GR_{shale} - GR)\cdot\mu_{shale}}{GR_{shale} - GR_{sand}}\right) \qquad \textbf{(Eq. 5-8)}$$

The brittleness index equation contains two independent variables: the UCS and maximum principle effective stress. The stress varies relatively slowly with depth, while UCS can change very fast, e.g. at the layer boundary or because of local change in rock properties. However, the logs in Figure 5-13 cover only an about 50 long vertical section where the stress condition is nearly constant. Therefore, the effect of the variation of the depth and stress on the different type of brittleness indices cannot be seen in Figure 5-13. To demonstrate this, brittleness index logs were calculated based with the same brittleness indices used above in Figure 5-13 for nine rock models based on three different UCS (20, 80 and 150 MPa) and three different internal friction angles (30˚, 40˚ and 50˚) (Figure 5-14). Since the B_3 index, which is calculated by gamma ray, does not involve the stress, it is constant in the entire section. B_3 index calculated from compressional wave velocity has an inverse relation with increasing stress, which was also concluded by Holt et al. (2015). As

BRI_3, BRI_2 and BRI_1 involve the stress, they are able to indicate the variation of the brittleness with depth. All of these curves have a decreasing trend with depth; however, the characteristics of these are different. The BRI_2 curves have a significant break where the minimum effective principal stress is zero, i.e. where the two functions of BRI_2 change. The BRI_1 function has a similar decreasing trend to the BRI_3 curve; however, the BRI_2 index is independent of the variation of the internal friction angle or cohesion. The BRI_3 function, considering the parameters of the linear failure criteria and the stress conditions, is able to provide more detailed brittleness estimation.

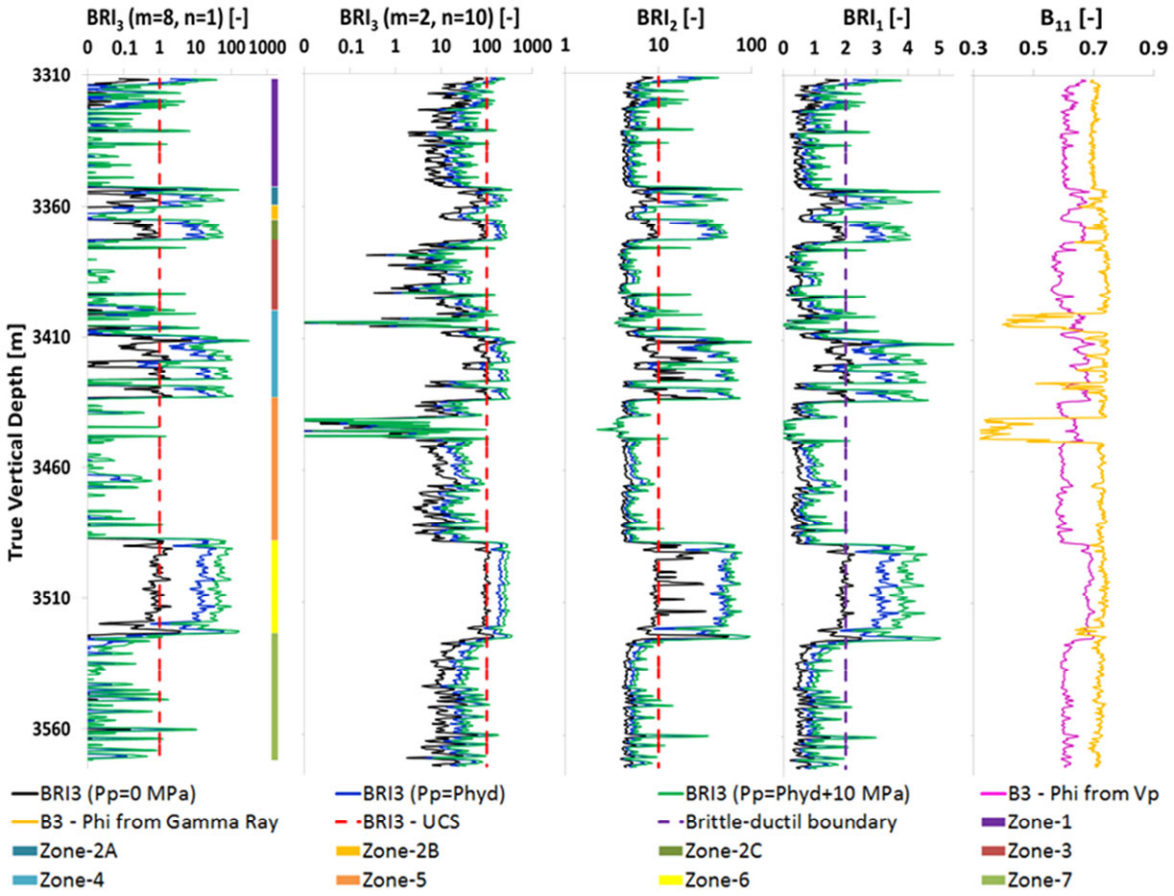

Figure 5-13 – Brittleness index logs for Rotliegend section in well P2-SE: BRI_3 (m=1 and n=8; m=10 and n=2), BRI_2, BRI_1, B_3 with zero, hydrostatic (Phyd) and hydrostatic + 10 MPa pore pressures (Phyd + 10 MPa). Internal friction angle (Phi) for B_3 logs were calculated Gamma Ray and acoustic velocity based empirical equations. The dashed red line indicates the BRI_3 for zero minimum principal effective stresses condition (UCS).

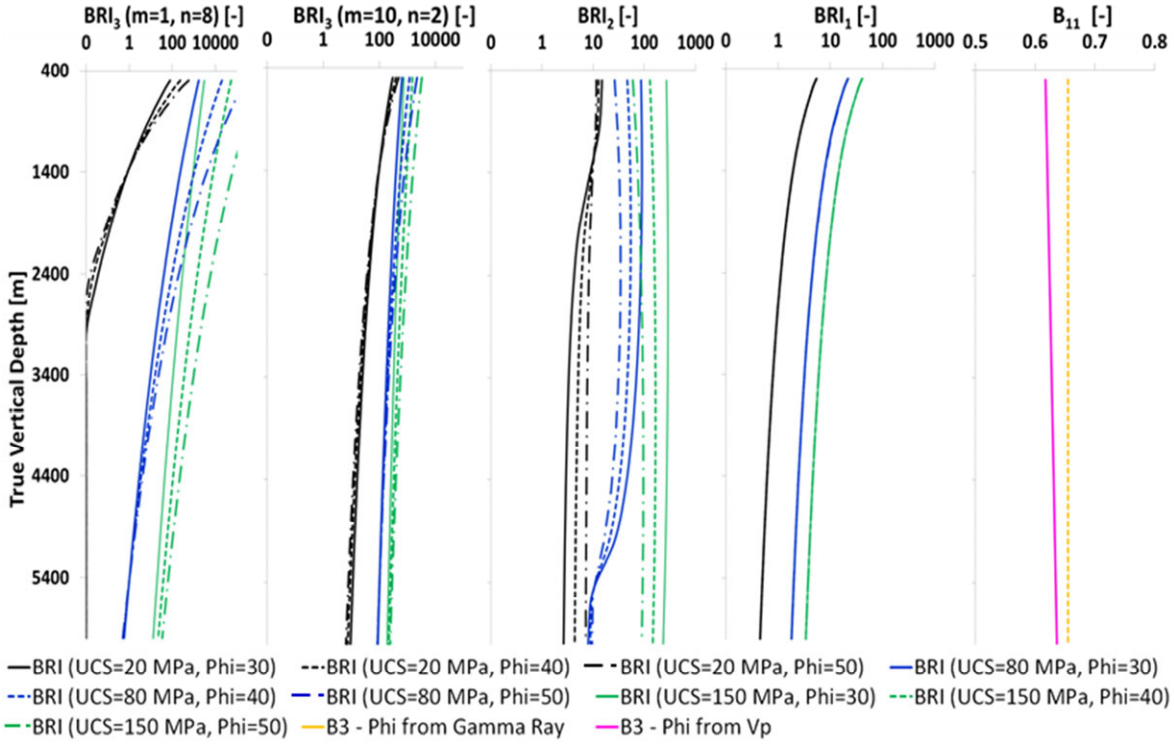

Figure 5-14 – Brittleness index log (BRI3, BRI2, BRI1 and gamma ray (GR) and compressional wave velocity based (Vp) B1) plots of a for nine rock models (UCS: 20, 80 and 150 MPa; and internal friction angle (Phi): 30˚, 40˚ and 50˚) with hydrostatic pore pressure.

Figure 5-15 shows the results of the triaxial measurement series of Kármán (1910) on sandstone. Brittleness indices were calculated for test results of Kármán applying the newly-developed brittleness index equation (BRI_3). In Figure 5-15/A, the stress and strain curve I, measured without confining pressure, shows brittle failure. Curve II and curve III (where the applied confining pressures were 28 MPa and 56 MPa , respectively) show that the rock fails in a transitional way between brittle and ductile failure mode. The test samples (curve IV. and curve V.) failed in a ductile way applying 157 MPa and 250.8 MPa confining pressure, respectively. Based on these results, the lower bound of the brittle-ductile transitional zone is between curve I and curve II, while the upper bound is between curve III and curve IV. Figure 5-15/B shows that the failure envelope has a parabola-like shape, which is common for sandstone. However, the curve is nearly linear below about 100 MPa normal stress. The linear approximation of the failure envelope is a commonly used simplification. Therefore, there is a difference between BRI values calculated with the linear failure envelope and calculated with the measured data (parabola-like failure envelope). Based on the results of test I, II and III, the cohesion (13 MPa) and the internal friction angle (42°) of this sandstone were calculated using linear failure criteria. Applying these rock properties, the minimum effective principal stresses were calculated and the BRI_3 curve (Figure 5 17) was calculated with two parameter sets. One is m=1.8, n=8, as introduced in the previous chapter. The other parameter set is m=10, n=4, which is able to separate the brittleness values in the transitional zone having elongated curvature in the lower effective stress section. BRI_3 values

were calculated for Kármán's test samples based on their measured strength as well as the applied confining pressures.

The difference between the two brittleness indices - the one calculated using the measured data and the one calculated based on the linear failure criteria - is not significant with respect to the interpretation of the brittleness index (Figure 5-16). The absolute difference is high in the brittle zone because the BRI curve is nearly parallel to the BRI axes; however, the relative difference is low. If the parameters are m=1.8, n=8, the relative difference increases with minimum effective stress out of the brittle section; however, the absolute difference is negligible. If the parameters are m=10, n=4, the relative difference is smaller; the absolute difference decreases too, but not as significantly as with the other settings. Nevertheless, the deviation of the brittleness index applying a linear approximation is not significant in comparison with the parabola envelope. The brittleness index using parameters m=1.8, n=8, the brittle zone can be distinguished by high brittleness index values, while the other parameter set m=10, n=4 also allows to distinguish the brittle-ductile transitional zone by very low values in the ductile zone.

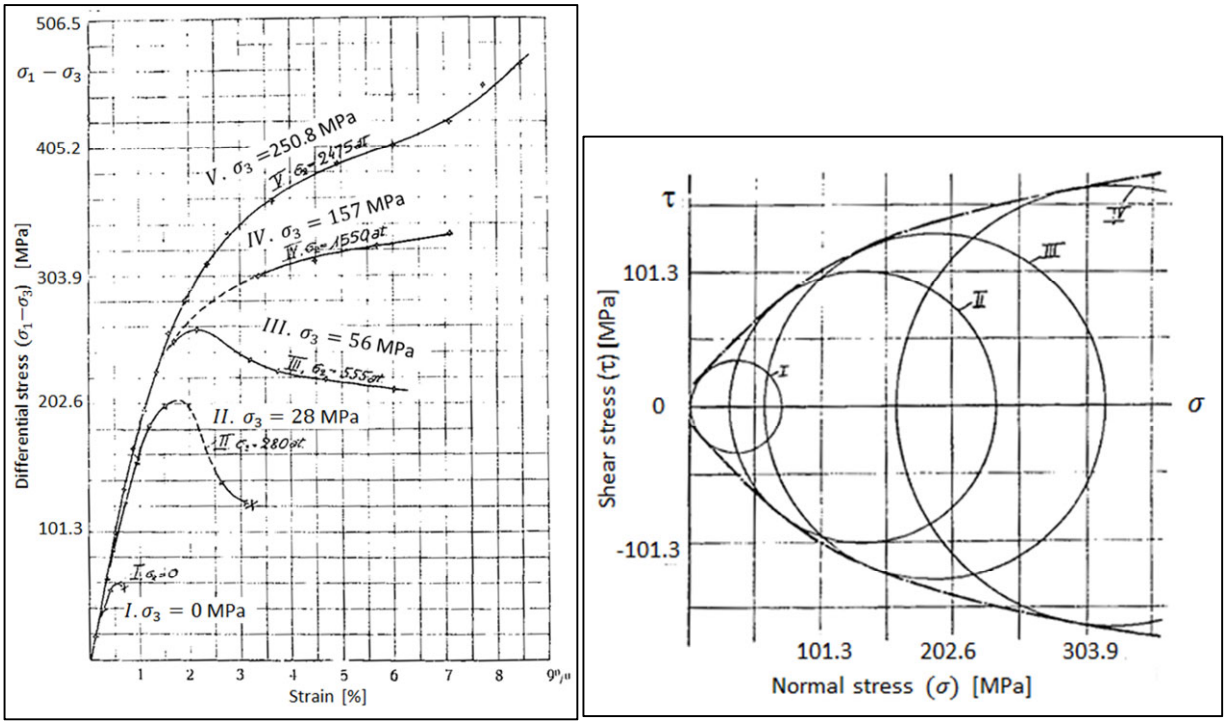

Figure 5-15 –Stress and strain diagrams (on the left) and Mohr diagram (with an assumed failure envelope) of (on the right) the triaxial test results of Kármán (1910) for sandstone (modified after Karman 1910).

Table 5-3 – Results of Kármán's triaxial test series for sandstone and their BRI_3 values calculated based on measured σ_3 and calculated σ_3 using linear failure criterion.

Results of triaxial tests of Kármán (1910) and calculated BRI3											
σ1 measured	σ3 measured	σ3 calculated based on linear failure envelope	Δ σ3	BRI3 based on measured σ3 (m=1.8; n=8)	BRI3 based on calculated σ3 (m=1.8; n=8)	Δ BRI3 (m=1.8; n=8)		BRI3 based on measured data (m=10; n=4)	BRI3 based on calculated σ3 (m=10; n=4)	Δ BRI3 (m=10; n=4)	
60	0.0	-0.6	0.6	160.5	148.8	11.75	7.90%	12069.6	11619.6	450	3.9%
232	28.0	33.5	-5.5	0.009	0.011	-2.2E-03	-19.71%	90.3	100.8	-10.5	-10.4%
313	55.5	49.6	5.9	0.001	1.16E-03	2.3E-04	19.95%	35.6	32.5	3.1	9.5%
485	155.0	83.7	71.3	1.32E-04	4.01E-05	9.2E-05	228.45%	10.9	6.0	4.9	81%
647.5	248.0	115.9	132.1	2.85E-05	4.23E-06	2.4E-05	574.91%	5.1	2.0	3.1	160%

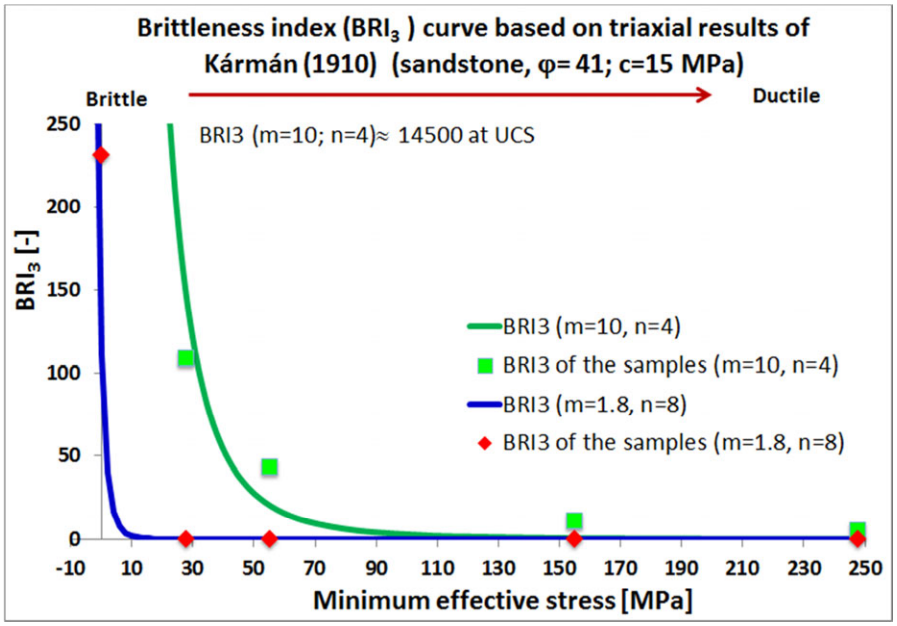

Figure 5-16 – BRI_3 curve of Kármán's studied sandstone together with the actually measured results.

Jizba (1991) measured triaxial tests in several sandstone samples with different clay content. These results showed that the linear failure envelope fit better with increasing clay content. Brittleness indices (BRI_3) were calculated for each sample of three triaxial test series. Brittleness indices were calculated based on the measured strength and confining pressure data. In addition, BRI_3 curves were calculated based on the estimated linear failure envelope derived from the Mohr circles of the triaxial tests (Figure 5-17 and Table 5-4). Because the failure envelope of the higher clay content samples is nearly linear, the difference is smaller between the brittleness indices based on the liner failure envelope and those that were calculated based on the measured data (Figure 5-17/A lower clay content; C and E higher clay content).

These triaxial test results, measured by Jizba (1991), show that the samples failed in a brittle way by applying no confining pressure and also with 15 MPa confining pressure. The failure of the samples under 50 MPa confining pressure seems to be in the brittle-ductile transition, which might be close to the boundary of the brittle stress range. The samples failed in a brittle-ductile transitional way under 100 MPa confining pressure. For these sandstones, the brittleness index equation with the parameters m=8 and n=1.8 provides high values only in cases of unconfined case. However, the brittleness index equation with the parameters m=4 and n=10 is able to provide larger separation between the brittle and less brittle failures. The zone of the ductile failure is not covered by the triaxial test series. Based on the BRI_3 curves the ductile zone starts above about 120 MPa confining pressure in the case of sample 9975 and 6853. In the case of sample 8675, the ductile zone starts above about 140 MPa confining pressure. The ductile zone of sample 8675, having lower UCS, starts at higher confining than those of the other two samples, because the internal friction angle of sample 8675 is lower. In comparison with the results of Kármán (1911) where the sandstone had a relatively low 28 MPa UCS, the boundary of the ductile zone is between 56 MPa and 157 MPa, based on the reported results, and 110 MPa is estimated by the BRI_3 function. The UCS of the measured samples of Jizba (1991) was higher; however, the estimated boundary of the ductile zone by the BRI_3 function is nearly the same. To set the parameters for the BRI_3 equation that provides good estimation in the entire range of the brittle-ductile transition zone, it is necessary to measure more tests with gradual steps to reach the ductile failure of the sample.

Table 5-4 – Brittleness indices (BRI3) of each sample based on the measured strength and confining pressure data and based on the estimated linear failure derived from the Mohr circles of the triaxial results.

Brittleness index - BRI_3 calculated data based on triaxial test results of Jizba (1991)										
Sample ID	Internal friction angle [deg]	Cohesion [MPa]	UCS calculated [MPa]	σ1 measured [MPa]	σ3 measured [MPa]	BRI3 based on measured σ3 (m=1.8; n=8)	BRI3 based on measured σ3 (m=10; n=4)	σ3 calculated [MPa]	BRI3 based on calculated σ3 (m=1.8; n=8)	BRI3 based on measured σ3 (m=10; n=4)
9975	52.6	30	177	177	0	112	10059.6	0.0	111	10053
				375	15	0.38	587.8	22.7	0.5	641
				700	50	0.003	55.3	59.9	0.0	59
				940	100	0.0004	19.8	87.4	0.0	19
6853	40	35	150	149	0	117	10303	-0.2	115	10236
				195	15	26	4837	9.8	20	4313
				360	50	0.3	550	45.6	0.3	520
				550	100	0.02	124	87.0	0.0	110
8675	34	21	79	78	0	122	10518	-0.3	118	10368
				155	15	1.1	1013	21	2	1225
				273	50	0.03	157	55	0.0	172
				405	100	0.002	45	92	0.0	41

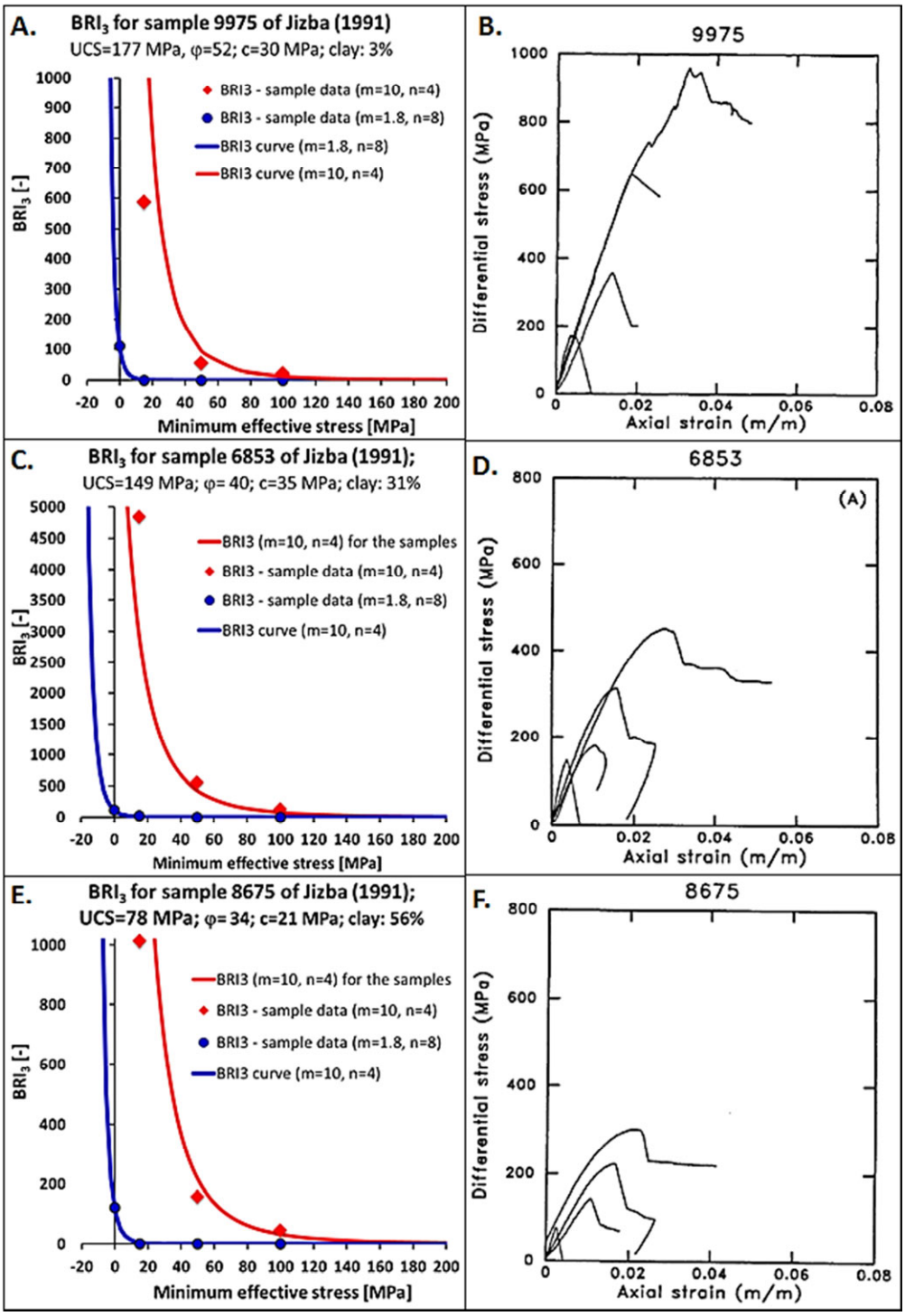

Figure 5-17 – BRI_3 curves of four sandstone samples of Jizba (1991) based the estimated linear failure envelope and BRI3 values based on the measured UCS, minimum and maximum stresses calculated with the with two parameter settings (m=1.8, n=8 and m=10, n=4).

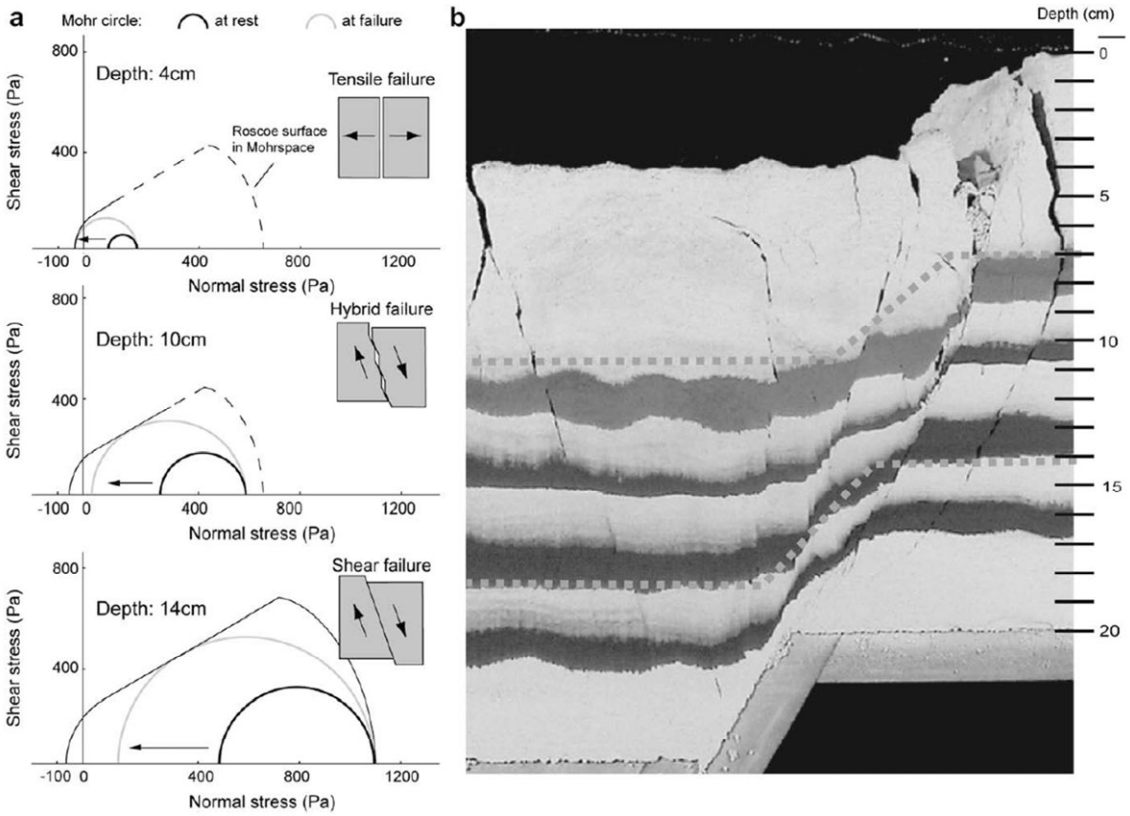

Figure 5-18 – Cross-section photo and Mohr diagrams of analogue normal fault model of van Gent (2010). The three Mohr diagrams indicate the difference in the mechanical properties of a fault with depth.

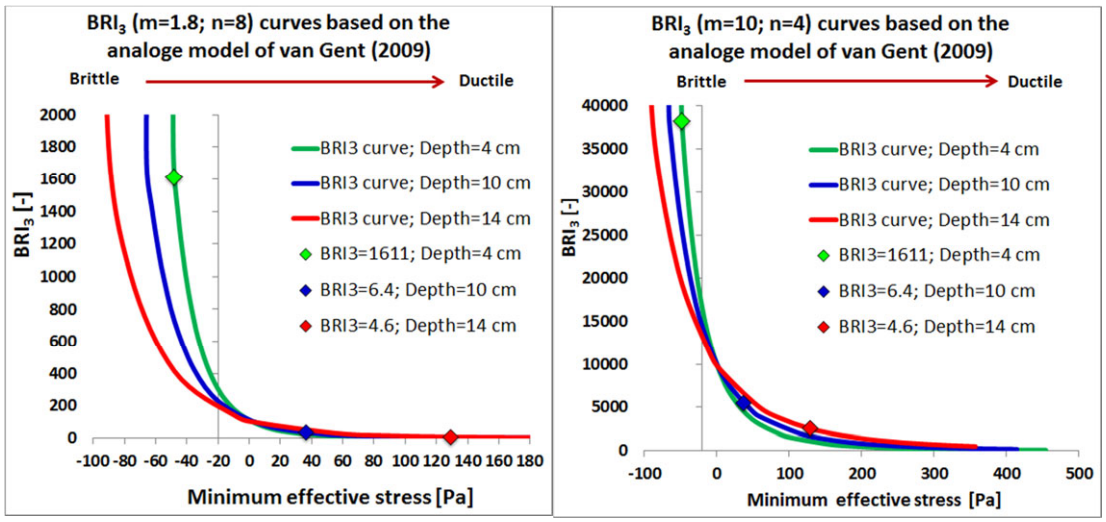

Figure 5-19 - BRI_3 curves based on analogue normal fault model of van Gent (2009) with two parameter settings (m=1.8, n=8 and m=10, n=4).

Table 5-5 – Brittleness indices - BRI3 calculated based on results of analogue model of van Gent (2009) and relevant parameters of the model.

Depth	Internal friction angle [deg]	Cohesion [Pa]	UCS [Pa]	σ1 [Pa]	σ3 [Pa]	BRI3 based on measured σ3 (m=1.8; n=8)	BRI3 based on measured σ3 (m=10; n=4)
4 cm	30	97.3	337.0	193.0	-48.0	1611	38234
10 cm	30	131.9	457.0	567.0	36.7	33.5	5514
14 cm	30	181.6	629.0	1016.0	129.0	7.0	2529

Van Gent (2010) performed an analogue experiment to model the mechanical properties of a normal fault along its vertical cross-section (Figure 5-18). The mechanical properties of this analogue model were designed to analyse the fault in carbonate rocks. Nevertheless, the elementary mechanical behaviour of carbonate rocks and the sandstones are similar, as shown by the results of triaxial investigation on sandstone and marble samples. The results of the van Gent (2009) model demonstrate that failure mode varies vertically a long a normal fault. In the shallow section, no or negative horizontal stress (confining pressure) resulted in tensile fractures. In the middle section, hybrid failure occurred under moderate horizontal stress. Whereas in the lower section, shear failure characterised the fault zone controlled by elevated horizontal stress where only a few dilatant fractures could be observed. Brittleness indices (BRI_3) were calculated for three stress conditions presented by van Gent (2010) applying the previously used two parameter sets (m=1.8, n=8 and m=10, n=4). The calculated BRI_3 values and the model data of the three cases are listed in Table 5-5 and plotted in Figure 5-19, showing the BRI_3 values for the three analysed depths and the BRI_3 curves. The model at the depth of 4 cm failed definitely in a brittle way. The BRI_3 values for this case were very high relative to the deeper cases with both parameter sets. At the depth of 10 cm, the failure mode still seems to be brittle, but it might be in the brittle-ductile transitional zone. At the depth of 14 cm, the failure mode is more plastic, presenting very few open fractures. The deformation in this section of the model is, between the brittle and ductile, probably close to the boundary of the ductile zone. The difference is between the magnitude of the BRI_3 values with parameters m=10, n=4 in two less brittle cases (depth= 10 cm and depth=14 cm). However, the characteristics of the BRI_3 function and the values, relative to each other with parameters m=1.8, n=8 in the less brittle zone (depth=10 cm and depth=14 cm), are fit better to the behaviour of the analogue model. The BRI_3 value for the deepest case (depth=14) is relatively low (seven), which indicates well numerically that the model is rather ductile. BRI_3 value drops below one at about maximum principle stress of 1400 Pa and about minimum principle stress of 257 Pa. Beyond this stress condition, the material will fail clearly in a brittle way. Based on the analogue model, the result of the BRI_3 equation with parameters m=1.8, n=8 seems to provide a good approximation. However, to validate the brittle-ductile boundary of this approximation more analysis or triaxial test series are required with higher confining pressure.

5.5 Conclusion

The newly-developed brittleness index equation (BRI_3), which is based on the idea of Hoogerduijn-Strating and Urai (2003), takes into account the unconfined compressive strength of the rocks and also the stress condition at failure. Predicting the UCS, the maximum and the minimum stresses and the pore pressure (for example, based on wireline log data) in a subsurface rock, the brittleness of the rock can be predicted. Knowing the brittleness of a rock, the tendency to form open fractures can be predictable, which is an important factor to estimate the fluid migration potential in reservoirs.

The new BRI equation without parameters ("m" and "n") works basically in the same way as the brittleness index equation of Hoogerduijn-Strating and Urai (BRI_2). They are both hyperbolic functions. The BRI_2 equation has a fixed value (BRI_2= 10) if the minimum effective stress is zero (UCS). The BRI_3 is equal to 1 under unconfined same stress condition; however, the characteristic of the function can be varied to allow setting the brittle-ductile transition for a particular case. The parameters "m" and "n" allow modifying the BRI curve according to the failure characteristics of the given rock. With the parameters of the newly proposed brittleness index equation, the brittle and ductile zones can be better separated numerically, which can improve the interpretation of the BRI logs. However, these parameters are required to be set carefully, considering the entire range of the UCS of the studied formation, since the brittle-ductile transition zone depends on the strength of the rock.

Applying the newly proposed equation, the brittleness index logs were calculated for the Rotliegend and the Lower German Triassic Sandstones in four wells in the North Sea. These logs allow classifying the sections of these sandstones by their brittleness. Four members of the Rotliegend sandstone in well P2-SE2, at a depth of around 3500-3650 m TVDSS, were found to be relatively brittle, even without any pore pressure. In contrast, other formations are ductile even in the case when pore pressure was over hydrostatic. In well L6-8, the Rotliegend Lower Slochteren sandstone was found ductile at a depth of around 4480 m TVDSS; even with over-hydrostatic pore pressure it is around the brittle-ductile transition limit. However, the Rotliegend Lower Slochteren sandstone seemed to be more brittle in well K18-8 than in well L6-8. The Upper Slochteren sandstone in well K18-8 and P6-9 seemed to be brittle. The Lower German Triassic sandstones were found to be brittle in general. The deeper section (depth > 4100 m TVDSS) of the Lower Buntsandstein strata was found very brittle, even without pore pressure in well L6-8, while the Volpriehausen sandstone was found to be very ductile, even applying over-hydrostatic pore pressure in shallower depth of this well. In the Upper Slochteren in well K18-8, Slochteren in well P6-9 and the Lower Buntsandstein in well L6-8, in both brittle and less brittle sections were distinguished by the brittleness index logs.

By applying the calculated BRI_3 logs to characterise the brittle and less brittle-ductile formations, intervals of North Sea sandstones were identified and provided good examples for the application of the BRI concept. Considering the analogue field experiences, Klondike Bluffs faults and fractures can be analogues for the high BRI sections of the North Sea sandstones, where we can expect brittle deformation and open fractures. Whereas, in the

sections with low brittleness index, more similar to Courthouse Junction faults, we can expect ductile deformation and baffle compaction fractures.

In order to be able to set the parameters of the proposed brittleness index equation more properly, it is necessary to know the stress condition of the brittle-ductile transition for the studied rock. Since, there is not an available adequate method to estimate the brittle-ductile transition, future work should aim to measure triaxial test series on different sandstones with small confining pressure steps in order to define the brittle-ductile transition zone of sandstones. This analysis also should involve rock physical, mineralogical and microstructure analysis of the studied rock to better understand the relationship between the rock properties and their brittle behaviour.

6 References

Adams, F. D. [1912] An experimental contribution to the question of the depth of the zone of flow in the earth's crust. The Journal of Geology 20(2), 97-118.

Agosta, F. and Aydin, A. [2006] Architecture and deformation mechanism of a basin-bounding normal fault in mesozoic platform carbonates, central italy. Journal of Structural Geology 28(8), 1445-1467.

Aguilera, R. [2002] Incorporating capillary pressure, pore throat aperture radii, height above free-water table, and winland r35 values on pickett plots. AAPG Bulletin 86(4), 605-624.

Ajdukiewicz, J. M. and Lander, R. H. [2010] Sandstone reservoir quality prediction: The state of the art. AAPG Bulletin 94(8), 1083-1091.

Allen, M. P. [1997] Understanding regression analysis. Springer Science & Business Media.

Altindag, R. [2002] The evaluation of rock brittleness concept on rotary blast hole drills. Journal of the South African Institute of Mining and Metallurgy 102(1), 61-66.

Anders, M. H. and Wiltschko, D. V. [1994] Microfracturing, paleostress and the growth of faults. Journal of Structural Geology 16(6), 795-815.

Anderson, E. M. [1905] The dynamics of faulting. Transactions of the Edinburgh Geological Society 8(3), 387-402.

Anderson, E. M. [1942] The dynamics of faulting and dyke formation with applications to britain. Oliver and Boyd, Edinburgh.

Andreev, G. E. [1995] Brittle failure of rock materials: Test results and constitutive models. Taylor & Francis Group.

Antonellini, M. and Aydin, A. [1994] Effect of faulting on fluid flow in porous sandstones; petrophysical properties. AAPG Bulletin 78(3), 355-377.

Antonellini, M. and Aydin, A. [1995] Effect of faulting on fluid flow in porous sandstones; geometry and spatial distribution. AAPG Bulletin 79(5), 642-671.

Antonellini, M., Aydin, A. and Orr, L. [1999] Outcrop-aided characterization of a faulted hydrocarbon reservoir: Arroyo grande oil field, california, USA. GEOPHYSICAL MONOGRAPH-AMERICAN GEOPHYSICAL UNION 113, 7-26.

Antonellini, M. A., Aydin, A. and Pollard, D. D. [1994] Microstructure of deformation bands in porous sandstones at arches national park, utah. Journal of Structural Geology 16(7), 941-959.

Asszonyi, C. and Richter, R. [1974] Bevezetés a kőzetmechanika reológiai elméletébe. Nehézipari Minisztérium Továbbképző Központja.

Asszonyi, C. and Richter, R. [1979] The continuum theory of rock mechanics. Trans Tech Publications, [Clausthal, Ger.].

ASTM-D7012. [2010] Astm d7012 - 10 standard test method for compressive strength and elastic moduli of intact rock core specimens under varying states of stress and temperatures. ASTM International.

Aydin, A. [1978] Small faults formed as deformation bands in sandstone. Pure and Applied Geophysics 116(4), 913-930.

Aydin, A. [2000] Fractures, faults, and hydrocarbon entrapment, migration and flow. Marine and Petroleum Geology 17(7), 797-814.

Aydin, A. and Johnson, A. M. [1978] Development of faults as zones of deformation bands and as slip surfaces in sandstone Pure and Applied Geophysics 116(4-5), 931-942.

Aydin, A. and Johnson, A. M. [1983] Analysis of faulting in porous sandstones. Journal of Structural Geology 5(1), 19-31.

Baldschuhn, R., Binot, F., Fleig, S. and Kockel, F. [2001] Geotektonischer atlas von nordwest-deutschland und dem deutschen nordsee-sektor. Hannover.

Ballivy, G., Ladanyi, B. and Gill, D. [1976] Effect of water saturation history on the strength of low-porosity rocks. ASTM special technical publication (599), 4-20.

Barefield, E. H. and Shakoor, A. [2006] The effect of degree of saturation on the unconfined compressive strength of selected sandstones.

Baron, L., Loguntsov, B. and Pozin, E. [1962] Determination of the properties of rocks. Gosgortekhizdat, Moscow.

Bell, F. G. and Culshaw, M. G. [1998] Petrographic and engineering properties of sandstones from the sneinton formation, nottinghamshire, england. Quarterly Journal of Engineering Geology and Hydrogeology 31(1), 5-19.

Bense, V. F., Van den Berg, E. H. and Van Balen, R. T. [2003] Deformation mechanisms and hydraulic properties of fault zones in unconsolidated sediments; the roer valley rift system, the netherlands. Hydrogeology Journal 11(3), 319-332.

Berg, R. R. [1975] Capillary pressures in stratigraphic traps. AAPG Bulletin 59(6), 939-956.

Berg, S. S. and Skar, T. [2005] Controls on damage zone asymmetry of a normal fault zone: Outcrop analyses of a segment of the moab fault, se utah. Journal of Structural Geology 27(10), 1803-1822.

Bernabe, Y. and Brace, W. F. [1990] Deformation and fracture of berea sandstone. The brittle-ductile transition in rocks, 91-101. American Geophysical Union.

Björck, A. [1996] Numerical methods for least squares problems. Siam.

Blenkinsop, T. G. [2008] Relationships between faults, extension fractures and veins, and stress. Journal of Structural Geology 30(5), 622-632.

Blindheim, O. and Bruland, A. [1998] Boreability testing norwegian tbm tunnelling 30 years of experience with tbms in norwegian tunnelling. Norwegian Soil and Rock Engineering Association 11, 29-34.

Borsaru, M., Rojc, A. and Stehle, R. [2001] The application of the pgnaa technique to in-situ analysis of coal. Exploration and Mining Report C 848.

Brace, W., Paulding, B. and Scholz, C. [1966] Dilatancy in the fracture of crystalline rocks. Journal of Geophysical Research 71(16), 3939-3953.

Brace, W. F. and Riley, D. K. [1972] Static uniaxial deformation of 15 rocks to 30 kb. International Journal of Rock Mechanics and Mining Sciences & Geomechanics Abstracts 9(2), 271-288.

Bradford, I., Fuller, J., Thompson, P. and Walsgrove, T. [1998] Benefits of assessing the solids production risk in a north sea reservoir using elastoplastic modelling. SPE/ISRM Rock Mechanics in Petroleum Engineering.

Broch, E. [1974] The influence of water on some rock properties. ISRM Congress.

Brogi, A. [2008] Fault zone architecture and permeability features in siliceous sedimentary rocks: Insights from the rapolano geothermal area (northern apennines, italy). Journal of Structural Geology 30(2), 237-256.

Brogi, A. [2011] Variation in fracture patterns in damage zones related to strike-slip faults interfering with pre-existing fractures in sandstone (calcione area, southern tuscany, italy). Journal of Structural Geology 33(4), 644-661.

Bruhn, R. L., Parry, W. T., Yonkee, W. A. and Thompson, T. [1994] Fracturing and hydrothermal alteration in normal fault zones. Pure and Applied Geophysics 142(3-4), 609-644.

Bryant, S., King, P. and Mellor, D. [1993] Network model evaluation of permeability and spatial correlation in a real random sphere packing. Transport in Porous Media 11(1), 53-70.

Byrne, P. M., Salgado, F. M. and Howie, J. A. [1990] Relationship between the unload shear modulus from pressuremeter tests and the maximum shear modulus for sand. Thomas Telford Services Ltd, London.

Caine, J. S., Evans, J. P. and Forster, C. B. [1996] Geology 24(11), 1025-1028.

Carmichael, R. S. [1982] Crc handbook of physical properties of rocks. CRC Press. Inc.

Cashman, S. and Cashman, K. [2000] Cataclasis and deformation-band formation in unconsolidated marine terrace sand, humboldt county, california. Geology 28(2), 111-114.

Chan, M. A., Parry, W. T. and Bowman, J. R. [2000] Diagenetic hematite and manganese oxides and fault-related fluid flow in jurassic sandstones, southeastern utah. Aapg Bulletin-American Association of Petroleum Geologists 84(9), 1281-1310.

Chang, C., Zoback, M. D. and Khaksar, A. [2006] Empirical relations between rock strength and physical properties in sedimentary rocks. Journal of Petroleum Science and Engineering 51(3), 223-237.

Cheng, C. H. and Johnston, D. H. [1981] Dynamic and static moduli. Geophysical Research Letters 8(1), 39-42.

Chester, F., Chester, J., Kirschner, D., Schulz, S. and Evans, J. [2004] Structure of large-displacement, strike-slip fault zones in the brittle continental crust. Rheology and Deformation in the Lithosphere at Continental Margins 1, 223-260.

Chester, F. M. and Chester, J. S. [1998] Ultracataclasite structure and friction processes of the punchbowl fault, san andreas system, california. Tectonophysics 295(1–2), 199-221.

Chester, F. M. E., J P; Biegel, R L J. [1993] Internal structure and weakening mechanisms of the san andreas fault International Journal of Rock Mechanics and Mining Sciences & Geomechanics Abstracts 30(5), 270.

Clarke, B. G. [1994] Pressuremeters in geotechnical design. Taylor & Francis.

Coates, D. and Parsons, R. [1966] Experimental criteria for classification of rock substances. International Journal of Rock Mechanics and Mining Sciences & Geomechanics Abstracts, 181-189.

Colback, P. and Wiid, B. [1900] The influence of moisture content on the compressive strength of rocks. Geophysics.

Collins, P. [2002] Geomechanics and wellbore stability design of an offshore horizontal well, north sea. SPE International Thermal Operations and Heavy Oil Symposium and International Horizontal Well Technology Conference.

Constantinides, G. N. and Payatakes, A. C. [1989] A three dimensional network model for consolidated porous media. Basic studies. Chemical Engineering Communications 81(1), 55-81.

Copur, H., Bilgin, N., Tuncdemir, H. and Balci, C. [2003] A set of indices based on indentation tests for assessment of rock cutting performance and rock properties. JOURNAL-SOUTH AFRICAN INSTITUTE OF MINING AND METALLURGY 103(9), 589-599.

Coskun, S. B. and Wardlaw, N. C. [1993] Estimation of permeability from image analysis of reservoir sandstones. Journal of Petroleum Science and Engineering 10(1), 1-16.

Cramer, B., Andruleit, H., Rempel, H., Babies, H., Schlömer, S., Schmidt, S., Schwarz-Schampera, U., Ochmann, N., MEßNER, J. and Rehder, S. [2009] Energierohstoffe 2009: Reserven, ressourcen, verfügbarkeit. Erdöl, Erdgas, Kohle, Kernbrennstoffe, Geothermische Energie. Bundesanstalt für Geowissenschaften und Rohstoffe (BGR), Hannover, 2009. www. bgr. bund. de.

Cruikshank, K. M. and Aydin, A. [1994] Role of fracture localization in arch formation, arches-national-park, utah. Geological Society of America Bulletin 106(7), 879-891.

Cruikshank, K. M. and Aydin, A. [1995] Unweaving the joints in entrada sandstone, arches national park,next term utah, u.S.A. Journal of Structural Geology 17(3), 409-421.

Cruikshank, K. M., Zhao, G. Z. and Johnson, A. M. [1991] Duplex structures connecting fault segments in entrada sandstone. Journal of Structural Geology 13(10), 1185-1196.

Dathe, A., Eins, S., Niemeyer, J. and Gerold, G. [2001] The surface fractal dimension of the soil–pore interface as measured by image analysis. Geoderma 103(1–2), 203-229.

Davatzes, N. C. and Aydin, A. [2003] Overprinting faulting mechanisms in high porosity sandstones of se utah. Journal of Structural Geology 25(11), 1795-1813.

Davatzes, N. C., Eichhubl, P. and Aydin, A. [2005] Structural evolution of fault zones in sandstone by multiple deformation mechanisms: Moab fault, southeast Utah. Geological Society of America Bulletin 117(1-2), 135-148.

Davis, G. H. [1999] Structural geology of the colorado plateau region of southern utah, with special emphasis on deformation bands. Geological Society of America.

De Jager, J., 2007. Geological Development. In: Wong, Th.E, Batjes, D.A.J. & De Jager, J. (eds): Geology of the Netherlands. Royal Netherlands Academy of Arts and Sciences (Amsterdam): p. 5 -26.

De Paola, N., Collettini, C., Faulkner, D. R. and Trippetta, F. [2008] Fault zone architecture and deformation processes within evaporitic rocks in the upper crust. Tectonics 27(4), TC4017.

Deng, J., Leguizamon, J. and Aguilera, R. [2011] Petrophysics of triple-porosity tight gas reservoirs with a link to gas productivity. SPE Reservoir Evaluation & Engineering 14(5), 566-577.

Desbois, G., Urai, J. and Kukla, P. [2009] Morphology of the pore space in claystones–evidence from bib/fib ion beam sectioning and cryo-sem observations. eEarth Discussions 4(1), 1-19.

Desbois, G., Enzmann, F., Urai, J. L., Baerle, C., Kukla, P. A., & Konstanty, J. [2010]. Imaging pore space in tight gas sandstone reservoir: insights from broad ion beam cross-sectioning. In EPJ Web of conferences (Vol. 6, p. 22022). EDP Sciences.

Doelling, H. H. [1985] Geological map of arches national park and vicinity, gran country, utah. State of Utach Department of Natural Resources Utah Geological and Mineral Survey, Utah.

Doelling, H. H. [2010] Geology of arches national park utah. Geology of utah's parks and monuments, P. B. Anderson, T. C. C. Jr. and D. A. Sprinkel (eds.). Utah Geological Association and Bryce Canyon Natural History Assotiation.

Doelling and Kuehne, 2013 Geologic maps of the Klondike Bluffs, Mollie Hogans, and The Windows Section 7.5' Quadrangles, Grand Count y, Utah, Utah Geological Survey

Downey, M. W. [1984] Evaluating seals for hydrocarbon accumulations. AAPG Bulletin 68(11), 1752-1763.

Draut, A. E. [2005] The geology of central and southeastern utah: Itinerary for a one-day field trip. Penrose Conference Field Trip Guide, 20. Geological Society of America.

Du Bernard, X., Eichhubl, P. and Aydin, A. [2002] Dilation bands: A new form of localized failure in granular media. Geophysical Research Letters 29(24), 2176.

Dullien, F. A. L. and Dhawan, G. K. [1974] Characterization of pore structure by a combination of quantitative photomicrography and mercury porosimetry. Journal of Colloid and Interface Science 47(2), 337-349.

Dunn, D. E., LaFountain, L. J. and Jackson, R. E. [1973] Porosity dependence and mechanism of brittle fracture in sandstones. Journal of Geophysical Research 78(14), 2403-2417.

Dyke, C. G. and Dobereiner, L. [1991] Evaluating the strength and deformability of sandstones. Quarterly Journal of Engineering Geology and Hydrogeology 24(1), 123-134.

Ehrenberg, S. [1993] Preservation of anomalously high porosity in deeply buried sandstones by grain-coating chlorite: Examples from the norwegian continental shelf. AAPG Bulletin 77(7), 1260-1286.

Ehrlich, R., Etris, E. L., Brumfield, D., Yuan, L. and CRABTREE, S. J. [1991] Petrography and reservoir physics iii: Physical models for permeability and formation factor (1). AAPG Bulletin 75(10), 1579-1592.

Eichhubl, P., Davatz, N. C. and Becker, S. P. [2009] Structural and diagenetic control of fluid migration and cementation along the moab fault, utah. AAPG Bulletin 93(5), 653-681.

Ellis, D. V. and Singer, J. M. [2008] Well logging for earth scientists. Springer.

Fahy, M. and Guccione, M. [1979] Estimating strength of sandstone using petrographic thin-section data. Bull Assoc Eng Geol 16(4), 467-485.

Faulkner, D., Mitchell, T., Healy, D. and Heap, M. [2006] Slip on'weak'faults by the rotation of regional stress in the fracture damage zone. Nature 444(7121), 922-925.

Faulkner, D. R., Lewis, A. C. and Rutter, E. H. [2003] On the internal structure and mechanics of large strike-slip fault zones: Field observations of the carboneras fault in southeastern spain. Tectonophysics 367(3–4), 235-251.

Fischer, G. J. and Paterson, M. S. [1989] Dilatancy during rock deformation at high temperatures and pressures. Journal of Geophysical Research: Solid Earth 94(B12), 17607-17617.

Fisher, Q. J. and Knipe, R. J. [2001] The permeability of faults within siliciclastic petroleum reservoirs of the north sea and norwegian continental shelf. Marine and Petroleum Geology 18(10), 1063-1081.

Fjær, E. [1999] Static and dynamic moduli of weak sandstones. stress 100, 80.

Fjær, E. [2009] Static and dynamic moduli of a weak sandstone. Geophysics 74(2), WA103-WA112.

Fjar, E., Holt, R. M., Raaen, A., Risnes, R. and Horsrud, P. [2008] Petroleum related rock mechanics. Elsevier Science.

Fletcher, R. C. and Pollard, D. D. [1981] Anticrack model for pressure solution surfaces. Geology 9(9), 419-424.

Flodin, E., Aydin, A., Durlofsky, L. and Yeten, B. [2001] Representation of fault zone permeability in reservoir flow models. SPE Annual Technical Conference and Exhibition.

Flodin, E. A. [2003] Structural evolution, petrophysics, and large-scale permeability of faults in sandstone, valley of fire, nevada. Stanford University.

Fodor, L. I. [2010] Mesozoic-cenozoic stress fields and fracture systems in the north-east of pannon-basin - methodology and structural analysis (mezozoos-kainozoos feszültségmezõk és törésrendszerek a pannonmedence ény-i részén – módszertan és szerkezeti elemzés). Hungarian Academy of Sciences.

Fossen, H. [2010] Deformation bands formed during soft-sediment deformation: Observations from se utah. Marine and Petroleum Geology 27(1), 215-222.

Fossen, H. [2010] Structural geology. Cambridge University Press.

Fossen, H. and Bale, A. [2007] Deformation bands and their influence on fluid flow. AAPG Bulletin 91(12), 1685-1700.

Fossen, H. and Hesthammer, J. [1997] Geometric analysis and scaling relations of deformation bands in porous sandstone. Journal of Structural Geology 19(12), 1479-1493.

Fossen, H. and Hesthammer, J. [1998] Deformation bands and their significance in porous sandstone reservoirs. First Break (16), 21-25.

Fossen, H. and Hesthammer, J. [2000] Possible absence of small faults in the gullfaks field, northern north sea: Implications for downscaling of faults in some porous sandstones. Journal of Structural Geology 22(7), 851-863.

Fossen, H., Hesthammer, J., Skeie Johansen, T. E. and Sygnabere, T. O. [2003] Structural geology of the huldra field, northern north sea--a major tilted fault block at the eastern edge of the horda platform. Marine and Petroleum Geology 20(10), 1105-1118.

Fossen, H., Schultz, R. A., Shipton, Z. K. and Mair, K. [2007] Deformation bands in sandstone: A review. Journal of the Geological Society 164, 755-769.

Fossen, H., Schultz, R. A. and Torabi, A. [2011] Conditions and implications for compaction band formation in the navajo sandstone, utah. Journal of Structural Geology 33(10), 1477-1490.

Foxford, K.A., Garden, I.R., Guscott, S.C., Burley, S.D., Lewis, J.L.L., Walsh, J.J., Watterson, J., 1996. The field geology of the Moab Fault. In: Huffman, A.C., Lund, W.R.J., Godwin, L.H. (Eds.), Geology and Resources of the Paradox Basin, 25. Utah Geological Association Guidebook, pp. 265–283.

Franks, S. G. and Zwingmann, H. [2010] Origin and timing of late diagenetic illite in the permian–carboniferous unayzah sandstone reservoirs of saudi arabia. AAPG Bulletin 94(8), 1133-1159.

Freyburg, E. [1972] Der untere und mittlere buntsandstein sw-thuringen in seinen gesteinstechnicschen eigenschaften. Ber. Dte. Ges. Geol. Wiss. A; Berlin 176, 911-919.

Garden, I. R., Guscott, S. C., Burley, S. D. and Foxford, K. A. [2001] An exhumed palaeo-hydrocarbon migration fairway in a faulted carrier system, entrada sanstone of se utah, USA Geofluids 1, 19.

Geluk, M. and Röhling, H.-G. [1997] High-resolution sequence stratigraphy of the lower triassic 'buntsandstein'in the netherlands and northwestern germany. Geologie en Mijnbouw 76(3), 227-246.

George, E. [1995] Brittle failure of rock material-test results and constitutive models. AA Balkema/Rotterdam/Brolkfield, 123-128.

Gerling, P., Geluk, M., Kockel, F., Lokhorst, A., Lott, G. and Nicholson, R. [1999] 'nw european gas atlas'–new implications for the carboniferous gas plays in the western part of the southern permian basin. Geological Society, London, Petroleum Geology Conference series, 799-808.

Gibson, R. G. [1998] Physical character and fluid-flow properties of sandstonederived

fault zones. Structural geology in reservoir characterization, M. P. Coward, Johnson, H. & Daltaban, T.S. (ed.), 83–97. The Geological Society, London.

Glennie, K. and Provan, D. [1990] Lower permian rotliegend reservoir of the southern north sea gas province. Geological Society, London, Special Publications 50(1), 399-416.

Göktan, R. M. [1991] Brittleness and micro-scale rock cutting efficiency. Mining Science and Technology 13(3), 237-241.

Gray, D., Anderson, P., Logel, J., Delbecq, F., Schmidt, D. and Schmid, R. [2012] Estimation of stress and geomechanical properties using 3D seismic data. First Break 30(3), 59-68.

Griffith, A. A. [1921] The phenomena of rupture and flow in solids. Philosophical transactions of the royal society of london. Series A, containing papers of a mathematical or physical character 221, 163-198.

Griggs, D. T. and Handin, J. [1960] Observations on fracture and a hypothesis of earthquakes. Rock deformation Geol. Soc Am (79), 347-364.

Gudmundsson, A. [2007] Infrastructure and evolution of ocean-ridge discontinuities in iceland. Journal of Geodynamics 43(1), 6-29.

Gudmundsson, A., Fjeldskaar, I. and Brenner, S. L. [2002] Propagation pathways and fluid transport of hydrofractures in jointed and layered rocks in geothermal fields. Journal of Volcanology and Geothermal Research 116(3), 257-278.

Gudmundsson, A., Simmenes, T. H., Larsen, B. and Philipp, S. L. [2010] Effects of internal structure and local stresses on fracture propagation, deflection, and arrest in fault zones. Journal of Structural Geology 32(11), 1643-1655.

Hale, P. A. and Shakoor, A. [2003] A laboratory investigation of the effects of cyclic heating and cooling, wetting and drying, and freezing and thawing on the compressive strength of selected sandstones. Environmental & Engineering Geoscience 9(2), 117-130.

Handin, J. and Hager Jr, R. V. [1958] Experimental deformation of sedimentary rocks under confining pressure: Tests at high temperature. AAPG Bulletin 42(12), 2892-2934.

Haney, M. and Shakoor, A. [1994] The relationship between tensile and compressive strengths for selected sandstones as influenced by index properties and petrographic characteristics. Proceedings of 7th Int IAEG Congress, Lisbon, Portugal, 493-500.

Hansen, J. and Skjeltorp, A. [1988] Fractal pore space and rock permeability implications. Physical review. B, Condensed matter 38(4), 2635-2638.

Harper, T. and Moftah, I. [1985] Skin effect and completion options in the ras bud ran reservoir. Middle East Oil Technical Conference and Exhibition.

Harper, T. R. and Lundin, E. R. [1997] Fault seal analysis: Reducing our dependence on empiricism. Norwegian petroleum society special publications, P. Møller-Pedersen and A. G. Koestler (eds.), 149-164. Elsevier.

Harris, S., McAllister, E., Knipe, R. and Odling, N. [2003] Predicting the three-dimensional population characteristics of fault zones: A study using stochastic models. Journal of Structural Geology 25(8), 1281-1299.

Hatherly, P., Medhurst, T., Zhou, B. and Guo, H. [2001] Geotechnical evaluation for mining–assessing rock mass conditions using geophysical logging. Final report ACARP Project C8022b.

Hatherly, P., Sliwa, R., Turner, R. and Medhurst, T. [2004] Quantitative geophysical log interpretation for rock mass characterisation. Final report to Australian Coal Association Research Program (ACARP), project C 11037.

Hawkins, A. B. and McConnell, B. J. [1992] Sensitivity of sandstone strength and deformability to changes in moisture-content. Quarterly Journal of Engineering Geology 25(2), 115-130.

Heard, H. C. [1960] Transition from brittle fracture to ductile flow in solenhofen limestone as a function of temperature, confining pressure, and interstitial fluid pressure. Geological Society of America Memoirs 79, 193-226.

Heid, J., McMahon, J., Nielsen, R. and Yuster, S. [1950] Study of the permeability of rocks to homogeneous fluids. Drilling and Production Practice.

Heidari, M., Khanlari, G. R., Torabi-Kaveh, M., Kargarian, S. and Saneie, S. [2013] Effect of porosity on rock brittleness. Rock Mechanics and Rock Engineering, 1-6.

Hesthammer, J. and Fossen, H. [1999] Evolution and geometries of gravitational collapse structures with examples from the statfjord field, northern north sea. Marine and Petroleum Geology 16(3), 259-281.

Hesthammer, J. and Fossen, H. [2001] Structural core analysis from the gullfaks area, northern north sea. Marine and Petroleum Geology 18(3), 411-439.

Hesthammer, J., Johansen, T. E. S. and Watts, L. [2000] Spatial relationships within fault damage zones in sandstone. Marine and Petroleum Geology 17(8), 873-893.

Hetenyi, M. I. [1950] Handbook of experimental stress analysis.

Hilgers, C., Koehn, D., Bons, P. D. and Urai, J. L. [2001] Development of crystal morphology during unitaxial growth in a progressively widening vein: Ii. Numerical simulations of the evolution of antitaxial fibrous veins. Journal of Structural Geology 23(6-7), 873-885.

Hirth, G. and Tullis, J. [1994] The brittle-plastic transition in experimentally deformed quartz aggregates. Journal of Geophysical Research: Solid Earth (1978–2012) 99(B6), 11731-11747.

Holditch, S. [2006] Tight gas sands. Journal of Petroleum Technology 58(6), 86-93.

Holt, R. M. [1994] Effects of coring on petrophysical measurements. 1994 International Symposium of the Society of Core Analysts, Proceedings, 77-86.

Holt, R. M., Brignoli, M. and Kenter, C. J. [2000] Core quality: Quantification of coring-induced rock alteration. International Journal of Rock Mechanics and Mining Sciences 37(6), 889-907.

Holt, R. M., Fjær, E., Stenebråten, J. F. and Nes, O.-M. [2015] Brittleness of shales: Relevance to borehole collapse and hydraulic fracturing. Journal of Petroleum Science and Engineering 131, 200-209.

Holt, R. M. and Kenter, C. J. [1992] Laboratory simulation of core damage induced by stress release. Rock Mechanics : Proceedings of the 33rd U S Symposium, 959-968.

Holt, R. M., Unander, T. E., Kenter, C. J. and Santarelli, F. J. [1993] Unloading effects on mechanical-properties of a very weak artificial sandstone - applications to coring. Geotechnical Engineering of Hard Soils - Soft Rocks, Vol 2, 1609-1614.

Hoogerduijn-Strating, E. and Urai, J. L. [2003] Brittleness index - a tool to quantify the probability of dilatant fracturing in mudrock topseals. Proceedings, EAGE Conference on Fault and Top Seals, ISBN, 2003, 90-73781.

Horsrud, P. [2001] Estimating mechanical properties of shale from empirical correlations. SPE Drilling & Completion 16(2), 68-73.

Hoshino, K. [1974] Effect of porosity on the strength of the clastic sedimentary rocks.

Houben, M. E., Desbois, G. and Urai, J. L. [2013] Pore morphology and distribution in the shaly facies of opalinus clay (mont terri, switzerland): Insights from representative 2d bib–sem investigations on mm to nm scale. Applied Clay Science 71(0), 82-97.

Hsieh, Y.-M., Li, H.-H., Huang, T.-H. and Jeng, F.-S. [2008] Interpretations on how the macroscopic mechanical behavior of sandstone affected by microscopic properties—revealed by bonded-particle model. Engineering Geology 99(1–2), 1-10.

Hubbert, M. K. and Willis, D. G. [1957] Mechanics of hydraulic fracturing.

Hucka, V. and Das, B. [1974] Brittleness determination of rocks by different methods. International Journal of Rock Mechanics and Mining Sciences & Geomechanics Abstracts 11(10), 389-392.

Ingram, G. M. and Urai, J. L. [1999] Top-seal leakage through faults and fractures: The role of mudrock properties. Geological Society, London, Special Publications 158(1), 125-135.

Ingram, G. M., Urai, J. L. and Naylor, M. A. [1997] Sealing processes and top seal assessment Norwegian Petroleum Society Special Publications 7, 165-174.

Ioannidis, M. A. and Chatzis, I. [1993] Network modelling of pore structure and transport properties of porous media. Chemical Engineering Science 48(5), 951-972.

Ioannidis, M. A., Kwiecien, M. J. and Chatzis, I. [1996] Statistical analysis of the porous microstructure as a method for estimating reservoir permeability. Journal of Petroleum Science and Engineering 16(4), 251-261.

Ishii, E., Sanada, H., Funaki, H., Sugita, Y. and Kurikami, H. [2011] The relationships among brittleness, deformation behavior, and transport properties in mudstones: An example from the Horonobe Underground Research Laboratory, Japan. Journal of Geophysical Research: Solid Earth 116(B9)

Jaeger, J. C., Cook, N. G. and Zimmerman, R. [2009] Fundamentals of rock mechanics. Wiley-Blackwell.

Jeng, F. S., Weng, M. C., Lin, M. L. and Huang, T. H. [2004] Influence of petrographic parameters on geotechnical properties of tertiary sandstones from taiwan. Engineering Geology 73(1-2), 71-91.

Jizba, D. and Nur, A. [1990] Static and dynamic moduli of tight gas sandstones and their relation to formation properties. SPWLA 31st Annual Logging Symposium, Paper BB.

Jizba, D. L. [1991] Mechanical and acoustical properties of sandstones and shales. Department of Geophysics, School of Earth Sciences. Stanford University. Dept. of Geophysics.

Johansen, T. E. S. and Fossen, H. [2008] Internal geometry of fault damage zones in interbedded siliciclastic sediments. Geological Society, London, Special Publications 299(1), 35-56.

Johansen, T. E. S., Fossen, H. and Kluge, R. [2005] The impact of syn-faulting porosity reduction on damage zone architecture in porous sandstone: An outcrop example from the moab fault, utah. Journal of Structural Geology 27(8), 1469-1485.

Jones, R. R., Wawrzyniec, T. F., Holliman, N. S., McCaffrey, K. J., Imber, J. and Holdsworth, R. E. [2008] Describing the dimensionality of geospatial data in the earth sciences—Recommendations for nomenclature. Geosphere 4(2), 354-359.

Jones, R. R., McCaffrey, K. J. W., Clegg, P., Wilson, R. W., Holliman, N. S., Holdsworth, R. E., Imber, J. and Waggott, S. [2009] Integration of regional to outcrop digital data: 3D visualisation of multi-scale geological models. Computers & Geosciences 35(1), 4-18.

Jourde, H., Flodin, E. A., Aydin, A., Durlofsky, L. J. and Wen, X. H. [2002] Computing permeability of fault zones in eolian sandstone from outcrop measurements. AAPG Bulletin 86(7), 1187-1200.

Kahraman, S. and Altindag, R. [2004] A brittleness index to estimate fracture toughness. International Journal of Rock Mechanics & Mining Sciences 41(2), 343–348.

Kármán, T. [1911] Festigkeitsversuche unter allseitigem druck. Z. Ver. Dt. Ing 55, 1749-1757.

Kármán, T. [1910] Mitől függ az anyag igénybevétele? (what influences the strength of the material?). Magyar Mérnök és Építészegylet Közlönye 10, 212–226.

Kattenhorn, S. A., Aydin, A. and Pollard, D. D. [2000] Joints at high angles to normal fault strike: An explanation using 3-d numerical models of fault-perturbed stress fields. Journal of Structural Geology 22(1), 1-23.

Katz, A. J. and Thompson, A. H. [1985] Fractal sandstone pores: Implications for conductivity and pore formation. Physical Review Letters 54(12), 1325.

Katz, A. J. and Thompson, A. H. [1986] Quantitative prediction of permeability in porous rock. Physical review. B, Condensed matter 34(11), 8179-8181.

Kenter, C. J., Brignoli, M. and Holt, R. M. [1997] Cms (constant mean stress) vs. Ucs (unconfined strength) tests: A tool to reduce core damage effects. International Journal of Rock Mechanics and Mining Sciences 34(3–4), 129.e1-129.e11.

King, M. [1983] Static and dynamic elastic properties of rocks from the canadian shield. Int. J. Rock Mech. Min. Sci. Geomech. Abstr.;(United States) 20(5).

Klaver, J., Desbois, G., Urai, J. L. and Littke, R. [2012] Bib-sem study of the pore space morphology in early mature posidonia shale from the hils area, germany. International Journal of Coal Geology 103(0), 12-25.

Knipe, R. J. [1992] Faulting processes and fault seal. Structural and tectonic modelling and its application to petroleum geology, R. M. Larsen, H. Brekke, B. T. Larsen and E. Talleraas (eds.), 325-342. Elsevier, Amsterdam.

Knott, S. D., Beach, A., Brockbank, P. J., Lawson Brown, J., McCallum, J. E. and Welbon, A. I. [1996] Spatial and mechanical controls on normal fault populations. Journal of Structural Geology 18(2,Äì3), 359-372.

Koestler, A., Buller, A., Milnes, A. and Olsen, S. [1994] A structural simulation tool for faulted sandstone reservoirs: Exploratory study using field data from utah and gullfaks. North Sea Oil and Gas Reservoirs III. Kluwer, Dordrecht, 157-165.

Kohonen, T. [2001] Self-organizing maps. Springer, New York.

Kokkalas, S., Jones, R., McCaffrey, K. and Clegg, P. [2007] Quantitative fault analysis at Arkitsa, central Greece, using terrestrial laser-scanning ("LIDAR"). Bulletin of the Geological Society of Greece 37, 1-14.

Kolodzie, S. [1980] Analysis of pore throat size and use of the waxman-smits equation to determine ooip in spindle field, colorado. SPE9382.

Kolor. [2012] Autopano giga 2.6.2. Challes-les Eaux, France.

Kolyukhin D., Schueller, S., Espedal, M. S. and Fossen, H. [2009] Deformation band populations in fault damage zone-impact on fluid flow. Computational Geosciences 14(2), 231-248.

Krohn, C. E. and Thompson, A. H. [1986] Fractal sandstone pores: Automated measurements using scanning-electron-microscope images. Physical Review B 33(9), 6366-6374.

Kutner, M. H., Nachtsheim, C. and Neter, J. [2004] Applied linear regression models. McGraw-Hill/Irwin.

Lacazette, A. [2009] Paleostress analysis from image logs using pinnate joints as slip indicators. AAPG Bulletin 93(11), 1489-1501.

Lama, R. and Vutukuri, V. [1978] Handbook on mechanical properties of rocks-testing techniques and results. Volume 2.

Laurich, B., Arndt, M., Virgo, S., Raith, A., Wuestefeld, P., Thronberens, S. and Urai, J. L. [2011] Insights in dynamics of high-pressure cells based on high-resolution outcrop panoramas: A geometry database for calcite vein networks in the Oman Mountains. EGU.

Li, H. and Zhang, J. [2011] Elastic moduli of dry rocks containing spheroidal pores based on differential effective medium theory. Journal of Applied Geophysics 75(4), 671-678.

Li, J. F., Li, L. and Stott, F. H. [2004] Fractal characteristics of apparent pores present on polished cross sections of alumina coatings prepared by laser-assisted flame hybrid spraying. Thin Solid Films 453–454(0), 229-233.

Li, Y. G. and Malin, P. E. [2008] San andreas fault damage at safod viewed with fault-guided waves. Geophysical Research Letters 35(8).

Zhishui, L. and Zandong, S. [2015] New brittleness indexes and their application in shale/clay gas reservoir prediction. Petroleum Exploration and Development 42(1), 129-137.

Lockner, D. A. and Beeler, N. M. [2002] Rock failure and earthquakes. International handbook of earthquake & engineering seismology, W. H. Lee, P. Jennings, C. Kisslinger and H. Kanamori (eds.), 505-537. Academic Press, Amsterdam.

Lockner, D. A., Byerlee, J. D., Kuksenko, V., Ponomarev, A. and Sidorin, A. [1991] Quasi-static fault growth and shear fracture energy in granite. Nature 350(6313), 39-42.

Mair, K., Elphick, S. and Main, I. [2002] Influence of confining pressure on the mechanical and structural evolution of laboratory deformation bands. Geophysical Research Letters 29(10), 49-1-49-4.

Mandelbrot, B. B. [1983] The fractal geometry of nature. Macmillan.

Mandl, G. and Harkness, R. [1987] Hydrocarbon migration by hydraulic fracturing. Geological Society, London, Special Publications 29(1), 39-53.

Manzocchi, T., Heath, A. E., Walsh, J. J. and Childs, C. [2002] The representation of two phase fault-rock properties in flow simulation models. Petroleum Geoscience 8(2), 119-132.

Martin, A. J. J., Solomon, S. T. and Hartmann, D. J. [1997] Characterization of petrophysical flow units in carbonate reservoirs. AAPG Bulletin 81(5), 734-759.

Martín, M. A. and Taguas, F. J. [1998] Fractal modelling, characterization and simulation of particle-size distributions in soil. Proceedings of the Royal Society of London. Series A: Mathematical, Physical and Engineering Sciences 454(1973), 1457-1468.

Matthäi, S. K., Aydin, A., Pollard, D. D. and Roberts, S. G. [1998] Numerical simulation of departures from radial drawdown in a faulted sandstone reservoir with joints and deformation bands. Geological Society, London, Special Publications 147(1), 157-191.

McCaffrey, K., Feely, M., Hennessy, R. and Thompson, J. [2008] Visualization of folding in marble outcrops, Connemara, western Ireland: An application of virtual outcrop technology. Geosphere 4(3), 588-599.

McCreesh, C. A., Ehrlich, R. and Crabtree, S. J. [1991] Petrography and reservoir physics ii: Relating thin section porosity to capillary pressure, the association between pore types and throat size (1). AAPG Bulletin 75(10), 1563-1578.

McNally, G. [1987] Estimation of coal measures rock strength using sonic and neutron logs. Geoexploration 24(4), 381-395.

Menéndez, I., Caniego, J., Gallardo, J. F. and Olechko, K. [2005] Use of fractal scaling to discriminate between and macro- and meso-pore sizes in forest soils. Ecological Modelling 182(3–4), 323-335.

Meng, Z. and Pan, J. [2007] Correlation between petrographic characteristics and failure duration in clastic rocks. Engineering Geology 89(3–4), 258-265.

Michalopoulos, A. [1976] Influence of water on hardness, strength and compressibiity of rock. Association of Engineering Geologists, Bulletin 13(1).

Mises, R. v. [1913] Mechanik der festen körper im plastisch-deformablen zustand. Nachrichten von der Gesellschaft der Wissenschaften zu Göttingen, Mathematisch-Physikalische Klasse 1913, 582-592.

Mitchell, T. M. and Faulkner, D. R. [2009] The nature and origin of off-fault damage surrounding strike-slip fault zones with a wide range of displacements: A field study from the atacama fault system, northern chile. Journal of Structural Geology 31(8), 802-816.

Moos, D., Zoback, M. and Bailey, L. [1999] Feasibility study of the stability of openhole multilaterals, cook inlet, alaska. SPE Mid-Continent Operations Symposium.

Morley, A. [1944] Strengh of materials. Longmans.

Naik, G. [2003] Tight gas reservoirs-an unconventional natural energy source for the future. www. sublette-se. org/files/tight_gas. pdf. Accessado em 1(07), 2008.

NAIP (National Agriculture Imagery Program) [2009] http://gis.utah.gov/; Automated Geographic Reference Center (AGRC)

Nelson, P. H. [2009] Pore-throat sizes in sandstones, tight sandstones, and shales. AAPG Bulletin 93(3), 329-340.

Nollet, S., Urai, J. L., Bons, P. D. and Hilgers, C. [2005] Numerical simulations of polycrystal growth in veins. Journal of Structural Geology 27(2), 217-230.

Nur, A. and Byerlee, J. D. [1971] An exact effective stress law for elastic deformation of rock with fluids. Journal of Geophysical Research 76(26), 6414-6419.

Obert, L. and Duvall, W. I. [1967] Rock mechanics and the design of structures in rock. Wiley.

Odling, N. E., Harris, S. D. and Knipe, R. J. [2004] Permeability scaling properties of fault damage zones in siliclastic rocks. Journal of Structural Geology 26(9), 1727-1747.

Olgaard, D. L., Urai, J., Dell'Angelo, L. N., Nüesch, R. and Ingram, G. [1997] The influence of swelling clays on the deformation of mudrocks. International Journal of Rock Mechanics and Mining Sciences 34(3–4), 235.e1-235.e15.

Palchik, V. [1999] Influence of porosity and elastic modulus on uniaxial compressive strength in soft brittle porous sandstones. Rock Mechanics and Rock Engineering 32(4), 303-309.

Panich, N. and Yong, S. [2005] Improved method to determine the hardness and elastic moduli using nano-indentation. KMITL Science Journal 5(2), 483-492.

Parry, W. T., Chan, M. A. and Beitler, B. [2004] Chemical bleaching indicates episodes of fluid flow in deformation bands in sandstone. AAPG Bulletin 88(2), 175-191.

Paterson, M. S. [1978] Experimental rock deformation - the brittle field. Springer-Verlag, Berlin Heidelberg New York

Paterson, M. S. and Wong, T.-f. [2005] Experimental rock deformation-the brittle field. Springer Verlag.

Peacock, D. C. P. and Sanderson, D. J. [1991] Displacements, segment linkage and relay ramps in normal fault zones. Journal of Structural Geology 13(6), 721-733.

Perez, R. J. and Boles, J. R. [2005] An empirically derived kinetic model for albitization of detrital plagioclase. American Journal of Science 305(4), 312-343.

Pollard, D. D. and Fletcher, R. C. [2005] Fundamentals of structural geology. Cambridge University Press.

Pomonis, P., Rigopoulos, I., Tsikouras, B. and Hatzipanagiotou, K. [2007] Relationships between petrographic and physicomechanical properties of basic igneous rocks from the pindos ophiolitic complex, nw greece. Bulletin of the Geological Society of Greece 37.

Priest, S. and Selvakumar, S. [1982] The failure characteristics of selected british rocks.

Protodyakonov, M. [1962] Mechanical properties and drillability of rocks. Proceedings of the 5th Symposium on rock mechanics, 103-118.

Radlinski, A. P., Ioannidis, M. A., Hinde, A. L., Hainbuchner, M., Baron, M., Rauch, H. and Kline, S. R. [2004] Angstrom-to-millimeter characterization of sedimentary rock microstructure. Journal of Colloid and Interface Science 274(2), 607-612.

Ramsay, J. G. [1967] Folding and fracturing of rocks. 568. McGraw-Hill Book Company, New York San Francisco St.Louis Toronto London Sydney.

Ramsey, J. M. and Chester, F. M. [2004] Hybrid fracture and the transition from extension fracture to shear fracture. Nature 428(6978), 63-66.

Rickman, R., Mullen, M. J., Petre, J. E., Grieser, W. V. and Kundert, D. [2008] A Practical Use of Shale Petrophysics for Stimulation Design Optimization: All Shale Plays Are Not Clones of the Barnett Shale. Society of Petroleum Engineers.

Rider, M. H. [1986] The geological interpretation of well logs.

Riley, P. R., Goodwin, L. B. and Lewis, C. J. [2010] Controls on fault damage zone width, structure, and symmetry in the bandelier tuff, new mexico. Journal of Structural Geology 32(6), 766-780.

Rotevatn, A., Torabi, A., Fossen, H. and Braathen, A. [2008] Slipped deformation bands: A new type of cataclastic deformation bands in western sinai, suez rift, egypt. Journal of Structural Geology 30(11), 1317-1331.

Roznovsky, T. A. and Aydin, A. [2001] Concentration of shearing deformation related to changes in strike of monoclinal fold axes: The waterpocket monocline, utah. Journal of Structural Geology 23(10), 1567-1579.

Rudnicki, J. W. [1980] Fracture mechanics aplied to the earth's crust. Annual Review of Earth and Planetary Sciences 8, 489.

Sági, D. [2013] Characterisation of the 2d and 3d density and connectivity attributes of fracture systems in carbonate reservoir analogues: Implications for fluid flow. Durham University.

Sahoo, A. K., Mukherjee, D., Mukherjee, A. and Srivastava, M. [2013] Reservoir Characterization of Eagle Ford Shale through Lithofacies Analysis for Identification of Sweet Spot and Best Landing Point.

Saillet, E. and Wibberley, C. A. [2013] Permeability and flow impact of faults and deformation bands in high-porosity sand reservoirs: Southeast basin, france, analog. AAPG Bulletin 97(3), 437-464.

Samsuri, A., Sukirman, Y. and Pham Vu, C. [1999] Effects of petrographical rock properties to the strength and behavior of rock.

Sangha, C. and Dhir, R. [1972] Influence of time on the strength, deformation and fracture properties of a lower devonian sandstone. International Journal of Rock Mechanics and Mining Sciences & Geomechanics Abstracts, 343-352.

Santarelli, F. J. and Dusseault, M. B. [1991] Core quality-control in petroleum engineering. Rock Mechanics as a Multidisciplinary Science : Proceedings of the 32nd Us Symposium, 111-120.

Savage, H. M. and Brodsky, E. E. [2011] Collateral damage: Evolution with displacement of fracture distribution and secondary fault strands in fault damage zones. Journal of Geophysical Research: Solid Earth (1978–2012) 116(B3).

Scholz, C. H. [1987] Wear and gouge formation in brittle faulting. Geology 15(6), 493-495.

Scholz, C. H., Dawers, N. H., Yu, J. Z., Anders, M. H. and Cowie, P. A. [1993] Fault growth and fault scaling laws: Preliminary results. J. Geophys. Res. 98(B12), 21951-21961.

Schön, J. H. [1996] Physical properties of rocks: Fundamentals and principles of petrophysics. Oxford, UK: Pergamon.

Schowalter, T. T. [1979] Mechanics of secondary hydrocarbon migration and entrapment. Journal Name: Am. Assoc. Pet. Geol. Bull.; (United States); Journal Volume: 63:5, Medium: X; Size: Pages: 723-760.

Schroeder, L. D., Sjoquist, D. L. and Stephan, P. E. [1986] Understanding regression analysis: An introductory guide. Sage.

Schueller, S., Braathen, A., Fossen, H. and Tveranger, J. [2013] Spatial distribution of deformation bands in damage zones of extensional faults in porous sandstones: Statistical analysis of field data. Journal of Structural Geology 52, 148-162.

Schultz, R. A. and Fossen, H. [2002] Displacement-length scaling in three dimensions: The importance of aspect ratio and application to deformation bands. Journal of Structural Geology 24(9), 1389-1411.

Scott, T. E. J. [1989] The effects of porosity on the mechanics of faulting in sandstones.

Shakoor, A. and Barefield, E. H. [2009] Relationship between unconfined compressive strength and degree of saturation for selected sandstones. Environmental & Engineering Geoscience 15(1), 29-40.

Shakoor, A. and Bonelli, R. [1991] Relationship between petrographic characteristics, engineering index properties and mechanical properties of selected sandstones. Bull Assoc Eng Geol 28(1), 55-71.

Shipton, Z. K. and Cowie, P. A. [2001] Damage zone and slip-surface evolution over μm to km scales in high-porosity navajo sandstone, utah. Journal of Structural Geology 23(12), 1825-1844.

Shipton, Z. K., Evans, J. P., Robeson, K. R., Forster, C. B. and Snelgrove, S. [2002] Structural heterogeneity and permeability in faulted eolian sandstone: Implications for subsurface modeling of faults. AAPG Bulletin 86(5), 863-883.

Sibson, R. H. [1977] Fault rocks and fault mechanisms. Journal of the Geological Society 133(3), 191-213.

Sigda, J. M., Goodwin, L. B., Mozley, P. S. and Wilson, J. L. [1999] Permeability alteration in small-displacement faults in poorly lithified sediments: Rio grande rift, central new mexico. Geophysical Monograph Series 113, 51-68.

Simmons, G. and Brace, W. [1965] Comparison of static and dynamic measurements of compressibility of rocks. Journal of Geophysical Research 70(22), 5649-5656.

Simpson, D. R. and Fergus, J. H. [1968] The effect of water on the compressive strength of diabase. Journal of Geophysical Research 73(20), 6591-6594.

Singh, S. [1988] Relationship among fatigue strength, mean grain size and compressive strength of a rock. Rock Mechanics and Rock Engineering 21(4), 271-276.

Solum, J. G., Brandenburg, J. P., Naruk, S. J., Kostenko, O. V., Wilkins, S. J. and Schultz, R. A. [2010] Characterization of deformation bands associated with normal and reverse stress states in the navajo sandstone, utah. AAPG Bulletin 94(9), 1453-1475.

Soong, T. T. [2004] Fundamentals of probability and statistics for engineers. John Wiley & Sons.

Srawley, J. E. and Brown Jr, W. F. [1965] Fracture toughness testing methods. ASTM STP 381, 133-198.

Storvoll, V., Bjørlykke, K., Karlsen, D. and Saigal, G. [2002] Porosity preservation in reservoir sandstones due to grain-coating illite: A study of the jurassic garn formation from the kristin and lavrans fields, offshore mid-norway. Marine and Petroleum Geology 19(6), 767-781.

Swanson, B. [1981] A simple correlation between permeabilities and mercury capillary pressures. Journal of Petroleum Technology 33(12), 2498-2504.

Swanson, J., Ward, C. R. and Franklin, B. J. [2002] Mineralogy of sydney building sandstones in relation to geotechnical properties 1: Relation of quantitative x-ray diffraction data to other chemical and petrographic indicators. Australian Geomechanics: Journal and News of the Australian Geomechanics Society 37(4), 53.

Swanson, J., Ward, C. R. and Franklin, B. J. [2002] Mineralogy of sydney building sandstones in relation to geotechnical properties 2: Relation of quantitative x-ray diffraction data and cation exchange capacity to geotechnical indicators of rock durability. Australian Geomechanics: Journal and News of the Australian Geomechanics Society 37(5), 97.

Takahashi, M., Mizoguchi, K., Kitamura, K. and Masuda, K. [2007] Effects of clay content on the frictional strength and fluid transport property of faults. Journal of Geophysical Research: Solid Earth 112(B8), B08206.

Tanaka, H., Omura, K., Matsuda, T., Ikeda, R., Kobayashi, K., Murakami, M. and Shimada, K. [2007] Architectural evolution of the nojima fault and identification of the activated slip layer by kobe earthquake. Journal of Geophysical Research: Solid Earth (1978–2012) 112(B7).

Taylor, T. R., Giles, M. R., Hathon, L. A., Diggs, T. N., Braunsdorf, N. R., Birbiglia, G. V., Kittridge, M. G., Macaulay, C. I. and Espejo, I. S. [2010] Sandstone diagenesis and reservoir quality prediction: Models, myths, and reality. AAPG Bulletin 94(8), 1093-1132.

Thompson, A. H. and Raschke, R. A. [1987] Estimation of absolute permeability from capillary pressure measurements. SPE Annual Technical Conference and Exhibition.

Tobin, R. C., McClain, T., Lieber, R. B., Ozkan, A., Banfield, L. A., Marchand, A. M. and McRae, L. E. [2010] Reservoir quality modeling of tight-gas sands in wamsutter field: Integration of diagenesis, petroleum systems, and production data. AAPG Bulletin 94(8), 1229-1266.

Tomosawa, F. and Noguchi, T. [1993] Relationship between compressive strength and modulus of elasticity of high-strength concrete. Proceedings of the Third International Symposium on Utilization of High-Strength Concrete, 1247-1254.

Torabi, A., Braathen, A., Cuisiat, F. and Fossen, H. [2007] Shear zones in porous sand: Insights from ring-shear experiments and naturally deformed sandstones. Tectonophysics 437(1-4), 37-50.

Trautwein-Bruns, U., Schulze, K. C., Becker, S., Kukla, P. A. and Urai, J. L. [2010] In situ stress variations at the variscan deformation front — results from the deep aachen geothermal well. Tectonophysics 493(1–2), 196-211.

Tuğrul, A. and Zarif, I. H. [1999] Correlation of mineralogical and textural characteristics with engineering properties of selected granitic rocks from turkey. Engineering Geology 51(4), 303-317.

Twiss, R. and Moores, E. [2007] Structural geology, 736 pp. WH Freeman and Company, New York.

Twiss, R. J. and Moores, E. M. [1992] Structural geology. WH Freeman & Company.

Ulusay, R. and Hudson, J. A. [2007] The complete isrm suggested methods for rock caracterization, testing and monitoring: 1974-2006. Suggested methods prepared by the commission on testing methods, international society for rock mechanics (isrm), I. T. N. Group (ed.), 628. ISRM Turkish National Group, Ankara.

Ulusay, R., Türeli, K. and Ider, M. [1994] Prediction of engineering properties of a selected litharenite sandstone from its petrographic characteristics using correlation and multivariate statistical techniques. Engineering Geology 38(1), 135-157.

Urai, J. L. [1995] Brittle and ductile deformation of mudrocks. American Geophysical Union, AGU 1995 fall meeting, F565, San Francisco, CA, United States.

Urai, J. L. [1995] Brittle and ductile deformation of mudrocks. EOS November 7(1995), F565.

Urai, J. L., Nover, G., Zwach, C., Ondrak, R., Schöner, R. and Krooss, B. M. [2008] Transport processes. Dynamics of complex intracontinental basins: The central european basin system, R. Littke (ed.). Springer.

Urai, J. L., Oort, E. v. and Zee, W. v. d. [1997] Correlations to predict the mechanical properties of mudrocks from wireline logs and drill cuttings. . EGS XXII General Assembly, Vienna.

Urai, J. L. and Wong, S. W. [1994] Deformation mechanisms in experimentally deformed shales. Euro. Geophys. Soc. Annales Geophysicae 12(1), C98.

van Gent, H. W., Holland, M., Urai, J. L. and Loosveld, R. [2010] Evolution of fault zones in carbonates with mechanical stratigraphy – Insights from scale models using layered cohesive powder. Journal of Structural Geology 32(9), 1375-1391.

Ván, P. [2001] Internal thermodynamic variables and failure of microcracked materials. Journal of Non-Equilibrium Thermodynamics 26(2), 167-189.

Ván, P. and Vásárhelyi, B. [2001] Second law of thermodynamics and the failure of rock materials. DC Rocks 2001, The 38th US Symposium on Rock Mechanics (USRMS).

Varga, R., Pachos, A., Holden, T., Pendrel, J., Lotti, R., Marini, I. and Spadafora, E. [2012] Seismic Inversion in the Barnett Shale Successfully Pinpoints Sweet Spots to Optimize Wellbore Placement and Reduce Drilling Risks. Society of Exploration Geophysicists.

Venkatappa Rao, G., Priest, S. and Selva Kumar, S. [1985] Effect of moisture on strength of intact rocks and the role of effective stress principle. Indian Geotechnical Journal 15(4), 246-283.

Verdier, J. [1996] The rotliegend sedimentation history of the southern north sea and adjacent countries. Geology of gas and oil under the netherlands, 45-56. Springer.

Vermilye, J. M. and Scholz, C. H. [1998] The process zone: A microstructural view of fault growth. J. Geophys. Res. 103(B6), 12223-12237.

Verweij, J. M., Echternach, M. S. C., & Witmans, N. (2009). Terschelling Basin and southern Dutch Central Graben, Burial history, temperature, source rock maturity and hydrocarbon generation: Area 2A, TNO Built Environment and Geosciences-National Geological Survey, Utrecht, The Netherlands. Built Environment and Geosciences–National Geological Survey, Utrecht, Netherlands, TNO report TNO-034-UT-2009-02065/A.

Verweij, J. M., & Witmans, N. (2009). Terschelling Basin and southern Dutch Central Graben, Mapping and modeling – Area 2A, TNO Built Environment and Geosciences-National Geological Survey, Utrecht, The Netherlands. Built Environment and Geosciences–National Geological Survey, Utrecht, Netherlands, TNO report TNO-034-UT-2009-01569

Walderhaug, O. [2000] Modeling quartz cementation and porosity in middle jurassic brent group sandstones of the kvitebjørn field, northern north sea. AAPG Bulletin 84(9), 1325-1339.

Walsh, J. [1965] The effect of cracks on the compressibility of rock. Journal of Geophysical Research 70(2), 381-389.

Walsh, J. J., Watterson, J., Bailey, W. R. and Childs, C. [1999] Fault relays, bends and branch-lines. Journal of Structural Geology 21(8-9), 1019-1026.

Walsh, J. J., Watterson, J., Heath, A. E. and Childs, C. [1998] Representation and scaling of faults in fluid flow models. Petroleum Geoscience 4(3), 241-251.

Wardlaw, N. C. and Cassan, J. P. [1978] Estimation of recovery efficiency by visual observation of pore systems in reservoir rocks. Bulletin of Canadian Petroleum Geology 26(4), 572-585.

Watts, N. L. [1987] Theoretical aspects of cap-rock and fault seals for single- and two-phase hydrocarbon columns. Marine and Petroleum Geology 4(4), 274-307.

Wawrzyniec, T. F., Jones, R. R., McCaffrey, K., Imber, J., Holliman, N. and Holdsworth, R. E. [2007] Introduction: Unlocking 3D earth systems—Harnessing new digital technologies to revolutionize multi-scale geological models. Geosphere 3(6), 406-407.

Wibberley, C. A. J., Petit, J.-P. and Rives, T. [2000] Mechanics of cataclastic deformation band faulting in high-porosity sandstone, provence. Comptes Rendus de l'Académie des Sciences - Series IIA - Earth and Planetary Science 331(6), 419-425.

Wilson, J. E., Chester, J. S. and Chester, F. M. [2003] Microfracture analysis of fault growth and wear processes, punchbowl fault, san andreas system, california. Journal of Structural Geology 25(11), 1855-1873.

Winkler, E. M. [1985] A durability index for stone. Ve congres international sur l'alteration et la conservation de la pierre. Actes. Vth international congress on deterioration and conservation of stone. Proceedings, lausanne, 25-27-9, 1985, 151-156.

Wong, T.-f. and Baud, P. [2012] The brittle-ductile transition in porous rock: A review. Journal of Structural Geology 44(0), 25-53.

Wong, T. E., Batjes, D. A. J. and Jager, J. d. [2007] Geology of the netherlands. Edita-the Publishing House of the Royal.

Wood, D. M. [1990] Soil behaviour and critical state soil mechanics. Cambridge university press.

Yagiz, S. [2009] Assessment of brittleness using rock strength and density with punch penetration test. Tunnelling and Underground Space Technology 24(1), 66-74.

Yagiz, S. and Gokceoglu, C. [2010] Application of fuzzy inference system and nonlinear regression models for predicting rock brittleness. Expert Systems with Applications 37(3), 2265-2272.

Yu, B., Cai, J. and Zou, M. [2009] On the physical properties of apparent two-phase fractal porous media. Vadose Zone Journal 8(1), 177-186.

Zhao, G. and Johnson, A. M. [1992] Sequence of deformations recorded in joints and faults, arches national park, utah. Journal of Structural Geology 14(2), 225-236.

Zhou, B., Fraser, S., Borsaru, M., Aizawa, T., Sliwa, R. and Hashimoto, T. [2005] New approaches for rock strength estimation from geophysical logs. Bowen Basin Symposium The Future For Coal—Fuel For Thought, Beeston, JW (ed.), 12-14.

Ziarani, A. S. and Aguilera, R. [2012] Pore-throat radius and tortuosity estimation from formation resistivity data for tight-gas sandstone reservoirs. Journal of Applied Geophysics 83(0), 65-73.

Ziegler, P. [1990] Geological atlas of western and central europe, shell internationale petroleum maatschappij bv/geological society of london. Elsevier, Amsterdam.

Zoback, M. D. [2007] Reservoir geomechanics. Cambridge University Press, Cambridge.